

# **Test beam and simulation studies on High Resistivity CMOS pixel sensors**

Dissertation  
zur  
Erlangung des Doktorgrades (Dr. rer. nat.)  
der  
Mathematisch-Naturwissenschaftlichen Fakultät  
der  
Rheinischen Friedrich-Wilhelms-Universität Bonn

von  
**Ruth Magdalena Muenker**  
aus  
Troisdorf

Bonn 2018

Dieser Forschungsbericht wurde als Dissertation von der Mathematisch-Naturwissenschaftlichen Fakultät der Universität Bonn angenommen und ist auf dem Hochschulschriftenserver der ULB Bonn [http://hss.ulb.uni-bonn.de/diss\\_online](http://hss.ulb.uni-bonn.de/diss_online) elektronisch publiziert.

Diese Dissertationsschrift wurde im Rahmen des Wolfgang-Gentner-Programms am europäischen Zentrum für Teilchenphysik CERN angefertigt. Betreuer: Dr. Philipp Roloff.

1. Gutachter: Prof. Dr. Klaus Desch  
2. Gutachter: Prof. Dr. Norbert Wermes

Tag der Promotion: 26.06.2018  
Erscheinungsjahr: 2018

---

*Für meine Familie* ♥

# Abstract

The Compact Linear Collider CLIC is an option for a future electron positron collider at CERN, with a centre of mass energy up to 3 TeV. The demanding physics goals at CLIC require a lightweight silicon vertex detector and a large area silicon tracker and impose challenging requirements on both, in view of a spatial resolution of a few micrometres, a timing resolution of a few nanoseconds and a material budget less than two percent of a radiation length per layer. To reach these requirements different silicon detector technologies are under investigation. Benefiting from the small fill factor design and the resulting low sensor capacitance, as well as from the possibility to implement the readout electronics in the sensor, High Resistivity CMOS sensors are attractive in view of fast timing, low material budget and large area production. In this context, High Resistivity CMOS test chips with a pixel size of  $28\ \mu\text{m}$  have been investigated using laboratory and test beam measurements and simulations. The setup used for the measurements allows for detailed studies of the full analogue response for different process variants, pixel layouts and operation conditions. Laboratory measurements show the advantage of the small fill factor design with a low noise down to  $\sim 20\ e^-$ . Corrections applied during the analysis allow for a further noise reduction down to  $\sim 10\ e^-$ . Test beam measurements show that the resulting low detection threshold allows for an improvement of the position resolution through charge interpolation, down to  $\sim 3\ \mu\text{m}$  for a pixel size of  $28\ \mu\text{m}$ . A timing resolution of  $\sim 6\ \text{ns}$  has been measured that is limited by the test setup. For low thresholds of  $\lesssim 350\ e^-$  an efficiency larger than 99% has been measured. In-pixel resolved measurements have been performed to gain a better understanding of the charge sharing and charge collection for different process variants and operation conditions. An even more detailed access to the technology could be reached with finite element simulations, showing the electric field distributions and the resulting charge propagation within the sensor. The finite element simulations have been further integrated in a simulation chain that has been developed to model the response measured in test beam experiments, including noise and energy fluctuations as well as the digitisation of the charge. The simulated response is in agreement with the test beam measurements and the simulation chain has been applied to predict the spatial resolution for different digitisation parameters. Overall, the performed studies give insights into various High Resistivity CMOS process variants and pixel designs that are relevant for CLIC and other applications.

# Contents

---

<b>1</b>	<b>Introduction</b>	<b>1</b>
<b>2</b>	<b>Introduction to particle physics and CLIC</b>	<b>3</b>
2.1	The standard model of particle physics . . . . .	3
2.2	Present and future particle colliders . . . . .	4
2.3	The Compact Linear Collider CLIC . . . . .	4
2.3.1	The CLIC physics programme . . . . .	5
2.3.2	The CLIC accelerator . . . . .	5
2.3.3	The CLIC detector model . . . . .	6
2.3.4	Requirements and layout of the CLIC vertex detector . . . . .	8
2.3.5	Requirements and layout of the CLIC tracker . . . . .	9
<b>3</b>	<b>Silicon detector principles</b>	<b>13</b>
3.1	Basic properties of silicon . . . . .	13
3.2	Doping of silicon . . . . .	14
3.3	Application of silicon for particle detectors . . . . .	14
3.3.1	pn junction . . . . .	14
3.3.2	$n^+n$ and $p^+p$ junctions . . . . .	16
3.3.3	Metal contacts . . . . .	17
3.3.4	MOS - Metal Oxide Semiconductor . . . . .	17
3.3.5	CMOS - Complementary Metal Oxide Semiconductor devices . . . . .	18
3.3.6	Basic silicon detector concept . . . . .	18
3.4	Signal formation in silicon detectors . . . . .	19
3.4.1	Signal generation in silicon . . . . .	19
3.4.2	Signal propagation and readout . . . . .	21
3.5	The importance of the capacitance and the ratio of Q/C for noise, timing measurements and low analogue power consumption . . . . .	23
<b>4</b>	<b>Silicon pixel tracking detector technologies</b>	<b>25</b>
4.1	Hybrid pixel detector technologies . . . . .	25
4.1.1	Direct coupling . . . . .	26
4.1.2	Capacitive coupling . . . . .	27
4.1.3	Silicon sensors . . . . .	27
4.2	Monolithic technologies . . . . .	30
4.2.1	High Voltage CMOS . . . . .	31
4.2.2	High Resistivity CMOS . . . . .	32
4.2.3	SOI CMOS . . . . .	34
4.3	Summary . . . . .	35

<b>5</b>	<b>Investigator HR CMOS chip and data taking setup</b>	<b>37</b>
5.1	Fabrication process and pixel layout	37
5.1.1	Fabrication process	37
5.1.2	Pixel geometry	37
5.1.3	In-pixel circuitry	38
5.1.4	Bias voltage	39
5.2	Matrix layout	39
5.3	Noise contributions	40
5.4	INvestigator ReadOut System INVROS	41
5.5	Test beam setup	42
5.5.1	CLICdp Timepix3 telescope	42
5.5.2	Investigator data taking	43
<b>6</b>	<b>Data reconstruction and analysis</b>	<b>45</b>
6.1	Investigator waveform reconstruction and event building	45
6.1.1	Reconstruction of Investigator pixel waveforms	45
6.1.2	Event building and offline synchronisation of Investigator and Timepix3 telescope data	49
6.2	Cluster and hit reconstruction	49
6.3	Alignment and track reconstruction	52
6.3.1	Telescope alignment	52
6.3.2	Telescope track finding and fitting	52
6.3.3	Investigator alignment	53
6.4	Analysis cuts	53
6.5	Observables	55
6.5.1	Definition of observables	55
6.5.2	Representation of observables	56
<b>7</b>	<b>Simulation of sensor response</b>	<b>59</b>
7.1	Geant4 simulation of the charge deposited by a particle traversing a silicon sensor	60
7.2	Finite element simulation of the sensor response with TCAD	61
7.2.1	Pixel layout	61
7.2.2	Edge effects and boundary conditions	63
7.2.3	Quasi stationary simulation	64
7.2.4	Transient simulation	66
7.2.5	Unit cell	66
7.3	Parametric model of energy and noise fluctuations and digitisation	67
7.3.1	Energy fluctuations	67
7.3.2	Noise fluctuations	68
7.3.3	Digitisation	68
7.3.4	Reconstruction of observables	69
7.4	Summary	70
<b>8</b>	<b>Results of TCAD simulations</b>	<b>71</b>
8.1	Quasi stationary simulation	71
8.1.1	Different bias voltages	72
8.1.2	Different spacings	85

8.1.3	Summary	86
8.2	Transient simulation	86
8.2.1	Different lateral incident positions - charge sharing	88
8.2.2	Different sensor depth - drift and diffusion	92
8.2.3	Impact of charge carriers on the electric field	95
8.2.4	Systematic uncertainties	99
8.2.5	Summary	103
<b>9</b>	<b>Calibration and noise characteristics</b>	<b>105</b>
9.1	Calibration	105
9.1.1	Procedure	106
9.1.2	Results for different bias voltages for the standard and modified process	107
9.1.3	Results for different spacings for the modified process	109
9.2	Noise and threshold	110
9.2.1	Procedure	110
9.2.2	Results for different bias voltages for the standard and modified process	111
9.2.3	Results for different spacings for the modified process	112
9.3	Leakage current	113
9.3.1	Procedure	113
9.3.2	Results for different bias voltages for the standard and modified process	114
9.4	Summary	115
<b>10</b>	<b>Test beam results</b>	<b>117</b>
10.1	Comparison of modified and standard process at fixed parameters and operation conditions	118
10.1.1	Cluster size and spatial resolution	118
10.1.2	Timing	123
10.1.3	Signal and efficiency	125
10.1.4	Summary	128
10.2	Scan of parameters and operation conditions	128
10.2.1	Threshold scan	129
10.2.2	Comparison of different bias voltages for the standard and modified process	133
10.2.3	Comparison of different spacings for the modified process	141
10.2.4	Summary	143
<b>11</b>	<b>Validation and application of the simulation</b>	<b>145</b>
11.1	Comparison of data and simulation	146
11.1.1	Standard process	146
11.1.2	Modified process	147
11.2	Application of the simulation	151
11.3	Summary	152
<b>12</b>	<b>Conclusions and outlook</b>	<b>153</b>
<b>A</b>	<b>Noise characteristics</b>	<b>157</b>
A.1	Pixel-by-pixel noise fluctuations	157
A.2	Noise before calibration	157
<b>B</b>	<b>Resolution for the standard process</b>	<b>161</b>

<b>Bibliography</b>	<b>165</b>
<b>List of Figures</b>	<b>173</b>
<b>List of Tables</b>	<b>183</b>

---

## Introduction

---

*High Energy Physics (HEP)* aims at the understanding of nature by the study of elementary particles and their interactions. For this purpose detectors need to be developed that can measure the properties of particles emerging from colliding high energy particle beams with high accuracy. One aim of future collider experiments is to improve the measurement precision and gain access to potentially existing new physics. This requires a large step forward for the next generation of detectors. For silicon tracking detectors, which are the topic of this thesis, several performance parameters such as the spatial and timing resolution need to be simultaneously improved while keeping a reasonable production effort and cost. This requires the invention and investigation of new technologies for future silicon tracking detectors.

This thesis presents test beam and simulation studies of a silicon pixel sensor prototype in view of the tracking detector requirements at the future Compact Linear Collider (*CLIC*) [1]. *CLIC* is a multi-TeV option for a future linear electron positron collider in the post-LHC era at CERN. The physics goals of precision Standard Model measurements and Beyond Standard Model searches at centre of mass energies up to 3 TeV set challenging requirements on the detector performance [2]. The *CLIC* detector and physics collaboration has optimised a detector design tailored specifically to the machine environment and physics constraints posed by the *CLIC* machine and the foreseen physics programme.

To reach high luminosity levels and to compensate for the low bunch train repetition rate of 50 Hz at *CLIC*, the incoming electron and positron bunches have to be focussed to the nanometre scale in the transverse plane at the interaction point. This strong focussing results in non-negligible electromagnetic interactions between the colliding bunches, creating additional background particles in the detector. These particles are overlaid to the hard physics interactions. In order to better separate the hard interaction from the out-of-time background, a time slicing of the hits in the vertex and tracking detector of the order of 10 ns is foreseen in the event reconstruction. This requires that the detectors measure the arrival time of individual particles to at least that precision.

Various silicon detector concepts are under investigation to meet the requirements for the vertex detector and tracker. To reach a low material budget forced air flow cooling is foreseen for the vertex detector. This limits the power dissipation of the readout electronics to  $\sim 50 \text{ mW/cm}^2$ . To achieve this, a large part of the electronics of the *CLIC* vertex detector is planned to be switched off during the time between two bunch trains. To meet the challenging requirements in terms of spatial resolution, analogue readout and a pixel size of  $25 \mu\text{m}$  are targeted for the vertex detector. The use of technologies, where the readout electronics is integrated in the sensor, is challenging for the vertex detector since all desired functionality needs to be implemented in the small size of a pixel cell. Thus, mainly silicon detector concepts where the readout electronics is implemented in an additional layer that is separated from the sensor are currently considered for the *CLIC* vertex detector.

For the tracker, technologies where the readout electronics are integrated in the sensor are possible since the required spatial resolution of  $7\ \mu\text{m}$  allows for a pixel size large enough to integrate all desired functionality in the pixel. Moreover, technologies with the readout electronics integrated in the sensor are attractive for the large surface and low mass tracker since the interconnection of the sensor and the readout chip can be avoided. Different CMOS technologies with the readout integrated in the sensor are under study for the CLIC tracker. Recent improvements of High Resistivity (*HR*) CMOS sensors, achieving a large depletion simultaneously with a small sensor capacitance, lead to short charge collection times compatible with the CLIC timing requirements.

HR CMOS technologies are the technology choice for the upgrade of the ALICE Inner Tracking System (*ITS*) [3]. The prototype chip studied in this thesis, the *Investigator* chip, has been originally developed as a technology demonstrator for the ALICE ITS upgrade. It includes different sections with different pixel layouts, making it an attractive test chip for a variety of applications. The chip has been implemented in two different processes [4] and the used analogue readout allows for a detailed investigation of the sensor performance for different processes, pixel layouts and operation conditions. Various test beam campaigns have been carried out with both processes and laboratory measurements have been analysed in the context of this thesis project. Complementing the experimental study of the performance of the investigated prototype detectors, finite element simulations have been used to gain a deeper microscopic understanding of the signal formation in the sensor. To complete the simulation of the full signal path including the detector frontend, a parametric model of noise and energy fluctuations and digitisation errors has been developed.

The thesis is structured as follows: first, a short introduction to particle physics, current and future particle colliders with emphasis on CLIC is given in Chapter 2, focussing on the requirements imposed on the CLIC tracking system. The basic principles of silicon detectors are explained in Chapter 3, followed by an overview of silicon tracking detector technologies in Chapter 4. Afterwards, the studied HR CMOS test chip and its readout are introduced in Chapter 5, as well as the setup for test beam measurements. This is followed by a description of the reconstruction and analysis in Chapter 6, before the developed simulation chain to model the sensor response is introduced in Chapter 7. Results are presented first for the finite element TCAD simulations (Chapter 8), followed by the presentation of the results of the calibration and noise characteristics (Chapter 9). Test beam results are summarised in Chapter 10 and discussed in relation with the trends observed in the TCAD simulations. Results of the simulation chain are compared to test beam data and an example of the application of the simulation for performance predictions is discussed (Chapter 11). Finally, a conclusion of the simulation and measurement results is drawn in Chapter 12 and an outlook is given, mentioning possible extensions of the studies presented in this thesis.

# Introduction to particle physics and CLIC

A short introduction to the Standard Model of particle physics as well as present and future colliders is given in this chapter. Afterwards, the Compact Linear Collider CLIC is introduced. A brief discussion of the CLIC machine is followed by an introduction to the CLIC physics programme. The detector model developed to meet the requirements from the physics goals in presence of the conditions defined by the machine environment is presented, focussing on the vertex detector and tracker.

## 2.1 The standard model of particle physics

The theoretical model used to describe elementary particles and their interactions is the *Standard Model (SM)* [5–8]. The elementary particles of the standard model are divided into matter particles, the fermions with an half integer spin (quarks and leptons), and mediator particles, the bosons with an integer spin. This is illustrated in Figure 2.1. The interaction between the matter particles is given by different forces,

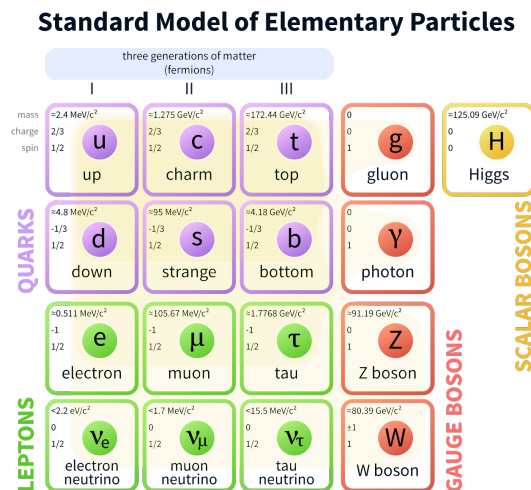


Figure 2.1: Elementary particles of the Standard Model in 2017. From [9].

the electromagnetic force, the weak force, and the strong force. The interaction of the matter particles by the forces is described by the exchange of a boson (*force carrier*): the photon for the electromagnetic

force, the W and Z bosons for the weak force and the gluon for the strong force (see red boxes in Figure 2.1). Each particle has an *anti-particle* with the inverse charge, while all other properties are the same as for the particle itself.

To test the SM of elementary particle physics and gain a more precise knowledge of fundamental particle physics, HEP experiments are performed, where particles are accelerated and collided. Many precision measurements have been performed to test the SM [10].

The electroweak theory, that unifies the electromagnetic and the weak interaction, predicts that all force carriers are massless. Experimental results have however shown that this prediction is not valid for the W and the Z boson [10].

Massive W and Z bosons and, more generally, massive particles are implemented in the SM through the Higgs mechanism [11], [12]. The *Higgs Mechanism* predicts the existence of a further particle, the Higgs boson, that has been discovered by the experiments ATLAS [13] and CMS [14] of the *Large Hadron Collider (LHC)* [15].

## 2.2 Present and future particle colliders

Presently the world's largest particle collider is the LHC. At the LHC two opposing proton beams are collided with a centre of mass energy of  $\sqrt{s} = 13$  TeV at four interaction points of a circular machine with a circumference of 27 km. To increase the statistical sensitivity to rare physics processes, the LHC accelerator and detectors are planned to be upgraded in the years from 2023 - 2025 to run with a ten times higher luminosity of  $O(10^{35}/\text{cm}^2/\text{s})$ . This project is called the *High Luminosity (HL) LHC* [16].

Different projects are under investigation for the future after the HL-LHC. One possibility is the *High Energy (HE) LHC* [17] that foresees an upgrade of the LHC accelerator, to reach centre of mass energies of  $\sqrt{s} = 26$  TeV. For a given radius, stronger deflection magnets are needed to reach higher centre of mass energies in a circular collider. Alternatively, higher centre of mass energies can be reached with the same magnets in a circular collider with a larger radius. The *Future Circular Collider (FCC)* [18], foresees the construction of a new tunnel, hosting an accelerator with a circumference of 100 km to reach centre of mass energies up to  $\sqrt{s} = 100$  TeV. Different options are currently studied for the FCC: the collision of hadrons (*FCC-hh*) as well as the option of hosting an electron positron collider in the same tunnel as a first stage of the machine (*FCC-ee*). Since the power loss from synchrotron radiation is inversely proportional to the radius and the fourth power of the mass, FCC-ee is limited by synchrotron radiation power losses to 365 GeV.

Thus, linear colliders are attractive to perform electron positron collisions because of synchrotron radiation power losses. Due to their well-defined initial state and the clean experimental environment, linear colliders are interesting machines for high precision measurements. Future possible linear electron positron colliders are the *International Linear Collider (ILC)* [19–23], aiming at a centre of mass energy up to 1 TeV and the *Compact Linear Collider (CLIC)* [1, 2, 24, 25], targeting centre of mass energies up to 3 TeV.

## 2.3 The Compact Linear Collider CLIC

CLIC is a possible future linear electron positron collider that is envisaged to be built near the site of the *Centre European pour la Recherche Nucleaire (CERN)*.

CLIC is currently in the "Development Phase", with a broad and extensive *Research and Development (R&D)* on the CLIC accelerator and the CLIC detector and physics goals. The R&D on detector

developments incorporates technology developments for several detector regions, such as a broad and extensive effort on tracking detector technologies [26–28].

### 2.3.1 The CLIC physics programme

CLIC is planned to be built and operated in three different centre of mass energy stages: 380 GeV, 1.5 TeV and 3 TeV [25]. At the highest energy stage, the CLIC accelerator complex will have an overall length of 50 km.

The different energy stages have been optimised to access different physics processes. The initial centre of mass energy of 380 GeV has been optimised to study SM top quark and Higgs physics. A rich top physics programme is accessible at a centre of mass energy of 380 GeV, including a  $t\bar{t}$  threshold scan that can be performed as well as model independent measurements of Higgs cross sections [29]. A centre of mass energy of 1.5 TeV can be built with only one single drive beam complex [25]. It provides a larger sensitivity to rare Higgs physics processes, such as double Higgs production or the associated production with two top quarks  $t\bar{t}H$ . Moreover, sensitivity to physics *Beyond the Standard Model (BSM)* can be reached. The last energy stage of CLIC at 3 TeV provides sensitivity to new physics and allows for precise measurements of the Higgs self-coupling and the HHWW quartic coupling [25]. The higher centre of mass energies of CLIC can be adapted depending on results e.g. from the LHC and the first energy stage of CLIC [25].

### 2.3.2 The CLIC accelerator

Two linear accelerator arms accelerate the electron and positron beams (*main beams*) in opposing directions, as presented in Figure 2.2, where the layout of the CLIC machine for the last energy stage of 3 TeV is shown. The two beams collide at the *Interaction Point (IP)* in the centre of the accelerator complex.

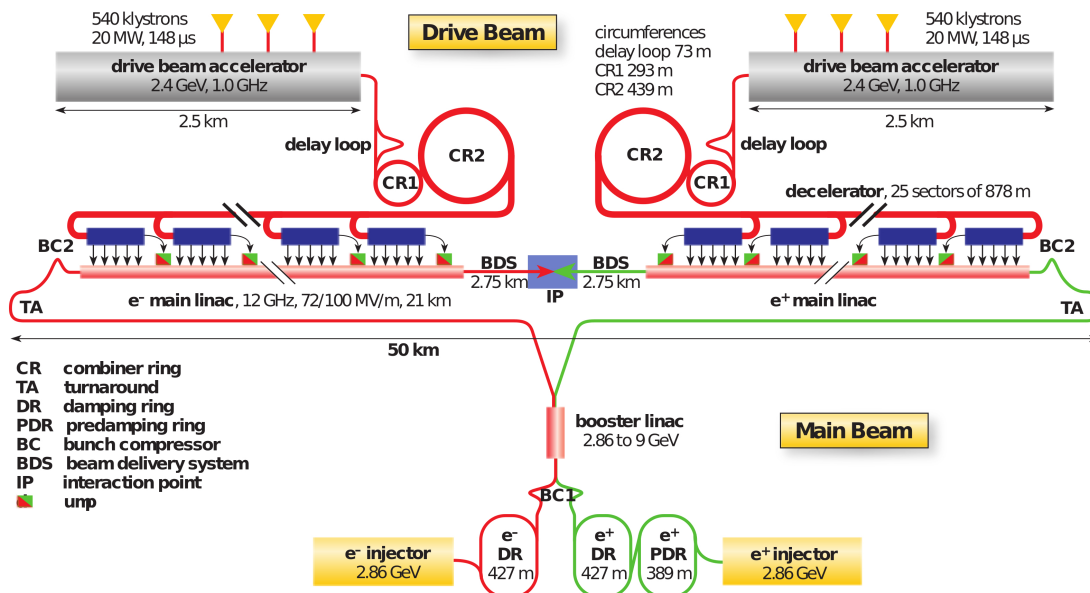


Figure 2.2: Schematic layout of the CLIC accelerator complex for the highest energy stage [25].

As illustrated in Figure 2.3, each of the main beams is structured in bunch trains. The bunch trains have a length of 156 ns and are separated by 20 ms, resulting in a 50 Hz repetition rate of the CLIC accelerator. Each train consists of 312 bunches, that are separated by 0.5 ns (*bunch spacing*).

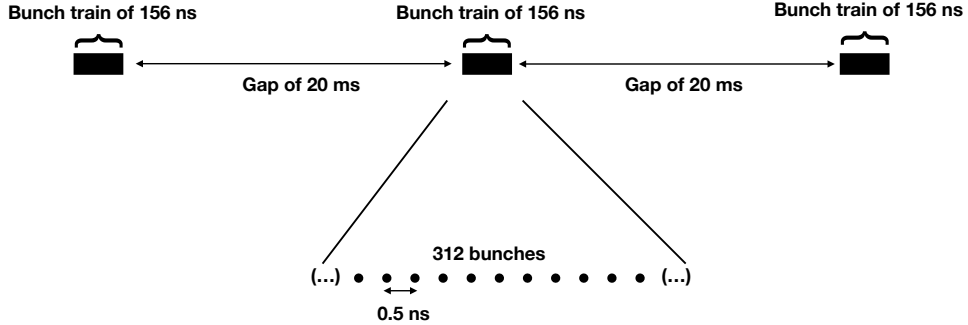


Figure 2.3: Schematic sketch of the CLIC beam structure (not to scale).

To accelerate the main beams to a maximal energy on a minimised distance, a maximal accelerating gradient is required. An acceleration gradient of 100 MV/m has been chosen for CLIC. The high field for the acceleration of the main beams is created by feeding *Radio Frequency (RF)* power with a frequency of 12 GHz into copper accelerating cavities. If the RF peak power of 9.2 TW is maintained over a longer time in the copper accelerating cavities, electrical breakdowns in the accelerating structure are more likely to occur [30]. This limits the length of a bunch train to 156 ns.

Traditional Klystron technologies are not considered for the energy stages of 1.5 TeV and 3 TeV due to their low efficiency for the generation and distribution of high RF frequencies of 12 GHz. To efficiently create and distribute the 12 GHz RF power for CLIC, a *two beam acceleration scheme* has been developed [1]. A *drive beam* with a low energy but high intensity is running parallel to each of the main beams. The drive beams are fed into *Power Extraction and Transfer Structures (PETS)*, that decelerate the drive beam and extract most of its energy. The produced RF energy is transferred via waveguides to the copper cavities and used to accelerate the lower intensity main beams.

To achieve a high integrated luminosity in a reasonable amount of time, the CLIC beam is strongly focused at the IP, to a transverse size of  $\sigma_x/\sigma_y \sim 40 \text{ nm}/1 \text{ nm}$  at a centre of mass energy of 3 TeV. Such small, dense particle bunches at high energy correspond to very strong electromagnetic fields: particles exposed to the field of the oncoming bunch may emit radiation (equivalent to *Bremsstrahlung*). For such particles, the centre of mass energy available at collision is lower than nominal. This leads to the *luminosity spectrum*, that is presented for the highest energy stage in Figure 2.4.

Moreover, the photons of the approaching beams interact with each other or the electric field of the opposing beam (*beam beam interactions*). By the choice of an opening angle of the beam pipe of  $> 10^{-2}$  rad, the main rate of particles produced in beam beam interactions that reach the main detector region, are particles produced in the collision of two photons ( $\gamma\gamma \rightarrow \text{hadrons}$ ). These are *incoherent electron positron ( $e^-e^+$ ) pairs* and hadrons ( $\gamma\gamma \rightarrow \text{hadrons}$ ).

As discussed in the next sections, timing requirements are set on the CLIC detector to mitigate the effect from the expected high rate of incoherent  $e^-e^+$  pairs and  $\gamma\gamma \rightarrow \text{hadrons}$ .

### 2.3.3 The CLIC detector model

A concept for a detector at CLIC is currently under development [32]. Full detector simulations are performed to optimise the layout of the detector with respect to the challenging requirements from the

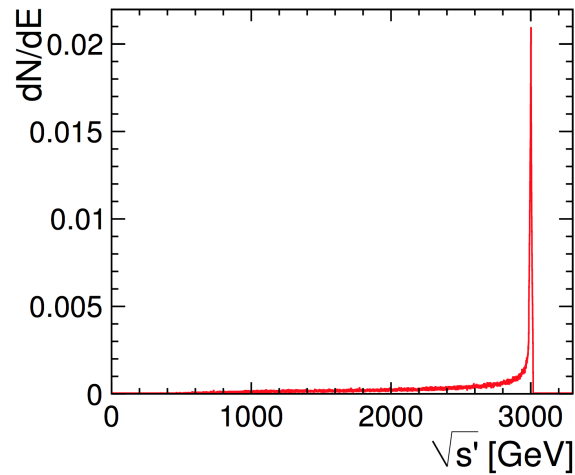


Figure 2.4: Luminosity spectrum for a CLIC centre of mass energy of 3 TeV. From [2].

physics goals and the experimental environment. Since the backgrounds from beam beam interactions are most challenging at the highest centre of mass energy stage, the CLIC detector concept has been optimised for a centre of mass energy of 3 TeV.

The current detector layout, as implemented in the simulations, is shown in Figure 2.5.

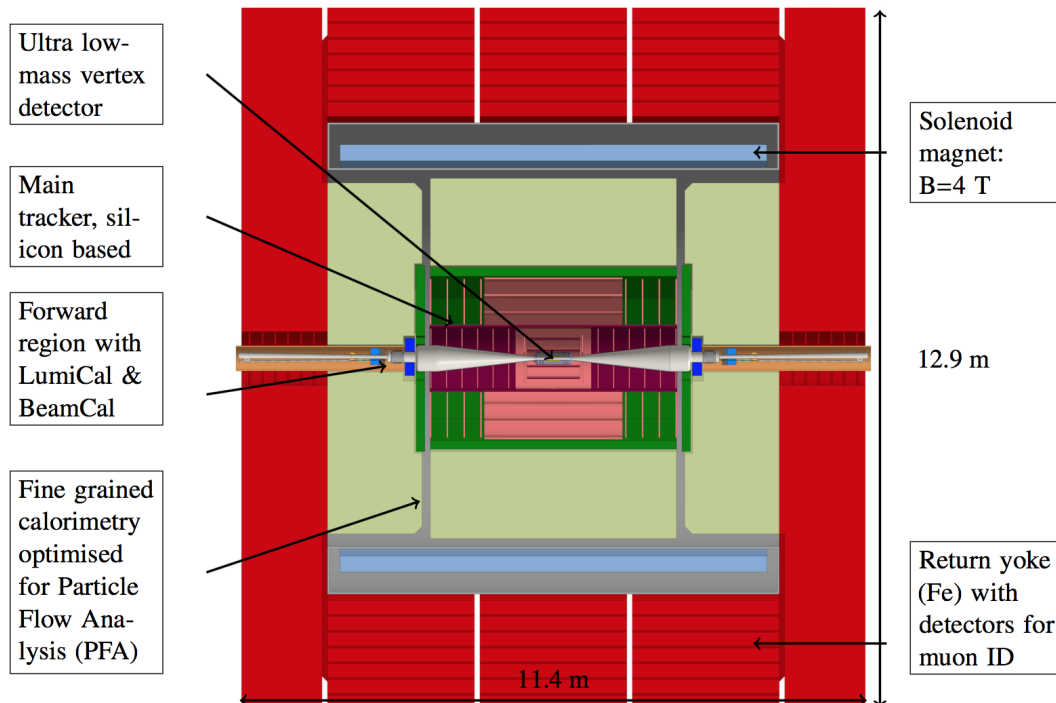


Figure 2.5: CLICdet - the CLIC detector model [32]. From [33].

Closest to the IP a light weighted silicon pixel vertex detector is placed with a material budget of  $\lesssim 0.2\%$  radiation length  $X_0$  per layer, surrounded by a large area ( $\sim 140\text{ m}^2$ ) silicon tracker.

Fine grained sandwich calorimeters are planned to be used, aiming at particle flow reconstruction. A silicon tungsten electromagnetic calorimeter (*ECAL*) with silicon diodes with a cell size of  $5 \times 5\text{ mm}^2$  in the active layers is currently under development. For the hadron calorimeter (*HCAL*) steel as absorber material and scintillator plates of  $3 \times 3\text{ mm}^2$  with Silicon Photomultipliers (*SIPMs*) as active layers are under investigation.

A superconducting coil surrounds the calorimeter system, creating a magnetic field of 4 T in the tracking and calorimeter system. The momentum of the charged particles can be measured from the resulting curvature of the tracks in the tracking system.

In the forward region of the detector fine grained radiation hard calorimeters are placed, the luminosity calorimeter (*LumiCal*) and the beam calorimeter (*BeamCal*). To measure the luminosity, the energy and trajectory of electron and positrons produced in Bhabha scattering is determined precisely in the *LumiCal*. The *BeamCal* extends the coverage of the detector down to 10 mrad and is used for the tagging of forward electrons.

The whole detector is surrounded with a return yoke, that is instrumented with detectors for muon identification.

At most one interesting physics event is expected per bunch train. To mitigate the effects from background from beam beam interactions a time slicing from 1 ns up to 10 ns is needed in the sub detectors. Then, the full bunch train is read out in the long time of 20 ms before the next bunch train arrives at the IP. Thus, the low duty cycle of the CLIC accelerator of 50 Hz allows for a *trigger less readout* of all described sub detectors.

### 2.3.4 Requirements and layout of the CLIC vertex detector

Many important physics processes such as hadronic Higgs decays or top quark decays have heavy flavour quarks in their final state [2]. The *primary vertex* is defined as the collision point. Because of the comparably long lifetime of heavy flavour hadrons, a decay vertex (*secondary vertex*) can be reconstructed and used for the tagging of heavy flavour quarks. The main requirement for the CLIC vertex detector is a precise measurement of the *transverse impact parameter*  $d_0$ , defined as the closest distance between a reconstructed track and the primary vertex.

The resolution of the transverse impact parameter can be written with the canonical parametrisation as [2]

$$\sigma(d_0) = \sqrt{a^2 + b^2 \cdot \text{GeV}^2 / (p^2 \cdot \sin^3(\theta))}, \quad (2.1)$$

with the momentum  $p$  and the polar angle  $\theta$ .

At high momenta, the constant term  $a$  and at low momenta the multiple scattering term  $b$  dominate the impact parameter resolution. As shown in simulations, a high momentum term of  $a \sim 5\ \mu\text{m}$  and a multiple scattering term of  $b \sim 15\ \mu\text{m}$  are required for CLIC [2].

These requirements can be achieved with a single point resolution of  $3\ \mu\text{m}$  and a material budget of  $\lesssim 0.2\% X_0$  per detection layer. To achieve the single point resolution, a cell size of  $(25 \times 25)\ \mu\text{m}^2$  and analogue signal readout is currently targeted for the CLIC vertex detector. The thickness allowed for the silicon sensors and for the readout chips is  $50\ \mu\text{m}$  each. *Forced air flow cooling* is envisaged for the CLIC vertex detector to reduce the material budget. This limits the power dissipation of the readout electronics to  $\sim 50\ \text{mW}/\text{cm}^2$ . To achieve this, large part of the electronics of the CLIC vertex detector are planned to be switched off during the 20 ms gap between two bunch trains (*power pulsing*).

To efficiently cool the vertex detector with forced air flow cooling, the design of the end cap layout has been adjusted, as presented in Figure 2.6, showing that the end cap disks are arranged in a spiral geometry. The vertex detector is composed of five barrel layers and four end cap spiral disks on each side of the barrel. The length of the barrel region of the vertex detector is 260 mm and the radii of the vertex barrel layers are between 31 mm and 60 mm.

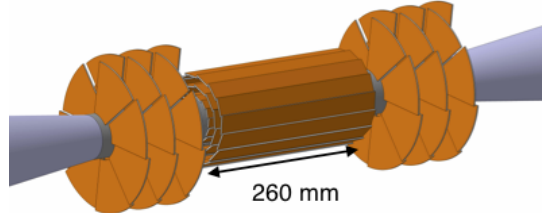


Figure 2.6: Layout of the CLIC vertex detector (orange) around the beam pipe (grey). From [32].

Moreover, to mitigate effects from beam beam background interactions, a time slicing of 10 ns is required.

Very low radiation levels are expected for the CLIC vertex detector compared to current LHC experiments. A non-ionising energy loss (*NIEL*) of  $< 10^{11} \text{ n}_{\text{eq}}/\text{cm}^2/\text{year}$  and a total ionising dose (*TID*) of  $< 1 \text{ kGy}$  are expected for the innermost vertex detector layer [31].

Overall, the requirement of simultaneously achieving a good single point resolution and a low material budget is particularly challenging: recent R&D has shown that for planar sensors with a thickness of  $50 \mu\text{m}$ , the charge sharing is significantly reduced when compared to thicker sensors. The aim of a spatial resolution of  $3 \mu\text{m}$  could not be achieved with a cell size of  $25 \mu\text{m}$  [34].

This motivates studies on alternative sensor technologies that can provide a better single point resolution via more charge sharing for a given cell size and/or studies on technologies with a smaller cell size. Smaller cell sizes are however challenging to be achieved due to the required functionality (e.g. precise time slicing, analogue readout and power pulsing).

### 2.3.5 Requirements and layout of the CLIC tracker

Simulation studies have shown that for high momentum tracks a transverse momentum resolution of  $\sigma(\Delta p_T/p_{T,\text{MC}}^2) \sim 2.5 \times 10^{-5} \text{ GeV}^{-1}$  is crucial for many physics measurements at CLIC, such as the measurement of the Higgs recoil mass [2]<sup>1</sup>

The requirement on the transverse momentum resolution translates into the requirement of a spatial resolution of at least  $7 \mu\text{m}$  in the transverse dimension of the detector. This is shown in Figure 2.7, where the transverse momentum resolution for muons simulated in the CLIC tracker barrel is presented for different spatial resolutions.

To minimise the transverse momentum resolution for low momenta, a material budget of  $\lesssim 1 - 2 \% X_0$  per layer is required for the tracker. This results in the constraint of a thickness of  $\lesssim 200 \mu\text{m}$  for the sensor and readout circuitry. The less stringent constraint on the material budget of the tracker compared

<sup>1</sup> Note that the difference between the *Monte Carlo (MC)* true transverse momentum  $p_{T,\text{MC}}$  and the reconstructed transverse momentum  $p_{T,\text{rec}}$  is referred to as  $\Delta p_T = p_{T,\text{MC}} - p_{T,\text{rec}}$  and  $\sigma(\Delta p_T/p_{T,\text{MC}}^2)$  denotes the width of a Gaussian fit to the residual  $\Delta p_T/p_{T,\text{MC}}^2$ .

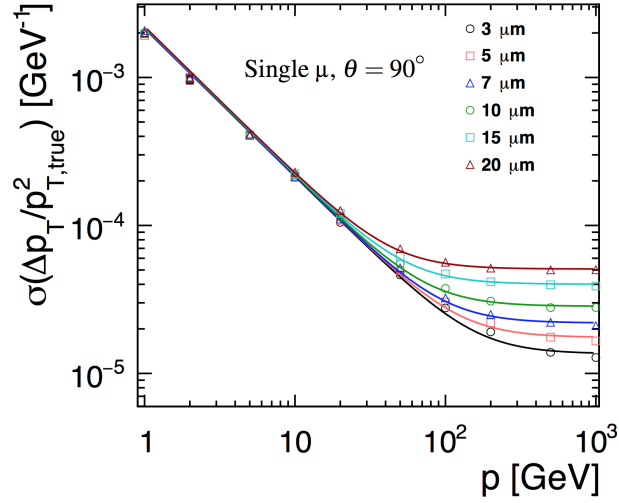


Figure 2.7: Transverse momentum resolution for different single point resolutions versus momentum for muons simulated in the barrel. From [35].

to the vertex detector allows for liquid cooling and thus a larger maximal power dissipation of the readout electronic of  $\sim 150 \text{ mW/cm}^2$  [35].

The tracker layout is sub-divided to an *inner tracker* and an *outer tracker*, separated by a carbon fibre support tube, as presented in Figure 2.8, where a quarter of the tracker and its dimensions are presented. The inner tracker is composed of three barrel layers and seven end cap disks on each side of the barrel. Three barrel layers and four tracker disks on each side of the barrel are composing the outer tracker.

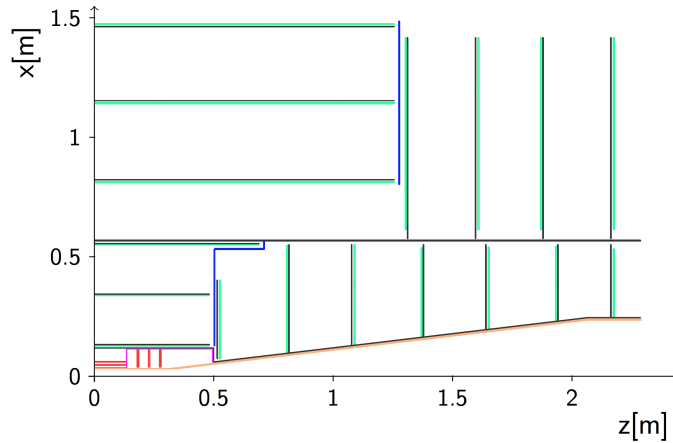


Figure 2.8: Layout of the CLIC tracker (green). The red structure presents the vertex detector, the orange structure the beam pipe. The black lines mark the support and the blue and magenta lines correspond to the cable routing path. From [35].

The arrangement of all tracker layers and end cap disks has been optimised to achieve a maximal number of hits for particles coming from the IP [32]. Overall the tracker has a large size with a surface of  $\sim 140 \text{ m}^2$ .

A time slicing of 10 ns is applied to reduce effects from background hits. To keep occupancies from beam beam interactions to a level of  $\lesssim 3\%$  the cell sizes as listed in Table 2.1 are foreseen. The innermost

Table 2.1: Cell sizes in the different tracker layers [35]. The *cell width* is defined in the  $r - \Phi$  plane transverse to the beam direction. The *cell length* is defined in the direction of the beam for the tracker barrel layers and in the direction of the radius for the tracker disks.

Detector layers	Cell length [mm]	Cell width [mm]
Inner barrel 1–2	1	0.050
Inner barrel 3	5	0.050
Outer barrel 1–3	10	0.050
Inner disc 1	0.025	0.025
Inner discs 2–7	1	0.050
Outer discs 1–4	10	0.050

tracker disks are pixelated with a cell size of  $25\ \mu\text{m}$  to sufficiently reduce the beam beam background occupancy. For the other layers a cell width of  $50\ \mu\text{m}$  and cell length from 1 mm – 10 mm are currently assumed.

Radiation levels expected for the CLIC tracker are moderate compared to current LHC experiments. A NIEL of  $< 10^{10}\ \text{n}_{\text{eq}}/\text{cm}^2/\text{year}$  and a TID of  $< 1\ \text{Gy}$  are expected for the innermost tracker layer [35].



---

## Silicon detector principles

---

In this chapter, the basic characteristics of silicon and its use for HEP detectors are summarised first. The use of silicon as a detection material is described as well as its application for the readout circuitry. Afterwards, the signal creation, propagation and formation in silicon detectors is briefly described.

### 3.1 Basic properties of silicon

In lattice structures the orbits of the single atoms overlap, resulting in a shift of the energy levels and the creation of *energy bands*. The *Fermi energy* is a characteristic property for the description of the occupancy probability of the energy states with the Fermi Dirac distribution. The Fermi energy defines the energy at which the occupancy probability is half. All energy states up to the Fermi energy are filled for a temperature of 0 K. The *valence band* is the highest fully occupied energy band at a temperature of 0 K. With increasing temperature, the electrons can be thermally excited to the next higher energy band, the *conduction band*, depending on the energy band structure. Since the states in the conduction band are not fully occupied the electrons can move freely in the conduction band through the lattice structure.

Materials can be classified according to their energy band structure and Fermi energy level as *conductors*, *semiconductors* and *insulators*.

For conductors, the valence band and conduction band overlap, such that the Fermi energy lies within the conduction band. Accordingly, free electrons occupy the conduction band.

Insulators are materials with a large energy gap between the valence and the conduction band and a Fermi energy above the valence and below the conduction band. Even at higher temperatures this energy gap is too large to excite electrons into the conduction band.

The Fermi energy of semiconductors also lies between the valence and the conduction band. Thus, semiconductors behave as insulators at a temperature of 0 K. However, semiconductors have a smaller energy gap between the valence and the conduction band. Silicon is a semiconductor with an energy gap of  $E_g = 1.12 \text{ eV}$  [10]. Electrons can be thermally excited at higher temperatures and occupy the conduction band. If an electron is thermally excited to the conduction band, the remaining non occupied state in the lower energy band is referred to as a *hole*. Similar to the excitation of electrons in the conduction band, electrons of the conduction band can *recombine* with the holes in the valence band. For a given temperature, the number of electrons in the conduction band ( $n$ ) and holes in the valence band ( $p$ ) is balanced

$$n \cdot p = n_i^2 \quad (3.1)$$

and the concentration of these charge carriers  $n_i$  is referred to as *intrinsic concentration*. Accordingly,

the silicon material is referred to as *intrinsic silicon*.

## 3.2 Doping of silicon

Impurity atoms can be inserted in the silicon lattice (*doping*), to add energy levels between the valence and the conduction band and thus change the electrical properties of the silicon intentionally. Silicon is a group IV element, with four electrons in the valence band.

Silicon with additional group V element atoms is referred to as *n type silicon*. The excess of electrons shifts the Fermi energy to higher levels closer to the conduction band and creates an additional energy band close to the conduction band. The atoms with more electrons in the valence band compared to silicon are named *donors*. A typically used element for the n doping of silicon is phosphorus.

The excess of holes by the insertion of a group III elements into the silicon (*p type silicon*), results in a shift of the Fermi energy to a lower level and the creation of an additional energy band close to the valence band. Elements with one valence electron less compared to silicon are named *acceptors*. A typically used element for the p doping of silicon is boron.

The change of the electric properties of the silicon via doping can be described by the conductivity  $\sigma$  or the resistivity  $\rho$

$$\sigma = 1/\rho, \quad \rho = 1/(q_e \cdot N \cdot \mu). \quad (3.2)$$

The electron charge is given as  $q_e$ ,  $N$  is the dopant concentration and  $\mu$  the *mobility* of the majority charge carriers (electrons for n type silicon and holes for p type silicon). The mobility is proportional to the speed of movement (*drift velocity*) of the charge carriers through the silicon lattice and inversely proportional to the electric field. It depends on various parameters, such as the temperature or the type of the moving charge carriers (electrons or holes).

A full silicon *bulk* can be doped (denoted in the following as n or p), however, also a precise placement of locally restricted highly doped regions can be achieved, that is usually referred to as an *implant*. The high implant doping is denoted as  $n^{+/-}/p^{+/-}$ , depending on the doping type. The type of the doping (n type or p type) is usually referred to as the *polarity*.

## 3.3 Application of silicon for particle detectors

In intrinsic silicon the concentration of charge carriers is orders of magnitude higher compared to the number of charge carriers expected from the interaction of a particle with the silicon material. Thus, to make use of silicon to detect particles, the number of charge carriers needs to be reduced. As discussed in the following, this can be realised by joining n type and p type silicon in a *pn junction*.

### 3.3.1 pn junction

In the following a planar pn junction is discussed. A gradient of charge densities is created by the combination of n type and p type silicon (*pn junction*), that causes the electrons from the n type region to diffuse to the p type region and the holes from the p type region to diffuse to the n type region to level out the different Fermi energies. The electrons that diffuse to the p type region recombine with the holes and the holes in the n type region recombine with the electrons, creating a region without charge carriers (*depleted region*). The atoms of the dopants remain as fixed charges in the depleted region, negatively charged in the p type silicon and positively charged in the n type silicon. The resulting potential difference acts against the diffusion of the charge carriers and the evolution of the depleted region is stopped when

the current from the diffusion of the charge carriers and the current from the potential difference are balanced (*thermal equilibrium*).

The potential in the pn junction is referred to as the *built-in potential* and can be calculated by solving the Poisson equation that describes the potential  $\Phi$  in dependence of the position  $x$

$$\frac{d^2\Phi(x)}{d^2x} = -\frac{\rho(x)}{\epsilon_0 \cdot \epsilon_r}, \quad (3.3)$$

with the permittivity in vacuum  $\epsilon_0$  and the relative permittivity of silicon  $\epsilon_r$  [10]. The solution of the Poisson equation in the p and n doped region can be calculated as

$$\Phi(x) = \begin{cases} \frac{-N_a}{2 \cdot \epsilon_0 \cdot \epsilon_r} \cdot (x + d_p)^2 & \text{in p type silicon.} \\ \frac{N_d}{2 \cdot \epsilon_0 \cdot \epsilon_r} \cdot (x + d_n)^2 & \text{in n type silicon.} \end{cases} \quad (3.4)$$

The dopant concentrations for acceptors and donors are given as  $N_a$  and  $N_d$ , while the thickness of the depleted region in the p and n type silicon is given as  $d_p$  and  $d_n$ . The voltage of the built-in potential  $V_{bi}$  can be calculated by evaluating equation 3.4 at the border between the n and p type silicon

$$V_{bi} = \frac{|N_{eff}|}{2 \cdot \epsilon_0 \cdot \epsilon_r} \cdot d^2. \quad (3.5)$$

with the effective doping  $N_{eff}$  and the overall thickness of the depleted region  $d$ . Equation 3.5 shows that the thickness of the depleted region without an externally applied voltage is inversely proportional to the square root of the effective doping: a lower doping (higher resistivity) results in a larger depleted region.

### Reverse bias

To increase the thickness of the depleted region for a given doping, an external bias voltage  $V_{bias}$  can be applied

$$d(V_{bias}) = \begin{cases} \sqrt{\frac{2 \cdot \epsilon_0 \cdot \epsilon_r}{|N_{eff}|} \cdot (V_{bi} + V_{bias})} & \text{if } (V_{bi} + V_{bias}) > 0. \\ 0 & \text{if } (V_{bi} + V_{bias}) \leq 0. \end{cases} \quad (3.6)$$

The diode created by the pn junction can be operated with *forward bias*, that allows a current to flow through the pn junction if the voltage of the built-in potential is acceded and the depletion thickness is zero or *reverse bias*, that extends the depletion thickness and is normally used for the application of silicon for particle detection to create a maximised sensitive volume. Equation 3.6 shows that the thickness of the depleted region with an externally applied reverse bias voltage is proportional to the square root of this applied voltage: a higher reverse bias voltage results in a larger depleted region.

### Characteristic properties

In the following, a few characteristics of a reversely biased pn junction, that are important for the principle of particle detection, are discussed.

**Capacitance** A capacitance can be calculated for a depleted region that evolves from a pn junction. This component of the capacitance is usually dominant for reverse biased junctions. As explained later in Section 3.5, this capacitance can significantly impact the magnitude of the noise and the readout signal.

Assuming the simplified model of a planar pn junction, the depleted region acts like a plate capacitor and the capacitance of the pn junction  $C_j$  can be calculated as

$$C_j = A \cdot \frac{\epsilon_0 \cdot \epsilon_r}{d} = A \cdot \sqrt{\frac{\epsilon_0 \cdot \epsilon_r \cdot |N_{eff}|}{2 \cdot (V_{bias} + V_{bi})}}, \quad (3.7)$$

where the area of the junction is denoted as  $A$ . The capacitance of the junction can be reduced by the application of higher bias voltages or lower doping concentrations (i.e. enlarging the depleted region), or by reducing the area of pn junction.

**Leakage current** A constant current can be measured in silicon detectors, even at the absence of a signal. This current is referred to as *leakage current*. An understanding of the leakage current is important to estimate its contribution to the measured signal in a silicon detector and understand its contribution to the noise (see Section 5.3).

The main contribution to the leakage current can be attributed to free charge carriers that are created by thermal excitations in the depleted volume. Since this contribution is proportional to the volume of the depleted region it is referred to as *volume current*

$$I_{vol} \propto T^2 \cdot e^{-E_g(T)/(2kT)}, \quad (3.8)$$

with the temperature  $T$ , the energy gap  $E_g$  and the Boltzmann constant  $k$  [10]. Beside this thermal generation of charge carriers, another contribution of the leakage current is coming from charge carriers that diffuse from the non-depleted silicon volume into the depleted region. Both contributions depend strongly on the temperature and are inversely proportional to the lifetime of the charge carriers.

Another contribution to the leakage current can come from surface effects or edge defects and are usually summarised as (*surface currents*). This contribution depends on processing parameters and the exact silicon detector layout as well as on the temperature and lifetime of the charge carriers in the silicon.

Moreover, in experimental setups such as the one discussed in this thesis (see Chapter 5.5), a full isolation of the detector from photons from light sources is often difficult. A constant flux of photons can create a signal that adds up to the measured leakage current.

### 3.3.2 $n^+n$ and $p^+p$ junctions

For the junction of silicon with the same type but different doping levels ( $n^+n$  or  $p^+p$ ) the charge gradient over the junction results in a diffusion of the charge carriers from the higher to the lower doped region. As for the pn junction a potential difference is created by the remaining fixed dopant atoms. The resulting electric field stops the diffusion process and a built-in voltage characterises the junction at thermal equilibrium.

Thus, the junction between silicon with the same type but different doping levels can be described with the dependencies and characteristics discussed in the previous sections for the pn junction. However, the charge gradient is much smaller and thus also the built-in potential.

### 3.3.3 Metal contacts

In particle detectors ohmic metal contacts are used to either apply a voltage to the silicon (*bias contact*) or read out the signal generated by a particle in the silicon (*readout contact*). Moreover, contacts between metal oxide and silicon (*MOS*) are used to implement elements of CMOS circuitry.

#### Ohmic silicon metal contacts

Different cases can be distinguished when joining metal and silicon, according to the energy that is needed to bring an electron from the Fermi level out of the lattice bound into the vacuum (*work function*). The work functions of metals depend on the material. Aluminium is often used to make bias and readout contacts for particle detectors. For semiconductors the work function can be changed by changing the Fermi energy with different doping values.

Schottky barrier contacts are silicon metal contacts with a (often unwanted) rectifying behaviour, rather than silicon metal contacts with an resistive behaviour (*ohmic contact*). To create an ohmic contact the potential barrier between the metal and the silicon needs to be minimised such that the electrons can traverse the transition region with almost no resistance. This can be realised by a heavy doping level ( $O(10^{19}/\text{cm}^2)$ ) and metals with a small work function.

### 3.3.4 MOS - Metal Oxide Semiconductor

In contrast to the metal silicon contacts, an additional insulation layer can be placed between the metal and the silicon (*MOS*), such that no charge carrier current can flow through the oxide. Metal and silicon can separately be considered to be in thermal equilibrium (their Fermi energies are different). However, a potential difference on the oxide silicon interface causes the energy bands in silicon to bend, resulting in accumulation of charge carriers at the silicon oxide interface. Figure 3.1 illustrates the energy bands in a MOS structure with n type silicon, where Sketch (a) illustrates the described *accumulation mode*.

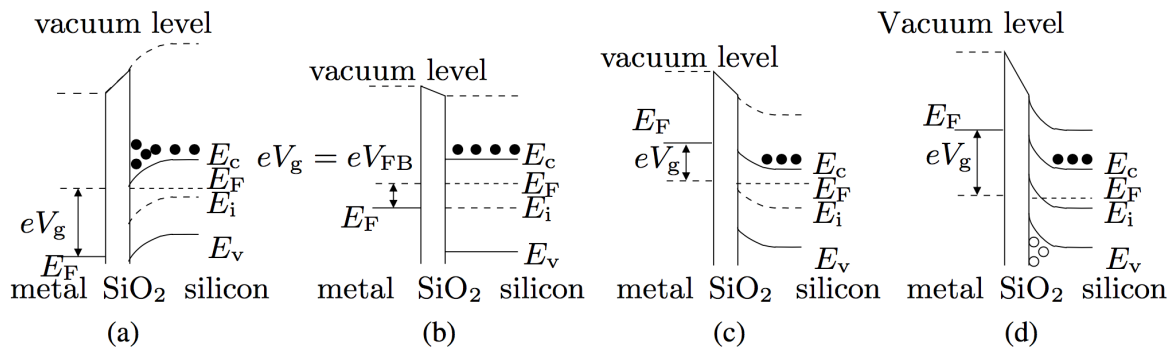


Figure 3.1: Different MOS operation modes. Sketch (a) illustrates the accumulation, Sketch (b) the flat band, Sketch (c) the depletion and Sketch (d) the inversion operation mode, as discussed in the text. From [36].

Applying a voltage in inverse direction to the potential difference between the metal and the semiconductor, the potential difference between metal and semiconductor can be levelled out (*flat band condition* in Sketch (b) of Figure 3.1). Going to higher values with the same polarity, minority charge carriers accumulate at the silicon oxide interface and recombine with the majority charge carriers, such that a depleted region is created (Sketch (c) of Figure 3.1). At even higher voltages, no majority charge carriers

are left for recombination and an accumulation of minority charge carriers is present at the oxide silicon interface. This is referred to as *inversion* and illustrated in Sketch (d) of Figure 3.1.

MOS structures can be used as transistors to steer a current flow and have an extraordinary importance for present microelectronics designs and developments.

### 3.3.5 CMOS - Complementary Metal Oxide Semiconductor devices

Complementary Metal Oxide Semiconductor (*CMOS*) devices make use of a p and n channel Metal Oxide Semiconductor Field Effect Transistor (*MOSFET*) on a common substrate. A p channel MOSFET is referred to as *PMOS*, an n channel MOSFET is referred to as *NMOS*. Figure 3.2 illustrates a CMOS structure, combining both.

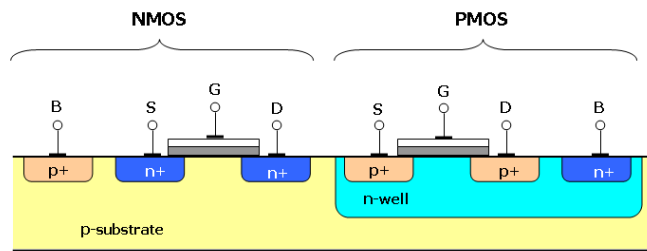


Figure 3.2: Schematic of a CMOS structure with an n and p type MOSFET, as described in the text. The metal is marked in white and the oxide in grey. From [37].

MOSFETs are four channel devices, consisting of a *source* (S), a *drain* (D), a *gate* (G) and a *body*. The source and drain are implants, that are locally separated on the surface of a silicon body. The distance of source and drain is referred to as the *minimum gate length*, an important characteristic of CMOS devices to quantify the amount of CMOS logic and thus the complexity possible in a certain space. Source and drain are connected to ohmic metal contacts. On the surface in the region between the source and drain, a MOS structure is placed. Changing the voltage between the gate and the source (*gate to source voltage*), the different MOS operation modes can be used to steer a current flow between source and drain.

The combination of NMOS and PMOS to a CMOS structure is attractive for logic designs, due to the resulting very low static currents: a voltage that allows a current flow through the NMOS blocks the current flow through the PMOS and vice versa. Main advantages of CMOS technologies are a low power dissipation and the fact that less resistors, producing heat dissipation, are needed in the circuitry [38].

In the silicon detector used in this thesis CMOS circuitry is used, for example to implement a source follower in the pixel design.

### 3.3.6 Basic silicon detector concept

Silicon detectors are composed of a silicon *sensor*, where the signal is generated and the readout, that can be designed using e.g. CMOS circuitry. As discussed in the next Chapter 4, the readout circuitry can be contained in a separate layer (*hybrid detectors*) or directly in the sensor layer (*integrated* or *monolithic detectors*).

Silicon sensors consists of a silicon *bulk*, where a depleted region can be created by the application of a bias voltage. The bias voltage is applied to ohmic metal contacts that are directly connected to highly doped silicon on the sensor *frontside* or *backside*. The sensor frontside refers to the side where the signal is read out.

To read out the signal created by a particle traversing the silicon sensor, implants with a high doping concentration (typically in the order of  $10^{19}/\text{cm}^2$ ) are placed to frontside of the sensor and connected to ohmic metal contact placed directly at the surface of the silicon. To gain information on the position parallel to the surface of the silicon where the charge carriers are created, the implants are segmented. For the silicon detector studied in this thesis the segmentation is done on an equal grid in both dimensions of the surface. One periodic unit cell of the structure is referred to as a *pixel*. The highly doped implantation for the readout of the current is referred to as the *pixel implant* or *collection electrode*. The latter name is derived from the fact that the high implantation of the pixel implant not only creates the ohmic contact but also collects the charge (see next Section 3.4).

A silicon sensor with p type pixel implants and an n type body bulk is referred to as *p in n* and vice versa.

### 3.4 Signal formation in silicon detectors

In this section the formation of a signal in silicon for different types of incident radiations is introduced. Afterwards the general concept of the signal readout for silicon detectors is discussed.

#### 3.4.1 Signal generation in silicon

If a particle traverses the depleted region of silicon detectors, it can deposit energy due to its interaction with the silicon material. With part of this energy electrons can be excited in the conduction band and electron hole pairs are created that can be detected as a signal. Part of the energy is used for phonon creation. Thus, the average energy needed to create an electron hole pair in silicon is with a value of 3.6 eV larger than the band gap in silicon of 1.12 eV.

#### Interaction of charged particles with matter

In this thesis a beam of pions with a momentum of 120 GeV has been used to characterise thin silicon detectors with a thickness of  $100\ \mu\text{m}$  and a depleted region of  $\sim 20\ \mu\text{m}$ . In the following the main aspects to describe the interaction of particle beams with detectors are briefly summarised. For a detailed description the reader is referred to [10].

**Energy loss** For charged particles heavier than the electron rest mass the mean energy loss  $dE/dx$  when traversing material is described by the *Bethe Bloch formula*

$$-\frac{1}{\rho} \left\langle \frac{dE}{dx} \right\rangle \propto z^2 \cdot \frac{Z}{A} \cdot \frac{1}{\beta^2} \cdot \frac{1}{2} \cdot \left( \ln \left( \frac{2 \cdot m_e c^2 \beta^2 \gamma^2 T_{\max}}{I^2} \right) - \beta^2 \right) \quad (3.9)$$

with the electron mass  $m_e$ , the atomic number  $Z$ , mass  $A$  and mean excitation energy  $I$  of the traversed material and the charge of the traversing particle  $z$ . The velocity  $v$  of the traversing particle is described in units of the speed of light  $c$  by  $\beta = v/c$  and  $\gamma = 1/\sqrt{1 - \beta^2}$  gives the relativistic Lorentz contraction of a particle with a certain velocity.

Different regions of the Bethe Bloch formula can be identified for different values of  $\beta\gamma$ : for small values of  $\beta\gamma \ll 3$  the incident particle loses most of its energy in ionisation and is usually stopped in the silicon detector. At a value of  $\beta\gamma \sim 3$  a minimum ionisation is reached because of the shorter interaction time of faster particles. This results in a minimal energy loss, such that particles in this

range are referred to as Minimum Ionising Particles (*MIPs*). The minimum energy loss value is very similar for particles of different types. *MIPs* traverse the full silicon detector and deposit energy along their trajectory. An example of particles with this property are 120 GeV pions, as used in this thesis for the characterisation of silicon detectors. Their energy loss normalised to the density of the traversed material is  $\sim 1.7 \text{ MeVcm}^2/\text{g}$  [39]. At large values of  $\beta\gamma \gg 3$  the energy loss increases again due to the contribution of radiative processes that increases for higher velocities.

Corrections have to be made to the Bethe Bloch formula for electrons and positrons, taking into account their low mass and the resulting contribution of energy loss via Bremsstrahlung, as well the interaction with identical particles in the silicon, the electrons of the silicon atoms [10].

**Energy loss fluctuations** While the Bethe Bloch formula describes the mean energy loss of charged particles, stochastic fluctuations impact the energy loss of a single particle passing the material. These fluctuations can be attributed to variations of the number of interactions and variations of the exchanged energy per interaction. A large energy can be transferred when the traversing particle collides with an electron of a silicon atom in a head on collision and the electron of the silicon atom can be kicked out of the bound state. These *delta* ( $\delta$ ) rays or *secondary electrons* pass the silicon on a trajectory that is different from the initial particle track and create further electron hole pair along their trajectory, that result in a large fraction of absorbed energy [40]. The *Landau distribution* approximately describes these fluctuations with a distribution that shows a Gaussian core with significant tails to higher energies that can be attributed to  $\delta$  rays. Thus, the *Most Probable Value (MPV)* is significantly lower than the mean value of the distribution. The Landau distribution  $f_L(\lambda)$  is defined by the integral

$$f_L(\lambda) = \frac{1}{\pi} \int_0^{\infty} e^{-t \cdot \ln(t) - \lambda \cdot t} \cdot \sin(\pi t) dt, \quad (3.10)$$

with the variable  $\lambda$  describing the tails of the distribution.

**Very thin silicon** Due to a lower number of interactions of the traversing charged particle with the silicon atoms the fluctuations are more prominent for thin silicon. The energy loss is accurately described by the Landau distribution for silicon with a thickness of  $\gtrsim 300 \mu\text{m}$ . For thinner silicon, as studied in this thesis, the *Bichsel model* gives a more accurate description of experimental data [40]. Moreover, corrections have to be made to the Bethe Bloch formula for very thin silicon, since  $\delta$  rays can leave the silicon without depositing all their energy [10].

**Multiple scattering** Scattering processes of the incoming particle deflect their trajectory by small angles and are mostly attributed to coulomb scattering with the nuclei of the silicon atoms [10]. The *Root Mean Square (RMS)* of the distribution of scattering angles is dependent on the momentum  $p$ , velocity  $\beta$  and charge  $z$  of the traversing particle and the thickness of the traversed material in units of radiation length  $x/X_0$

$$\theta_{\text{ms}}^{\text{RMS}} \propto \frac{z}{p \cdot \beta} \cdot \sqrt{\frac{x}{X_0}} \cdot \left( 1 + 0.036 \cdot \ln \left( \frac{x}{X_0} \right) \right). \quad (3.11)$$

Thus, a higher momentum and velocity of the traversing particle reduces the width of the distribution of scattering angles, while a larger material budget increases the width of the distribution of scattering angles. This process is referred to as *multiple scattering* and is important for the achievable measurement precision.

### Interaction of photons with matter

In this thesis a  $^{55}\text{Fe}$  source, emitting photons with an energy of 5.89 keV (K-alpha lines) and 6.45 keV (K-beta line) [10], has been used to characterise the silicon detector. The interaction of photons in matter is briefly summarised in the following. More information can be found elsewhere [10].

The interaction of photons with matter is mainly given by three different processes: the *photo effect*, the *Compton effect* and the *pair production*.

At low photon energies ( $\lesssim 10$  keV in silicon<sup>1</sup>) the interaction of photons with the silicon is dominated by the photo effect. The incoming photon is stopped in the silicon and all its energy is transferred to a silicon atom. An electron of the silicon atom is excited from the orbit that creates electron hole pairs along its trajectory.

At higher energies between 100 keV and 1 MeV the interaction of photons with the silicon is dominated by the Compton effect, where the incoming photon scatters with an electron of a silicon atom.

At even higher energies of  $\gtrsim 1$  MeV, the interaction of photons with the silicon is dominated by the pair production. The incoming photon interacts with the electric field of a nucleus of a silicon atom and converts into an electron positron pair.

For the energy of photons from an  $^{55}\text{Fe}$  source the interaction is dominated by the photo effect. The probability of contributions from the Compton effect is approximately three orders of magnitude lower [10]. For photon energies of 5.89 keV the range of the primary electron from the photo effect is smaller than  $1\ \mu\text{m}$  [41]. Thus, the interaction can be assumed to be point like.

The absorption of the photons in silicon can be described by the loss of intensity  $I(x)$  of a photon beam after traversing a thickness  $x$  of the silicon

$$I(x) = I_0 \cdot e^{-x/\lambda}, \quad (3.12)$$

with the intensity  $I_0$  of the photon beam before entering the silicon and the *attenuation length*  $\lambda$ , giving the depth after which the intensity of the photon beam is reduced by a factor of  $1/e$ . The attenuation length depends on the material of the detector and the energy of the photon.

For photons from a  $^{55}\text{Fe}$  source the attenuation length is  $29\ \mu\text{m}$  (K-alpha lines) and  $37\ \mu\text{m}$  (K-beta line) [42]. The depletion of the studied sensor ranges up to a depth of  $\sim 20\ \mu\text{m}$ . Thus, a contribution of photon being stopped (*photon conversion*) in the non-depleted part of the studied silicon detector can be expected.

#### 3.4.2 Signal propagation and readout

The propagation and readout of the signal in silicon is briefly summarised by discussing the dependencies of relevant equations. A derivation of the equations and more informations can be found elsewhere [38].

##### Signal propagation - drift and diffusion

Electron hole pairs created in the silicon sensor can move either by *drift* or *diffusion*.

The diffusion describes the random movement of the charge carriers in the silicon, if the force of the electric field on the charge carriers is negligible. The charge carriers scatter with the silicon lattice or the impurity atoms. A characteristic parameter for the movement of the charge carriers via diffusion is the *mean free path length*, describing the mean path between the scattering. The mean free path length of electrons and holes in silicon is  $\sim 0.1\ \mu\text{m}$  [36]. Due to the random nature of the diffusion, the averaged

<sup>1</sup> The cross section of the photo effect strongly depends on the atomic number  $Z$  of the material.

travelled distance of the charge carriers in equilibrium is zero. However, if a particle traverses the silicon, electron hole pairs are created, resulting in a gradient of charge carriers. The random movement of the charge carriers via diffusion follows the charge carrier gradient, resulting in an averaged traveled distance of the charge carriers that is larger than zero and a current inverse to the charge carrier gradient is created.

The drift describes the additional movement of the charge carriers in the presence of an electric field. The *drift velocity*  $v$  can be described as a function of the mobility  $\mu$  and the electric field strength  $E$

$$v = \mu \cdot E. \quad (3.13)$$

The overall current  $J_{e/h}$  created by drift and diffusion of electrons  $e$  or holes  $h$  can be written as a function of the charge  $q$ , the mobility  $\mu_{e/h}$ , the charge carrier concentration  $n_{e/p}$  the electric field  $E$  and the electron and hole concentration  $n_{e/h}$

$$J_{e/h} = q \cdot \mu_{e/h} \cdot n_{e/p} \cdot E + q \cdot D_{e/h} n_{e/h}. \quad (3.14)$$

The first term describes the movement of the charge carriers via drift, the second term describes the movement of the charge carriers via diffusion in dependence of the diffusion constant  $D_{e/h}$ . The diffusion constant can be expressed as a function of the mobility of the charge carriers and the temperature  $T$  using the Einstein relation

$$D_{e/h} = \frac{k \cdot T}{q} \cdot \mu_{e/h}, \quad (3.15)$$

with the Boltzmann constant  $k$ , showing that the diffusion of the charge carriers is proportional to their mobility.

As presented in equation 3.2, the mobility is inversely proportional to the charge of the moving charge carriers and is thus approximately a factor of three lower for holes compared to electrons. Moreover, the mobility depends on the temperature due to different scattering probabilities for different temperatures and on the electric field. The dependency on the electric field can be understood considering equation 3.13. The mobility is constant at low electric field strength  $\lesssim 10^3$  V/cm [38] since in this range the drift velocity is proportional to the electric field. At higher electric fields the drift velocity saturates, resulting in a change of the mobility to lower values. Typical values for the mobility of electrons and holes in silicon are [38]

$$\mu_e \sim 1450 \text{ cm}^2/(\text{Vs}), \quad \mu_h \sim 500 \text{ cm}^2/(\text{Vs}). \quad (3.16)$$

However, as shown in equation 3.2, the mobility is also dependant on the dopant concentration and thus different for various silicon materials.

Note that in presence of a magnetic field the movement of charge carriers changes due to the Lorentz force acting on them, as discussed in more detail elsewhere [38].

### Readout signal

The creation of a signal on the pixel implant is described by Ramo's theorem [43]. Ramo's theorem describes the current  $I$  induced on a collection electrode as

$$I = q \cdot E_w v, \quad (3.17)$$

with the charge  $q$  of the moving charge carrier, its velocity  $v$  and the weighting field  $E_w$ . The weighting field correlates the movement of a charge carrier to an induced current on the collection electrode. Thus, a current is induced on the electrode during the whole time of the movement of the charge carrier and not only when the charge carrier arrives physically at the collection electrode.

### 3.5 The importance of the capacitance and the ratio of $Q/C$ for noise, timing measurements and low analogue power consumption

Some characteristic properties for the performance of silicon detectors are the noise, the *signal to noise ratio* (SNR) and the analogue power consumption, i.e. the power needed to amplify the readout signal.

A low noise is important to measure small signals with a low detection threshold. A large SNR is favourable for better timing measurements. The specific characteristics of signal and noise depend on the exact design of the sensor and the readout circuitry. Frequently used circuitry for silicon detectors in HEP consist of a preamplifier and a shaper. At the output of the shaper, thermal and  $1/f$  noise contributions are proportional to the capacitance [36]. Further, the signal is measured as the charge over the capacitance, resulting in a magnitude of the measured voltage signal inversely proportional to the total capacitance. Accordingly, a lower capacitance reduces the noise and improves the SNR and is therefore attractive for a low detection threshold and fast timing measurements.

Moreover, it has been shown [44] that when the thermal noise of the input transistor is dominant (which is often the case), the analogue power consumption for a given SNR  $P_{\text{analogue}}$  is inversely proportional to the charge  $Q$  and proportional to the capacitance  $C$

$$P_{\text{analogue}} \propto \left(\frac{Q}{C}\right)^{-m} \quad \text{with } 2 \leq m \leq 4. \quad (3.18)$$

Thus, the analogue power consumption can be significantly reduced by minimising the capacitance.



---

## Silicon pixel tracking detector technologies

---

Silicon pixel detector technologies have a wide range of applications in HEP detectors. Among other applications (such as fine grained calorimetry) they are used for tracking of charged particles. They are applied for this purpose in current experiments at the LHC and are tracking detector technology options for different future colliders.

Depending on the physics requirements and machine environment, different requirements are imposed on the silicon tracking detectors, resulting in different technology choices. Requirements for future high precision lepton colliders have been discussed with focus on CLIC in Chapter 2.3.4 and 2.3.5. Requirements at hadron colliders differ mainly in view of hit rates and radiation tolerance that play a major role at high luminosity hadron machines. One example referred to in this Chapter is the HL-LHC.

Different tracking detector technologies are discussed in the following with focus on their performance and possible applications. Radiation tolerance is mentioned as one performance aspect since it is often a driving requirement for silicon tracking detector technologies. Radiation damage can either be attributed to surface or bulk damage. Surface damage occurs due to ionisation of atoms in the oxide or passivation layer by traversing particles. Bulk damage describes the damage from non-ionising energy loss in the silicon sensor bulk. However, being not relevant for the CLIC tracking system (see Chapter 2.3.4 and 2.3.5), radiation damage is not a topic of this thesis and it is referred to elsewhere for a description of radiation damage in silicon detectors [45].

Silicon pixel detectors are composed of an active silicon sensor material where the charge is generated, the readout electronics where the signal from the generated charge is processed and an electronics layer (such as a *Printed Circuit Board (PCB)*), providing e.g. the supply and bias voltages and the signal routing. Different silicon pixel detector technologies are in the following sections classified according to the arrangement and the properties of these common elements.

### 4.1 Hybrid pixel detector technologies

Technologies with the sensor separated from the readout chip are referred to as hybrid technologies (see Figure 4.1).

A main advantage of this separated design is that both parts can be independently optimised for their different requirements. Moreover, smaller feature sizes are currently available for separate ASIC designs (e.g. CLICpix, 65 nm technology [46]), while commercial integrated CMOS processes make use of feature sizes in the range of 150 – 200 nm (e.g. ALPIDE, 180 nm technology [3]).

A main challenge of hybrid technologies is the need of an interconnection between the sensor and the readout, resulting in higher material budget and additional challenging and possibly cost intensive

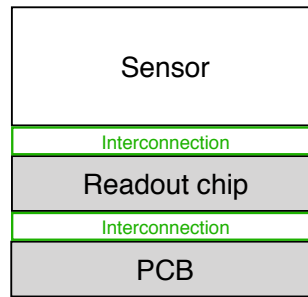


Figure 4.1: General concept of hybrid pixel detectors.

production steps.

The interconnection between the readout chip and the PCB can be realised with established technologies like wire bonds or large solder bump bonds [38] and is thus not discussed further in the following.

Hybrid technologies are widely used in running HEP experiments and are well studied [47]. In the following, different technologies to connect the sensor and readout chip are briefly discussed and some examples of the optimisation of different silicon sensor designs with respect to different requirements are mentioned.

#### 4.1.1 Direct coupling

A commonly used interconnection between the sensor and the readout chip is bump bonding, where a direct electrical connection (*DC coupling*) between pads provided on the sensor and readout chip side is realised by the deposition of small (typically  $\gtrsim 20 \mu\text{m}$  diameter) solder metal balls [48], as illustrated in Figure 4.2.

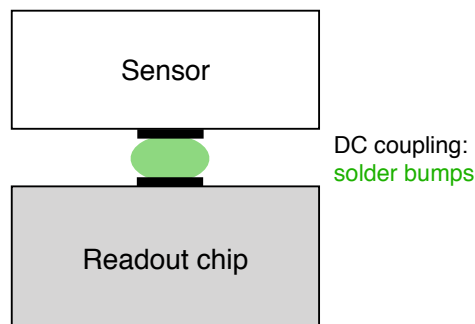


Figure 4.2: Sketch of DC coupling between sensor and readout chip, using *bump bonds*.

With the need of finer pixel granularities for future tracking detectors, bump bonding technologies are limited by the solder bump dimensions and placement precision: a small size and/or an accurate placement of the bumps is needed to avoid electrical shorts between them.

### 4.1.2 Capacitive coupling

An alternative interconnection technique is the capacitive coupling (*AC coupling*) of the signal from the sensor to the readout chip e.g. via a layer of glue (see Figure 4.3).

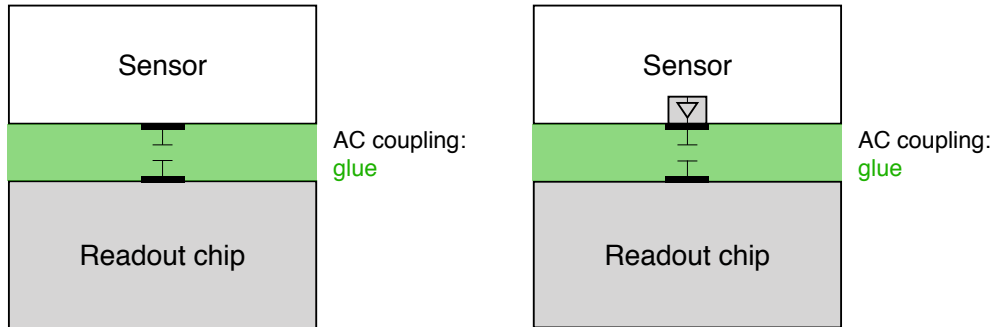


Figure 4.3: Sketch of capacitive coupling between sensor and readout chip with a layer of glue: *without amplification in the sensor (left) and with an amplification stage integrated inside the pixel implant (right)*.

A main challenge of this technique is that if the signal from the sensor and/or the capacitance between the pads on the sensor and chip side are too small, it is challenging to reliably detect the signal at the readout chip [49]. To address this, active sensors with an amplification stage integrated in the sensor are studied (see right sketch of Figure 4.3) [50], [51]. Challenges of this interconnection technology are a uniform and planar deposition of a thin coupling layer to obtain a homogenous and high signal that can be efficiently detected over the full chip size.

### 4.1.3 Silicon sensors

A variety of silicon sensor designs are used for hybrid pixel detector technologies, optimising the sensor design for the use for different applications. Some examples are mentioned in the following.

#### Planar sensors

In the past, sensors were mainly produced with a n type bulk and p type pixel implants (p in n, collection of holes [52]), such as illustrated in Figure 4.4.

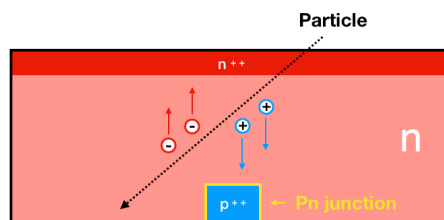


Figure 4.4: Planar p in n sensor.

For p in n sensors the main part of the signal read out by the pixel implants is induced by the movement of holes. Since holes have a higher probability to be trapped by defect levels after radiation damage compared to electrons [45], doping configurations where electrons induce the main signal on the pixel implant are more attractive candidates for high radiation environments, e.g. for the HL-LHC.

### Active edge sensors

In standard sensor productions the edge of the sensors is not depleted and therefore inactive, resulting in inefficient regions. To achieve a full coverage of the detection layer, the sensor edges are overlapping, resulting in additional inactive material. A fully efficient operation of the sensors up to the physical edge would allow for full coverage by seamless tiling (almost no inefficient regions between the sensors).

To achieve this, *active edge sensors* are produced, by placing the cut edge close to the edge pixels and extending the backside implantation to the side of the sensor (*edge implant*), as illustrated in Figure 4.5.

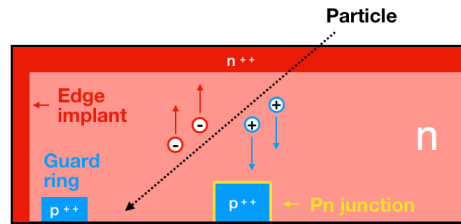


Figure 4.5: Schematic cross section of an active edge sensor.

The edge implant deforms the electric field lines such that charges created between the implant and the edge pixels can be collected by the edge pixel. A challenge of active edge sensors is to avoid a current breakdown at low voltages by placing guard rings close to the edge implant to smoothen the electric field lines in the edge region, while avoiding a loss of charge collected by the guard ring. A good performance of a design with one floating guard ring in view of fully efficient operation up to the physical edge of the sensor and higher breakdown voltages has been demonstrated for sensors with a thickness down to  $50\mu\text{m}$  and a pixel size of  $(55 \times 55)\mu\text{m}^2$  in [33]. Radiation hardness of active edge sensors is currently under investigation [53].

### 3d sensors

Another concept studied especially in view of radiation hardness are *3d sensors*, where the pixel junctions and the backside ohmic contact extend deep inside the sensor bulk (see Figure 4.6).

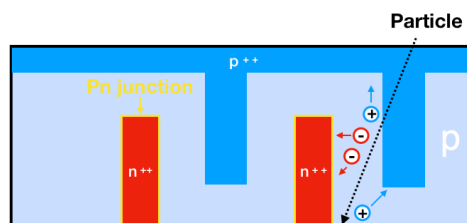


Figure 4.6: Schematic cross section of a 3d sensor.

To obtain a precise geometry, the 3d implants are etched into the sensor and different process flows and designs (e.g. frontside and backside etching) are under investigation [54]. The charge carriers need to propagate only a short way before they are collected and the probability of charge trapping after irradiation is thereby reduced. Moreover, less bias voltage is needed to obtain a larger electric field, resulting in a larger depleted region and thus a higher signal after irradiation. The good performance of 3d sensors has been shown and they are installed and operated in the ATLAS *Insertable B Layer (IBL)* [54].

Due to the inactive regions in the sensor where the vertical implants are placed, the charge collection efficiency can be reduced for particle incidents perpendicular to the sensor surface. Moreover, the increase of the size of the pixel junctions as well as the reduced distance between the pixel junctions and the ohmic contact result in a larger sensor capacitance that can lead to a degradation of the ratio of signal over noise and a degradation of the timing resolution (see Section 3.5).

### Avalanche silicon sensors

Silicon pixel sensors can be optimised for precise timing measurements (in the order of ps) by making use of charge amplification in high electric field regions, resulting in fast drift and large signals. The amplification can be exploited in *Geiger mode*, where the device performs in a non-linear range only providing the digital information if particle has traversed a cell or not. An examples of this technology are *Silicon Photomultipliers (SiPMs)* [38]. No information about the deposited charge in a single cell is measurable with this technology, such that charge interpolation can not be used for the position reconstruction. SiPMs have a timing resolution in the order of ps that might improve the track reconstruction by the exploitation of timing as additional information in the track reconstruction (*4d tracking* [55]).

To make use of the fast timing and large signal from charge amplification while still measuring the amount of the generated charge for the position reconstruction, the amplification can be exploited below the breakdown voltage (*Avalanche mode* [38]). One example are *Low Gain Avalanche Diodes (LGAD)*, where a thin layer of higher doping concentration of the same type as the bulk material (*amplification layer*) is added close to the pn junction, as illustrated in Figure 4.7.

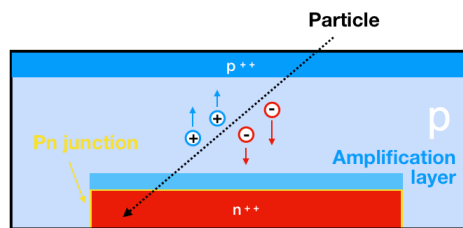


Figure 4.7: Schematic cross section of an LGAD sensor.

For an n in p sensor the amplification layer is added under the n type pixel implant, resulting in a non-uniform response over the lateral size of the pixel for segmented readout implants. This aspect is addressed using p in p sensors, where the pn junction is at the junction to an n type backside, that extends over the full lateral dimension of the sensor [56].

An advantage of LGAD sensors is the fast and large signal that can be achieved with very thin sensors due to the amplification layer. This makes LGAD sensors also interesting candidates for the proposed timing layers of ATLAS and CMS, surrounding parts of the tracker volume [57], [58]. Challenges of LGAD sensor technologies are the achievement of a uniform response over the lateral pixel size and a stable gain after irradiation [59].

### Enhanced Lateral Drift Sensors

To achieve a better spatial resolution for a given cell size *Enhanced Lateral Drift Sensors (ELAD)* [60] make use of deep implants in the sensor (see Figure 4.8), that bend the electric field lines such that more charge sharing can be achieved.

Simulations of the sensor design have shown an almost linear charge sharing behaviour [60]. The design is promising to achieve an improved spatial resolution for thin sensors for detectors where a low

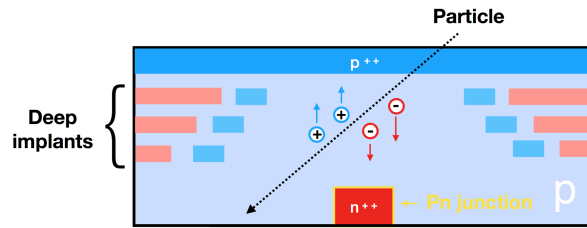


Figure 4.8: Schematic cross section of an ELAD sensor.

material budget needs to be reached simultaneously with a fine spatial resolution, such as the CLIC vertex detector.

Challenges of this sensor design are a complex production process and possible low field regions close to the deep implants, that can result in a loss of charge due to recombination.

### CMOS sensors

Even though CMOS sensors typically correspond to technologies where the readout is integrated in the sensor (see next Section), one can consider also to use CMOS technology to fabricate the sensor only or a sensor with internal gain only. The production of sensors in commercialised CMOS foundries is attractive in view of low-cost mass production. To obtain a sizeable depleted region in the sensors, they usually have a bulk material with a high resistivity and/or allow for the application of a high bias voltage (see next Section 4.2).

CMOS sensors with an amplification stage integrated in the pixel implant to obtain a signal large enough to be read out via capacitive coupling to the readout chip (see left sketch of Figure 4.3) have been produced and tested [51]. Since with the capacitive coupling the challenge of fine pitch bump bonding can be avoided as well as the challenge of integrating all needed functionality in the small pixelated sensor (as for monolithic technologies discussed in the next section), this technology is an interesting option to achieve a smaller pixel size and thus an improved spatial resolution, e.g. for the CLIC vertex detector.

Using the advantage of metal redistribution layers available in CMOS foundries, a flexibility between the sensor and readout pixel geometry can be achieved. Thus, several readout chips with a pixel size smaller than the pixel size of the sensor can be used on a single large sensor to minimise sensor edge effects [61]. With this, overlapping regions between sensors can be reduced. This makes hybrid CMOS technologies also attractive in view of a reduction of the material budget.

## 4.2 Monolithic technologies

Technologies with the readout electronics integrated in the sensor, referred to as *integrated technologies* or *monolithic technologies* (see Figure 4.9), avoid the need of possibly challenging and expensive interconnection technologies and can possibly allow to go to smaller pixel sizes since no bump bonding is needed, provided that all needed electronics can still be integrated inside the size of a pixel. In addition, monolithic technologies allow for a reduction of the material budget since the readout electronics is already integrated in the sensor. A further advantage of monolithic CMOS technologies is the possibility of low-cost mass production in commercialised CMOS foundries. The above given arguments make integrated technologies attractive for the tracking systems for the HL-LHC and especially for future projects with large scale silicon trackers and tight requirements on the material budget, such as CLIC.

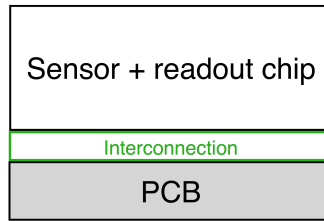


Figure 4.9: General concept of monolithic pixel detector technologies.

Different concepts are followed to integrate the CMOS logic in the sensor, which impact the design and the performance of the sensor. The different technologies presented in the previous section (such as active edge or 3d sensors) could often be combined with the concepts of integrated sensors. However, as many of these technologies are subject to ongoing specific R&D for HEP experiments, their implementation is often not part of commercialised processes and not available for standard monolithic CMOS technologies.

First generation *Monolithic Active Pixel Sensors (MAPS)* integrate the CMOS circuitry in doped wells separated from the collection electrode [62]. To achieve a sizeable depletion, further developments have been performed, following different design ideas of how to integrate the CMOS circuitry in the sensor. In this section a classification according to these different ideas is presented. However, it should be noted that current prototypes of monolithic technologies often combine various aspects of them.

### 4.2.1 High Voltage CMOS

*High Voltage (HV) CMOS* sensors integrate the CMOS logic in the pixel implant, as sketched in Figure 4.10. The name of this technology concept is derived from the fact that the electronics is shielded by the

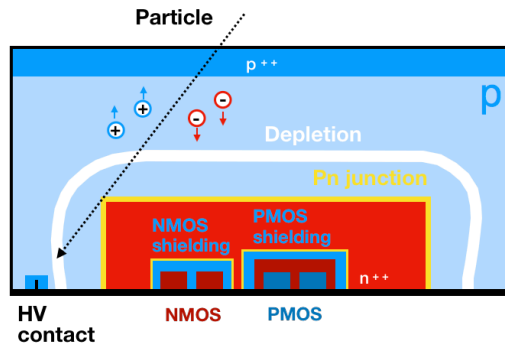


Figure 4.10: Schematic cross section of HV CMOS sensors.

pixel implant and a high voltage can be applied to the sensor bulk. The NMOS transistor is isolated from the pixel implant by its p type body and the PMOS is shielded by a p well. To fit all electronics inside the pixel implant, the size of the pixel implant is enlarged with respect to planar sensors and to HR CMOS technologies discussed in the next section.

The concept of a large collection electrode design has several implications on the performance. One consequence is the enlargement of the pn junction around the pixel implant. This leads to a large and homogenous depletion and electric field over the lateral size of the pixel, resulting in a homogenous response over the lateral pixel size and a short drift distance for the charges created in the bulk. However, the homogenous electric field over the lateral size of the pixel also results in a reduction of charge sharing which limits the gain in position resolution from charge interpolation. Moreover, the large collection

electrode design results in a large sensor capacitance that is attributed to the junction surface of the large pixel implant and to the junctions between the n type pixel implant and the p type body of the NMOS and the p well isolating the PMOS transistor. The larger sensor capacitance results in a lower gain for a given analogue power consumption, as well as a larger noise and a degradation of the timing measurement (see Section 3.5).

When a high voltage is applied to the frontside, a depletion starts to evolve around the pixel implant. Challenges of HV CMOS sensors are the achievement of a full depletion. Recent studies have shown that the depletion of the investigated designs does not extend over the full pixel size, such that large non-depleted regions are present in the pixel edges and at larger sensor depth. HV CMOS sensor with a frontside bias contact have been simulated for the CLIC vertex detector, showing the resulting fast component of the collected charge from the depleted region and a slow component from the non-depleted region [63].

The depletion of the studied HV CMOS sensors is limited by the resistivity of the bulk and the application of the high bias voltage from the frontside. When a high bias voltage is applied to the frontside, it is connected to the backside substrate, as long as the region between the high voltage contact on the frontside and the backside substrate is not depleted. As soon as the depletion grows under the high voltage contact, the backside substrate is disconnected from the high voltage, limiting the depletion of the sensor in depth. Options that are considered to achieve a full depletion are either the application of the bias voltage to the backside substrate or a higher bulk resistivity [64].

Fully integrated HV CMOS sensors have been developed and studied e.g. for the *Mu3e experiment* [65] and the *ATLAS Inner Tracker (ITk) HL upgrade* [66, 67]. They are also being evaluated in view of the CLIC tracker requirements.

## 4.2.2 High Resistivity CMOS

To achieve a small sensor capacitance, HR CMOS sensors integrate the readout electronics in a well that is separated from the pixel implant, as sketched in Figure 4.11. As a consequence, the size of the pixel

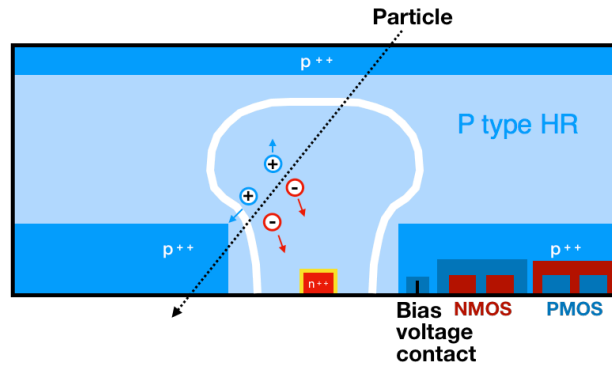


Figure 4.11: Schematic cross section of standard HR CMOS sensors (*standard process*).

implant can be minimised. To avoid charge loss due to charges being attracted by the well shielding the electronics and not by the pixel implant, this well needs to be doped with the same polarity as the bulk substrate.

The small collection electrode design has several implications on the performance. To expand the depletion in depth and lateral size of the pixels, the bias voltage is applied to the p wells. When applying a negative bias voltage to terminals in the p well, the voltage gets connected to the backside substrate of the chip via non-depleted regions between the pixels and a depleted region starts to evolve from the pn

junction around the pixel implant, growing into the p type bulk. Note that the region of the pn junction around the pixel implant is very small compared to full lateral size of the pixel.

A pn junction is also created between the  $n^{++}$  implants of the NMOS transistor and the p wells, being reversely biased by the bias voltage applied to the terminals in the p wells. To avoid breakdowns of this pn junction, the bias voltage is limited [39].

To obtain a sizeable depleted volume despite the small pn junction and low bias voltage, a high resistivity silicon bulk is used, giving the name to this technology concept. Even with very high resistivities a full lateral depletion is challenging to be achieved for the small collection electrode design, since the depletion needs to evolve from the small pixel implant into the region under the p wells. Thus, sizeable non-depleted regions are presents for this HR CMOS process, resulting in signal contributions from both drift and diffusion, as studied in detail in this thesis.

To achieve a full lateral depletion over the pixel cell, the HR CMOS process has been modified: an n layer has been inserted between the high resistivity p type bulk and the frontside implantations [4], as illustrated in Figure 4.12. Hereby a planar pn junction is created between the n layer and the high

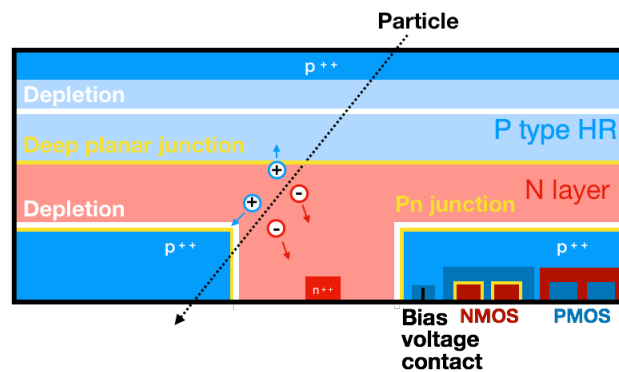


Figure 4.12: Schematic cross section of HR CMOS sensors with the modification of an additional N layer (*modified process*).

resistivity p type bulk, which extends homogeneously over the lateral size of the pixel (*deep planar junction*). When applying a voltage to the backside, a depletion evolves from this junction into the high resistivity bulk. Moreover, a pn junction is created between the n layer and the p wells and a bias voltage is applied to the p wells to fully deplete the n layer. This junction isolates the CMOS logic from the bias voltage applied to the backside. Thus, the modified process allows for an application of a higher bias voltage to the backside, that is not limited by the breakdown of the CMOS transistors. However, the voltage applied for the modified process to the backside is limited by punch through effects between the backside and the p wells, as simulated in [4].

Another possibility to create a full depletion in HR CMOS sensors has been studied in [68], where a high resistivity n bulk has been used with a p type backside implementation.

The main advantage of the small collection electrode design is the minimisation of the sensor capacitance and the resulting larger SNR and a faster rise time for a given power consumption as well as a lower noise (see Section 3.5). The low noise allows for a very low detection threshold in the order of a few tens of electrons, as shown in this thesis. The detection of small signals implicates that thinner sensors can be used, being an advantage in view of a low material budget. Moreover, the detection of small signals leads to more information available for the charge interpolation, allowing for an improved position resolution, as investigated in this thesis. Additionally, the fact that less power is needed to amplify the signal leads to a low analogue power consumption that can also reduce the material budget due to less needed cooling

and cable mass.

Integrated HR CMOS technologies have been developed and studied for the ALICE ITS upgrade [3] to achieve the tight requirement of a material budget of  $0.3\% X_0$  radiation length per detection layer. A fully integrated chip, the ALPIDE, has been produced in a HR 180 nm CMOS process, using the standard process. For the application in a harsher radiation environment such as for the ATLAS ITk upgrade, a full lateral depletion of the sensor bulk is desirable. Test chips of the modified process have been studied for the ATLAS ITk upgrade, especially in view of charge collection time and efficiency after irradiation, showing that the requirements of the ITk outer layers can be reached for the HL-LHC upgrade [69].

A comparative study of both processes and a performance evaluation in view of the requirements for CLIC is part of this thesis.

### 4.2.3 SOI CMOS

Another concept to apply a high bias voltage while maintaining a small collection electrode design are *Silicon On Insulator (SOI)* CMOS processes [70]. In this concept an additional insulation layer is added on a high resistivity sensor wafer, that shields a low resistivity layer containing the CMOS logic (see Figure 4.13). The pixel implants are connected to the CMOS transistors with vertical vias through the insulation layer.

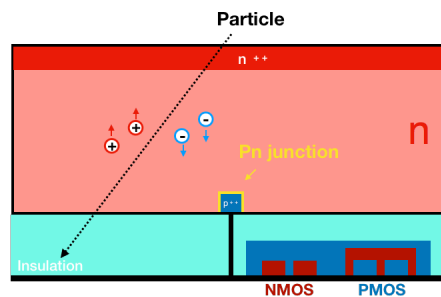


Figure 4.13: Schematic cross section of a SOI CMOS sensor.

Due to the shielding of the CMOS logic by the insulation layer from the bulk, a high bias voltage can be applied to the bulk to achieve a full depletion and a high electric field over the lateral size of the pixel. At the same time, the SOI CMOS concept benefits from the advantages of a small collection electrode design, since the pixel implant does not incorporate the CMOS logic.

To obtain a better shielding of the CMOS logic, additional deep p wells are added under the p type pixel implant for some designs, resulting again in a larger collection electrode design and an increased sensor capacitance [71]. Moreover, to compensate voltage shifts in the CMOS transistors due to surface accumulation or inversion layers from ionising radiation, an additional biased silicon layer can be added inside the insulation layer [72]. This additional biased silicon layer also acts as shielding of the CMOS transistors. Accordingly, double SOI designs are studied without the additional deep p well, maintaining the small collection electrode design. However, the additional biased silicon layer adds to the capacitance due to couplings to the CMOS transistors.

The SOI CMOS concept provides the advantage of more space for the readout electronics (compared to HV and HR CMOS) since the regions where the electronics can be implemented is a complete additional layer and not restricted to certain pixel regions (such as the size of the collection electrode for HV CMOS sensors or the size of the p wells for HR CMOS sensors). This makes SOI CMOS technologies interesting for fine pitch technologies, as needed e.g. for the CLIC vertex detector.

## 4.3 Summary

Hybrid silicon pixel detector technologies are an attractive technology choice since their split functionality allows for a separate optimisation of the sensor and readout chip. They are well studied and sensors used for hybrid technologies meet the requirements for the HL-LHC pixel detectors especially in view of radiation hardness. Thus, they serve as a possible but also often expensive solution for the HL-LHC, since the production of specific non-commercialised sensors as well as the process steps needed to interconnect the sensor and the readout chip can be cost intensive. For future experiments such as CLIC, the demanding requirements imposed on the tracking detectors are difficult to be reached by standard hybrid technologies. Especially challenging is the requirement of a low material budget simultaneously with a very precise spatial resolution, since thicker sensors results in more charge sharing and a better spatial resolution, but do not fulfil the requirement of a low material budget.

A broad R&D on the optimisation of sensor designs is currently taking place, to target the requirements for future tracking detectors, such as low material budget, fast timing, improved spatial resolution and radiation hardness. A selective choice of the R&D on sensor designs has been presented in this chapter. Active edge sensors are attractive candidates to reduce the material budget and 3d sensors provide a promising sensor design for high radiation environments. LGAD sensors are a suited technology for fast timing measurements, while ELAD sensors are promising candidates for an improved spatial resolution for a given pixel size and sensor thickness. Hybrid technologies using sensors produced in commercialised CMOS foundries are appealing for low-cost mass production and a reduction of the pixel size and the material budget.

To minimise the production effort, reduce cost and reach a low material budget, monolithic technologies are developed and studied for several HEP experiments. Various monolithic technology concepts have been discussed in this chapter. HV CMOS technologies are attractive in view of radiation hardness since they allow for the application of a high voltage to the sensor bulk. Minimising the sensor capacitance, HR CMOS technologies are interesting in view of low power consumption, low threshold and fast timing. Recent progress in HR CMOS technologies allows for a full lateral depletion, making them an interesting option for the upgrade of tracking detectors for the HL-LHC. For future experiments with large surface silicon tracking detectors and very tight requirements on the material budget, monolithic technologies are appealing technology options. Silicon tracking detectors such as the CLIC vertex detector, that require in addition a very fine position resolution and pixel size, can benefit from monolithic SOI CMOS technologies that provide more space for the CMOS logic compared to HR and HV CMOS technologies.



---

## Investigator HR CMOS chip and data taking setup

---

The Investigator HR CMOS chip is referred to as a *test chip* for a monolithic technology, since it only contains the analogue circuitry in the pixel (see Section 5.1.3) and an external readout is used to access the full analogue response (see Section 5.4). By this, the performance can be studied in great detail. Moreover, the Investigator contains various sections with different pixel layouts, that can be investigated and the optimal design e.g. in terms of efficiency, spatial and timing resolution can be determined (see Section 5.2).

In this chapter, the Investigator chip is introduced. First, the process cross section and pixel layout are discussed. Afterwards, the in-pixel circuitry of the Investigator chip is explained, followed by a brief presentation of the chip layout and a summary of main noise contributions. The external readout is described in a next section, followed by a presentation of the test beam data taking setup.

### 5.1 Fabrication process and pixel layout

#### 5.1.1 Fabrication process

A 180 nm HR CMOS technology is used to fabricate the chip. The Investigator has been produced in two different processes, the standard process (see Figure 4.11) and the modified process (see Figure 4.12).

The high resistivity bulk is produced by epitaxial grow in a highly p doped backside substrate silicon, using chemical vapour deposition [73], [39]. The epitaxial layer is in the following referred to as *epi layer*. Chips with different epi layer resistivities (1 – 8 k $\Omega$  cm) and epi layer thickness (15 – 40  $\mu$ m) have been produced. Moreover, different chips have been thinned to various total silicon thickness, ranging down to 50  $\mu$ m. The chips studied in this thesis have a total thickness of 100  $\mu$ m, including the backside substrate and metal layers.

#### 5.1.2 Pixel geometry

As illustrated in Figure 5.1, the collection electrode is implanted with an octagonal shape. Geometrical parameters of the pixel layout are: the size of a single pixel cell (*pitch*), the size of the n well collection electrode (*electrode size*) and the distance between the edge of the collection electrode and the p well (*spacing*).

Top view on pixel cell:

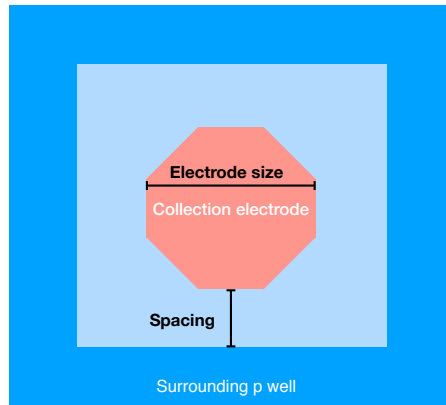


Figure 5.1: Schematic of view on the top of the pixel cell and definition of geometrical parameters.

### 5.1.3 In-pixel circuitry

A source follower is integrated in each pixel, converting the charge  $Q$  on the diode capacitance  $C$  to a voltage  $U = Q/C$  (see Figure 5.2). Consequently, when a particle traverses the sensor, a voltage drop

In-pixel circuitry:

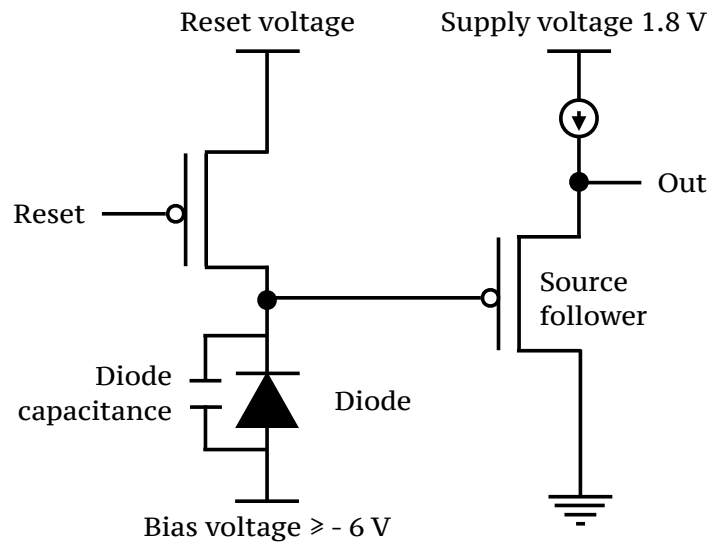


Figure 5.2: Simplified schematic of the in-pixel circuitry of the Investigator.

with a magnitude inversely proportional to the diode capacitance can be measured. The small diode capacitance of a few fF [4] leads accordingly to a large voltage drop. Thus, low power is needed to amplify the signal and a total power consumption of  $\sim 30$  mW has been achieved [74].

The voltage  $U$  is set back to the pedestal by discharging the diode capacitance  $C$  with a reset pulse, sent to  $p^{++}$  terminals in the n well collection electrode.

### 5.1.4 Bias voltage

For the standard and modified process, the bias voltage is applied to terminals in the p wells. When applying a negative bias voltage, the voltage gets connected to the backside substrate of the chip via non depleted regions at the matrix edge. To avoid breakdowns of the pn junction of the NMOS transistors (see e.g. Figure 4.12), the bias voltage is limited to  $-6\text{ V}$  [39].

## 5.2 Matrix layout

The Investigator chip consists of several sections with different pixel layouts, so called *mini matrices*. Different electronics and geometrical parameters have been changed for the various mini matrices, such as the pitch ( $20\mu\text{m} - 50\mu\text{m}$ ), the collection electrode size ( $2\mu\text{m} - 20\mu\text{m}$ ) and the spacing ( $1\mu\text{m} - 18.5\mu\text{m}$ )<sup>1</sup>. By this, various pixel layouts can be investigated and the optimal design e.g. in terms of efficiency, spatial and timing resolution can be determined.

Each mini matrix consists of  $10 \times 10$  pixels, with the  $8 \times 8$  innermost pixels being read out. The layout of the Investigator chip with its  $2 \times 134$  mini matrices is presented in Figure 5.3. The chip is

Investigator chip layout:

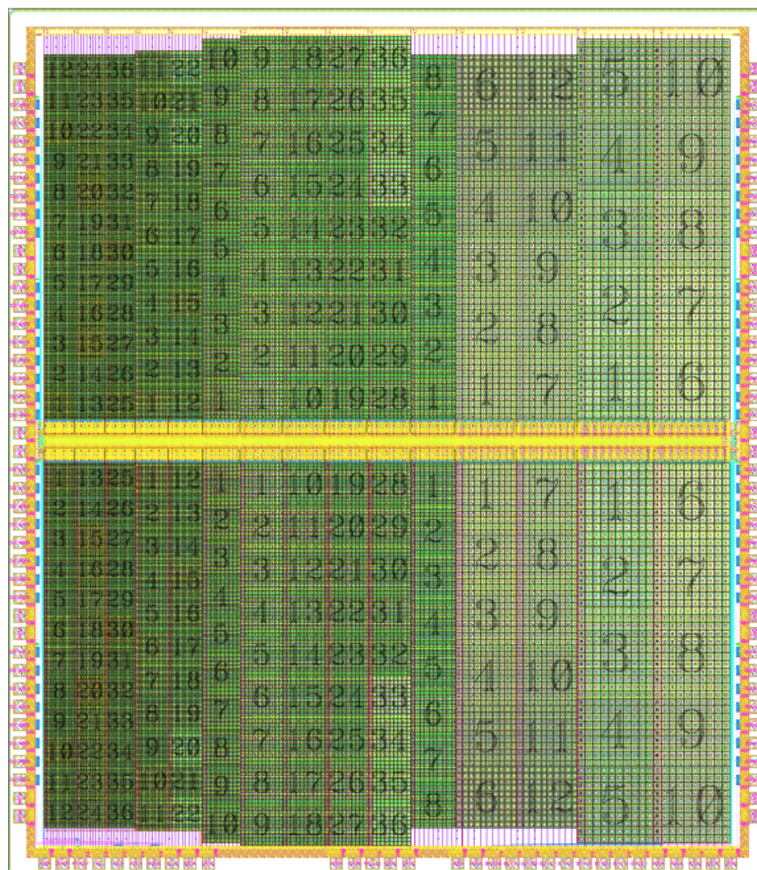


Figure 5.3: Layout of the Investigator chip. From [75].

<sup>1</sup> Note that the parameters can only be varied in a consistent way, for example a pitch of  $20\mu\text{m}$  can not allow for a spacing of  $18.5\mu\text{m}$

divided in two sections, which differ in the functionality of injecting a test charge in the pixels that is only implemented in the lower section on the chip in Figure 5.3. The periphery of the Investigator is equipped with pads for the supply as well as the bias voltage and 64 output buffers. By selecting one mini matrix, their pixels are read out by connecting the output of the source follower to a dedicated output buffer. Thus, one mini matrix can be read out at a time.

The rise time of the output buffers in the Investigator periphery, defined as the time the signal needs to rise from 10 – 90 % of its total amplitude, is  $\sim 10$  ns [74]. In future submissions different output buffers are used with a faster rise time.

### 5.3 Noise contributions

A detailed discussion of different noise contributions can be found in [76]. The noise of the studied design is composed of different components [39]:

- **Reset noise:**

The thermal noise from the resistor of the reset switch results in variations of the charge on the capacitor when opening the switch (*kTC noise* [76]). This noise contribution leads to a shift of the measured voltage  $V$  in the active window. Measuring this shift after many reset pulses results in a variation proportional to the temperature  $T$  and inversely proportional to the capacitance  $C$

$$\langle V_{\text{thermal}}^2 \rangle = kT/C, \quad (5.1)$$

with the Boltzmann constant  $k$  [10].

- **Shot noise:**

During the time of the active window the leakage current  $I_{\text{leakage}}$  results in a charge  $Q_{\text{leakage}}$  of

$$Q_{\text{leakage}} = I_{\text{leakage}} \cdot \Delta t, \quad (5.2)$$

with the integration time  $\Delta t$ . Thus, the corresponding number  $N_{\text{leakage}}$  of charge carriers  $q$  can be calculated as

$$N_{\text{leakage}} = Q_{\text{leakage}}/q = I_{\text{leakage}} \cdot \Delta t/q. \quad (5.3)$$

This leads to fluctuation of the measured charge from the leakage current

$$\sqrt{N_{\text{leakage}}} = \sqrt{I_{\text{leakage}} \cdot \Delta t/q}. \quad (5.4)$$

The corresponding variation of the measured voltage

$$\langle V_{\text{leakage}}^2 \rangle = q \cdot I_{\text{leakage}} \cdot \Delta t/C^2 \quad (5.5)$$

is referred to as *shot noise*.

- **1/f and thermal noise:**

Noise can occur due to thermal processes (*thermal noise*) or due to other capture and release processes (*1/f noise*). Thermal and 1/f noise can originate e.g. from the NMOS or the switching circuitry, resulting in sample by sample fluctuations of the measured voltage around the pedestal amplitude.

- **Random telegraph noise:**

*Random telegraph noise (RTN)* can be considered as 1/f noise with a low frequency, that originates from defects near the channel of the NMOS transistor and manifests itself in discrete voltage steps during the active window. The time the voltage remains at this noise level (*down time*) is randomly distributed.

- **Common mode noise:**

In all data a systematic deviation from the pedestal amplitude has been observed. In contrast to the above discussed noise contributions, the deviation is the same for each pixel in one readout frame and therefore referred to as *Common Mode Noise (CMN)*. It can originate from external sources, such as the power supply used in the test beam and laboratory setups.

## 5.4 INvestigator ReadOut System INVROS

As the Investigator is a test chip, it does not contain the digital logic on chip. To record the full analogue data for each pixel, an external readout system, the *INVROS*, has been designed for the Investigator [77], [39]. One *Analogue to Digital Converter (ADC)* per readout pixel is placed on the *INVROS*. The ADCs sample the front end output with a frequency of 65 MHz and 14-bit resolution (AD9249 [78])<sup>2</sup>.

The supply voltage, the bias voltage and the reset signal are also provided by the *INVROS* to the corresponding pads in the Investigator periphery. Regardless if a voltage drop has been created by a particle hit in the pixel or not, the reset pulse is sent with an adjustable period to all  $10 \times 10$  pixels. The time between two reset pulses is referred to as one *time cycle* and shown in Figure 5.4. The start of the

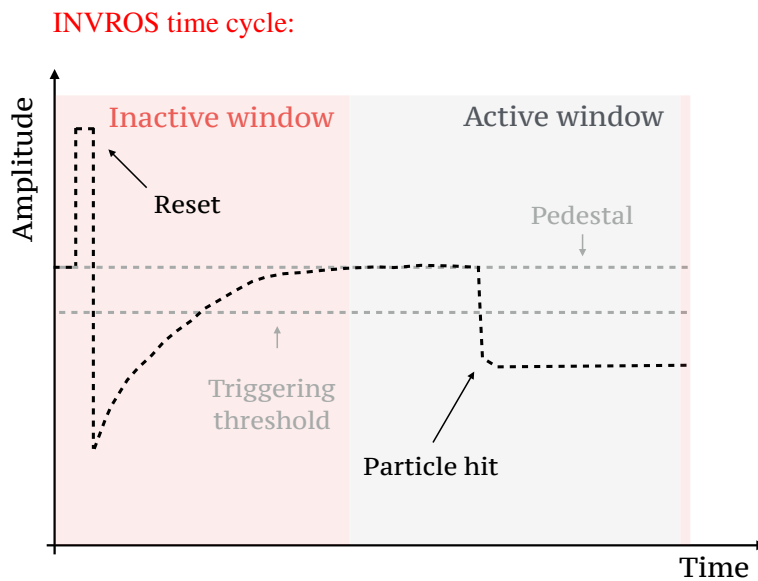


Figure 5.4: Simplified schematic of Investigator waveform for one time cycle (not to scale), as discussed in the text.

first part of the time cycle (*inactive window* in Figure 5.4) has been set shortly (150 ns) before the start of the reset pulse. Data observed by the Investigator during the inactive window is rejected by the *INVROS*.

<sup>2</sup> Note, that the 65 MHz sampling of the analogue response limits the achievable precision of timing measurements.

By this, a fake signal created by the reset pulse can be avoided, since the reset pulse results in a negative voltage drop, as does a signal from a particle hit. The length of the inactive window of  $12.4\ \mu\text{s}$ , has been selected such, that the output stabilises back to its pedestal value after the reset pulse. The rejection of the data during the  $12.4\ \mu\text{s}$  long inactive window results in dead times of the Investigator.

In the following *active window* of the Investigator time cycle, the INVROS stores the data observed by the Investigator for 1024 time samples, corresponding to  $15.75\ \mu\text{s}$ . A next reset pulse is sent after a dead time of  $0.15\ \mu\text{s}$ , and the described time cycle is periodically repeated.

## 5.5 Test beam setup

In this section the test beam data taking setup is described. The telescope test beam setup is presented, followed by a detailed description of the trigger logic used during test beam data taking.

### 5.5.1 CLICdp Timepix3 telescope

To perform test beam measurements, the INVROS has been integrated in the CLICdp Timepix3 telescope setup [33]. In Figure 5.5 the test beam setup is presented, showing the INVROS placed in the centre position of six telescope planes. The CLICdp Timepix3 telescope is placed in the H6 beam line of the

CLICdp Timepix3 test beam telescope setup:

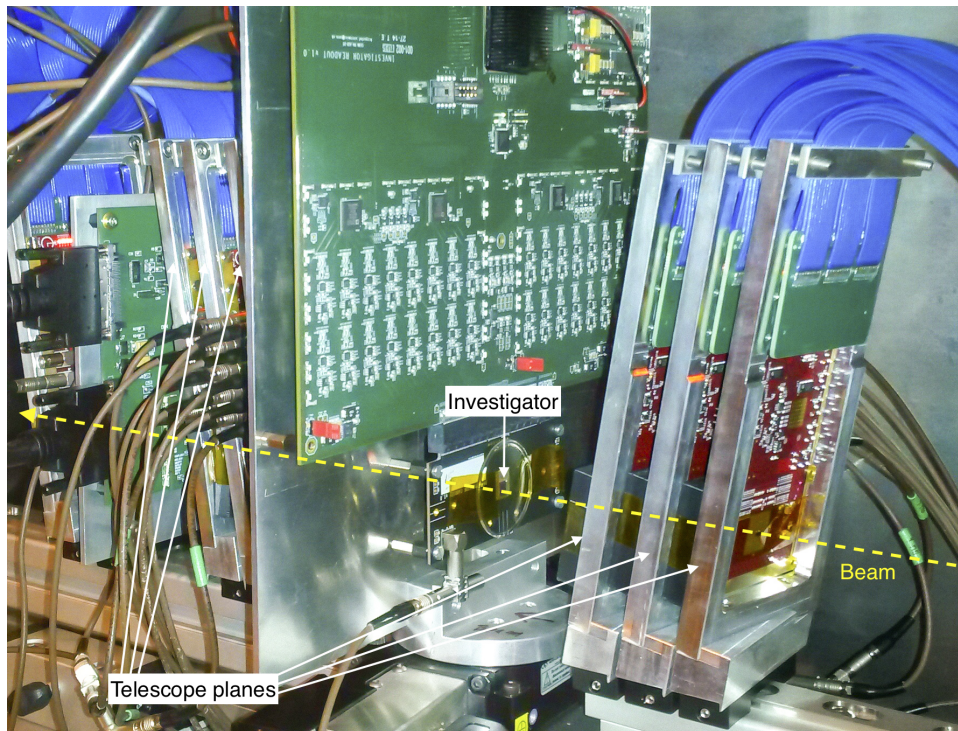


Figure 5.5: Test beam setup of the CLICdp Timepix3 telescope in the H6 beam line of the CERN SPS.

CERN SPS [79] and used as reference system for particle tracking. Test beam measurements have been performed using a beam of positively charged hadrons with an energy of 120 GeV.

The geometry of the telescope is described with a Cartesian right handed coordinate system, with the  $z$  direction pointing along the beam axis and the  $y$  direction pointing vertically upwards. For the Investigator, the same reference coordinates are used: the  $x$  and  $y$  direction being in the sensor plane parallel to the row and column direction of the Investigator mini matrices and the  $z$  direction pointing along the sensor depth.

The telescope planes are moved as close to each other and to the Investigator, as mechanically possible. This has been done to optimise the telescope track resolution on the Investigator. A spatial telescope track resolution of  $1.8\ \mu\text{m}$  and a telescope track timing resolution of  $\sim 1\ \text{ns}$  has been achieved on the Investigator [33], [80].

The Timepix3 readout ASIC [81] allows for a continuous readout with a high particle rate. The beam line parameters were set for a beam spot size of  $\sim 1\ \text{cm}^2$  and a particle rate of  $\sim 3 \cdot 10^6$  during the  $\sim 5\ \text{s}$  spills. The small Investigator mini matrix area, as well as dead times of the Investigator during the reset pulse and the data readout result in a trigger rate during the  $\sim 5\ \text{s}$  spills in the order of a few hundred Hz for the Investigator data taking.

### 5.5.2 Investigator data taking

First, the threshold setting during data taking is explained, followed by a description of the trigger logic used to integrate the Investigator in the telescope setup.

#### Threshold definition

A *triggering threshold* is set individually for each pixel. The noise, defined as the fluctuations around the pedestal, is calculated per pixel. For each pixel the amplitude of each readout sample is compared to the previous. If this difference is larger than a certain multiplicity of the noise in at least one pixel during the active window, the full frame of the amplitudes of the  $8 \times 8$  active pixels gets recorded by the computer. Particle hits seen by the Investigator during the time the INVROS sends the recorded amplitude frame to the computer are not recorded resulting in an additional dead time in the order of a few ms.

#### Test beam trigger logic

To be able to perform efficiency measurements, the dead times of the Investigator chip and its readout need to be time stamped to discard telescope tracks passing through the Investigator while it is not able to record a particle hit.

To achieve this, the INVROS creates a veto signal during all times in which the Investigator chip or the readout system are inactive. This happens periodically during the recovery time after the reset pulse (*reset veto*, see Section 5.4) for about  $13\ \mu\text{s}$ , and for a few ms during the readout phase after a particle hit has been detected (*readout veto*).

The Investigator veto output defines the time stamp of the end of the reset and the readout veto. However, the readout veto could not be reliably generated by the INVROS firmware: it was released too early, and tracks passing through the Investigator during the dead time of the readout could not be discarded. To still be able to perform an efficiency measurement, the veto signal has been extended using a *Nuclear Instrument Module-Standard (NIM)* gate generator, as shown in Figure 5.6 and 5.7. The gate generator is started by a trigger pulse, sent from the INVROS if a particle hit has been detected in the Investigator. The gate reset is triggered by the readout software and sent via an Arduino Uno micro controller board to the gate reset input and issued as close as possible to the end of the inactive period during the readout cycle, directly before the readout software is ready to acquire the next frame.

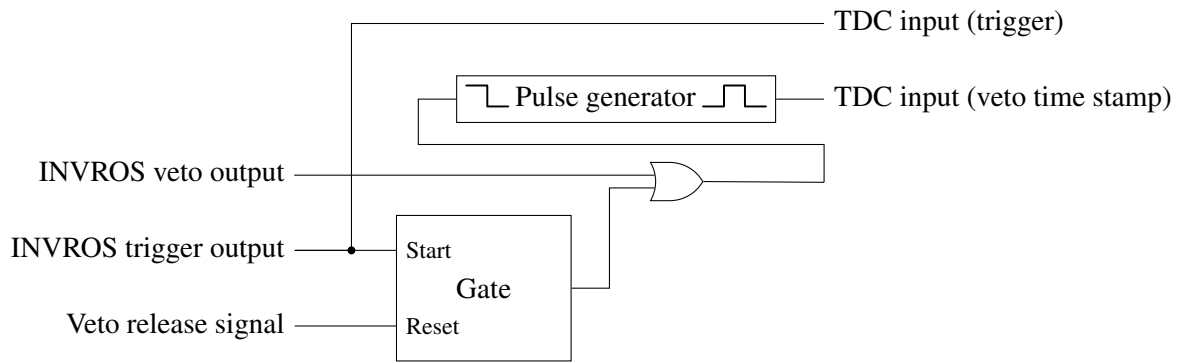


Figure 5.6: Schematic of the veto and trigger logic.

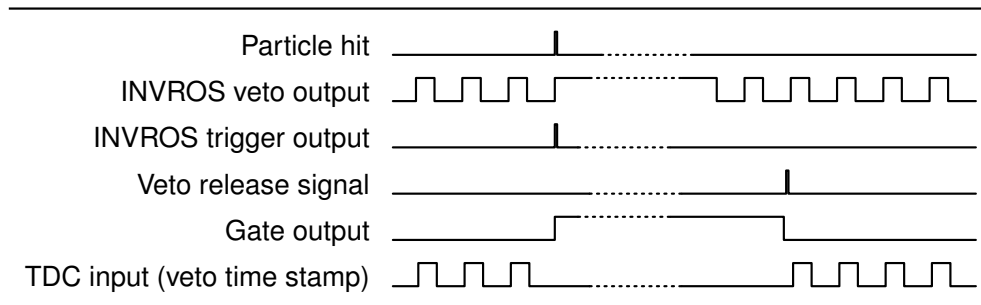


Figure 5.7: Timing diagram illustrating the extension of the veto signal after a particle hit.

The output signal of the gate generator and the Investigator veto output are connected in an OR gate to obtain the time stamp of both, the end of the reset veto and the extended end of the readout veto. A pulse generator has been used to convert the falling edge of the output signal from the OR gate into a short pulse.

This pulse is time stamped using one of the *Time to Digital Converter (TDC)* inputs of the telescope readout system and then stored in the telescope data file with a time stamp from the telescope reference clock (*veto time stamp*). This time stamp is later used to offline mask the telescope tracks during the times, where the Investigator is inactive. The telescope shutter has been kept open in the dead times of the Investigator to avoid artefacts created by the opening of the telescope shutter [82].

The Investigator clock and the telescope clock are not synchronised during data taking. To be able to offline synchronise the Investigator data with the telescope data, the INVROS trigger signal is sent to one of the telescope TDC inputs, if a particle hit has been detected. This trigger signal is sent with a constant delay after the end of the active Investigator window (see Figure 5.4) and then stored in the telescope data file with a time stamp from the telescope reference clock.

---

## Data reconstruction and analysis

---

For the reconstruction of the telescope tracks and hits on the Investigator, the *EUTelescope* test beam reconstruction framework has been used [83]. The *EUTelescope* framework depends on the *ILCSoft* software [84] and makes use of it for basic elements like the event data model (*Linear Collider Input Output LCIO* [85]) and the geometry description toolkit *GEAR* [86]. The event reconstruction and analysis is performed by a modular application framework of *ILCSoft* (*Marlin* [87]). Different reconstruction steps are implemented by different processors, which are executed for each event in a modular way by the use of steering files.

Example plots are presented for an Investigator mini matrix with a pitch of  $28\ \mu\text{m}$ , a spacing of  $3\ \mu\text{m}$  and a collection electrode size of  $2\ \mu\text{m}$  located on an Investigator chip implemented in the modified process with an epitaxial layer thickness of  $25\ \mu\text{m}$  and a bias voltage of  $-6\ \text{V}$ .

### 6.1 Investigator waveform reconstruction and event building

A data driven readout is used for the Timepix3 telescope data. Thus, in contrast to the frame based triggered readout of the Investigator, the telescope hits are continuously recorded.

The first processor `EUTelTimepix3TelescopeReader` reads out the Investigator and telescope data and builds the events, used for the following analysis steps. Before the events can be built for the analysis, the Investigator waveform needs to be reconstructed to obtain the time stamp of the Investigator hits and perform a synchronisation of the Investigator and telescope data.

In this section, the reconstruction of the Investigator waveforms is described, followed by a detailed description of the offline synchronisation and event building.

#### 6.1.1 Reconstruction of Investigator pixel waveforms

The basic procedure to reconstruct the Investigator pixel waveforms for source and test beam measurements is described in the next section. To be able to reconstruct the Investigator pixel waveform more precisely and reduce the threshold, a noise correction is performed in a first step. After describing the noise correction, the reconstruction of the Investigator pixel waveforms is explained.

##### Common mode noise (CMN) correction

A typical waveform read out for a pixel with and without a particle hit is presented in Figure 6.1. The impact of the CMN (see Chapter 5.3) is clearly visible in the waveform without a particle hit. The overall

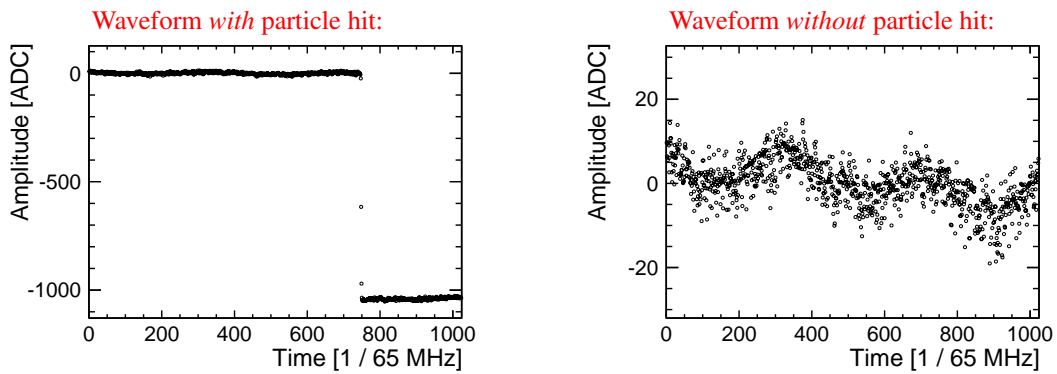


Figure 6.1: Example of a waveforms of a pixel *with* (left) and *without* (right) a particle hit.

noise is defined as the RMS of the pedestal amplitudes and is thus increased by the CMN. An *analysis threshold* is applied on single pixel level in the following analysis with respect to the noise of each pixel. As a consequence, the CMN also shifts this threshold to higher values. Therefore, the CMN needs to be calculated and subtracted from the single pixel waveforms before the analysis threshold is applied, to be able to apply a lower threshold.

The waveform of the CMN is extracted individually for each readout frame, using the waveforms of pixels without a particle hit. To identify pixels without a particle hit, the difference in amplitude between the first time sample and the last time sample is calculated for each pixel in a readout frame. If this difference is smaller than a value of 30 ADC, a pixel is considered to have no particle hit. The value of 30 ADC has been selected such, that it exceeds the amplitude of the CMN but is still below an amplitude drop created by a particle hit.

Looping over all Investigator events in one run and extracting the average amplitude for each pixel without a particle hit, the pedestal amplitude for a single pixel is calculated. The pedestal value is then subtracted from each sample in the waveform of each pixel and the waveforms of pixels with no particle hit are averaged to obtain the mean waveform of the CMN. Figure 6.2 shows a typical example of a CMN waveform. The frequency of the CMN waveform has been found to be  $\sim 1.7$  MHz, independent of the

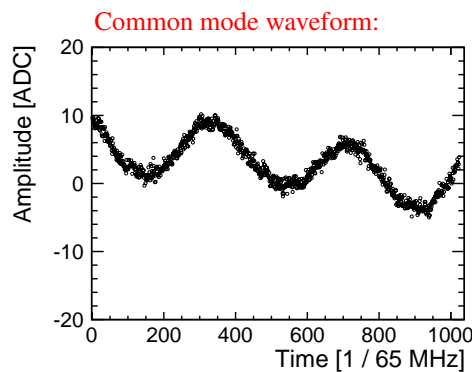


Figure 6.2: Typical example of a calculated common mode noise waveform.

bias voltage applied to the chip [82]. A possible origin of the CMN can be a coupling from external sources, e.g. the power supplies.

The mean CMN waveform is then subtracted from the waveform of each pixel in the readout frame.

Waveforms are presented before and after this CMN correction, in Figure 6.3 for a pixel with no particle hit. The comparison to the waveforms in Figure 6.1 shows that the common mode correction significantly

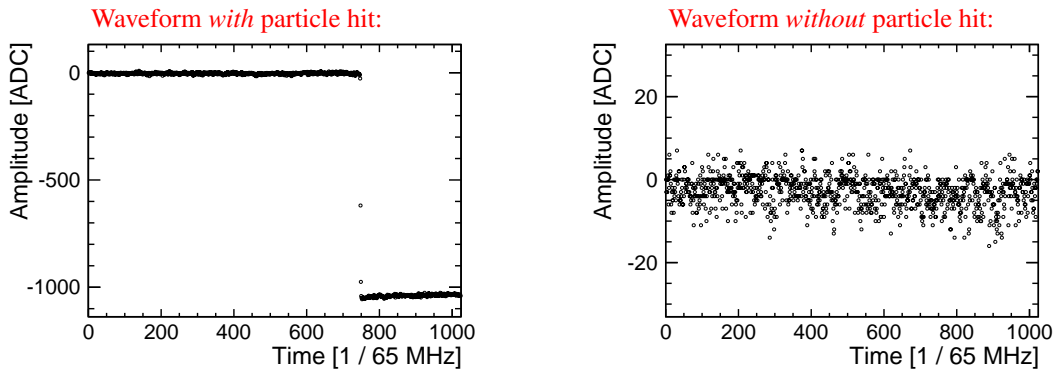


Figure 6.3: Example of a waveforms of a pixel *with* (left) and *without* (right) a particle hit after the common mode correction.

reduces the pedestal variations. The impact of the common mode on the noise and threshold values is discussed in Chapter 9.2.

The analysis threshold can be reduced with respect to the triggering threshold, since the common mode noise has been filtered out before applying the analysis threshold, but not during data taking.

### Reconstruction of observables

A zoom into a typical waveform of a pixel with a particle hit, manifesting in a voltage drop, is presented in Figure 6.4. To find a voltage drop in a pixel, the following procedure is applied: a loop through all time samples is performed and for each time sample the distance in amplitude to the third time sample before is calculated (see Figure 6.4). The distance in amplitude is calculated to the third time sample before since at most two readout samples lie within the slope of the waveform with a particle hit. If this distance is maximal (see sample indicated as "i" in Figure 6.4), a first *estimate of the hit time* is set to the third time sample before (see sample indicated as "i-3" in Figure 6.4).

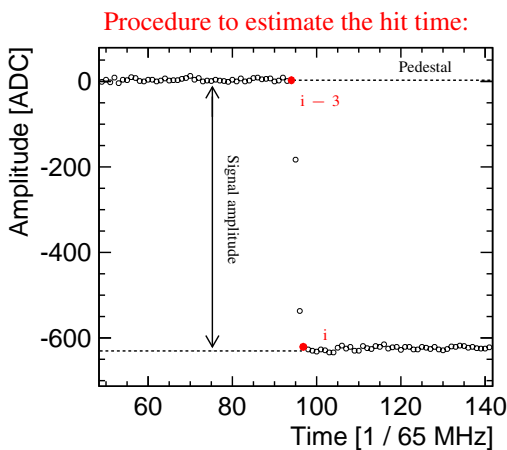


Figure 6.4: Illustration of procedure to estimate the particle hit time within the readout window.

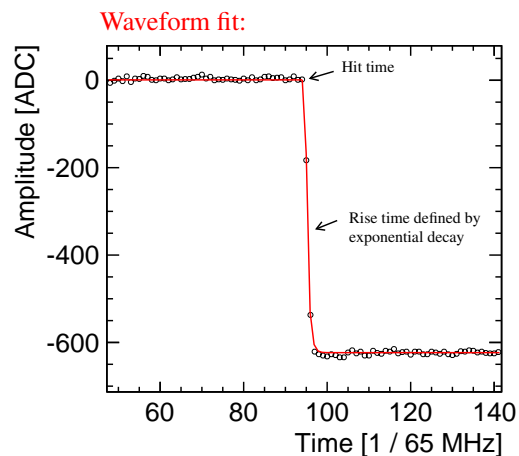


Figure 6.5: Fit (red line) of a constant function with an exponential decay to the single pixel waveform.

This estimate of the hit time is needed to calculate the signal and the noise: ten samples around the estimated hit time are masked and the signal is calculated by averaging all remaining amplitudes later in time and subtracting it from the average of the amplitudes earlier in time. An Investigator hit is not reconstructed by the analysis, if a particle hit occurs in the first or last five samples of the readout window ( $< 1\%$  of the active window). This does not result in a loss of efficiency since the first 100 ns and last  $\mu\text{s}$  of the active window are masked, as discussed later in Section 6.4.

The RMS of the amplitude values in the non masked regions is then defined as the *noise* and the analysis threshold is applied, requiring the signal to be larger than a multiplicity of  $N$  times the noise. The analysis threshold is applied at this stage of the analysis to remove possible noise contributions, which can lead to a fail of a fit to the waveforms. This fit uses the estimated hit time and signal as start values and is performed, to improve the timing measurement. The function  $f(t)$  is fitted to the single pixel waveforms

$$f(t) = \begin{cases} \text{constant}, & \text{if } t \leq t_{\text{hit}} \\ \text{constant} + (\text{signal amplitude}) \cdot (e^{-(t-t_{\text{hit}})/t_{\text{rise}}} - 1), & \text{if } t > t_{\text{hit}}. \end{cases} \quad (6.1)$$

For all times  $t$  before the hit time  $t_{\text{hit}}$  the function  $f(t)$  describes a constant. The function  $f(t)$  further describes an exponential drop after the hit time. The magnitude of the exponential drop is defined by the signal amplitude (see Figure 6.5) and its time constant is characterised by the rise time constant  $t_{\text{rise}}$ . The constant and signal amplitude, as well as the hit time  $t_{\text{hit}}$  and the rise time constant  $t_{\text{rise}}$  are free parameters of the fit. Motivated by the typical waveform shown e.g. Figure 6.4 and 6.5, the start value for the rise time constant  $t_{\text{rise}}$  of the fit has been set to two time samples.

To evaluate the quality of the fit, the  $\chi^2/\text{ndof}$  for a few thousands of waveform fits, is presented in Figure 6.6. The narrow peak of the  $\chi^2/\text{ndof}$  distributions around a value of one shows the stable fit

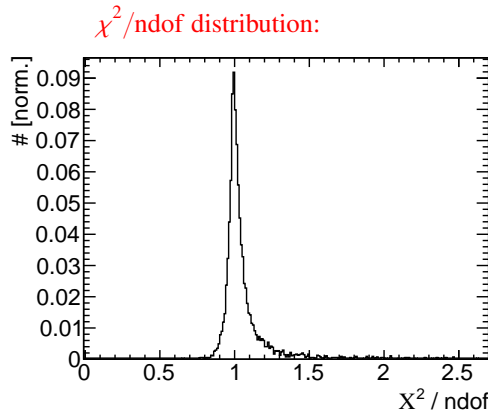


Figure 6.6:  $\chi^2/\text{ndof}$  of the waveform fits in equation 6.1.

performance.

During data taking the signal is defined as the difference in amplitude between one time sample and the previous. In contrast to this, the signal in the analysis is defined as the difference between the average amplitude before and after a particle hit. Therefore, the signal definition applied during the analysis is more stable since it is less sensitive to sample by sample noise fluctuations (e.g. from thermal of  $1/f$  noise, see Chapter 5.3). Moreover, since the signal is defined as the differences of two amplitude values in one readout frame, the contribution from the offset of the reset noise is expected to be suppressed.

### 6.1.2 Event building and offline synchronisation of Investigator and Timepix3 telescope data

Since no synchronised clock has been used for the Investigator and the Timepix3 telescope data taking, the synchronisation has been performed by an offline procedure during the event building. Moreover, the event building in the EUTelescope framework (data converter step) has been adapted to the data driven readout of the Timepix3 telescope chips [33]. The event building procedure, including the offline synchronisation of the Investigator and telescope data, is shown in Figure 6.7.

During the event building, 100 ms of the recorded raw data are read out from the event files and filled into a vector. The recorded raw data includes the hits from the telescope planes as well as the veto and the Investigator trigger. To explain the synchronisation, these objects are in the following identified by their time stamps. This is illustrated in Step 1 of Figure 6.7, where the different numbers correspond to different time stamps in arbitrary units.

To calculate the absolute Investigator hit time with respect to the Timepix3 reference clock, the  $n^{\text{th}}$  Investigator trigger time stamp is assigned to the  $n^{\text{th}}$  Investigator event (see Step 2 in Figure 6.7). A constant time delay has been observed in a later stage of the analysis by comparing the time stamp of a track through the Investigator to the time stamp of the matched Investigator hit. This constant time delay can be attributed to different effects: the length of the cables bringing the Investigator trigger signal from the INVROS to the telescope readout system, and the fixed time delay after a triggered Investigator frame, at which the trigger signal is sent from the INVROS to the telescope planes. The offset has been found to be in the order of a few hundred nanoseconds. The time stamp assigned to the  $n^{\text{th}}$  Investigator event is then calculated as

$$t_{\text{Investigator event } n} = t_{\text{trigger } n} - \text{offset}. \quad (6.2)$$

The difference  $\Delta$  between the single pixel hit time  $t_{\text{hit}}$  (which can be at an arbitrary time within the readout window and is described in the previous section) and the end of the readout window is subtracted from this time to obtain the absolute time stamp  $t_{\text{hit absolute}}$  of a hit in an Investigator pixel

$$t_{\text{hit absolute}} = t_{\text{Investigator event } n} - \Delta. \quad (6.3)$$

The reconstructed Investigator hits with their absolute single pixel Investigator time stamp  $t_{\text{hit absolute}}$ , are further inserted in the 100 ms vector, which already contains the telescope hits, as well as the veto and the trigger signals (see Step 3 of Figure 6.7).

Next, the time stamps in the 100 ms vector are ordered descending in time, since the Timepix3 hit data is not sent out of the chip in strict time order (see Step 4 in Figure 6.7).

Starting from the earliest time stamp at the end of the vector, the time stamps in the 100 ms vector are separated into smaller units of  $10 \mu\text{s}$  duration and removed from the 100 ms vector (see Step 5 in Figure 6.7). Each  $10 \mu\text{s}$  unit is defined as an *event* in the following analysis.

Before the 100 ms vector is empty, it gets refilled with new data (see Step 6 in Figure 6.7) and the procedure repeats iteratively from Step 2 in Figure 6.7, until all data has been read out. By refilling the 100 ms vector before it is empty and building the  $10 \mu\text{s}$  events from this vector, an assignment of hits into the wrong event, due to effects in the transition region between two 100 ms data chunks, can be avoided.

## 6.2 Cluster and hit reconstruction

A clustering of the pixels in an event is performed using the processor EUTelClustering Processor of the EUTelescope framework. For each event, the algorithm starts with an arbitrary pixel and combines it

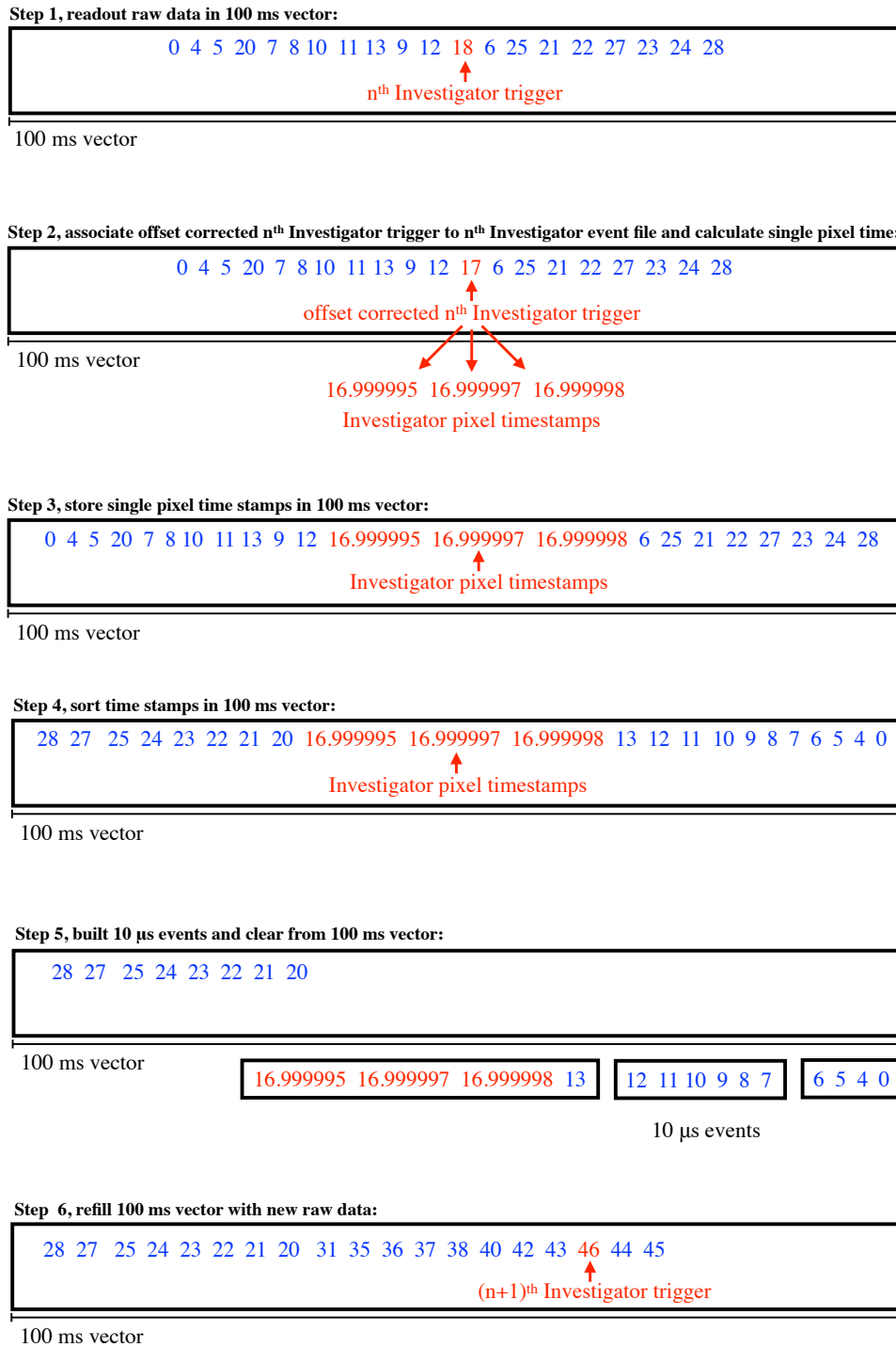


Figure 6.7: Flowchart of the steps for the offline synchronisation of the Investigator and Timepix3 telescope data. The integer numbers symbolise telescope time stamps in arbitrary units. The floating point numbers symbolise Investigator pixel time stamps.

with all adjacent pixels. For each adjacent pixel the procedure is iteratively repeated and all pixels found by this procedure are combined to an object referred to as a *cluster*. The pixel with the highest signal in a cluster is in the following referred to as *seed pixel* and all other pixels of the cluster are referred to as *neighbouring pixels*.

The position of each cluster in X and Y dimension of the pixel matrix is obtained by charge interpolation between the pixels  $i$ , using the *Centre of Gravity (CoG)* algorithm

$$\text{CoG}_{X/Y} = \frac{\sum_{\text{pixel } i} X_i/Y_i \cdot \text{charge}_i}{\sum_{\text{pixel } i} \text{charge}_i}, \quad (6.4)$$

with the single pixel centre position  $X_i/Y_i$ . An  $\eta$  correction has been applied, to correct for non-linear charge sharing effects [88]. For the  $\eta$  correction the EUTelescope processor `EUTelCalculateEtaProcessor` has been used, which calculates the  $\eta$  correction in a data driven way during the analysis. The  $\eta$  variable is defined as

$$\eta = \begin{cases} \frac{\sum_{\text{pixel } i=1}^2 X_i/Y_i \cdot \text{charge}_i}{\sum_{\text{pixel } i=1}^2 \text{charge}_i} & \text{for multi-pixel clusters} \\ X_1/Y_1 & \text{for single-pixel clusters} \end{cases} \quad (6.5)$$

with  $\text{pixel}_{1/2}$  being the pixels with the highest and second highest signal in a cluster. The  $\eta$  correction is performed independently for the reconstructed positions on each detector (telescope planes and Investigator), assuming homogenous illumination with tracks within the pixel. For the  $\eta$  correction a histogram with the dimensions of the pixel cell is filled with the  $\eta$  variable, as presented in Figure 6.8. A spike can be observed at zero in the  $\eta$  histogram, originating from single-pixel clusters, where the  $\eta$  variable is always set to the pixel centre (see equation 6.5). The integral of the  $\eta$  histogram, as presented in Figure 6.9, is used to correct the reconstructed cluster position. Note that the  $\eta$  correction does not impact single-pixel clusters, since the evaluation of the  $\eta$  integral for single-pixel clusters gives the value of pixel centre, as the reconstructed single-pixel cluster position. This is visible in Figure 6.9 by the step of the integral at the centre pixel position. As shown in Figure 6.8 and 6.9, the  $\eta$  correction is performed independently for the X and Y dimension of the pixel matrix, assuming the charge sharing in X to be independent of Y (and vice versa).

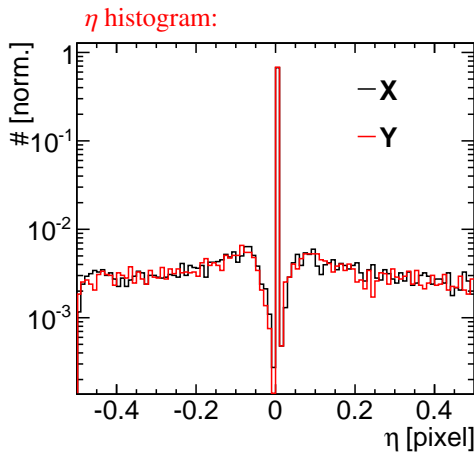


Figure 6.8: Example of histogram of the  $\eta$  variable, as defined in the text.

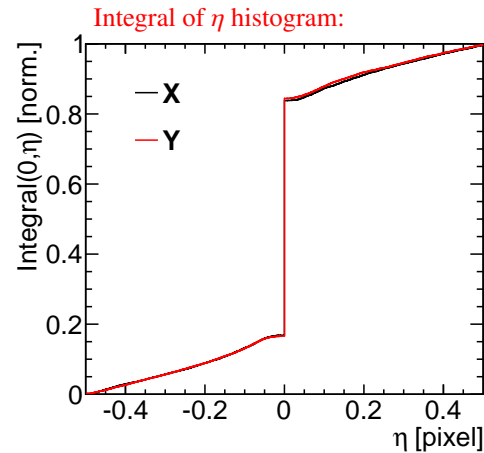


Figure 6.9: Integral of the histogram in Figure 6.8, used to calculate the  $\eta$  corrected position.

Using the calculated cluster positions *hits* are defined on the different telescope planes and the Investigator by transforming the position of the clusters from the *local coordinate system* of the Investigator reference system to the *global coordinate system* of the telescope reference system.

## 6.3 Alignment and track reconstruction

### 6.3.1 Telescope alignment

In a next step, the planes of the telescope are aligned with respect to each other. This telescope alignment has been performed with the processor EUTelMille of the EU Telescope framework, where straight tracks are defined using the hits on the telescope planes. The processor makes use of the Millepede II algorithm [89] to do a least squares minimisation of the track  $\chi^2$ . The track residuals are defined in this stage of the analysis as the spatial distance between the intercept position of the straight track on the considered telescope plane and the reconstructed hit position on that telescope plane. The first and second plane of the telescope with respect to the beam direction have been used as fixed reference for the alignment. The degrees of freedom during the alignment are the dimensions x, y and z (as defined in Chapter 5.5.1) and the rotations around these axes.

### 6.3.2 Telescope track finding and fitting

After the alignment of the telescope planes with respect to each other, the EU Telescope processor EUTelTestFitter is used to find and fit telescope tracks. This processor fits the hits on the telescope planes, taking into account multiple scattering (non-straight lines). During the fit, the  $\chi^2$  of the tracks is minimised.

A reconstructed telescope track is required to have at least five hits in the telescope and to have a  $\chi^2/\text{ndof} < 10$ . The biased residual is defined as the spatial distance between the intercept position of the telescope track on the considered telescope plane and the reconstructed hit position on that telescope plane<sup>1</sup>. The biased residual distribution on the third telescope plane with respect to the beam direction is presented in Figure 6.10. The residual is centred around zero with an RMS on a range of  $\pm 20 \mu\text{m}$  of

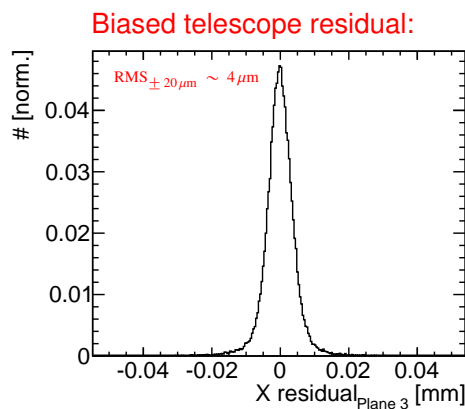


Figure 6.10: Biased residual on the third telescope plane with respect to the beam direction.

<sup>1</sup> The residual defined as such is named biased, since the hits on the considered telescope plane are also used for the track reconstruction.

$\sim 4 \mu\text{m}$ , showing the good performance of the telescope alignment. As studied in detail in [33], this single plane resolution is compatible with the  $1.8 \mu\text{m}$  achieved for the track resolution on the Investigator reference plane, when using all six telescope planes for the track reconstruction.

### 6.3.3 Investigator alignment

To align the Investigator with respect to the telescope reference system, the difference between the reconstructed Investigator hit position and the interpolated track position on the Investigator is calculated and the Investigator position is changed along the dimensions  $x$  and  $y$  until the residuals are centred around zero. To be sensitive to a movement of the Investigator over a longer time scale the alignment is performed for each run separately. For the studied Investigator mini matrices with a size of  $0.224 \times 0.224 \text{mm}^2$ , this results in too low statistics to be sensitive to the rotations of the small chip within the telescope. For this reason, tilts of the Investigator with respect to the telescope reference system are not corrected.

## 6.4 Analysis cuts

In addition to the cuts mentioned above, further quality cuts are performed during the analysis.

**Matching of tracks and Investigator hits** For each telescope track all Investigator hits in the same event are considered. The spatial distance between the telescope track position and the Investigator hit position is calculated for all hits in one event. Note that by this, the event size defines the cut in time to match an Investigator hit to a telescope track. The hit in the event with the minimal spatial distance to the track is considered and matched to the telescope track, if their spatial distance in  $X$  and  $Y$  direction is smaller than  $100 \mu\text{m}$ .

**Edge masking** Tracks passing through the outer half of the active Investigator edge pixels are discarded to avoid a bias of charge sharing observables due to missing neighbouring pixels and to avoid effects from the track prediction resolution. The remaining area on the Investigator is in the following referred to as *region of interest (roi)*. Tracks passing through that region are referred to as *roi-tracks*.

**Timing cuts** Further cuts are performed to cut out the *roi-tracks* reconstructed during the dead times of the Investigator. These cuts are performed on the difference between the time stamp of *roi-tracks* and the closest earlier veto time stamp, as illustrated in Figure 6.11.

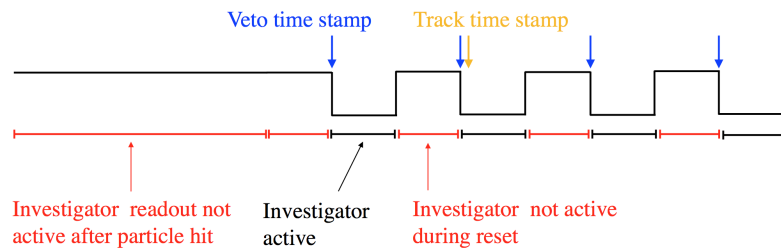


Figure 6.11: Illustration of the procedure to cut out the time windows where the Investigator or its readout are inactive, using the veto time stamp. The sketch shows the case where the Investigator active window is aligned with the veto time stamp.

The difference calculated between the time stamp of a roi-track (orange) to the previous veto time stamp (blue) is presented in Figure 6.12. Directly after the veto time stamp (zero value of the X axis in

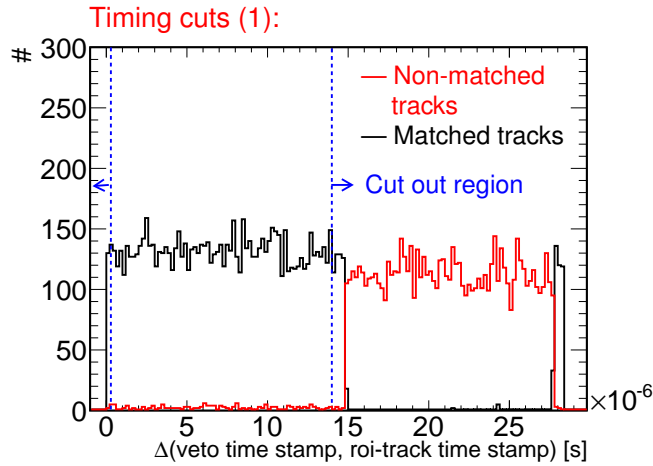


Figure 6.12: Histogram of the difference between the track time stamp and time stamp of the telescope veto release. All tracks outside a range of  $[100 \text{ ns}, 14 \mu\text{s}]$  are masked, as discussed in the text.

Figure 6.12) the Investigator is expected to be active for  $\sim 15.6 \mu\text{s}$  and most tracks are matched to an Investigator hit (*matched tracks*). After this time the Investigator is inactive during the reset pulse and no Investigator hit can be matched to the tracks (*non-matched tracks*).

To be able to perform a proper efficiency measurement, tracks with times larger than  $14 \mu\text{s}$  in Figure 6.12 are cut out by the analysis. Moreover, the first  $100 \text{ ns}$  in Figure 6.12 are also cut out from the analysis to avoid an efficiency loss due to the reconstruction of the Investigator signal, as described in Section 6.1.1.

The occurrence of matched tracks at  $\sim 28 \mu\text{s}$  in Figure 6.12 can be explained by delays of the veto time stamp, as illustrated in Figure 6.13. If the veto time stamps are delayed, they can be shifted to times

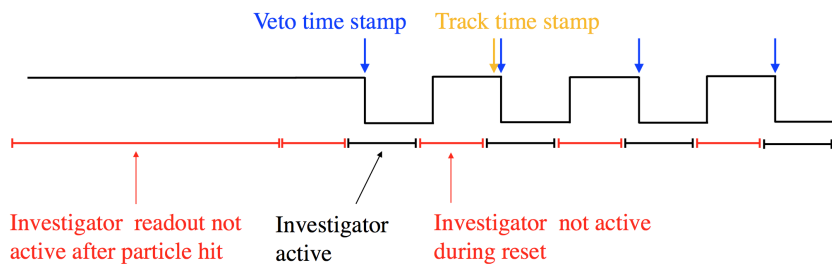


Figure 6.13: Illustration of the procedure to cut out the time windows where the Investigator or its readout are inactive, using the veto time stamp. The sketch shows the case where the veto time stamp is shifted to later times and thus not aligned with the veto time stamp.

after the track time stamp. Accordingly, the veto time stamp from the previous reset veto is used as the closest earlier veto time stamp. This results in the occurrence of matched tracks at  $\sim 28 \mu\text{s}$  in Figure 6.12 and explains that matched tracks can only be observed for  $\sim 14.8 \mu\text{s}$  after the veto time stamp (compared to the expected time of  $\sim 15.6 \mu\text{s}$ ).

To cross check if the extended long readout veto after a particle hit has been reliably generated by the Aduino-NIM logic presented in Figure 5.6 and 5.7, the number of reset vetoes counted between the track time stamp and the closest earlier readout veto is presented separately for matched and non-matched tracks in Figure 6.14. The non matched tracks peak at a value close to zero (directly after the extended

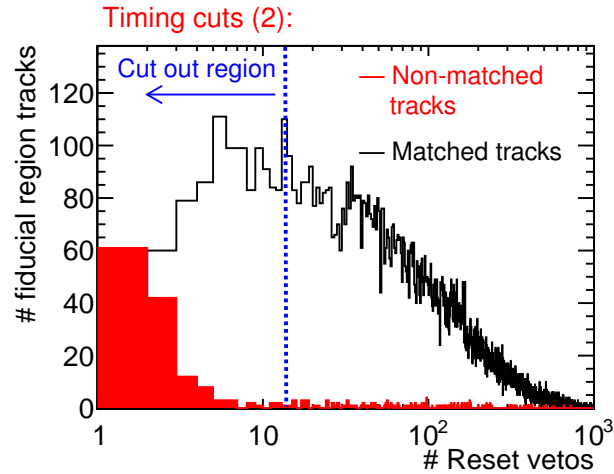


Figure 6.14: Histogram of number of reset vetoes before a roi-track and after the long readout veto.

long readout veto), indicating that the long readout veto has not been extended sufficiently long to cover the dead time of the readout. For this reason, the readout veto has been extended offline by only considering tracks with at least 15 reset vetoes between the long readout veto and the roi-track.

## 6.5 Observables

In the following, the basic observables are defined. Afterwards common representations of the observables are introduced.

### 6.5.1 Definition of observables

To characterise the Investigator performance, the following observables are calculated from the telescope tracks and Investigator hit properties:

- **Telescope track position:**

The track is interpolated on the Investigator and its intersect point with the Investigator plane is calculated. Moreover, the pixel geometry of the Investigator is used to determine the local position of the telescope track within the Investigator pixel cell.

- **Investigator hit position:**

The pixel geometry of the Investigator is used to determine the local position of the reconstructed hit.

- **Spatial residual:**

The spatial residual is defined as the spatial distance of the reconstructed track position with respect

to the reconstructed Investigator hit position. The spatial residual is calculated independently for the X and Y direction of the matrix.

- **Spatial resolution:**

The spatial resolution is defined as the RMS of the spatial residual distribution on a range of  $\pm 20 \mu\text{m}$ . The telescope spatial resolution of  $\sim 2 \mu\text{m}$  is not unfolded from this value.

- **Telescope track time:**

The time of the telescope track is defined as the mean time of all telescope hits associated to the telescope track, whereas the time of a telescope hit is defined as the time stamp of the earliest pixel of the cluster associated to the hit.

- **Investigator hit time:**

The Investigator hit time is defined as the time of the earliest pixel of the associated cluster.

- **Timing residual:**

The timing residual is calculated by subtracting the telescope track time from the time of the associated Investigator hit.

- **Timing resolution:**

The timing resolution is defined as the width of a Gaussian fit to the timing residual distribution on a range of  $\pm 50 \text{ ns}$ . The telescope timing resolution of  $\sim 1 \text{ ns}$  is not unfolded from this value.

- **Investigator  $T_{10-90}$  time:**

The time  $T_{10-90}$  the first pixel in a cluster needs to rise from 10 – 90 % of its total amplitude is calculated from the time constant  $\tau_{\text{rise}}$  extracted from the exponential fit (see Section 6.1.1) as

$$T_{10-90} = 2.2 \times \tau_{\text{rise}}. \quad (6.6)$$

- **Cluster size:**

The cluster size is defined as the number of pixels in a cluster.

- **Efficiency:**

The efficiency is defined as the number of roi-tracks with a matched Investigator hit divided by the total number of roi-tracks.

- **Seed signal:**

The seed signal is defined as the signal of the seed pixel.

- **Cluster signal:**

The cluster signal is defined as the sum of the signal of all pixels in cluster.

## 6.5.2 Representation of observables

### In-pixel representation

To gain a more detailed understanding of how the observables are impacted by the pixel layout, observables are shown in an *in-pixel representation*:

A histogram with the dimensions of a single pixel cell is filled at the track intercept position within the hit pixel. Using this representation, all tracks are mapped into a single pixel cell and the observables

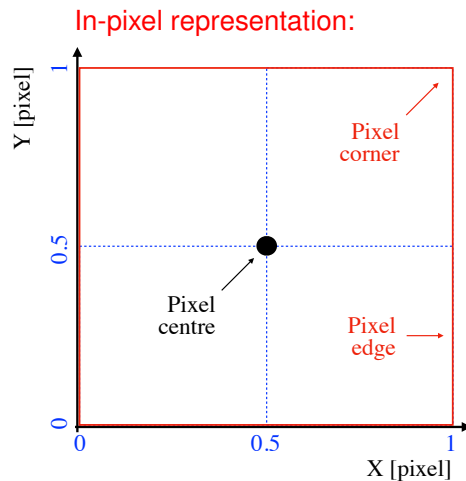


Figure 6.15: Description of the in-pixel representation.

can be studied in dependence of the position, at which the track passes through the pixel, as sketched in Figure 6.15.

For the in-pixel representation the coordinates are defined in units of the pixel size, ranging from a value of zero (corresponding to one pixel edge) and a value of one (corresponding to the other pixel edge). In this coordinate system, the pixel centre is defined at a value of  $(X, Y) = (0.5, 0.5)$  and the pixel corners are at values of  $(X, Y) = (a, b)$  with  $a, b \in \{0, 1\}$ .

### Comparison of observables to 2 dimensional simulations

As described in the next chapter, two dimensional simulations have been performed. To compare the results of the two dimensional simulations to the test beam results the observables from the test beam data need to be reduced to the dimensions considered in the simulation. For this reason, the test beam observables are considered only in one dimension of the pixel matrix, equivalent to the one simulated matrix dimension.

Moreover, observables can depend on the track intercept position within the pixel cell. One example is the charge sharing in X dimension: if the track intercept position is close to the Y edge of the pixel cell, the total charge is more likely to be shared in Y dimension and the probability of the charge sharing in X dimension can be reduced. These effects on the edges of the pixel cell in the non-simulated dimension need to be suppressed for the comparison of the two dimensional simulation results to the measurement results. For this reason, a cut on the pixel centre has been performed on the non-simulated dimension, as presented in Figure 6.16. This cut is only applied for the comparison of the test beam data to the simulations, presented in a later Chapter 11.

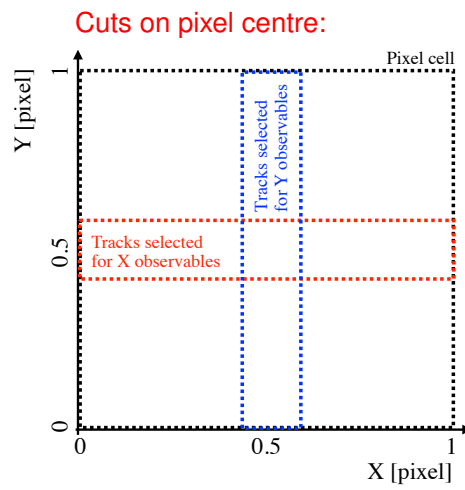


Figure 6.16: Description of the cut performed on the test beam data to compare the observables to the two dimensional simulation.

---

## Simulation of sensor response

---

To model the response of silicon detectors, validate the measurements, and gain a better understanding of the different technologies, a simulation chain has been developed in course of this thesis. In this chapter, the simulation chain is explained using the example of the Investigator.

The different steps of this simulation chain are:

- **Geant4 simulation:**

*Geant4* is a toolkit to simulate the interaction of particles when passing through matter [90], that is used in a first step of the simulation to determine the charge deposited by particles traversing the silicon sensor. To model different kinds of interactions, *physics lists* can be selected in *Geant4*. For the simulations in this thesis, the *Geant4* version 09.06 has been used and the *QGSP\_BERT* physics list with the *Photon Absorption Ionisation Model (PAI)* [91], to describe the energy loss distribution in thin sensors.

- **TCAD simulation:**

*Technology Computer Aided Design (TCAD)* simulation tools can be used to simulate semiconductor devices and their operation. To determine the properties as well as the charge propagation in the device, the equations describing the physics of the simulated device are solved numerically on a position grid, using finite element calculations. For the simulations in this thesis the *Synopsys Sentaurus framework* version I – 2013.12 is used [92].

TCAD simulations have been used to simulate electrical properties of the Investigator, the charge propagation in the Investigator after a particle incident, as well as to calculate the induced charge on the pixel implants. The charges are placed according to a predefined track and the charge density along this track is obtained from the *Geant4* simulation.

- **Fast model for energy and noise fluctuations and digitisation:**

To model noise and energy fluctuations as well as the digitisation of the charge induced in the different pixel contacts, a parametric model has been implemented in a dedicated C++-tool. Finally, a reconstruction is performed to calculate different observables, which characterise the performance of the simulated sensor.

The different steps of the simulation chain are discussed in more detail in the following sections.

## 7.1 Geant4 simulation of the charge deposited by a particle traversing a silicon sensor

The distribution of the charge created by a particle traversing a silicon sensor strongly impacts the charge sharing and thus the performance, such as the spatial resolution. When simulating an ionising particle traversing a silicon sensor in TCAD, the distribution of the charge density in the sensor is defined by parameters that need to be specified by the user (e.g. a Gaussian with a selected width). Alternatively, the distribution of the charge density can be provided as input for the TCAD simulation, such that it does not need to be set by a free parameter. To model this distribution of the charge density created by a particle traversing the silicon sensor, a Geant4 simulation has been performed.

A particle with a defined type (e.g. electron or pion) and energy is shot into a three dimensional silicon block. The charge deposited on the different three dimensional space points is calculated in the coordinate system presented in Figure 7.1.

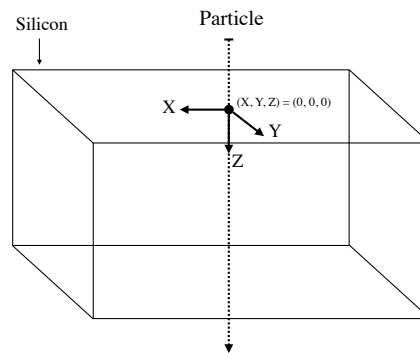


Figure 7.1: Schematic and coordinate system of the Geant4 simulation (not to scale). A particle is shot into a silicon block.

The dimension  $Z$  of the sensor depth is defined perpendicular to the sensor surface, where the particle enters the silicon block. The thickness of the silicon is defined along the dimension  $Z$  and set to the Investigator chip thickness of  $100\ \mu\text{m}$ . The dimensions perpendicular to the dimension  $Z$  are denoted as the *transversal coordinates*  $X$  and  $Y$ . Transversal dimensions of  $5\ \text{mm}$  have been simulated for the silicon block. The point on the sensor surface where the particle enters the silicon has been set to  $(X, Y, Z) = (0, 0, 0)$ .

One particle per event is fired into the sensor and the simulation has been performed for 1000000 events. A three dimensional histogram has been filled with the calculated charge deposited on the three dimensional space points of the sensor. The problem is symmetrically under transposition of the  $X$  and  $Y$  dimension. Therefore, to obtain a distribution of the charge deposit for the two dimensional TCAD simulations, the distribution has been projected into the  $X$ - $Z$  plane. An example of this projection is presented in Figure 7.2, showing a peak of the deposited charge along the tracks where the particles have been shot into the silicon. The deposited charge decreases strongly outside this peak, however, tracks from delta rays are observable far outside the peak.

As presented in Figure 7.3, the spatial charge distribution shown in Figure 7.2 has been further projected separately along the sensor thickness  $Z$  and the transversal dimension  $X$ , giving the average spatial charge distribution along these dimensions. To model the spatial charge distribution in the following TCAD simulations, both distributions are evaluated for different  $X$ - $Z$  space points of the mesh defined in the

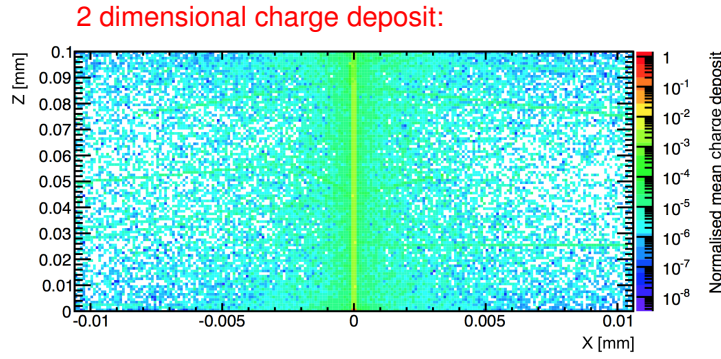


Figure 7.2: Charge deposited by 120 GeV pions traversing a silicon block of  $100\ \mu\text{m}$  thickness projected into the X, Z plane.

TCAD simulations. The X and Z profiles in Figure 7.3 have been used instead of the two dimensional distribution in Figure 7.2, in order to limit the computation time for the TCAD simulations.

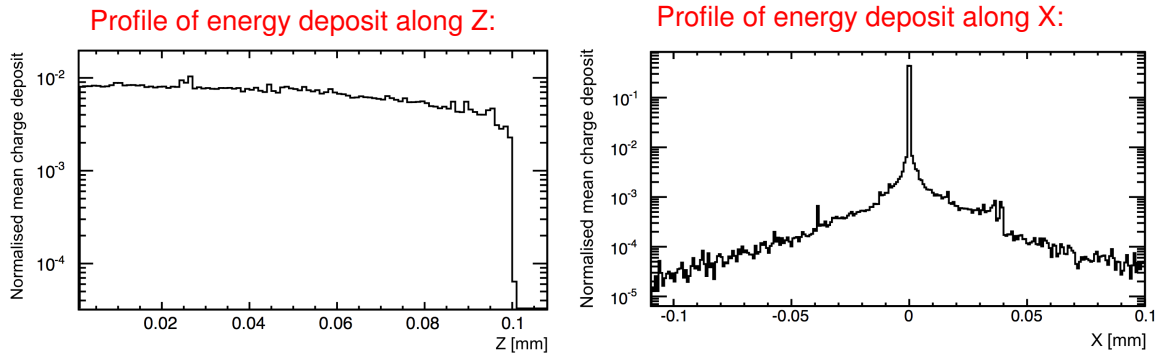


Figure 7.3: Charge deposited by 120 GeV pions traversing a silicon block of  $100\ \mu\text{m}$  thickness projected along the depth Z (left) the transverse coordinate X (right) of the sensor (see Figure 7.1).

## 7.2 Finite element simulation of the sensor response with TCAD

Two dimensional TCAD simulations have been performed for the modified and standard process of the Investigator. The simulations have been performed in two instead of three dimensions to reduce the computing time. The aim of the simulations is to gain a detailed understanding of the electric field distribution in devices fabricated in the standard and modified process (*quasi stationary simulation*) and understand the resulting charge collection behaviour (*transient simulation*). Moreover, the TCAD simulations are used in further simulation steps, to validate test beam measurements and make performance predictions.

First the simulated Investigator sensor design is presented, followed by a short description of the quasi stationary and transient simulation, illustrated by some characteristic examples. Systematic studies of the quasi stationary and transient simulation are presented in Chapter 8.

### 7.2.1 Pixel layout

In the first step of the TCAD simulations the pixel geometry is implemented. A structure of five adjacent pixels has been used for all TCAD simulations to obtain a realistic simulation of the charge sharing

between the pixels. The doping profiles sketched in Figure 7.4 for a single pixel cell for the standard and modified process are implemented in the TCAD simulations. In addition to the standard process, the



Figure 7.4: Schematic of the simulated cross section of a single pixel cell for the *standard process* (left) and the *modified process* (right), with the pn junctions marked in yellow (not to scale). The colour intensities illustrate the doping levels: lower doping levels are indicated by a lighter colour.

modified process contains a planar n layer. This modification results in a pn junction that extends over the full lateral size of the simulated structure in contrast to the standard process, where the pn junction is locally restricted to the small region around the collection electrode (see yellow lines in Figure 7.4).

The simulated five-pixel structure of the standard process is presented in Figure 7.5. The simulated structure has an overall thickness of 100 μm and an epitaxial layer thickness of 25 μm. The doping of the epitaxial layer and backside has been taken from [39] and shows a gradient from the out diffusion from the p type backside to the low doped (high resistivity) region. The CMOS logic has not been implemented in the p wells, since it is expected to have no impact on the electric field and the charge collection within the sensor. The grey structures represent aluminium metal contacts. Contacts are placed at the p wells close to each pixel implant and at the backside of the simulated structure to apply the bias voltage (*bias contacts*). For the tested Investigator chip, the bias voltage is shorted via non-depleted regions at the matrix edges to the backside of the chip. Since the simulation contains of a periodic structure not simulating the edge structures, the bias voltage in the simulation has been set to the backside by this additional contact. Note that this contact is not important as long as the pixel is not depleted over the full lateral size of the pixel, since the voltage is then connected via the non-depleted regions between the p wells and the backside. Other contacts have been placed on the pixel implants (*pixel contacts*) to

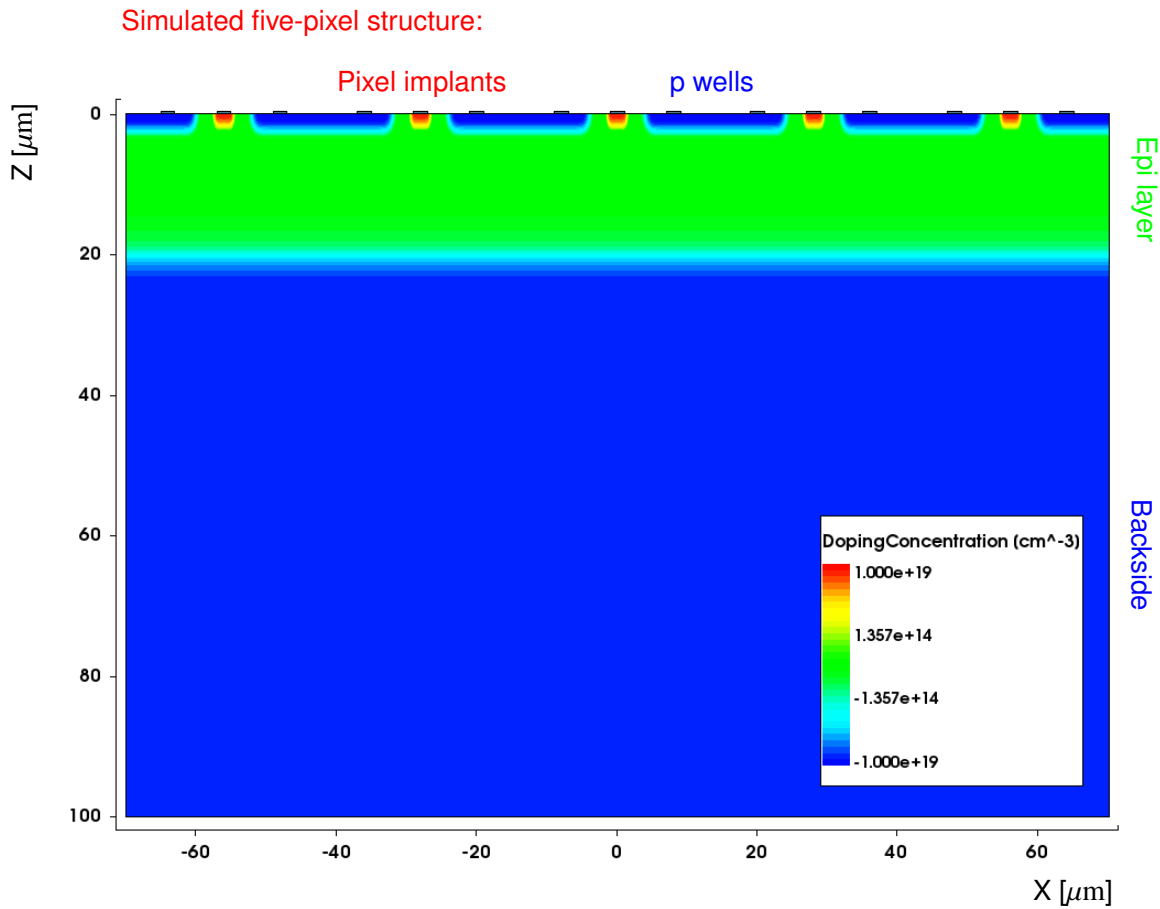


Figure 7.5: Five-pixel structure of the Investigator standard process.

apply the reset voltage and read out the signal. For the modified process the doping profile and geometry of the pixel implants, p wells and n layer have been taken from [4].

A mesh is defined across the simulated structure by small triangles, at which corners the solutions of the finite element simulation is calculated, as presented in Figure 7.6. The mesh has been adjusted to the gradient in the doping concentration. A fine mesh is used in the regions of a high gradient in the doping concentration around the pixel implants, the p wells and close to the rise of the doping of the backside substrate. A coarser mesh is used in the regions with a low doping gradient in the epitaxial layer and backside substrate. At the position where a particle incident is simulated later, a fine mesh has been used over the full depth.

### 7.2.2 Edge effects and boundary conditions

Edge effects of the simulation can impact the results of the quasi stationary simulation as well as of the transient simulation.

For the quasi stationary simulation, properties such as the electric field are expected to be changed by edge effects, i.e. the electric field is different when the adjacent pixel is missing. To avoid this problem, the option of periodical boundary conditions has been used in the TCAD simulations.

For the transient simulation periodical boundary conditions are not sufficient to obtain a realistic response of the simulated sensor, as discussed in the following. Periodic boundary conditions would imply that charges drifting e.g. outside of the simulated sensor on side B in Figure 7.7 would drift

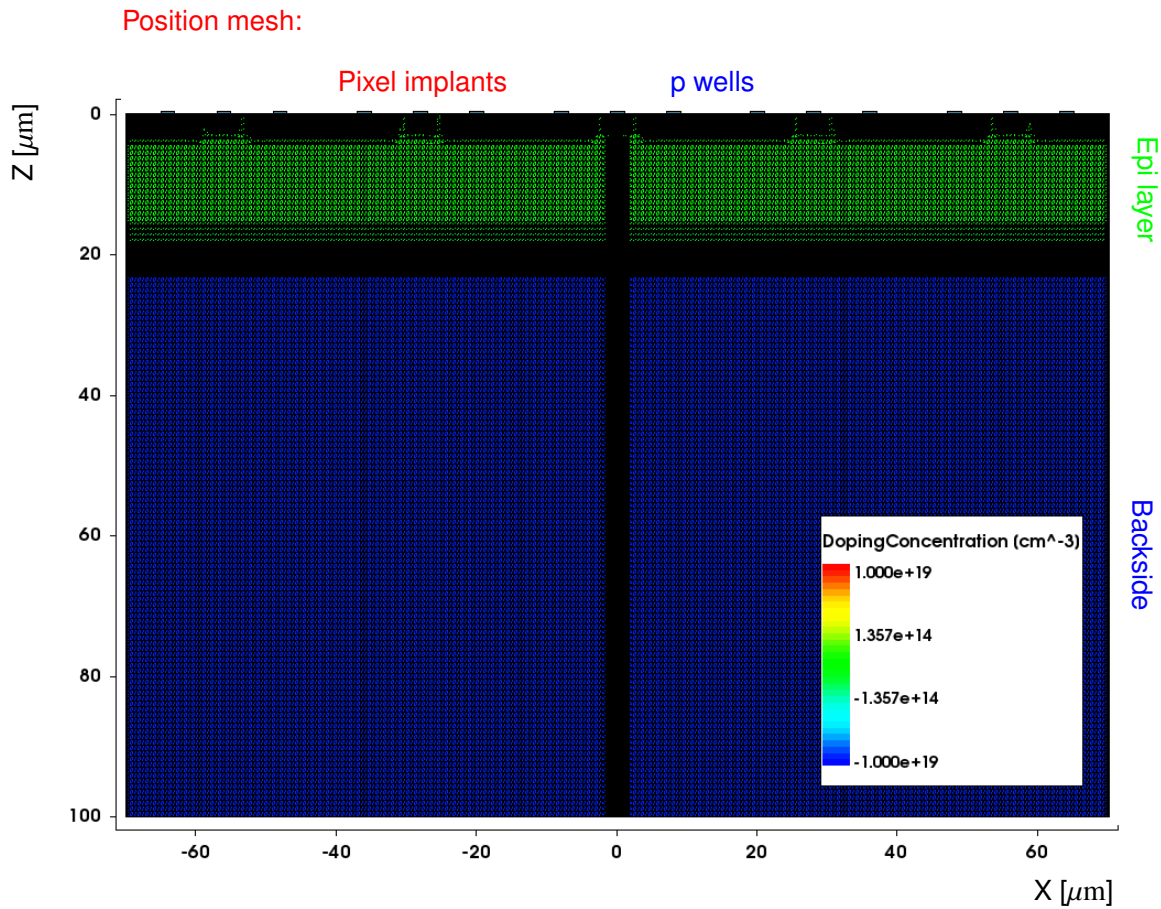


Figure 7.6: Position mesh of the Investigator standard process. The mesh has been adjusted to the gradient of the doping profile.

into the sensor on side A. Due to the periodicity of the simulated sensor, the same charge would be induced in the pixel contacts and not be lost. However, one goal of the simulation chain is to calculate the spatial resolution of a specific sensor design, that is calculated from the induced charge on the pixel contacts weighted by the position. Following the argument above the periodic boundary conditions in the simulations would result in a loss of the information of the position of the pixel contacts. To avoid this loss of position information, the dimension of the simulated sensor has to be sufficiently large to ensure that the position of the particle can be reconstructed correctly, motivating the simulation of five pixels.

### 7.2.3 Quasi stationary simulation

The potentials corresponding to the voltages are applied to the contacts of the simulated structure. For the quasi stationary simulations, the voltages are ramped up in fine predefined steps to ensure the convergence of the simulations. The solution of the Poisson equation is numerically calculated on the crossing points of the triangles of the mesh presented in Figure 7.6. The calculation is performed iteratively using the predefined step size. Properties such as the evolution of the electric field and the depletion region are calculated for each step.

The reset voltage of 0.8 V is applied in a first quasi stationary simulation step to the pixel contacts. A negative bias voltage of the maximal allowed voltage of  $-6$  V is applied to the bias contacts in a second quasi stationary simulation step. As discussed in Section 5.1, the maximal allowed bias voltage is limited

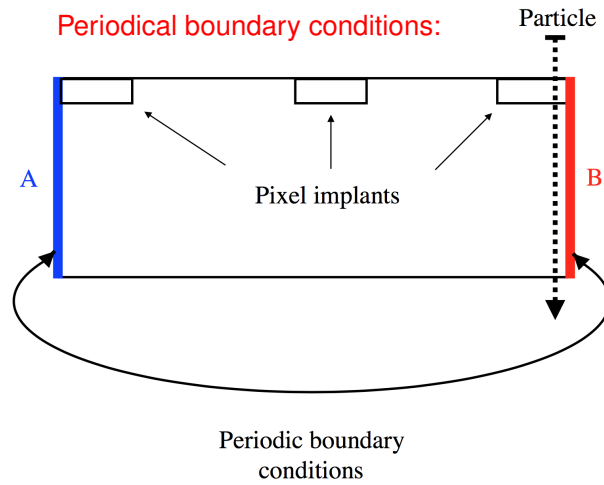


Figure 7.7: Sketch to illustrate the application of periodic boundary conditions to the TCAD simulation.

for the tested Investigator chip by the breakdown of the NMOS transistors to  $-6\text{ V}$ . The limitation of the bias voltage to  $-6\text{ V}$  has been taken into account in the simulations, despite the fact that the CMOS logic has not been implemented in the simulations, to compare to the test beam data.

An example of the hole density after ramping up the reset and bias voltage is presented in Figure 7.8. The depletion in the modified process extends homogeneously over the lateral size of the structure to

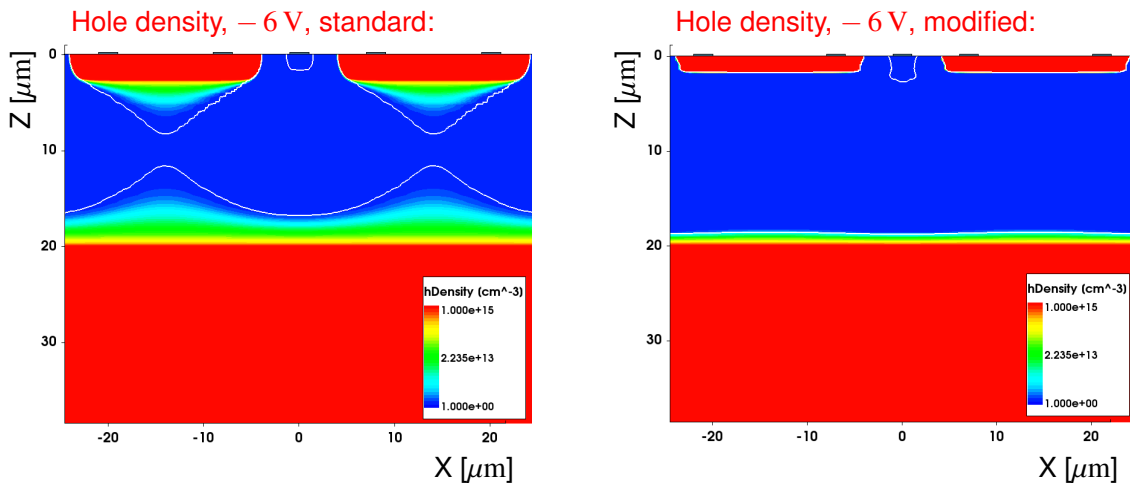


Figure 7.8: Hole density for a bias voltage of  $-6\text{ V}$  for the *standard process* (left) and the *modified process* (right). The white line marks the edge of the depleted region.

a depth of  $\sim 18\text{ }\mu\text{m}$ . For the standard process non-depleted regions are present at the pixel edges. A detailed discussion of the results of the evolution of the the depleted region and the electric field for different processes and bias voltages is presented in Chapter 8.

### 7.2.4 Transient simulation

In the following transient simulation a particle incident is described, using the charge distributions from the Geant4 simulation. For the transient simulations time steps need to be defined. The transient simulations are performed by iteratively solving the drift and diffusion equations on the mesh presented in Figure 7.6, numerically at each time step.

An example of the current induced in the centre pixel is presented in Figure 7.9. Each of the markers represent one time step of the transient simulation.

As a next step the charge induced in the different pixel contacts is calculated. The charge  $Q$  per pixel is defined as

$$Q = \int_0^{t_{\text{int}}} I_{\text{pixel}} dt \quad (7.1)$$

with the current per pixel  $I_{\text{pixel}}$  and the integration time  $t_{\text{int}}$ . An example of the charge versus integration time is presented in Figure 7.10. An integration time of  $1.5 \mu\text{s}$  has been selected for all simulations presented in this thesis to consider possible late contributions from diffusion.

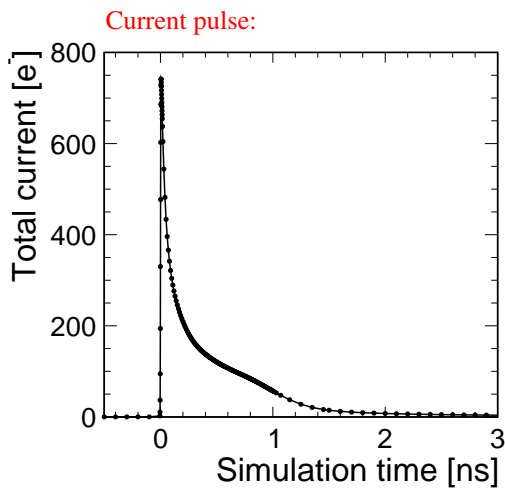


Figure 7.9: Pixel current  $I_{\text{pixel}}$  versus simulation time for a particle shot into the structure at the pixel centre for the standard process at a bias voltage of  $-6 \text{ V}$ . The particle enters the simulated Investigator at  $0 \text{ ns}$ .

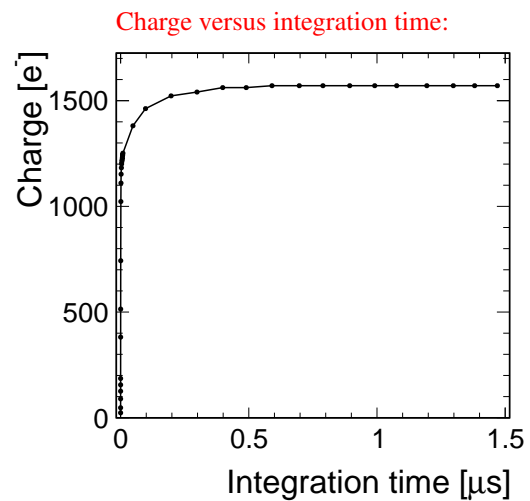


Figure 7.10: Charge versus integration time for a particle shot into the structure at the pixel centre for the standard process at a bias voltage of  $-6 \text{ V}$ .

### 7.2.5 Unit cell

The induced charge values on the pixel contacts depend on the position, where the particle penetrates the sensor between two pixels. Effects that can result in a variation of the Investigator response in dependence of the lateral incident position of the particle are:

- From geometrical considerations, charges created at the centre of the pixel are expected to be shared less and to be faster collected.
- The electric field can be inhomogeneous over the lateral dimension of the pixel.

Thus, for a complete description of the sensor performance, it is necessary to perform the TCAD simulation for several positions within a range which covers the full physical problem. This range is in

the following named *unit cell*. The unit cell for a particle track perpendicular to the sensor surface and without magnetic field is defined from the pixel centre to a distance of half a pitch from the pixel centre. The cell represents the full physical problem, since any track outside this unit cell can be mirrored inside the unit cell due to the periodicity of the sensor.

In the following the X coordinate where the particle enters the sensor is always defined in units of the pitch. The origin is set to the *pixel centre* and the highest value of the unit cell at half a pitch is referred to as the *pixel edge*. The pixel closest to the particle incident position is named the *centre pixel*, whereas the second closest pixel is referred to as the *first neighbour pixel*.

To integrate the Investigator response from the TCAD simulation into the simulation chain, particle incidents have been simulated at various lateral incident positions within the unit cell and the charge induced in the different pixel contacts has been calculated. The position mesh has been adjusted for each incident position such that it is finer spaced around the corresponding particle track position.

## 7.3 Parametric model of energy and noise fluctuations and digitisation

The TCAD simulations takes neither energy fluctuations nor noise into account. Moreover, the charge induced on the different pixel contacts is not digitised after the TCAD simulations. Hence, a parametric model has been setup to model these effects.

The tool for the parametric modelling reads as input the charge for different incident positions in the unit cell separately for each pixel. Next, these distributions are interpolated between the simulated points. The obtained functions are evaluated with a very fine step size, in order to simulate the homogeneous illumination of the sensor surface with particle hits. For each single evaluation step a few thousand iterations of the following steps are performed to model the noise and energy fluctuations.

### 7.3.1 Energy fluctuations

Fluctuations of the energy deposited by a particle traversing the silicon block, simulated in Geant4, result in a fluctuation of the charge density distributions used for the TCAD simulations. Conceptually the simulation steps discussed so far could be used to simulate accurately the fluctuations of deposited charge, by performing for each event of the Geant4 simulation a dedicated TCAD simulation, which includes the implementation of the exact charge deposit of this event. This would then account for fluctuations of the total charge the particle deposits in the sensor, as well as for local fluctuations along the track (single  $\delta$  rays). However, because of the limited computing resources a dedicated TCAD simulation for each event is not performed. Thus, the fluctuations of the deposited charge are taken into account with the fast parametric model.

The Investigator has an overall thickness of  $100\mu\text{m}$  and the modified process is fully depleted up to a depth of  $\sim 18\mu\text{m}$  (see Figure 7.8). As presented in the next Chapter (see Figure 8.24),  $\sim 40\%$  of the total charge is collected from the non-depleted backside region of the sensor. Making the approximation that the charge contribution from the non-depleted region is dominated from regions close to the depleted region, a thickness of  $18\mu\text{m} + 0.4 \cdot 18\mu\text{m} = 25.5\mu\text{m}$  has been simulated with Geant4 and the total deposited charge distribution has been calculated, as shown in Figure 7.11. Despite non-depleted regions at the pixel edges, no charge loss has been measured for the standard process (see Figure 10.11). Thus, the same distribution has been used to model the charge fluctuations for the standard process.

The total charge per event is then scaled with a random number  $R_{\text{Landau}}$  generated according to this

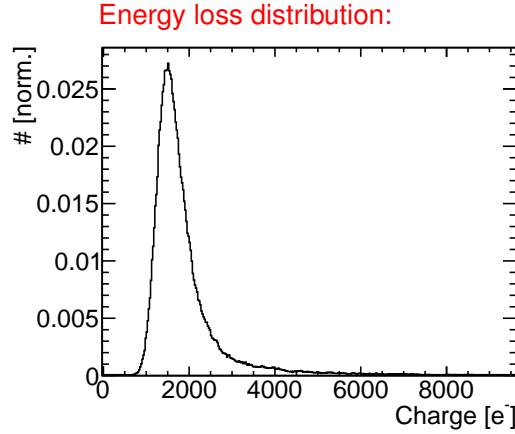


Figure 7.11: Total charge deposited by 120 GeV pions in a 25.5  $\mu\text{m}$  thick silicon sensor.

distribution. Hence, the charge induced in the single pixel contacts  $i$  gets modified according to

$$Q_{i,\text{Landau}} = Q_i \cdot (R_{\text{Landau}}/Q_{\text{total}}). \quad (7.2)$$

### 7.3.2 Noise fluctuations

Since the noise is not correlated between the pixels (e.g. electronic noise and shot noise), it needs to be modelled for each pixel individually. Therefore, a random number  $R_{\text{noise},i}$  is generated for each single pixel  $i$ , which follows a Gaussian distribution with a mean value of  $\mu = 0$  and a standard deviation  $\sigma$ . The random number  $R_{\text{noise},i}$  is then added to the charge  $Q_{i,\text{Landau}}$

$$Q_{i,\text{noise,Landau}} = Q_{i,\text{Landau}} + R_{\text{noise},i}. \quad (7.3)$$

### 7.3.3 Digitisation

A threshold is applied to the readout charges of the single pixels to suppress the contribution of the noise. Only charge values higher than the applied threshold are used for the further steps. After applying the threshold, the analogue signal read out from the sensor can be converted to discrete values by the digitisation.

Note that for the Investigator test setup the full waveform is read out with a 14-bit resolution of the amplitude (as described in Chapter 5.4). Hence, the digitisation is negligible and has not been applied to compare the Investigator simulations to test beam measurements. However, the digitisation has been applied in a further study to investigate the impact of the digitisation on the spatial resolution (see Chapter 11.2).

In this simulation, the digitisation is parameterised by three different parameters: the threshold, the saturation and the number of bits. First, a range is defined in which the values of the charge are converted to discrete steps. The lower bound of this range is defined by the threshold, whereas the upper bound of this range is defined by the saturation. Further, a number of bits  $n_{\text{Bits}}$  is set and the resulting number of equally spaced states  $n_{\text{States}}$  with a size of  $\Delta\text{Bit}$  are then distributed within this range

$$n_{\text{States}} = 2^{n_{\text{Bits}}} \quad (7.4)$$

$$\Delta \text{Bit} = (\text{Saturation} - \text{Threshold}) / (n_{\text{States}} - 1). \quad (7.5)$$

The digitisation is applied for each induced charge  $Q_{i, \text{noise}, \text{Landau}}$  on the different pixel contacts  $i$  separately. The digitised charge values  $Q_{i, \text{Digi}}$  are set to zero if they are below the threshold. No bit state is used for this zero-state, assuming zero suppressed data readout

$$Q_{i, \text{Digi}} = 0, \quad \text{if } Q_{i, \text{noise}, \text{Landau}} < \text{Threshold}. \quad (7.6)$$

Moreover, the digitised charge values  $Q_{i, \text{Digi}}$  are set to the value of the saturation if they are larger than the saturation

$$Q_{i, \text{Digi}} = \text{Saturation}, \quad \text{if } Q_{i, \text{noise}, \text{Landau}} \geq \text{Saturation}. \quad (7.7)$$

In the range between the threshold and the saturation the digitised charge values  $Q_{i, \text{Digi}}$  are set to the discrete values of the next lower state

$$Q_{i, \text{Digi}, i} = \lfloor (Q_{i, \text{noise}, \text{Landau}} - \text{Threshold}) / (\Delta \text{Bit}) \rfloor \cdot \Delta \text{Bit}. \quad (7.8)$$

Figure 7.12 shows an example of the digitised charge values in dependence of the readout charge values.

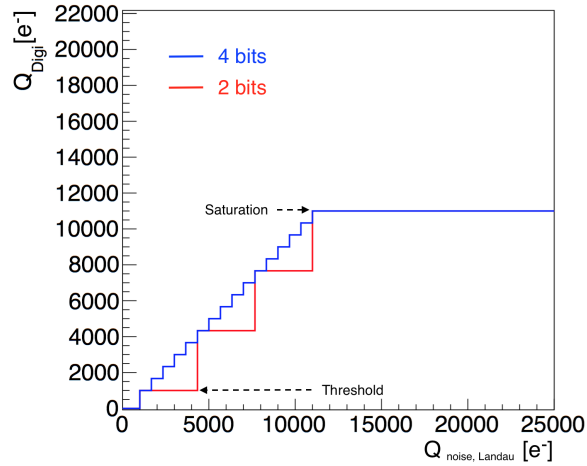


Figure 7.12: Digitised charge  $Q_{\text{Digi}}$  versus readout charge  $Q$  for different number of bits, a saturation of  $11000 e^-$  and a threshold of  $1000 e^-$ .

### 7.3.4 Reconstruction of observables

Different observables are calculated from the obtained charges (digitised or analogue) to characterise the performance of the simulated sensor.

The track position from the test beam data is considered equivalent to the known *true position* in the simulations. The true position can be extracted from the known particle incident position of the TCAD simulations. A Gaussian distributed random number  $R_{\text{tele}}$  is generated, with a mean value of  $\mu = 0$  and a width of  $\sigma_{\text{telescope}}$ , and added to the true particle hit position  $X_{\text{true}}$

$$X_{\text{true}, \text{tele}} = X_{\text{true}} + R_{\text{tele}}, \quad (7.9)$$

to account for the non-zero telescope resolution. Apart from this, all observables are defined as for the test beam data.

## **7.4 Summary**

A two dimensional simulation chain has been developed to model the response of silicon sensors. In this chapter, the simulation chain has been explained for the modelling of the Investigator response. However, by adjusting the dimensions for the Geant4 simulation and changing the TCAD model, the simulation chain can be used for other technologies. In [26] results of the simulation of 25  $\mu\text{m}$  pitch CLICpix planar sensor assemblies are compared to test beam data.

## Results of TCAD simulations

Results of the TCAD simulations for the standard and modified process (see Figure 7.4) are presented in this chapter. The doping profile of the epi layer has been obtained by a *Spreading Resistance Profiling (SRP)* measurement [93], which is accurate only for doping values  $\gtrsim 1.3 \cdot 10^{13}/\text{cm}^3$  [39]. To estimate the impact of this uncertainty, simulation results are compared between the case where the measured profile is used (referred to as *norm*) and the case where all doping levels below this value are set to this limit (referred to as *limit*). Thus, the norm case corresponds to a lower epi layer doping compared to the limit case.

Results are presented for the standard and modified process, simulating a pixel design with the parameters specified in Table 8.1. Moreover, the quasi stationary simulation has been performed for

Table 8.1: Parameters used for the TCAD simulations for the standard and modified process.

Parameter	Nominal value
Pitch [ $\mu\text{m}$ ]	28
Spacing [ $\mu\text{m}$ ]	3
Collection electrode size [ $\mu\text{m}$ ]	2
Thickness epitaxial layer [ $\mu\text{m}$ ]	25

different spacings, while keeping all other simulated parameters as defined in Table 8.1.

All simulations have been performed for a temperature of  $20^\circ\text{C}$  and an overall silicon thickness (including the backside substrate) of  $100\mu\text{m}$ .

### 8.1 Quasi stationary simulation

Results of the quasi stationary simulations of the standard and modified process are presented. The evolution of the depleted region, the electric field and the electrostatic potential are calculated by solving the Poisson equation, described in Chapter 3.3.1. For higher bias voltages and lower epi layer doping values the depletion extends and the electrostatic potential and electric field increase accordingly.

For both processes the evolvement of the depleted region, the electrostatic potential and the electric field are discussed in detail for different bias voltages. Moreover, the change of the depleted region and the electric field is presented for the modified process for different spacings for a bias voltage of  $-6\text{V}$ .

### 8.1.1 Different bias voltages

The results are shown after the quasi stationary simulation to ramp up the reset voltage on the pixel contacts. Different voltage steps of the quasi stationary simulation to ramp up the bias voltage are compared.

#### Standard process

The depleted region is calculated by the TCAD Synopsys software according to the density of majority charge carriers. The hole density and depleted region for different bias voltages is presented in Figure 8.1. Generally, a larger depletion can be observed for lower epi layer doping values (norm) and higher absolute bias voltages.

Already without applying a bias voltage a depleted region is present around the pixel implants, originating from the built-in potential of the pn junction and the 0.8 V applied to the pixel implants. For higher absolute bias voltages of  $-3$  V the depleted region grows in depth and lateral dimension but non-depleted regions are still dominating the region under the p wells. For the lower epi doping (norm) and a bias voltage of  $-6$  V the depleted regions grow enough in lateral size of the pixels to overlap and extends in depth to the limit where the epi profile rises steeply, while for the higher epi doping (limit) larger non-depleted regions are visible at the pixel edges and close to the backside.

The electrostatic potential for different bias voltages is presented in Figure 8.2. Generally, one can observe the positive reset voltage on the pixel implants as well as the negative bias voltage applied to the p wells and the backside of the simulated structure. Due to the built-in potential the electrostatic potential is higher by a few percent than the applied voltage of 0.8 V on the pixel implants and lower by a few percent on the p wells and backside compared to the applied bias voltages. For higher absolute bias voltages and lower doping, the electrostatic potential is increased according to the change of the depleted region.

Since the electrostatic potential grows from the pn junction around the small region of the pixel implants, the electrostatic potential in the high resistivity epi layer shows a non-homogenous distribution along the lateral dimension X of the simulated structure. To quantify this non homogeneity, cuts are performed along the sensor depth Z:

- At the pixel *centre* (vertical black solid lines in Figure 8.2)
- At the pixel *edge* (vertical black coarse dashed lines in Figure 8.2)
- At the *intermediate* lateral position between the centre and edge (vertical black fine dashed lines in Figure 8.2)

These cuts are used in the following and are presented for the electrostatic potential for different bias voltages in Figure 8.3. For all bias voltages the potential starts to fall steeper at a depth of  $\sim 20 \mu\text{m}$ , which can be explained by the steep rise of the epi layer profile at this depth value.

In the pixel centre (solid lines in Figure 8.3) the electrostatic potential decreases significantly from the positive reset voltage applied to the pixel implants to the negative bias voltage on the sensor backside. For the higher epi layer doping a plateau can be observed at depth values of  $\sim 15 \mu\text{m}$ , that can be explained by the fact that the depletion is not extending so far in depth.

At the pixel edge (coarse dashed lines in Figure 8.3) and at the intermediate position (fine dashed lines in Figure 8.3) the voltage rises from the negative bias voltages applied to the p wells to a maximum before it decreases again to the same negative bias voltage applied to the backside. At the pixel edges, relatively far from the small collection electrode in the pixel centre, the potential remains relatively constant over

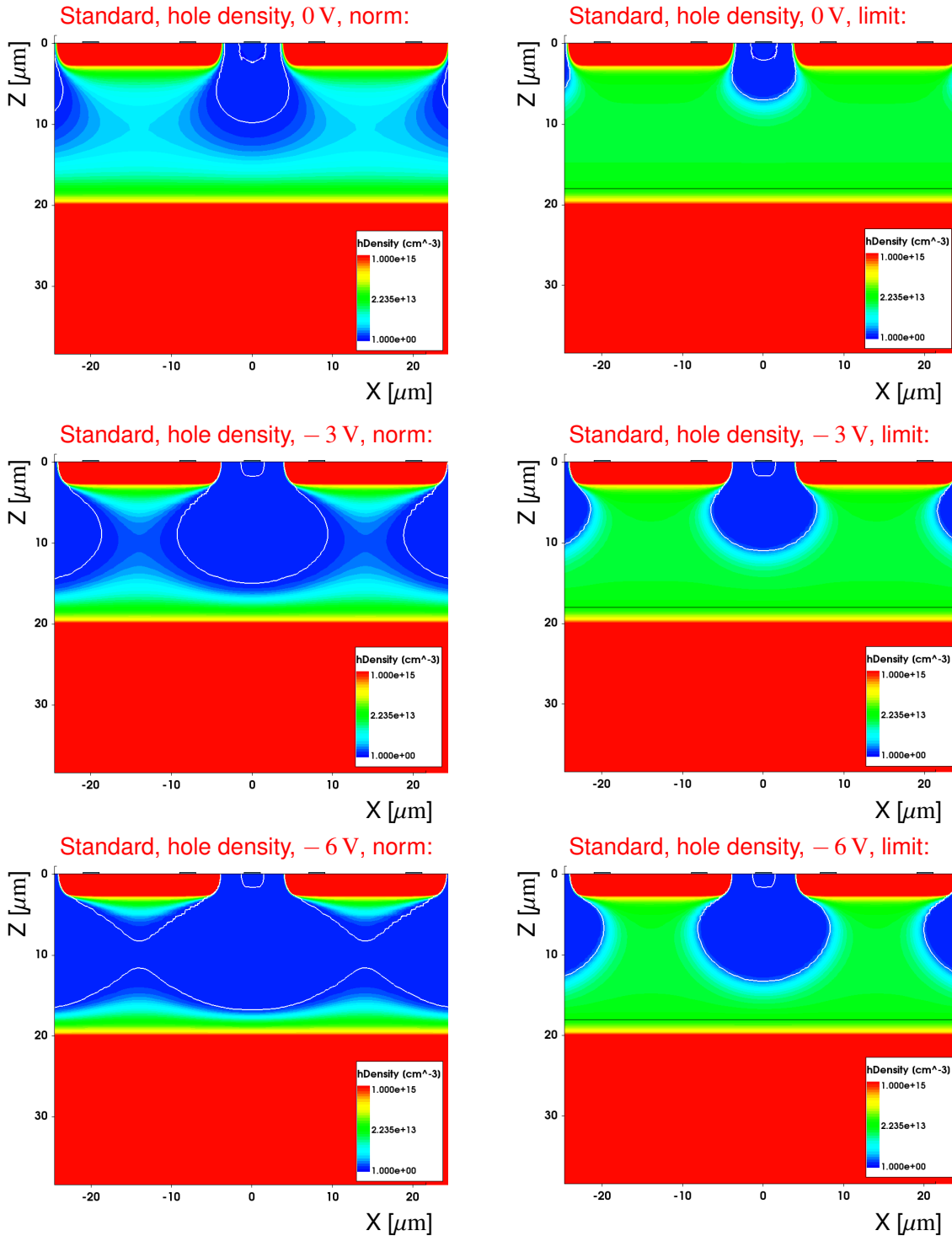


Figure 8.1: Hole density for different bias voltages for the epi layer doping measured in [39] (*norm*, left) and for minimal doping values of  $1.3 \cdot 10^{13}/\text{cm}^3$  (*limit*, right). The horizontal black line marks the depth up to where the doping values of the epi layer are set to a value of  $1.3 \cdot 10^{13}/\text{cm}^3$ . The white line marks the edge of the depleted region.

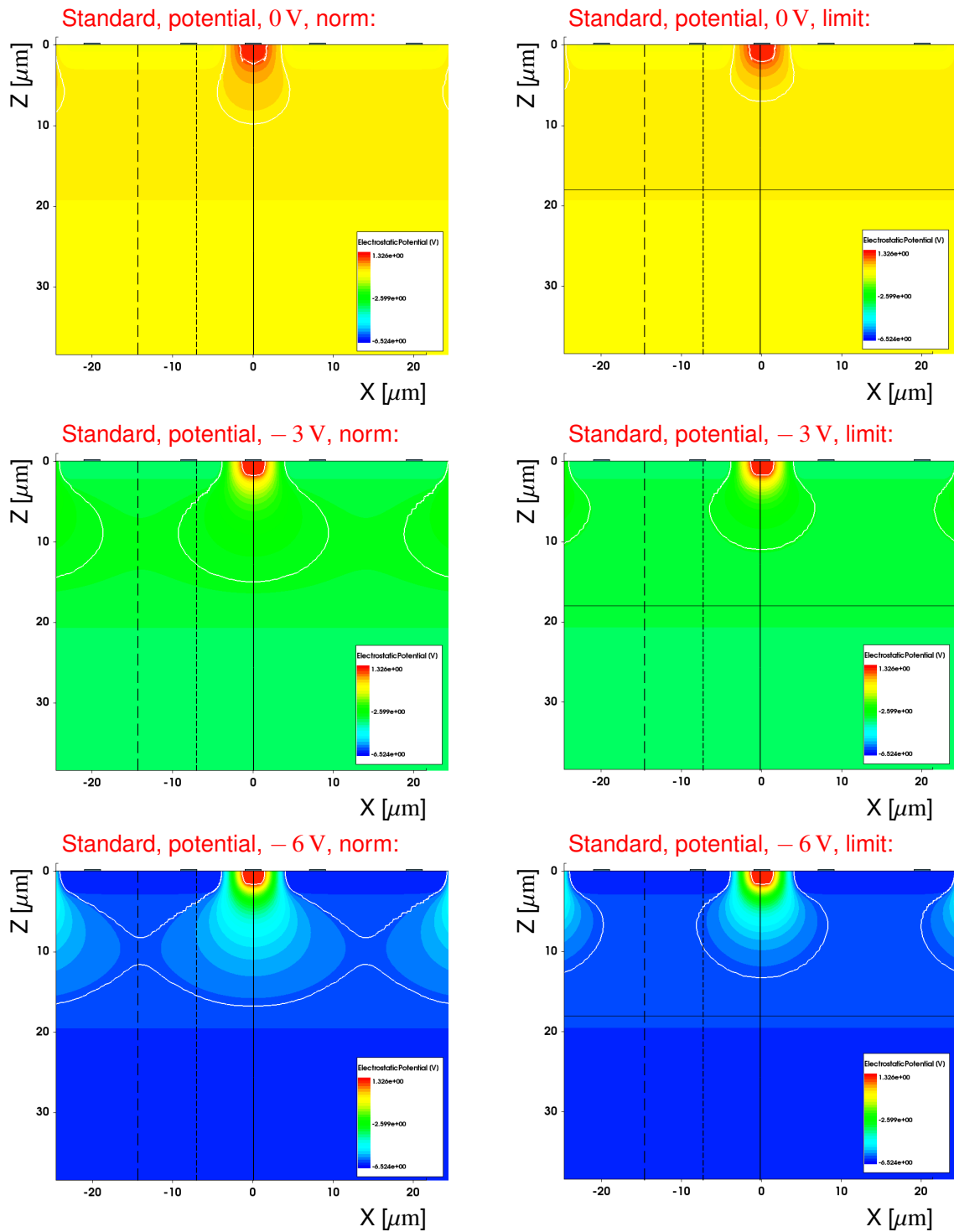


Figure 8.2: Electrostatic potential for different bias voltages for the epi layer doping measured in [39] (*norm*, left) and for minimal doping values of  $1.3 \cdot 10^{13}/\text{cm}^3$  (*limit*, right). The horizontal black line marks the depth up to where the doping values of the epi layer are set to a value of  $1.3 \cdot 10^{13}/\text{cm}^3$ , the white line the edge of the depleted region.

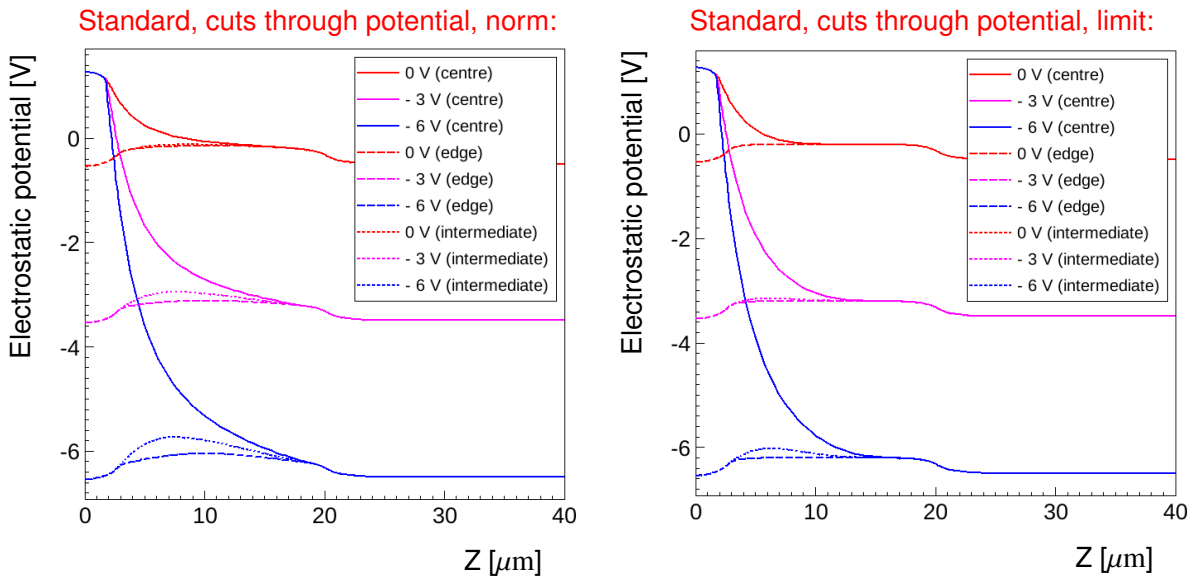


Figure 8.3: Cuts along the sensor depth  $Z$  through the electrostatic potential presented in Figure 8.2.

the depth of the epi layer. Even at an intermediate position, the depth dependence of the potential is relatively minor. This results in a relatively small electric field far away from the collection electrode, as visible in Figure 8.4.

The trends observed for the electrostatic potential are reflected in the electric field for different applied bias voltages: the electric field is high in regions of high gradients in the electrostatic potential around the pixel implants, the p wells and close to the backside. The highest electric field can be observed in the regions of the highest gradient around the pixel implants. A higher electric field can be observed for the lower epi layer doping and the rather flat dependency of the electrostatic potential from the sensor depth at the pixel edges results in sizeable low electric field regions, especially for the higher epi layer doping.

Cuts through the electric field along the sensor depth  $Z$  are presented in Figure 8.5 for a bias voltage of  $-6$  V on a linear and logarithmic scale. The linear presentation shows at the pixel centre (solid lines) a maximal field at the pn junction around the pixel implant and a local maximum at the backside, consistent with the doping gradient of the epi layer. The higher doping of the epi layer shows a slightly larger maximum at the pn junction compared to the lower epi layer doping due to the larger doping and potential gradient to the n well pixel implants.

At the pixel edges (coarse dashed lines) the maximal field is visible at the border of the p wells and at the backside of the simulated structure, in line with the high doping gradient from the p wells and the backside to the epi layer. As visible in the logarithmic presentation, the electric field shows a sharp minimum at the pixel edges. This can be explained by the fact, that the electric field in the lateral  $X$  dimension has to be zero at the pixel edge due to the symmetry of the simulated structure, as presented in the upper plots of Figure 8.6, where the electric field component in  $X$  is shown for a bias voltage of  $-6$  V. Moreover, the electrostatic potential along the sensor depth reaches a maximum, meaning that at this depth the electric field along the sensor depth goes to a zero value as well. This is presented in the lower plots of Figure 8.6, where the electric field component along the sensor depth is shown for a bias voltage of  $-6$  V. As a consequence, the total electric field has to reach a zero value at the pixel edge. The minimum of the electric field visible in the logarithmic presentation in Figure 8.5 does not reach a value of exactly zero due to the limited position mesh on which the electric field has been calculated.

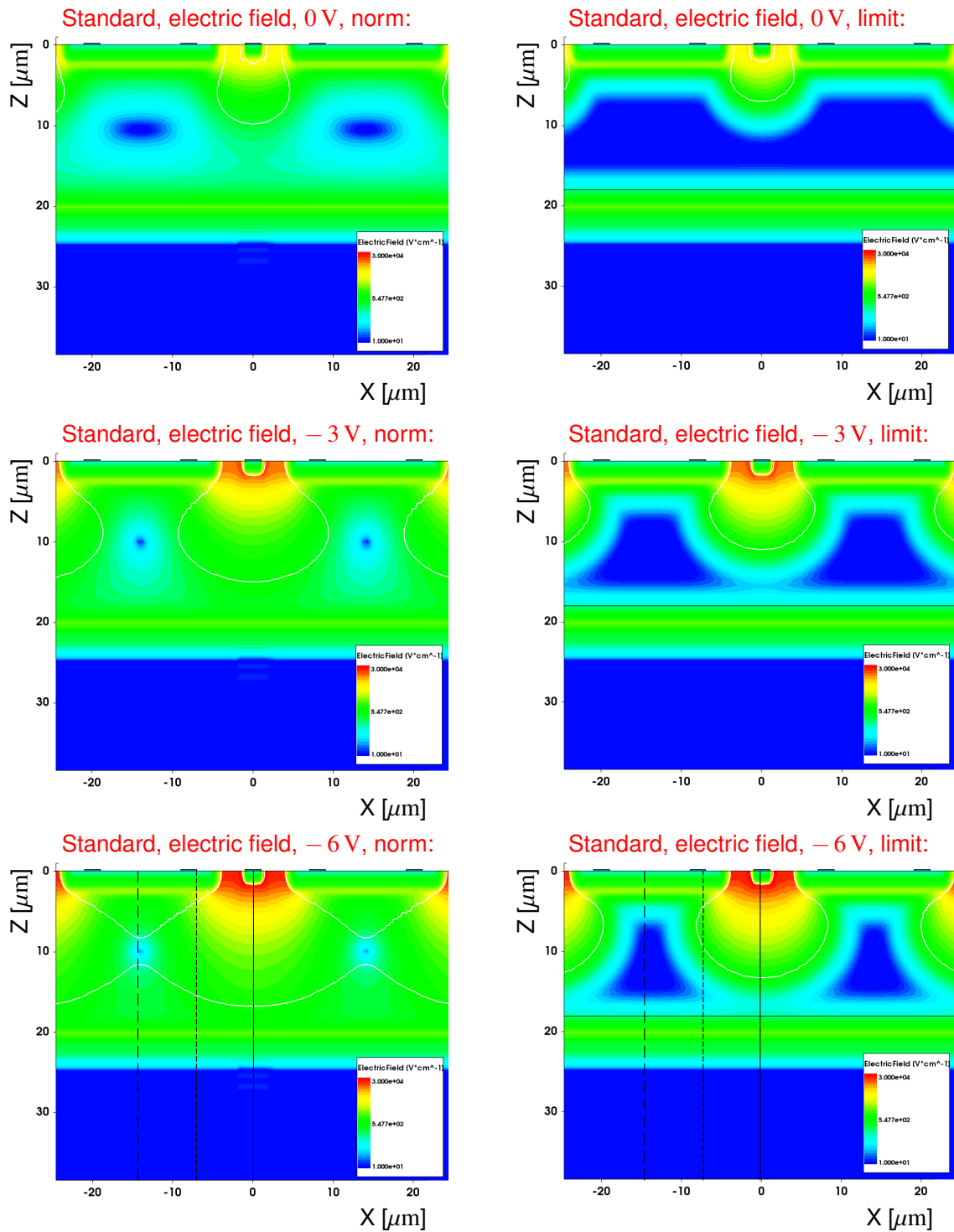


Figure 8.4: Absolute value of the electric field for different bias voltages for the epi layer doping measured in [39] (*norm, left*) and for minimal doping values of  $1.3 \cdot 10^{13} / \text{cm}^3$  (*limit, right*). The horizontal black line marks the depth up to where the doping values of the epi layer are set to a value of  $1.3 \cdot 10^{13} / \text{cm}^3$ , the white line the edge of the depleted region.

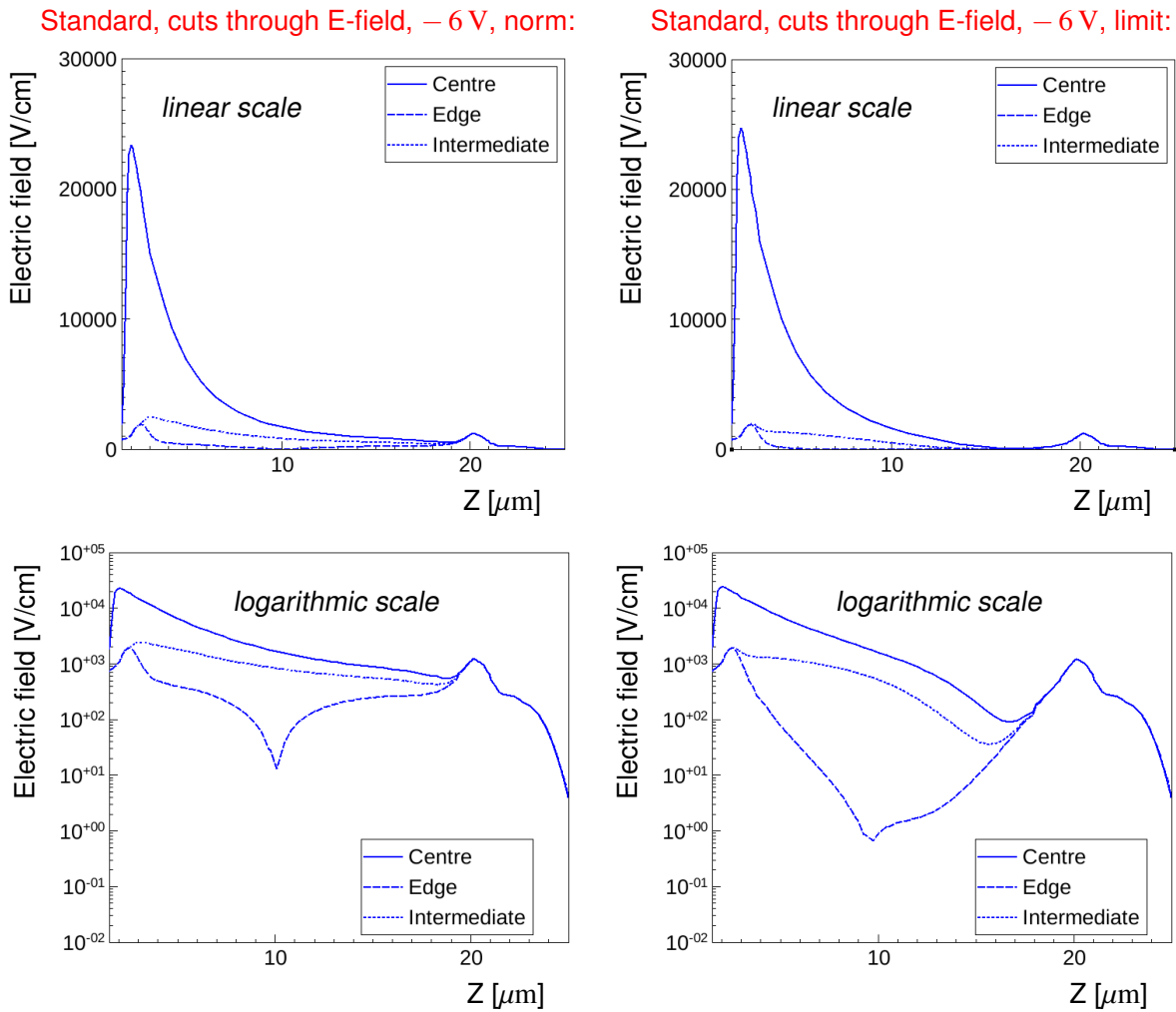


Figure 8.5: Cut along the sensor depth  $Z$  through the electric field presented in Figure 8.4 for a bias voltage of  $-6$  V. The plots are presented on a *linear scale* (up) and a *logarithmic scale* (down).

The described zero value of the electric field at the pixel edge is accordingly a feature of the simulated process. Different pixel geometries, bias voltages and doping values can not change the occurrence of this minimum but can change the dependency of the electric field around this zero value (i.e. a faster or slower drop close to that minimum). This can be observed by comparing different bias voltages and doping values of the epi layer: for higher bias voltages and lower epi doping values the electric field rises steeper out of the zero value along the sensor depth and along the lateral position (compare dashed lines of the cut through the pixel edge in Figure 8.5 to dotted lines of intermediate cut position). For lower bias voltages and higher epi doping a more extended lower electric field region can be observed around the minimum.

The maximum of the potential between the p wells and the backside results also in a change of the sign of the electric field along the sensor depth  $Z$ . This is visible in the lower plots of Figure 8.6: the electric field in  $Z$  around the p wells is negative (blue), crosses the zero value (green) and rises to positive values to the backside. Since the electric field in  $X$  drops towards the pixel edges, the force on charge carriers created in that region is dominated by the electric field in  $Z$ . As a consequence, negative charge carriers created close to the pixel edge get pushed to minimum value of the electric field in  $Z$ . When they

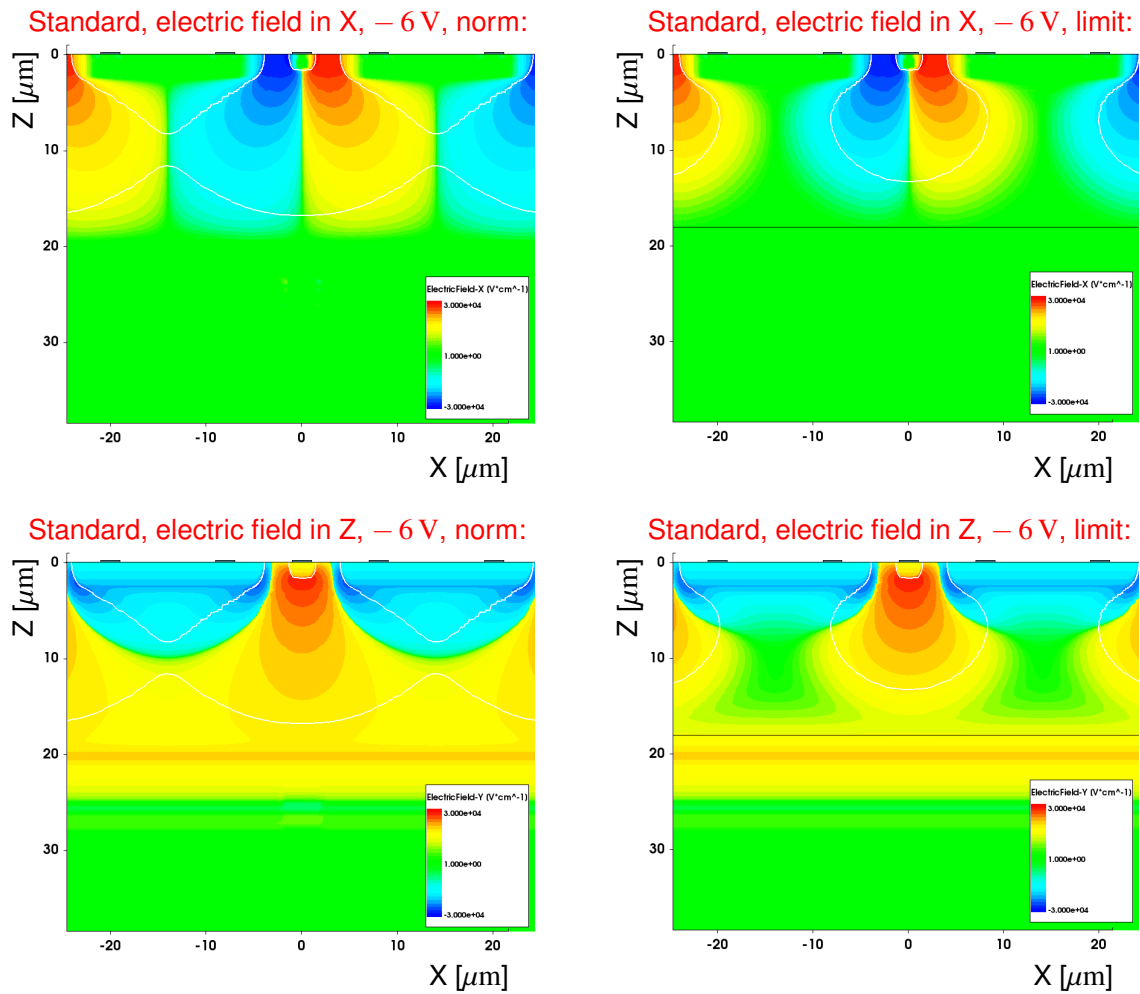


Figure 8.6: Components in X and Z of the electric field presented in Figure 8.4 for a bias voltage of  $-6$  V. The horizontal black line marks the depth up to where the doping values of the epi layer are set to a value of  $1.3 \cdot 10^{13}/\text{cm}^3$ , the white line the edge of the depleted region.

reach close to the minimum value of the electric field in Z, the electric field component in X dominates the force on the negative charge carriers and they move according to the electric field in X to the pixel implants. Note that at the exact value of the pixel edge the electric field in X is zero, meaning that charge carriers created there have to diffuse in X to be affected by the electric field in X and move to the pixel implant. The movement of charge carriers created in the simulated structure is discussed in more detail in Section 8.2.

### Modified process

For the modified process the evolution of the depleted regions can be understood by separately considering the two reversely biased pn junctions of the process:

- **pn junction between p wells and n layer:**

The depleted region starts to evolve in the n layer, since the n layer is lower doped compared to the p wells. Electrons, the majority charge carriers in the n layer, get removed until the full region of the n layer is depleted.

- **pn junction between n layer and HR p type epi layer (*deep planar junction*):**

The depleted region starts to evolve in the HR epi layer, which is lower doped compared to the n layer. Holes, the majority charge carriers of the epi layer, get removed until the depletion depth reaches the highly p doped backside of the epi profile.

Figure 8.7 shows the hole density and depleted regions (white line) for different applied bias voltages. Already for zero bias, as for the standard process, a sizeable depletion can be observed around the junctions. The doping level of the epi layer impacts the extension of the depletion especially for low reverse bias voltages: for the norm case the epi layer is almost fully depleted even without applying a bias voltage, whereas for the limit case the depletion of the epi layer up to the highly p doped backside is only reached for a bias voltage of  $-6$  V. For a bias voltage of  $-6$  V differences can be observed in the depleted region of the norm and limit case in small regions close to the backside of the pixel edge. However, compared to the full depth of the depletion the effect is very small and the depletion of the modified process at a bias voltage of  $-6$  V is almost not affected by the variation of the epi layer doping within the uncertainties of the SRP measurement. The depleted region in the n layer corresponds to the regions with very low hole density and is not affected by different doping values of the epi layer.

The electrostatic potential is presented for different applied bias voltages in Figure 8.8. For zero bias, the lowly doped n type implant is not fully depleted such that the structure behaves like a standard planar junction where the electrostatic potential is constant over the pixel area for a given depth. For higher reverse biases the lowly doped n type layer depletes towards the collection electrodes, and the structure starts to deviate from the standard planar junction, showing significant lateral variations of the electrostatic potential.

To study this in more detail, as done for the standard process in the previous section, plots are made of the potential versus depth for various positions within the pixel, and presented for different bias voltages in Figure 8.9. Apart from the trends also observed for the standard process (see discussion in the previous section), the planar behaviour of the electrostatic potential at a zero bias voltage is clearly visible by the overlapping of all red lines at depth values deeper than the pixel implant and p well. For larger absolute values of applied bias voltage inhomogeneities of the electrostatic potential are observable over the lateral size of the pixel by the discrepancies of the lines of one colour, corresponding to one bias voltage.

Contrary to the standard process, where the electrostatic potential shows an almost flat behaviour in the pixel edges, a clear maximum of the potential can be observed for the modified process. This can be attributed to the n layer, creating high doping gradients between the p wells and the n layer and between the n layer and the p doped epi layer. Comparing the lower epi layer doping to the higher epi layer doping, the potential drops steeper after the maximum for the latter case, which can be attributed to the larger doping gradient between the n layer and the p doped epi layer.

The discussed trends of the electrostatic potential are reflected in the electric field in the sensor presented in Figure 8.10, showing the planar behaviour without an applied bias voltage, the deformation towards the pixel implants for higher absolute bias voltages and the higher electric field at the pixel edges compared to the standard process. The electric field of the modified process is maximal around the p wells (pixel edges and intermediate lateral X positions), due to the large doping gradient between the pn junction of the highly doped p wells and the n layer. This is in contrast to the standard process, where the electric field is maximal at the pixel centre around the pn junction between the pixel implant and the epi layer.

Comparing the different epi layer doping values, higher electric field values extend deeper and further to the pixel edges for the lower compared to higher epi layer doping values. However, compared to the standard process (see Figure 8.4) the impact of different epi layer doping values on the electric field is less significant, since the electric field in the sensor is dominated by the planar n layer.

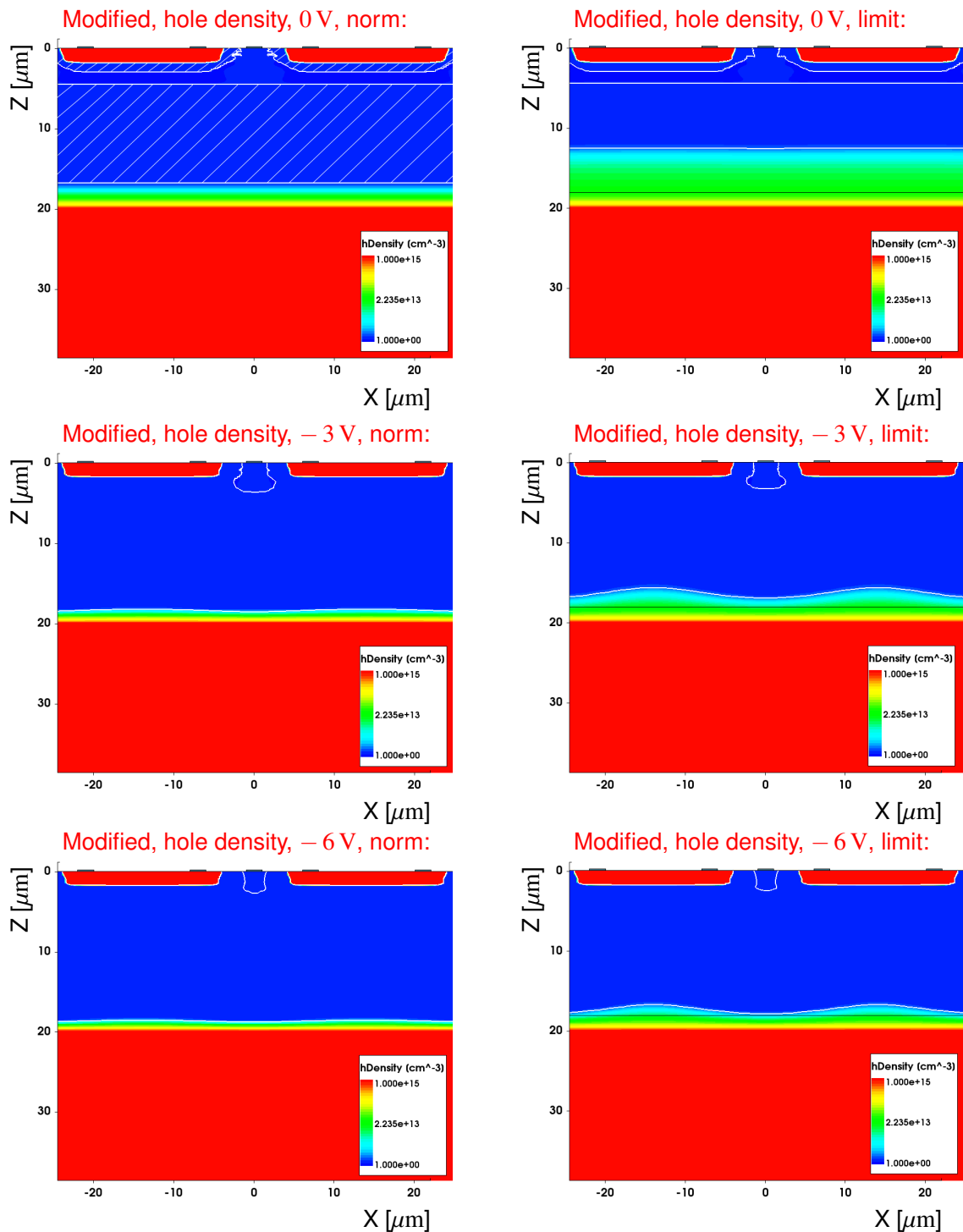


Figure 8.7: Hole density for different bias voltages for the epi layer doping measured in [39] (*norm*, left) and for minimal doping values of  $1.3 \cdot 10^{13}/\text{cm}^3$  (*limit*, right). The horizontal black line marks the depth up to where the doping values of the epi layer are set to a value of  $1.3 \cdot 10^{13}/\text{cm}^3$ , the white line the edge of the depleted region. Without an applied bias voltage the three depleted regions evolving around the two p wells and from the deep planar junction are not overlapping and the n layer is not fully depleted. This is emphasised in the plot of the limit case at 0 V, where the depleted regions are hatched in white.

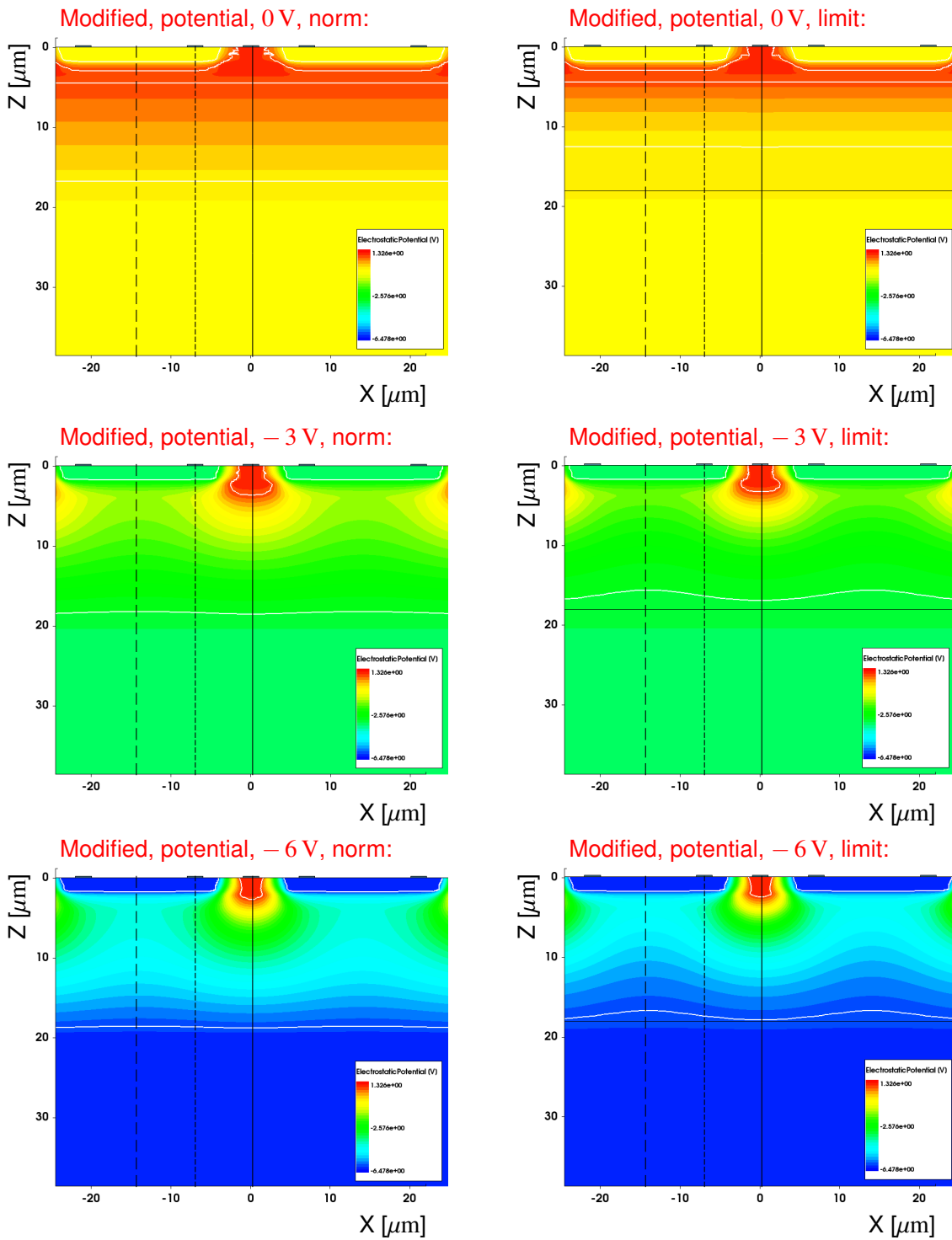


Figure 8.8: Electrostatic potential for different bias voltages for the epi layer doping measured in [39] (*norm*, left) and for minimal doping values of  $1.3 \cdot 10^{13}/\text{cm}^3$  (*limit*, right). The horizontal black line marks the depth up to where the doping values of the epi layer are set to a value of  $1.3 \cdot 10^{13}/\text{cm}^3$ .

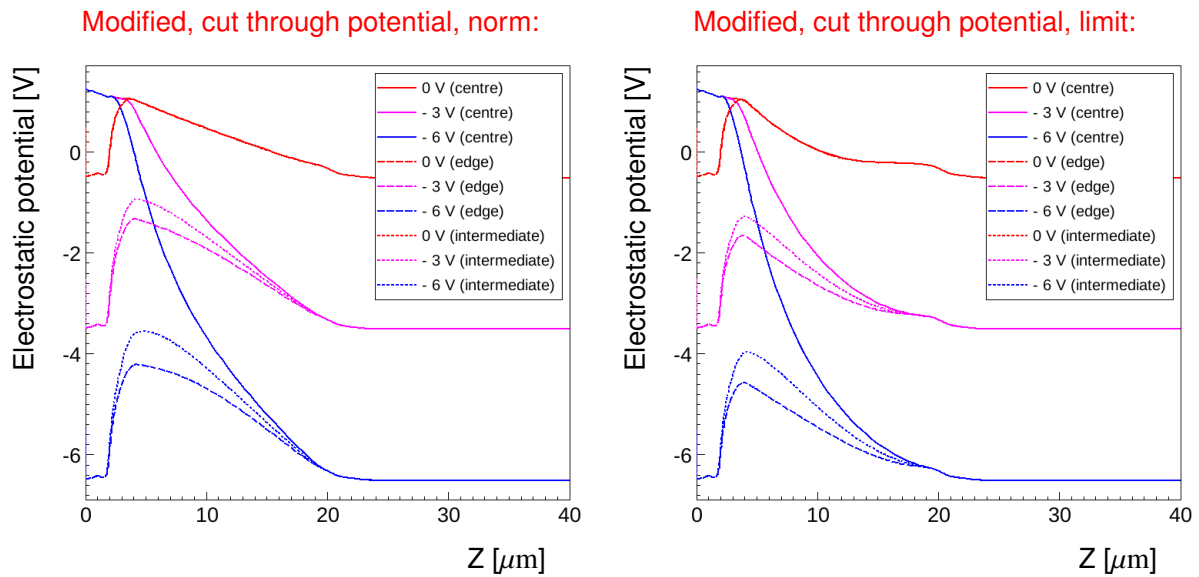


Figure 8.9: Cuts along the sensor depth  $Z$  through the electrostatic potential presented in Figure 8.8 for different bias voltages.

Cuts through the electric field along the sensor depth  $Z$  are presented for a bias voltage of  $-6$  V in Figure 8.11. For the cuts through the pixel centre (solid lines) the electric field rises to a maximum close to the deep planar junction and decreases from this maximum to the backside, where a small peak can be observed due to the change of potential at the backside.

For the cuts through the pixel edge and intermediate lateral positions two pn junctions are crossed: the junction between the p wells and the n layer and the deep planar junction. A high peak of the electric field can be observed close to the junction between the p wells and the n layer, consistent with the fast rise of the potential originating from the high doping gradient. A minimum of the electric field is visible at the depth where the electrostatic potential shows a maximum. As discussed for the standard process, this minimum is a feature of the studied process. However, the electric field around that minimum rises much faster in depth and lateral pixel position (compare dashed line of pixel edge to dotted line of intermediate pixel position) for the modified compared to the standard process (compare Figure 8.5 and 8.11).

Comparing the different doping values of the epi layer, differences can be observed in the electric field cuts through the pixel edges (dashed lines in Figure 8.11) and intermediate positions (dotted lines in Figure 8.11) close to the sensor backside: for higher values of the epi layer doping the electric field rises quickly from the minimum to a local maximum and decreases to the backside, whereas for lower values of the epi layer doping the electric field increases slowly from the minimum to a local maximum much closer to the backside.

This, as well as the steeper (compared to the standard process) rise of the electric field around the minimum can be understood by considering the electric field components along the lateral dimension  $X$  and along the sensor depth  $Z$ , as presented in Figure 8.12. Compared to the standard process, a slightly higher electric field in  $X$  can be observed, which is less affected by the different epi layer doping values. Moreover, the electric field along the sensor depth  $Z$  is significantly enhanced, as expected from the pn junctions created by the n layer. The electric field in  $Z$  around the p wells is dominated by the pn junction to the n layer and thus not effected by the different epi layer doping values. The electric field in  $Z$  in the epi layer is dominated by the deep planar junction between the n layer and the epi layer and thus affected by the different epi layer doping values.

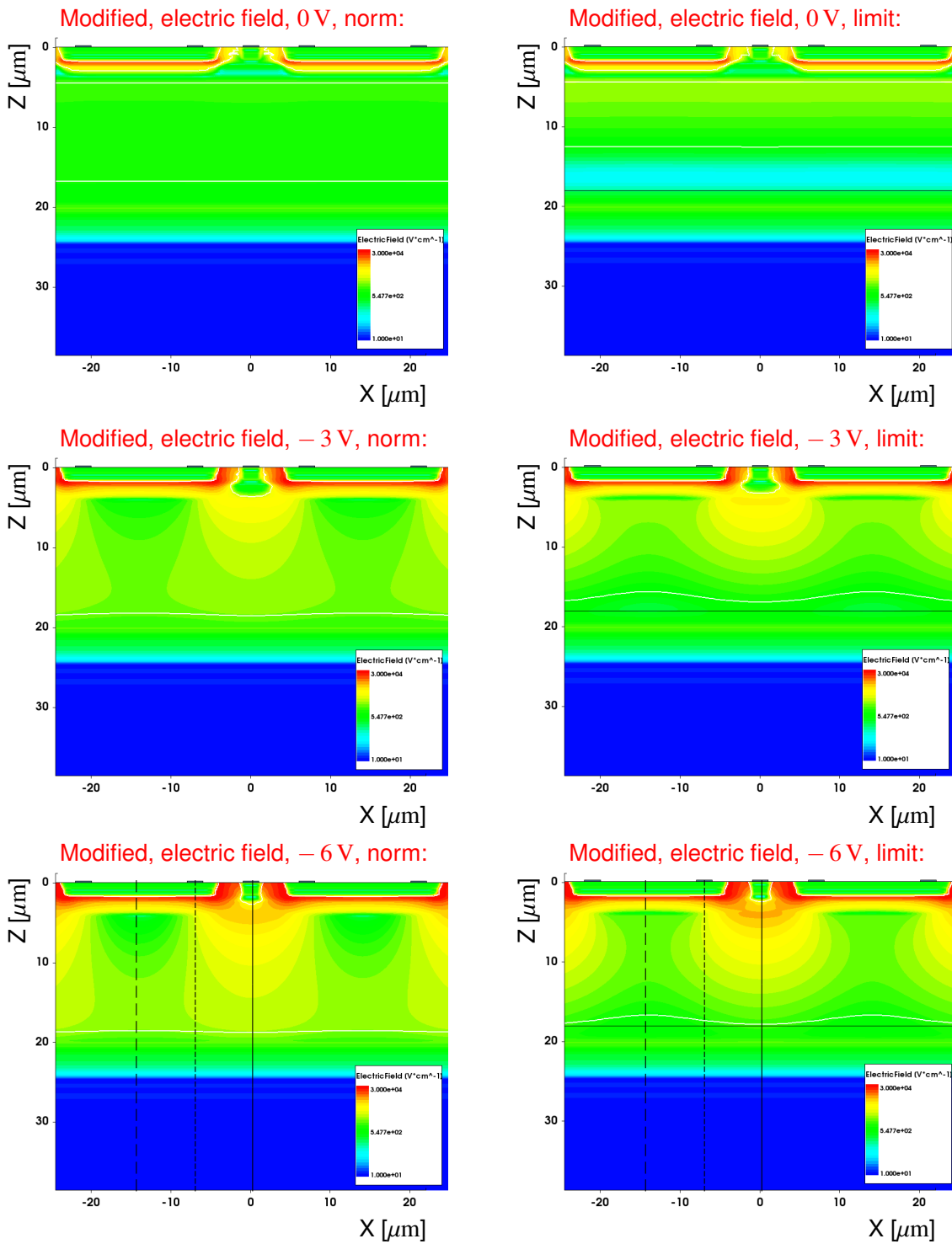
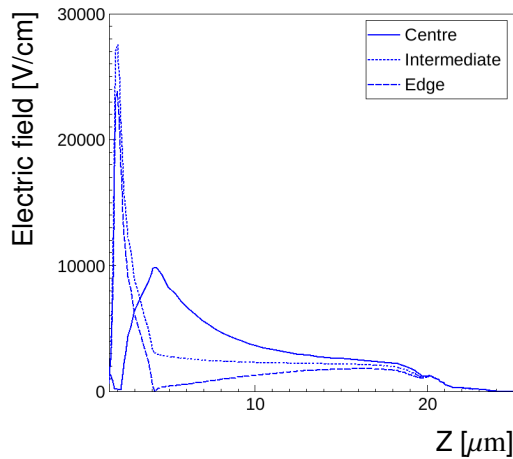


Figure 8.10: Absolute value of electric field for different bias voltages for the epi layer doping measured in [39] (*norm*, left) and for minimal doping values of  $1.3 \cdot 10^{13}/\text{cm}^3$  (*limit*, right). The horizontal black line marks the depth up to where the doping values of the epi layer are set to a value of  $1.3 \cdot 10^{13}/\text{cm}^3$ , the white line the edge of the depleted region.

Modified, cut through E-field, - 6 V, norm:



Modified, cut through E-field, - 6 V, limit:

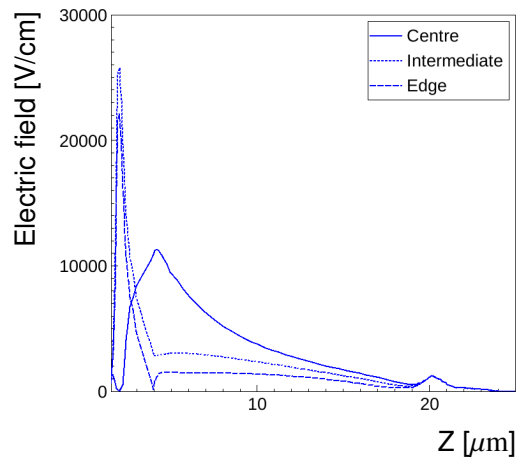
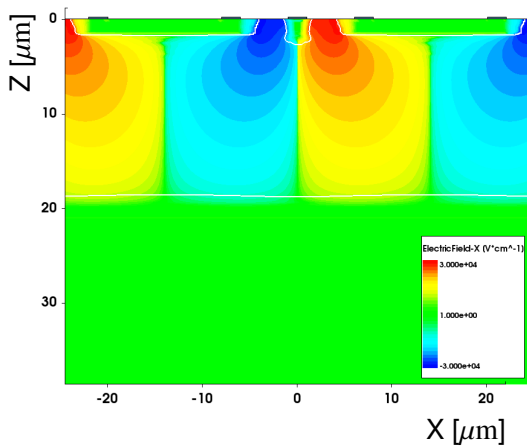
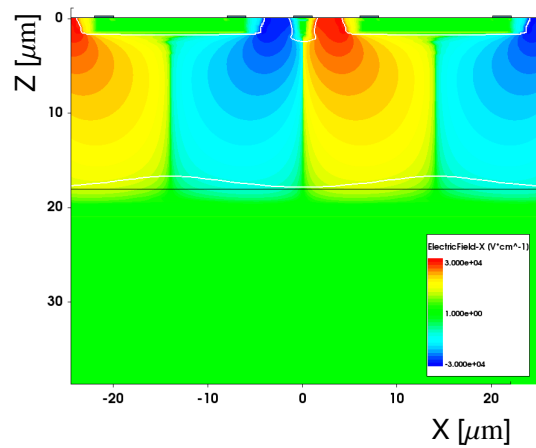


Figure 8.11: Cut along the sensor depth Z through the electric field shown in Figure 8.10 for - 6 V.

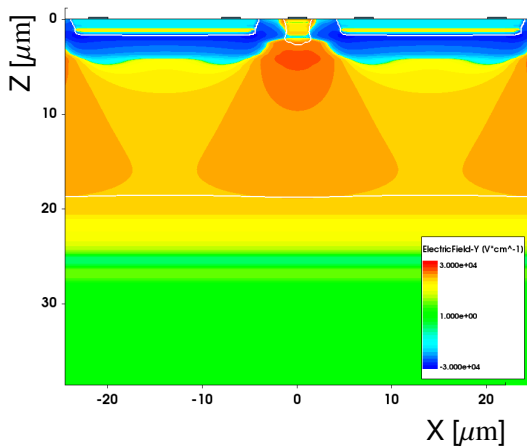
Modified, electric field in X, - 6 V, norm:



Modified, electric field in X, - 6 V, limit:



Modified, electric field in Z, - 6 V, norm:



Modified, electric field in Z, - 6 V, limit:

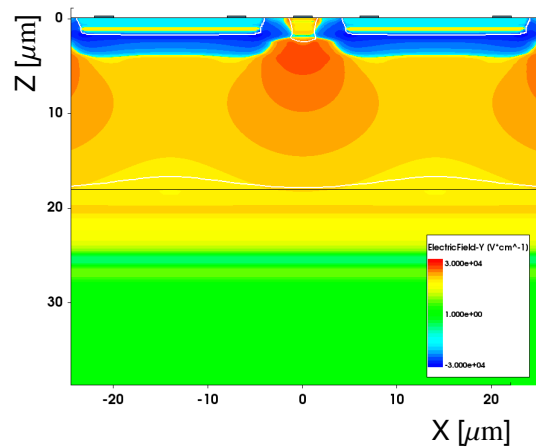


Figure 8.12: Components in X (up) and Z (down) of the electric field presented in Figure 8.10 for a bias voltage of -, 6 V. The horizontal black line marks the depth up to where the doping values of the epi layer are set to a value of  $1.3 \cdot 10^{13} / \text{cm}^3$ , the white line the edge of the depleted region.

### 8.1.2 Different spacings

For the modified process different spacings (defined as the distance between the pixel implant and the p wells, see Figure 5.1) have been compared after ramping up the reset voltage to 0.8 V and the bias voltage to  $-6$  V. The simulation has been performed for the epi profile presented in [39] (norm). Compared to the design studied before, a larger spacing of  $5\ \mu\text{m}$  and a smaller spacing of  $1\ \mu\text{m}$  have been simulated.

The electric field components in X and Z are presented for the different spacing values in Figure 8.13. The plots also present the depleted region, marked by the white line. For larger spacings the depletion

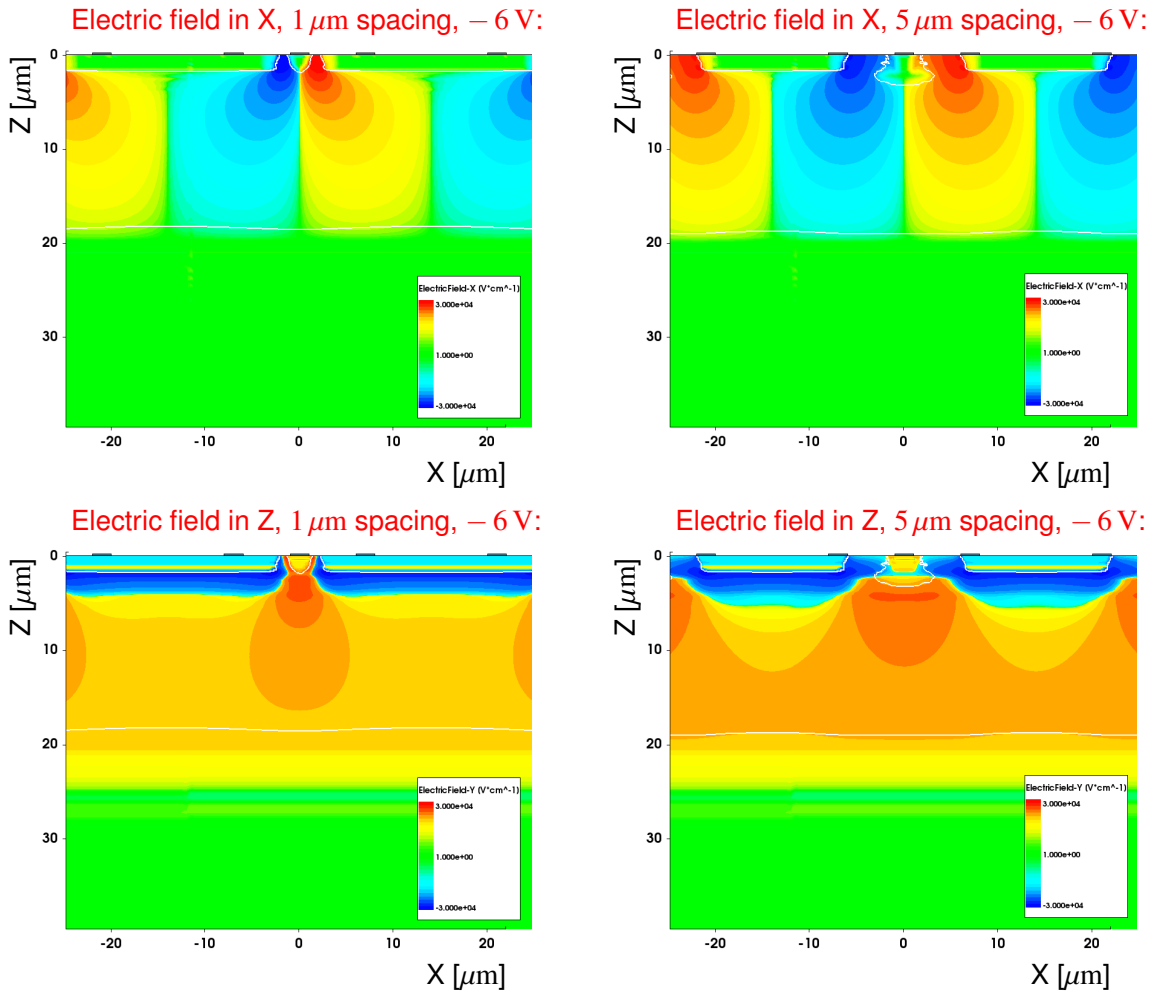


Figure 8.13: Electric field in X (up) and in Z (down) for a spacings  $1\ \mu\text{m}$  (left) and  $5\ \mu\text{m}$  (right), at  $-6$  V for the modified process and the epi profile presented in [39]. The white line marks the edge of the depleted region.

growing from the p wells does not reach the full area under the pixel implants, resulting in non-depleted regions directly around them.

Moreover, a change of the electric field can be observed: for smaller spacings the high potential difference between the pixel implants and the p wells is concentrated on a smaller area. This results in a locally higher field around the pixel implants for smaller spacings. However, reducing the spacing also results in a "shielding" of the pixel implant from the negative potential on the backside substrate. As a consequence, the high electric field region is less extended over the lateral pixel size for smaller compared to larger spacings.

Overall, the electric field is in most sensor regions higher and more homogenous over the lateral pixel size for larger spacings. Only at very small regions directly around the pixel implant the electric field is higher for the smaller spacing.

### 8.1.3 Summary

The depleted region, the electrostatic potential and the electric field produced by a two dimensional TCAD simulation have been presented and compared for the standard and the modified process at different bias voltages.

A comparison between the standard and modified process for the main results of the electrostatic simulations is presented in Figure 8.14 for a bias voltage of  $-6$  V. For the modified process the sensitive layer can be fully depleted by increasing reverse bias, resulting in a significantly larger electric field at the pixel edges. In the standard process significant fractions of the sensitive layer remain non-depleted, resulting in very low or zero electric fields at the pixel edges.

Moreover, the results show the feature that the electric field has to reach a zero value at the pixel edges for both process cross sections, which is less prominent for the modified compared to the standard process due to the overall higher electric field.

The impact of varying the epi layer doping within the uncertainties of the SRP measurement of the epi profile has been discussed and found to have little impact on the depleted region, electrostatic potential and electric field for the modified process at a bias voltage of  $-6$  V. For the standard process a significant impact of the epi layer doping variation has been observed at a bias voltage of  $-6$  V, especially in the lateral depletion of the simulated structure.

The results show that for the simulated epi thickness of  $25 \mu\text{m}$  the depletion in depth at a bias voltage of  $-6$  V is limited to  $\sim 18 \mu\text{m}$  by the epi layer profile, namely the out diffusion of the dopants from the backside into the epi layer.

Moreover, different spacings have been investigated for the modified process. Larger spacings show the advantage of a higher and more homogenous electric field over the lateral pixel size but the disadvantage of non-depleted regions around the pixel implant. These non-depleted regions around the pixel implant contribute to the sensor capacitance, as shown in laboratory measurements in Chapter 9.

## 8.2 Transient simulation

The transient simulations are performed for particle incidents perpendicular to the sensor surface. After the signal charge is deposited its movement inside the structure is calculated. The induced current on the collection electrodes is calculated (Ramo's theorem), even before it physically arrives at the junction. The time resolved (transient) behaviour of the simulated response is compared between the standard and modified process for a bias voltage of  $-6$  V. Results are discussed in detail for the epi layer doping measured in [39], referred to as norm.

In the TCAD simulations the lifetime  $\tau$  of the charge carriers is calculated in dependence of the doping  $N_{\text{dop}}$  using the Scharfetter relation [92]

$$\tau(N_{\text{dop}}) = \tau_{\text{min}} + \frac{\tau_{\text{max}} - \tau_{\text{min}}}{1 + (N_{\text{dop}}/10^{16})} \quad (8.1)$$

with the parameters of the minimal lifetime  $\tau_{\text{min}}$  and the maximal lifetime  $\tau_{\text{max}}$ . The minimal lifetime has not been restricted (i.e.  $\tau_{\text{min}} = 0$ ) for the simulations presented in this thesis. For the epi layer with

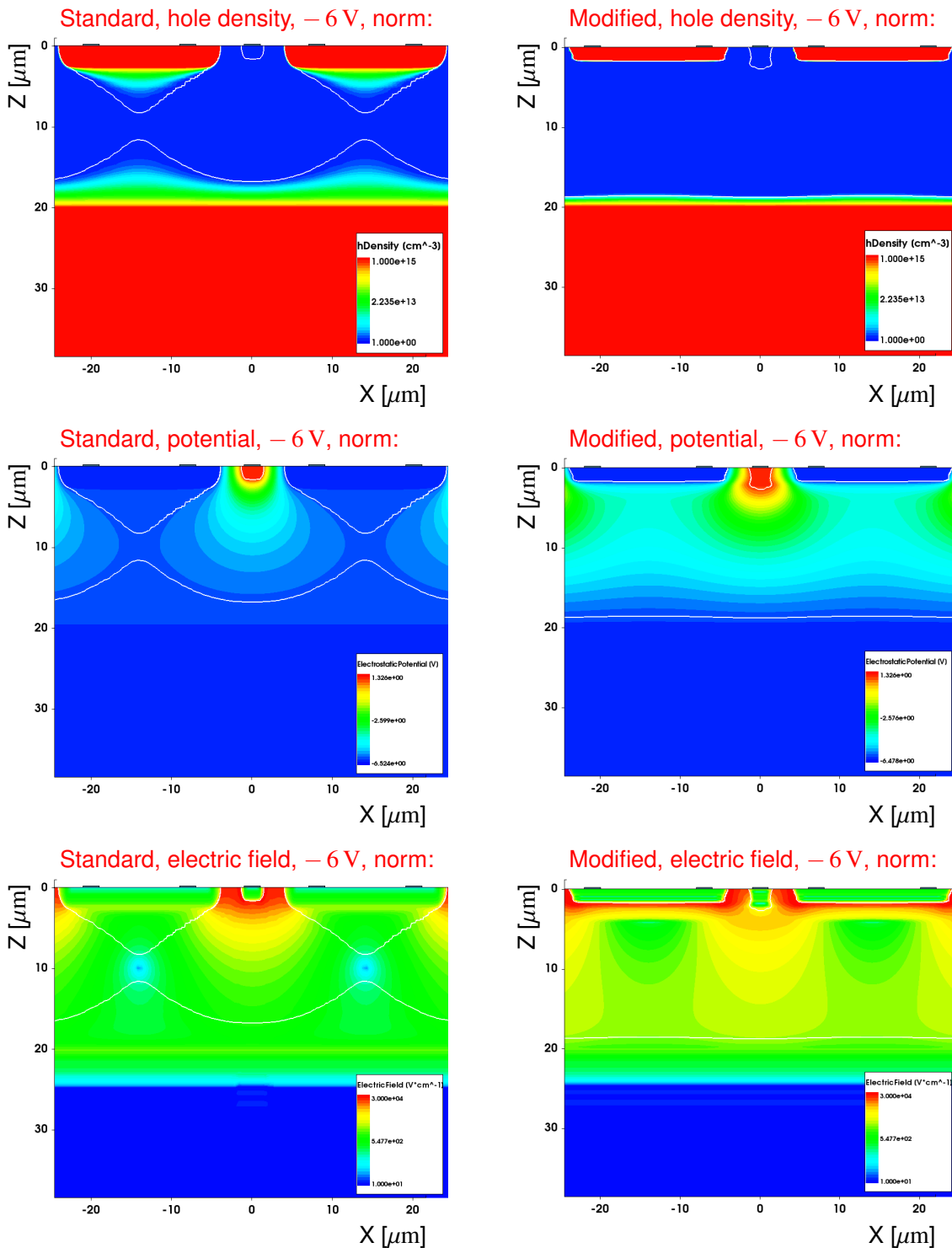


Figure 8.14: Summary of the comparison of the electrostatic simulations for the *standard process* (left) and the *modified process* (right). The hole density (up), the electrostatic potential (middle) and the electric field (down) are presented for the epi layer doping measured in [39] (norm). The white line marks the edge of the depleted region.

a doping concentrations  $N_{\text{dop}}$  at least three orders of magnitude smaller compared to  $10^{16}$ , the leftover second term of the equation reduces to the value of the maximal lifetime

$$\tau_{\text{epi}} \sim \tau_{\text{max}}. \quad (8.2)$$

To reach a lifetime of  $\tau_{\text{max}} \sim 1$  ms in the epi layer [39], the maximal lifetime has been set to  $\tau_{\text{max}} = 1$  ms. For the backside substrate with a doping concentration  $N_{\text{dop}}$  at least three orders of magnitude above the reference value of  $10^{16}$ , the denominator in the leftover term significantly contributes, resulting in a reduced lifetime of

$$\tau_{\text{substrate}} \sim \tau_{\text{max}} \cdot 10^{-3}, \quad (8.3)$$

giving a value of  $\tau_{\text{substrate}} \sim 1$   $\mu$ s for a maximal lifetime of  $\tau_{\text{max}} = 1$  ms.

In this section, different lateral incident positions are investigated first. Secondly, the time resolved contribution from drift and diffusion to the readout charge is disentangled by generating charges separately in the depleted and non-depleted sensor depth. Afterwards the impact of the charges created in the sensor on the electric field is presented, followed by a discussion of systematic effects of the simulation, including the impact of varying the epi layer doping and lifetime of charge carriers.

### 8.2.1 Different lateral incident positions - charge sharing

To study variations of the response for example due to geometrical effects (different drift distances) or variations of the electric field, a particle is simulated at different lateral incident positions between the pixel centre and edge. This is exemplarily illustrated in Figure 8.15 for the standard process and a particle incident at the pixel centre and edge.

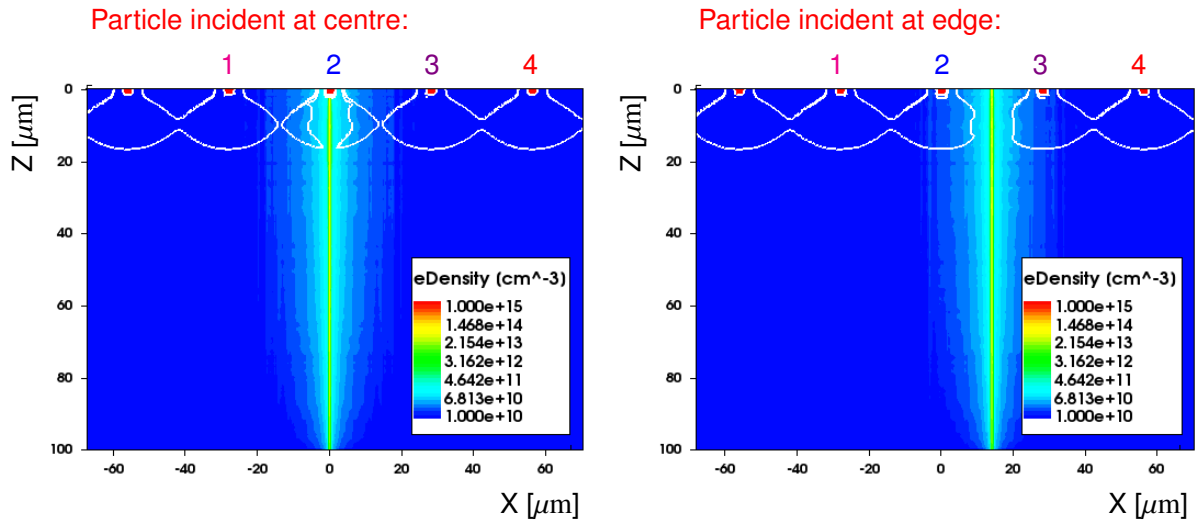


Figure 8.15: Electron density 1 ps after the charge generation for a particle incident at the *pixel centre* (left) and *pixel edge* (right) for the standard process.

Using the pixel labels presented in Figure 8.15, the charge read out by the different pixels and defined as the integral over the current pulse, is shown for different incident positions on a logarithmic scale in Figure 8.16. Note that these charge sharing functions are integrated in a later step in the simulation chain described in Chapter 7, to compare the full simulation to the test beam results.

As expected from the symmetry of the simulated structure the charge is shared half between the pixels

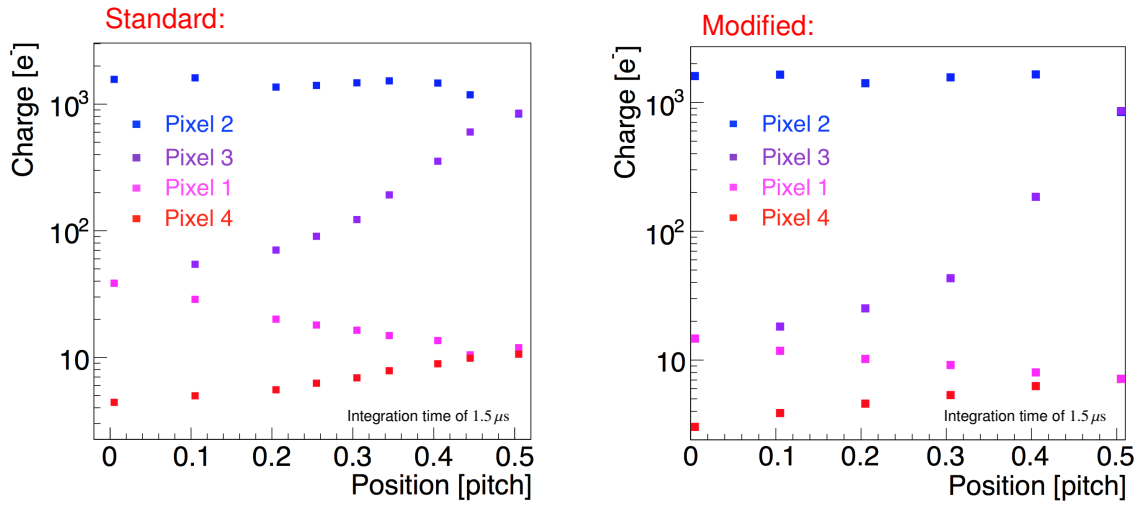


Figure 8.16: Charge sharing functions for the *standard process* (left) and the *modified process* (right).

2 and 3 at the pixel edge (X axis value of 0.5). The amount of charge shared for particle incidents closer to the pixel centre (X axis value closer to zero) depends on the electric field in the sensor.

The charge sharing is significantly enhanced for the standard process due to the large non-depleted regions within the pixel where the electric field is very low and the charge is allowed to spread by diffusion. To illustrate this origin of charge sharing from the low electric field regions, a snapshot of the electron density 1.5 ns after the charge generation is compared for a particle incident at the pixel centre, the pixel edge and in between, as presented in Figure 8.17 for the standard and modified process.

For a particle incident at the pixel centre a larger lateral spread and sharing of the charge is visible for the standard process, while all charge is collected only by the centre pixel for the modified process. For a particle incident at intermediate lateral incident positions a higher electron density can be observed for the standard compared to the modified process 1.5 ns after the charge generation. Moreover, significant sharing of the charge to the closest neighbouring pixel can be observed for the standard process, while being barely visible for the modified process. Both, the slower charge collection as well as the enhanced charge sharing for the standard compared to the modified process are consistent with the significantly decreasing electric field over the lateral size of the pixel for the standard process.

At the pixel edge the charge is shared for both the standard and modified process, as defined by the geometry. The slower collection and larger charge spread is especially visible for the standard process at the pixel edges due to the very low electric field regions. Further, for both processes an enhanced electron density can be noted around the electric field minimum, being discussed in the previous Section 8.1. This can be either attributed to the slower charge collection in the lower electric field regions or to the fact that electrons are pushed into the region of this minimum, as discussed in Section 8.1. To disentangle both, the hole density is as well considered 1.5 ns after the charge generation. Results are shown in Figure 8.18 for the standard and modified process. Despite their lower mobility compared to the electrons, the holes are moved away from the electric field minimum at the pixel edge. Thus, the enhanced electron density close to the electric field minima can be attributed to the negative charges being pushed into the region of the minima.

Figure 8.18 shows as well that the deformation of the depleted region for the standard process can be explained by the density of holes, as expected for the p type epi layer. For the modified process, the deformation of the depleted region is correlated with both hole and the electron density, consistent with the p type epi layer and the n type implant.

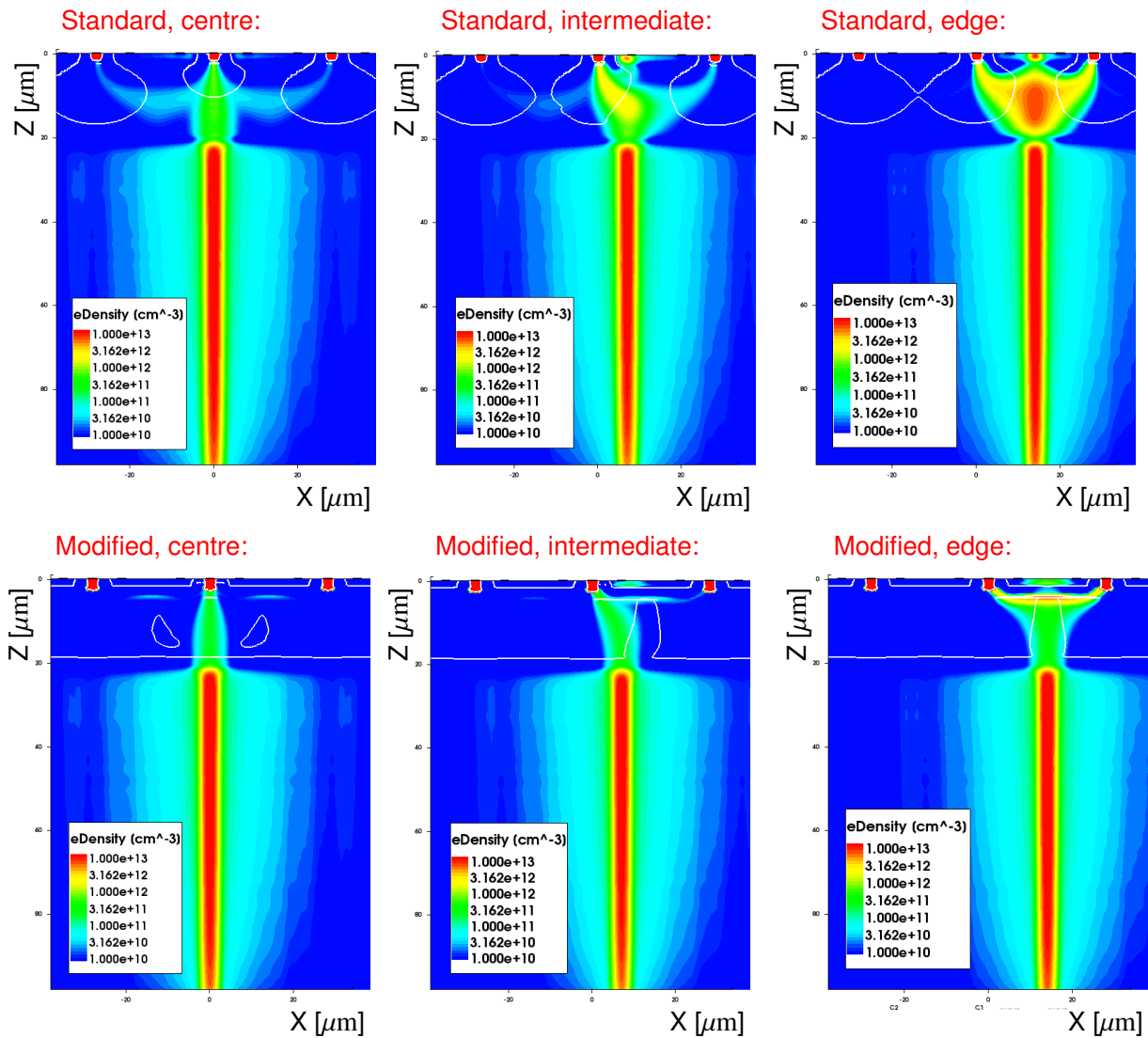


Figure 8.17: Electron density 1.5 ns after the particle incident at the *pixel centre* (left) the *pixel edge* (right) and in between, called *intermediate* (middle) for the *standard process* (up) *modified process* (down).

Overall the charge densities 1.5 ns after the charge generation illustrate the trade-off between the charge sharing and the charge collection time: lower electric field regions result in more charge sharing (and potentially a better spatial resolution) while simultaneously degrading the timing performance, due to a slower charge collection and larger variations of the electric field in the sensor. More quantitatively, this correlation can be shown comparing the total current induced on the centre pixel versus time for a particle incident at the pixel centre and edge, as presented in Figure 8.19. The Figure clearly illustrates that the current pulse is significantly delayed when the particle traverses the sensor at the pixel edge due to the lower electric field in that region. This is much more pronounced for the standard process where the field at the pixel edge approaches zero.

For a particle incident at the pixel centre the current pulse of the standard process shows a faster rise but also a later contribution compared to the modified process. This can be understood by the electric field discussed in the previous Section 8.1. The faster rise for the standard compared to the modified

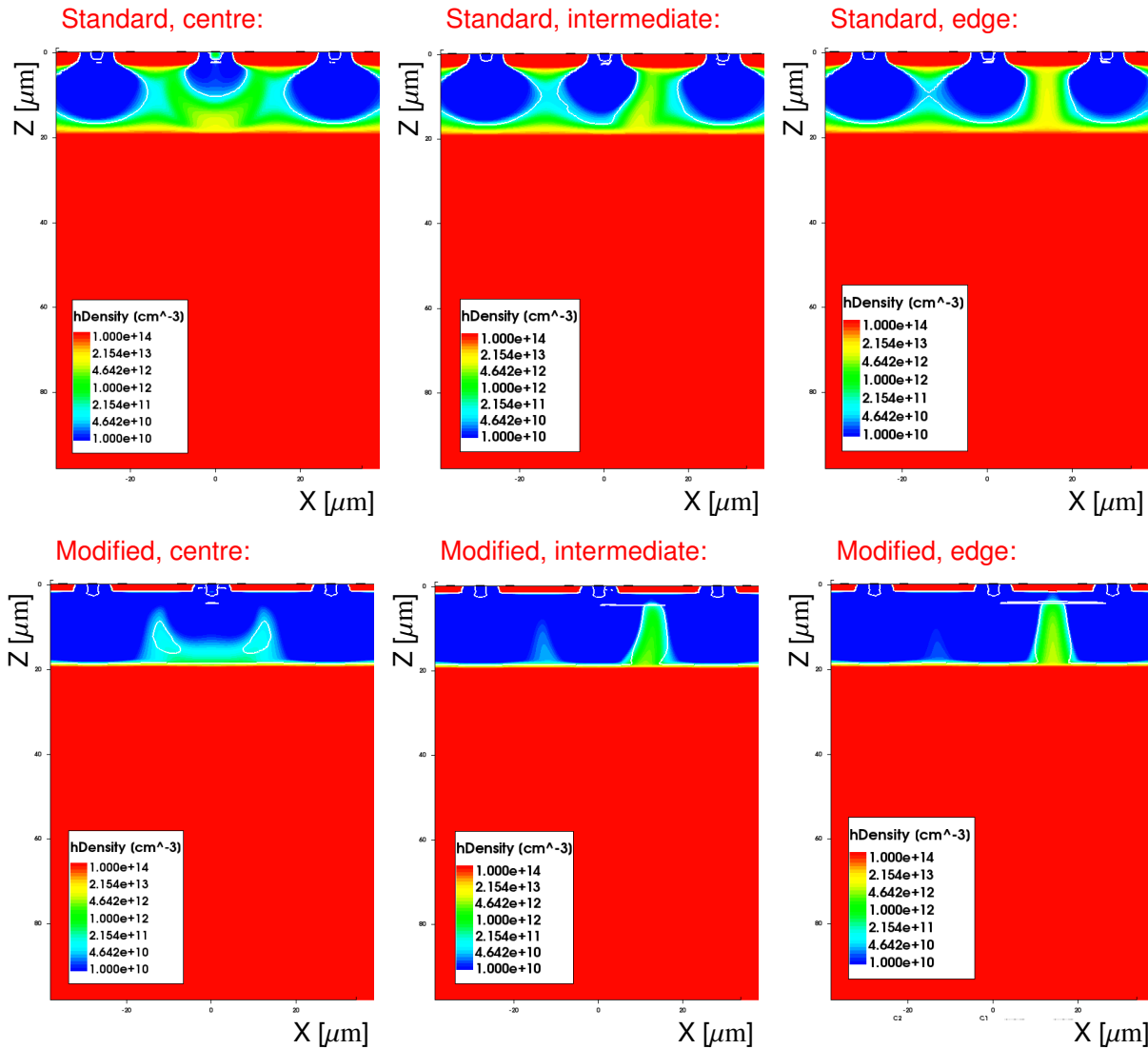


Figure 8.18: Hole density 1.5 ns after the particle incident at the *pixel centre* (left) the *pixel edge* (right) and in between, called *intermediate* (middle) for the *standard process* (up) and the *modified process* (down).

process can be attributed to the higher electric field for the standard process at the pn junction around the pixel implant, while for the modified process no pn junction is present around the pixel implant (n type pixel implant in n type layer). The later contribution of the standard compared to the modified process can be explained by the lower electric field at larger sensor depth, while a higher electric field can be observed for larger sensor depth for the modified process due to the deep planar junction.

The difference in charge collection time between standard and modified process is clearly illustrated in Figure 8.20, where the charge versus integration time is presented on a logarithmic time scale. The faster charge collection for the modified process compared to the standard process is visible by comparing the charge 1 ns and 3 ns (green lines) after the particle incident: at the pixel centre the first rise of the fast component is fully collected after 1 ns for the modified process, while being fully collected after  $\sim 3$  ns for the standard process. At the pixel edge the fast component for the modified process rises within  $\sim 3$  ns, while extending to later times of  $\sim 10$  ns for the standard process.

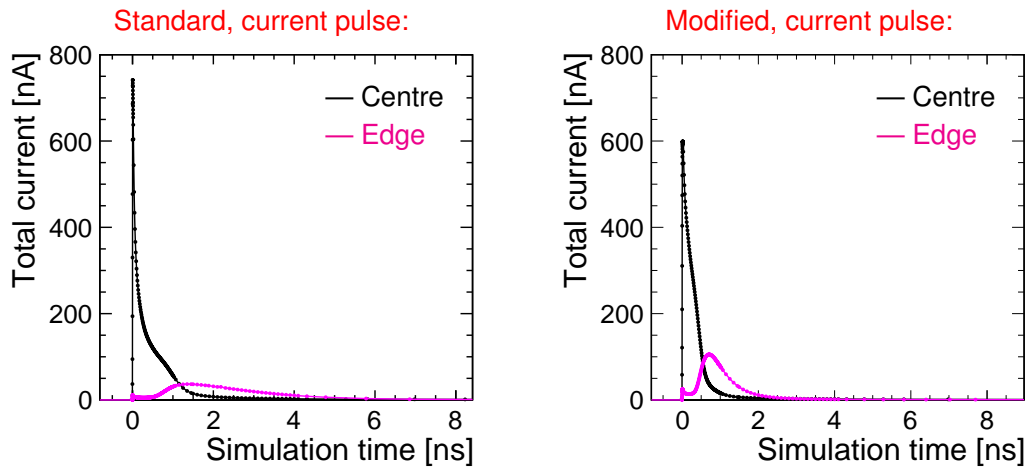


Figure 8.19: Total current versus simulation time for a particle incident at the pixel centre and edge for the *standard process* (left) and the *modified process* (right).

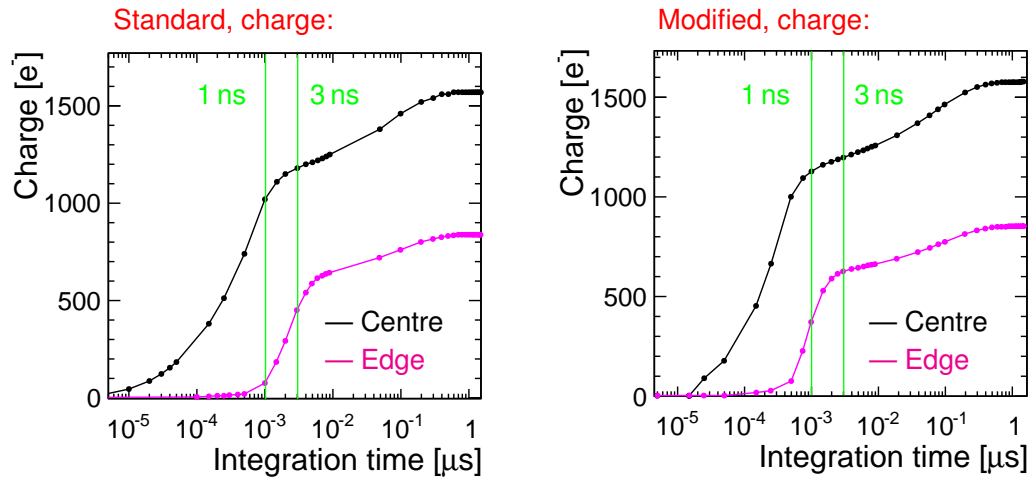


Figure 8.20: Charge versus integration time for a particle incident at the pixel centre and edge for the *standard process* (left) and the *modified process* (right).

Moreover, though not visible in the linear presentation of the current pulse, a small contribution of the pulse extends to late simulation times and adds up to the charge until integration times in the order of a few hundreds of ns. The fact that this late component is observed for both processes and incident positions suggest that it might be attributed to a contribution from diffusion in the non-depleted backside substrate. This motivates a separate simulation of the charge generation for different sensor depth. Moreover, a separate simulation at different sensor depth is interesting to investigate if the fast charge component can be attributed to charges created in the depleted region of the sensor.

## 8.2.2 Different sensor depth - drift and diffusion

As shown in Figure 8.21 and 8.22, a particle is simulated at the centre pixel position along the full depth (*combined*), within the depleted region (*drift*) and outside the depleted region (*diffusion*). Note that the charge carriers of the so-called diffusion component can either recombine in the non-depleted region or diffuse to the depleted region, where they are then also collected via drift.

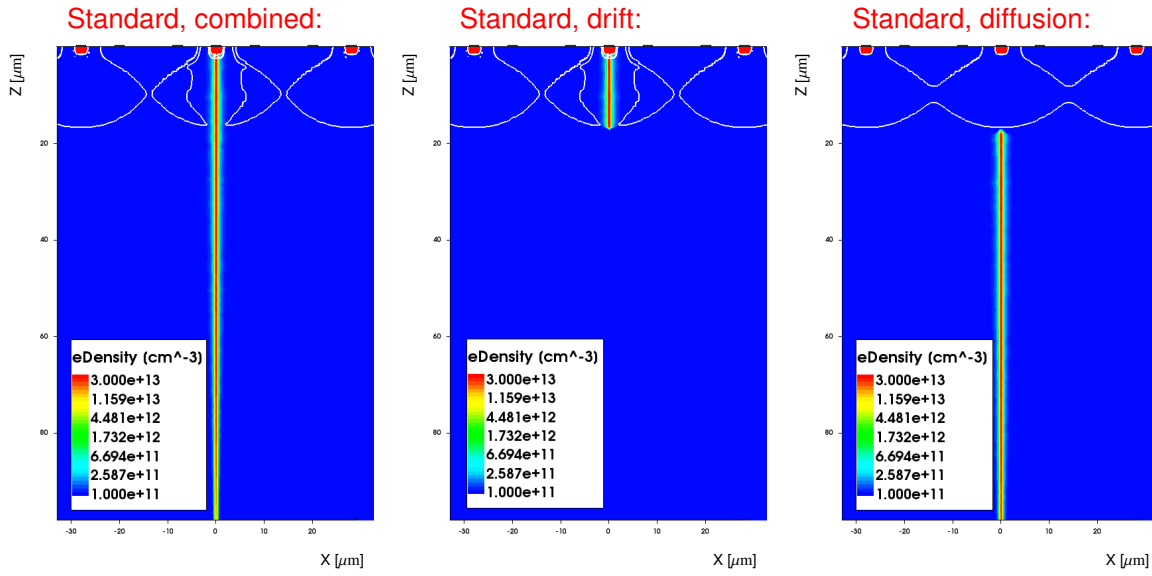


Figure 8.21: Electron density 1 ps after the charge generation for different sensor depth for the *standard process*.

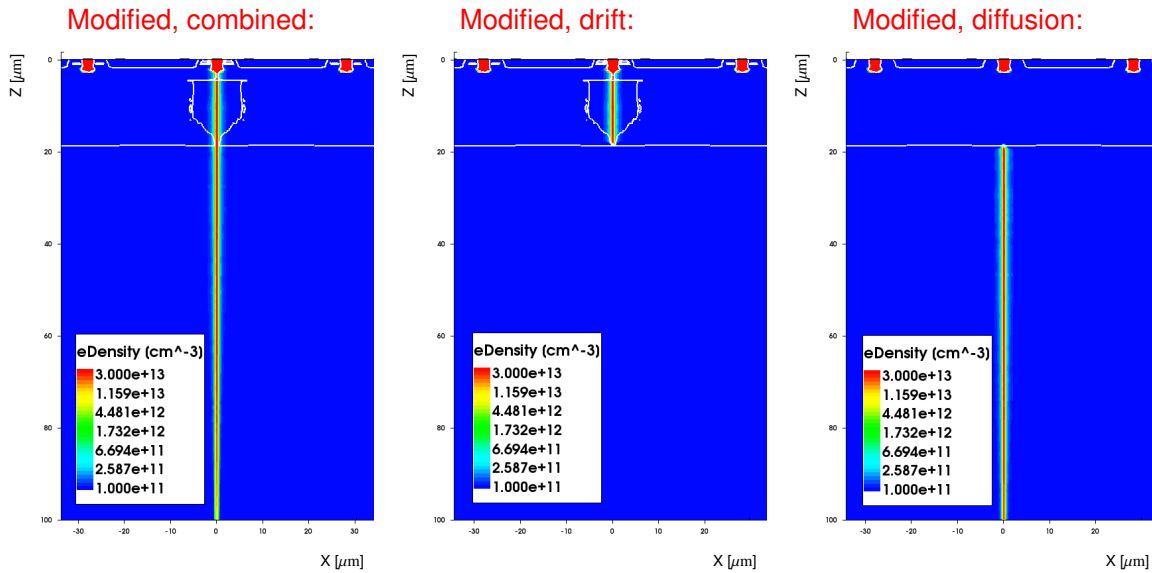


Figure 8.22: Electron density 1 ps after the charge generation for different sensor depth for the *modified process*.

To investigate the contribution of drift and diffusion to the overall response, the total current induced on the centre pixel is presented separately for the three different cases in Figure 8.23. The shape of the total current (red) is composed of a faster component from drift (black) and a slower component from diffusion (blue). Especially for the modified process the drift current dominates the visible contribution within the first few ns. However, also the diffusion component gives a visible contribution already on the time scale of sub ns after the charge generation, originating from charge carriers diffusing from the backside to the depleted region, where they are collected by drift. Since the drift collection is faster in the higher electric field of the modified process, also the so-called diffusion component is faster for the modified compared to the standard process, despite the fact that the charges are generated at similar depth values.

To study if the late component observed in the previous section can be explained by charges collected

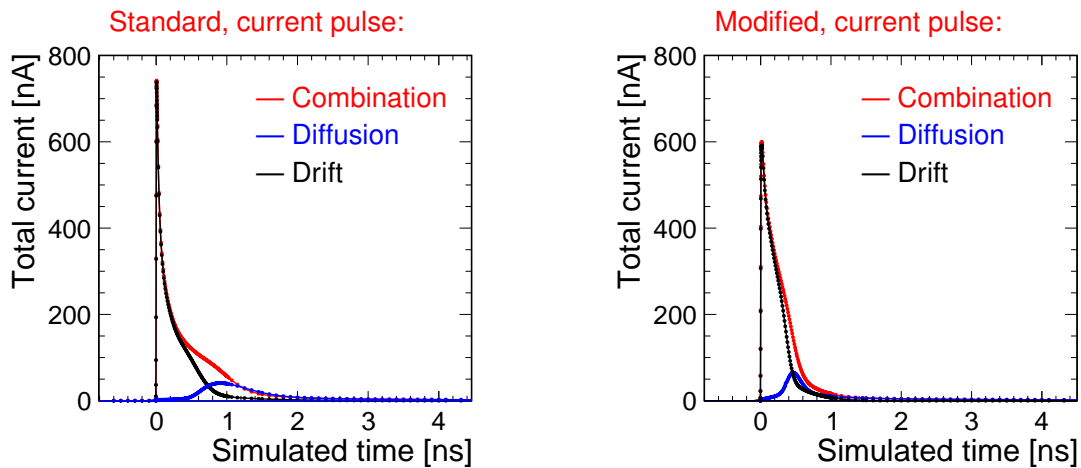


Figure 8.23: Total current versus simulation time for the combined, the drift and the diffusion case for the *standard process* (left) and the *modified process* (right).

from the backside and if the fast component can be attributed to charges created in the depleted region, the charge versus integration time is presented in Figure 8.24 for the three different cases. The fast rise of

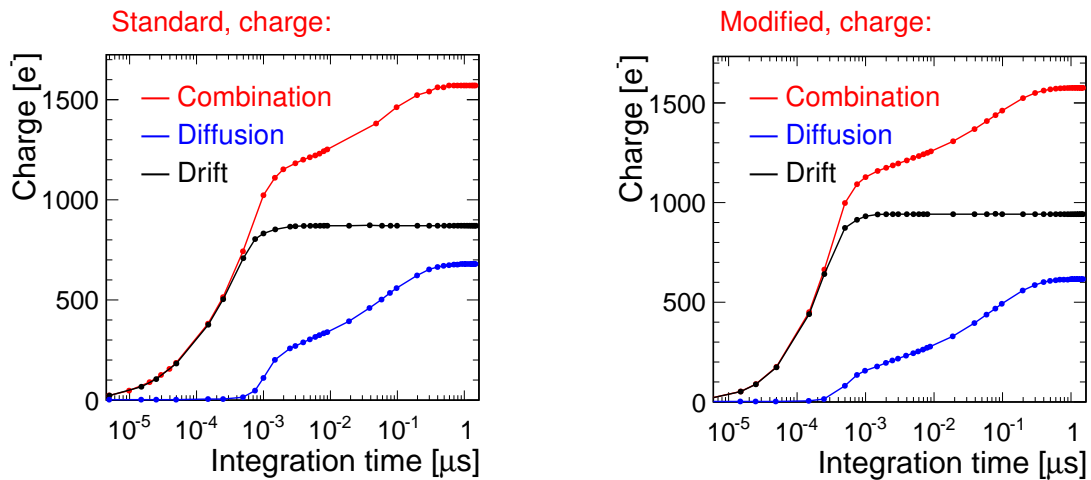


Figure 8.24: Readout charge for the combined, the drift and the diffusion case for the *standard process* (left) and the *modified process* (right).

the charge can be attributed to charges created in the depleted region and collected by drift. This drift component dominates the charge up to a few ns after the particle incident. The charge added after a few ns is given by the contribution from the diffusion component, corresponding to charge generated in the backside substrate. In total  $\sim 40\%$  of the charge originates from the diffusion component. The diffusion current contribution strongly depends on the minority carrier lifetime. In heavily irradiated samples the lifetime may degrade due to radiation and the diffusion component might be lost completely. The lifetime depends on the fabrication process and is not known very precisely [94]. Thus, the impact of different lifetimes on the results is discussed as a systematic uncertainty in Section 8.2.4.

### 8.2.3 Impact of charge carriers on the electric field

The total current of the combined case is compared to the sum of the drift and diffusion component in Figure 8.25, showing that the drift and diffusion component do not exactly add up to the simulated current of the combined case. A discrepancy is visible for both the standard and modified process: the sum of

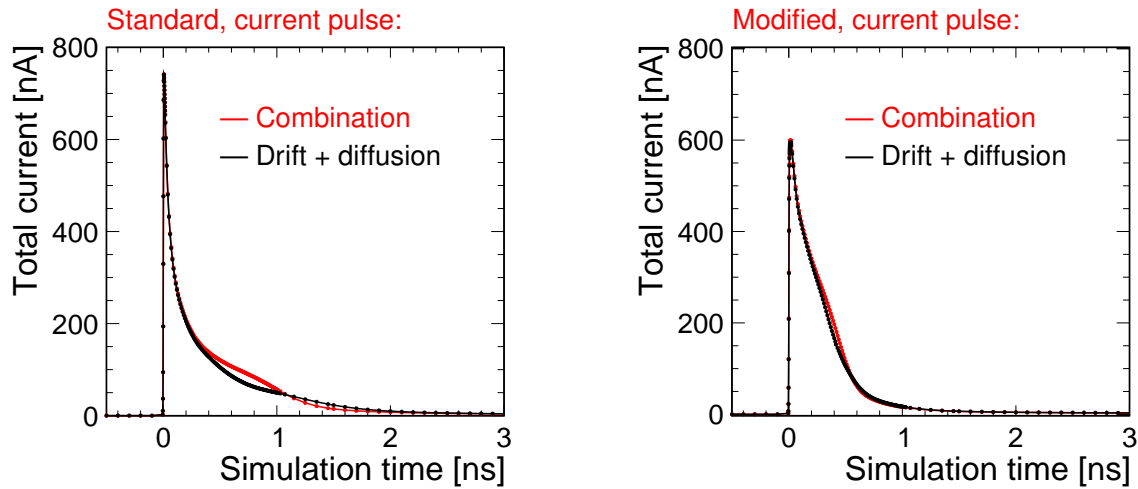


Figure 8.25: Total current versus simulation time for the combined case and the sum of drift and diffusion. Results are presented for the *standard process* (left) and the *modified process* (right).

drift and diffusion is for both processes a little slower compared to the total current of the combined case. If the electric field in the simulated structure is static after ramping up the voltages, the combination of the total current of the drift and the diffusion component should match exactly the total current of the combined case.

Thus, the electric field at the time where the discrepancy between the sum of drift and diffusion is observed is selected: 0.75 ns after particle incident for the standard and 0.3 ns after the particle incident for the modified process (the particle incidents the sensor at 0 ns). The electric field map at that simulation time is subtracted from the electric field map of the electrostatic case after ramping up the voltages. Results are presented for the combined, drift and diffusion case in Figure 8.26, showing the impact of the incident charge on the electric field. Since the difference of the electric field is calculated with respect to the electrostatic case, red regions in Figure 8.26 correspond to a decrease of the electric field and blue regions correspond to an increase of the electric field after the particle incident.

A very similar map can be noted comparing the standard and modified process for the individual cases. Moreover, apart from the fact that the deformations are more prominent for the combined case compared to the drift case, a very similar map can be observed for both: an increased electric field after the charge generation closer to the backside and a decreased electric field after the charge generation closer to the pixel implant. The opposite structure is visible for the diffusion case.

To investigate this, the electron and hole densities are presented in Figure 8.27 and 8.28 for the standard process at the same times after the charge generation where the electric field difference is shown<sup>1</sup>. For the combined and the drift case the electrons are already closer to the pixel implant at the considered simulation times, while for the diffusion case the electrons have a larger drift distance to the pixel implant and are thus at the same time still further away from the pixel implant.

<sup>1</sup> Since a similar behaviour has been observed for the standard and modified process, results are discussed exemplary only for the standard process.

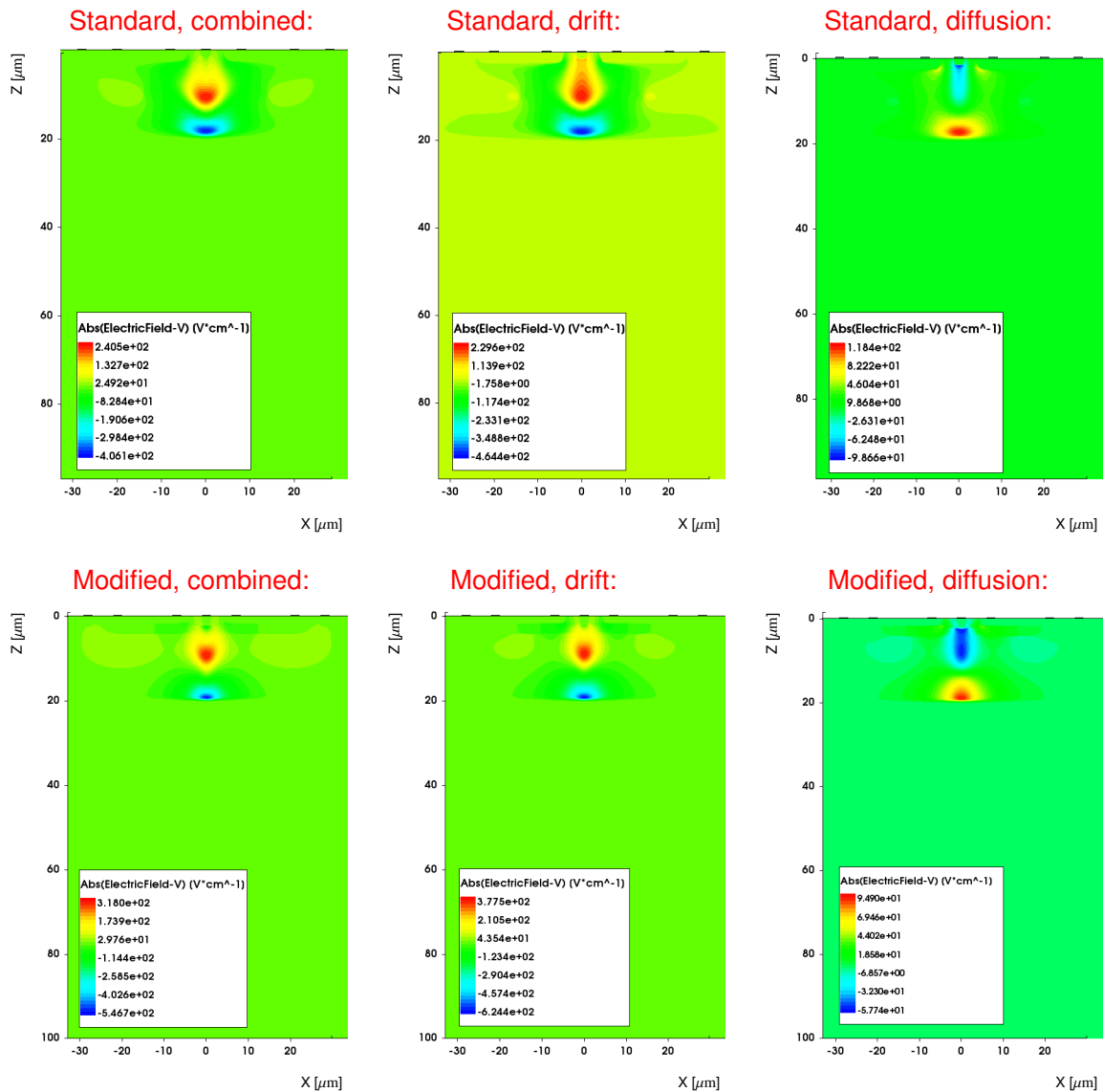


Figure 8.26: Difference of the electric field map after the particle incident with respect to the electrostatic case for the *standard process* (up, 0.75 ns after the particle incident) and the *modified process* (down, 0.3 ns after the particle incident).

For the combined and the drift case the holes created in the depleted high electric field region get accelerated in direction of the backside substrate. Since the force acting on the holes is reduced closer to the backside, an instantaneous locally higher hole density can be observed in that region. For the diffusion case no holes are created outside the backside substrate region, and accordingly no enhanced hole density can be observed.

Following the argumentation above, a region of higher electron densities is located beside a region of higher hole densities for the combined and drift case at the considered time after the charge generation. This results in the charge configuration sketched in Figure 8.29. Due to the potential difference between the negative voltage on the backside and the positive charge of the holes, an enhanced electric field close to the backside substrate is visible by the blue regions of the combined and drift case in Figure 8.26. A potential difference in the opposite direction and thus a reduction of the electric field is created

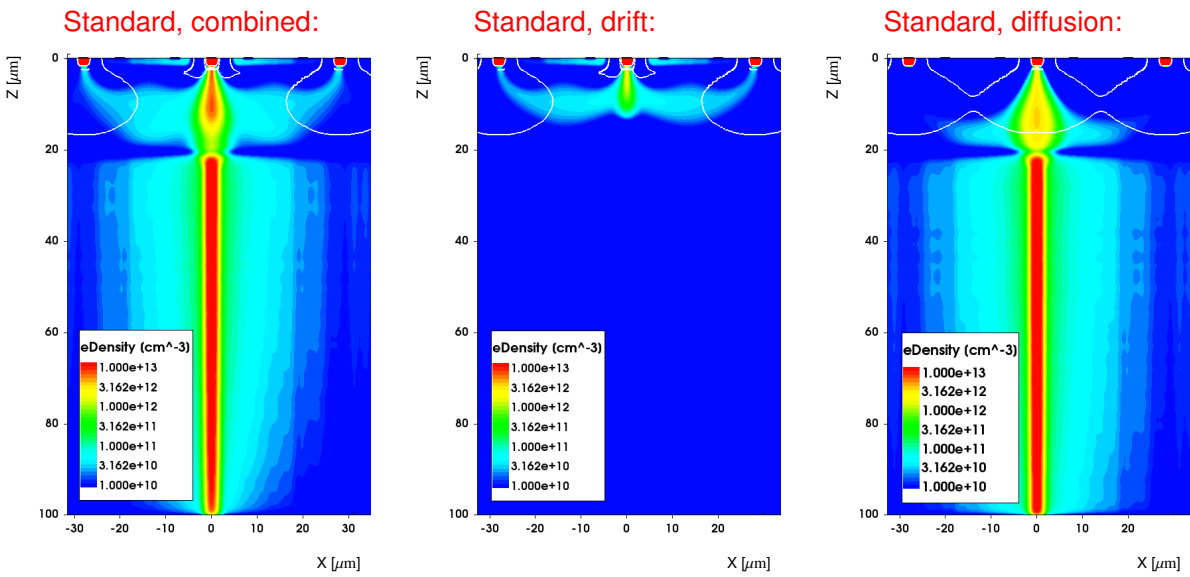


Figure 8.27: Electron density 0.75 ns after the particle incident for different sensor depth for the *standard process*.

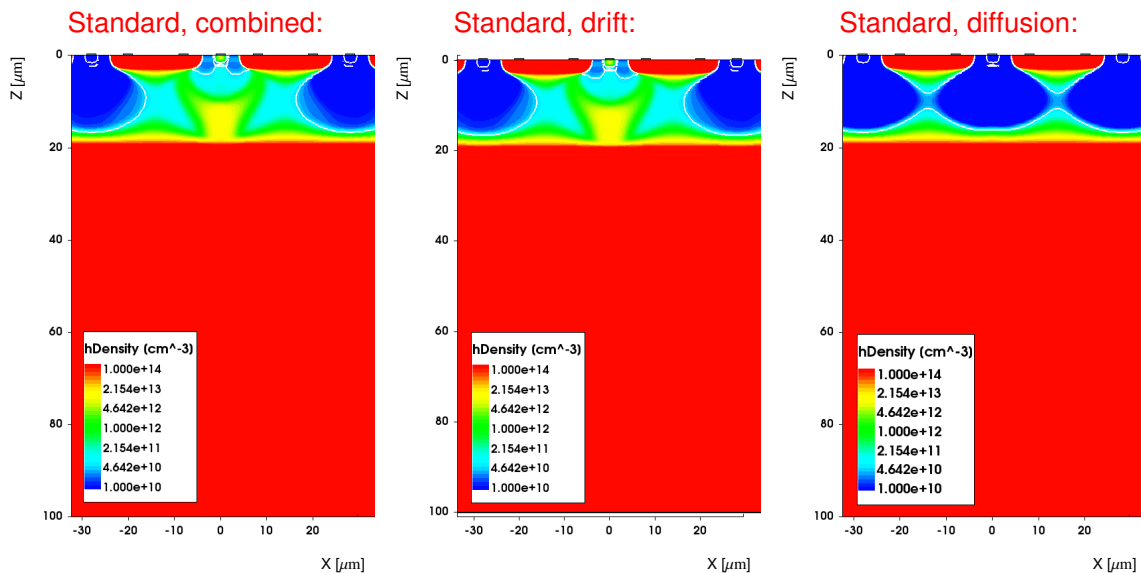


Figure 8.28: Hole density 0.75 ns after the particle incident for different sensor depth for the *standard process*.

between the regions with higher electron density and the region with higher hole density closer to the pixel implant. This is visible by the red regions of the combined and drift case in Figure and 8.26. The impact of the enhanced electric field by the potential difference between the negative electron charge and the positive voltage on the pixel implant is negligible and thus not observable in Figure 8.26.

For the diffusion case the higher electron densities closer to the backside lead to the charge configuration sketched in Figure 8.30. Due to the potential difference between the negative electron charges and the positive voltage on the pixel implant an enhanced electric field is visible by the blue region of the diffusion case in Figure 8.26. Moreover, the negative electron charges shield the negative voltage of the backside from the positive pixel implant voltage, resulting in the decrease of the electric field close to the backside substrate (see red region in Figure 8.26).

Combined and drift case:

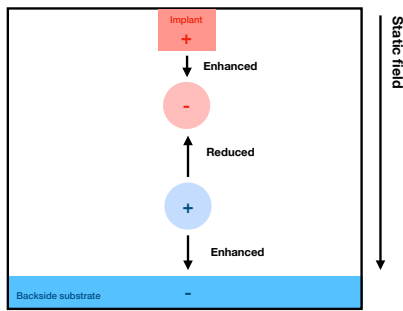


Figure 8.29: Charge configuration after the particle incident for the combined and drift case.

Diffusion case:

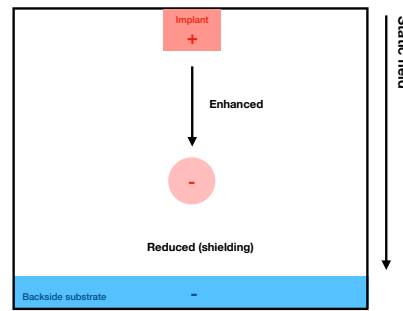


Figure 8.30: Charge configuration after the particle incident for the diffusion case.

The discussed transient behaviour of the electric field after the charge generation impacts the propagation of the charge carriers. The impact is negligible compared to the electrostatic field in the high electric field regions close to the pixel implants (approximately two orders of magnitude below) but significant in the low electric field regions closer to the backside (same order of magnitude). The lower electric field closer to the backside is increased after the charge generation for the combined and drift case but decreased for the diffusion case. Thus, the electrons created in the backside substrate in the diffusion case pass through a lower electric field that accelerate the electrons from the backside to the pixel implant. Consequently, the current pulse of the sum of the drift and diffusion component is slightly slower compared to the combined case, at times after the particle incident where the diffusion component starts to significantly contribute.

To further proof, that the observed changes of the electric field originate from the impact of the generated charges on the electric field, a particle incident is simulated over the full depth and the charge generated in the TCAD simulations is scaled down by a factor of 1000. The resulting simulated pulse shape is then scaled up by a factor of 1000 (referred to as *rescaled charge*) and compared to the combined case. This is presented in Figure 8.31, showing that the observed electric field deformations can be attributed to the density of generated charges and not e.g. to numerical issues.

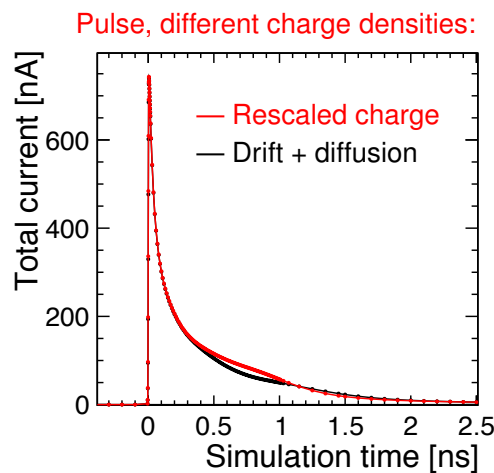


Figure 8.31: Comparison of the shape of the total current for different charge densities for the *standard process*.

Overall, the impact of the observed transient behaviour of the electric field on the overall response depends on the charge collection (i.e. the local charge densities at a certain time after the charge generation) and on the electrostatic field in the sensor (i.e. how high the electrostatic field is compared to the changes by local charge densities).

### 8.2.4 Systematic uncertainties

The impact of the variation of the epi layer doping to the value up to where the SRP measurement has been calibrated on the simulated response is discussed as one source of a systematic uncertainty. Moreover, the effect of varying the lifetime of the charge carriers is considered as a systematic uncertainty. Afterwards further possible systematic effects are briefly mentioned.

#### Different epi layer doping values

To investigate the impact of different epi layer doping values on the charge sharing, the charge of the neighbouring pixel (pixel 3 in Figure 8.15) is shown versus particle incident position for the different epi layer doping values in Figure 8.32. For the standard process the charge sharing is visibly impacted by the

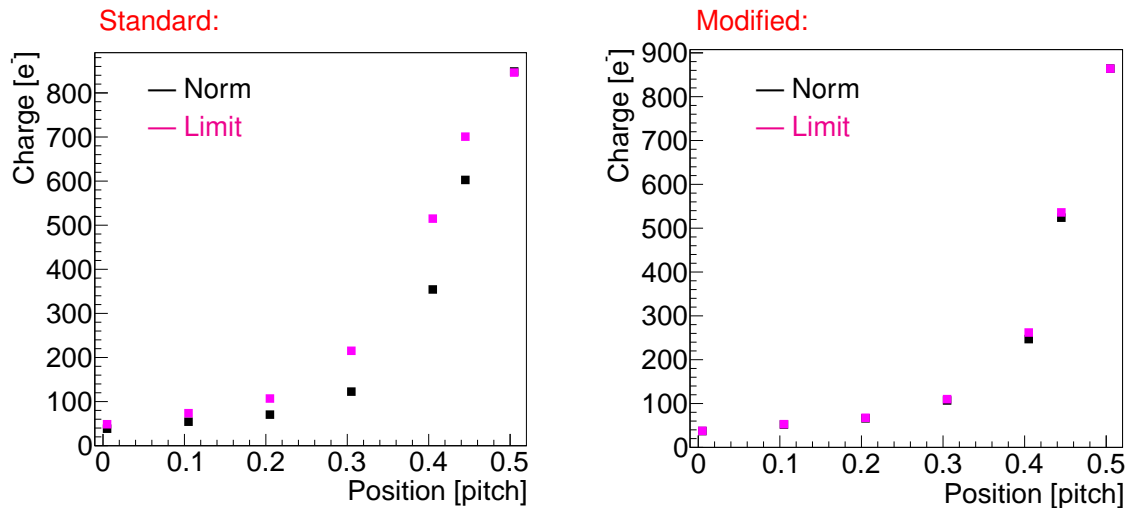


Figure 8.32: Charge induced on the neighbouring pixel for different epi layer doping values for the *standard process* (left) and the *modified process* (right).

change of the epi layer doping: for higher epi layer doping values (limit, magenta) the charge sharing is increased at an incident position of 0.3 pitch by approximately a factor of two. For the modified process the charge sharing is almost not impacted by different epi layer doping values. This is consistent with the significant reduction of the electric field and depleted region observed for higher epi layer doping values for the standard process, while the impact of different epi layer doping on the electric field and depleted region for the modified process is much less prominent (see discussion in Section 8.1).

Since the different epi layer doping values result in a change of the electric field and depleted region, they are expected to not only impact the charge sharing but also the timing. This is investigated by considering the total current induced on the centre pixel (pixel 1 in Figure 8.15) for a particle incident at the pixel centre (see Figure 8.33) and edge (see Figure 8.34). For both processes, the lower doping (black) shows a faster response compared to the higher doping (magenta), as expected from the higher electric field discussed in Section 8.1. Moreover, the effect is more prominent for the standard process,

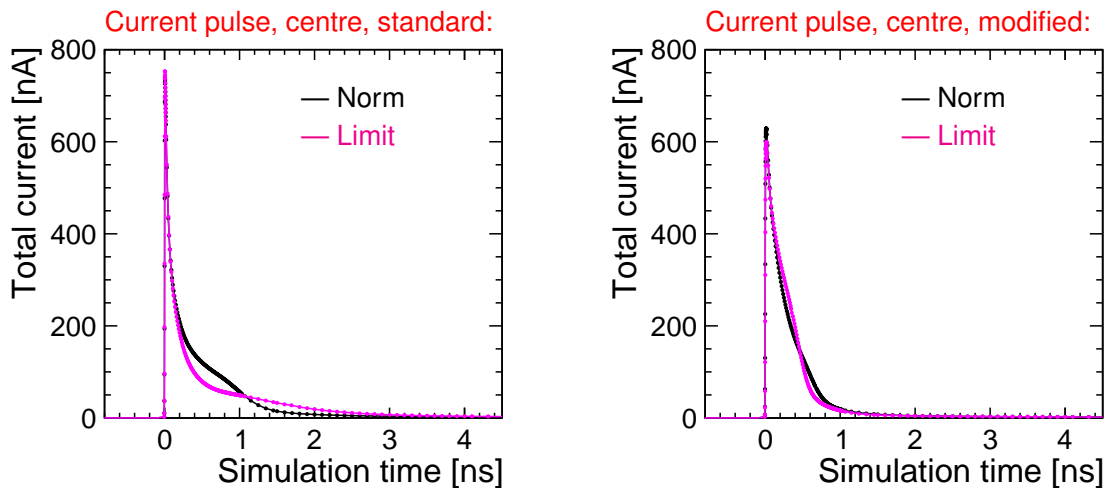


Figure 8.33: Total current versus simulation time for a particle incident at the pixel centre and different epi layer doping values. Results are presented for the *standard process* (left) and the *modified process* (right).

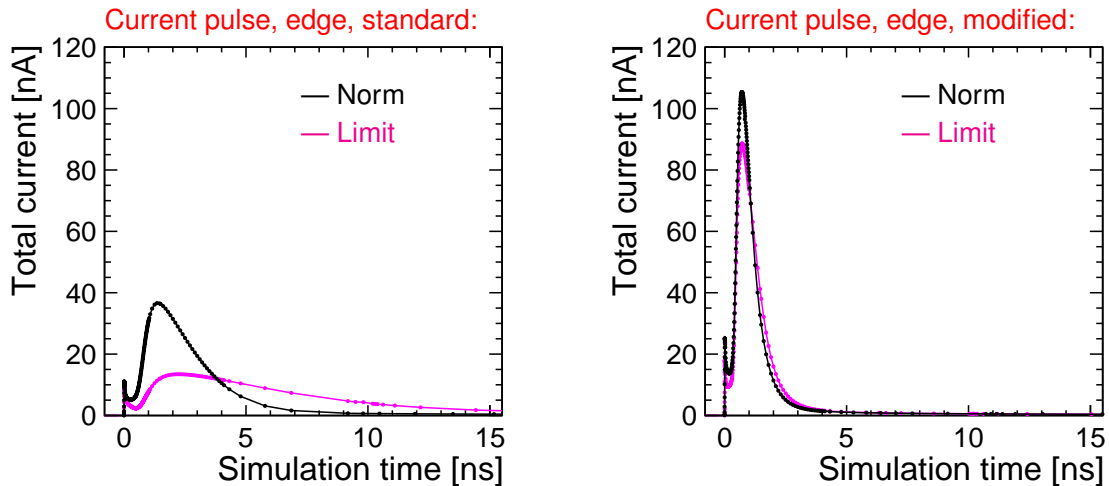


Figure 8.34: Total current versus simulation time for a particle incident at the pixel edge and different epi layer doping values. Results are presented for the *standard process* (left) and the *modified process* (right).

while less significant for the modified process, consistent with the observed significant impact of different epi layer doping on the electric field and depleted region of the standard process, especially at the pixel edge.

The systematic uncertainty of the different epi layer doping values is propagated on the final results (i.e. the comparison with test beam data) by performing the full simulation as described in Chapter 7 for the different epi layer doping values.

### Different charge carrier lifetimes

To investigate the effect of different charge carrier lifetimes on the simulated response, the maximal lifetime  $\tau_{\max}$  has been changed by one order of magnitude as presented in Figure 8.35, where the total current for a particle incident at the pixel centre is presented. Changing the lifetime by one order of

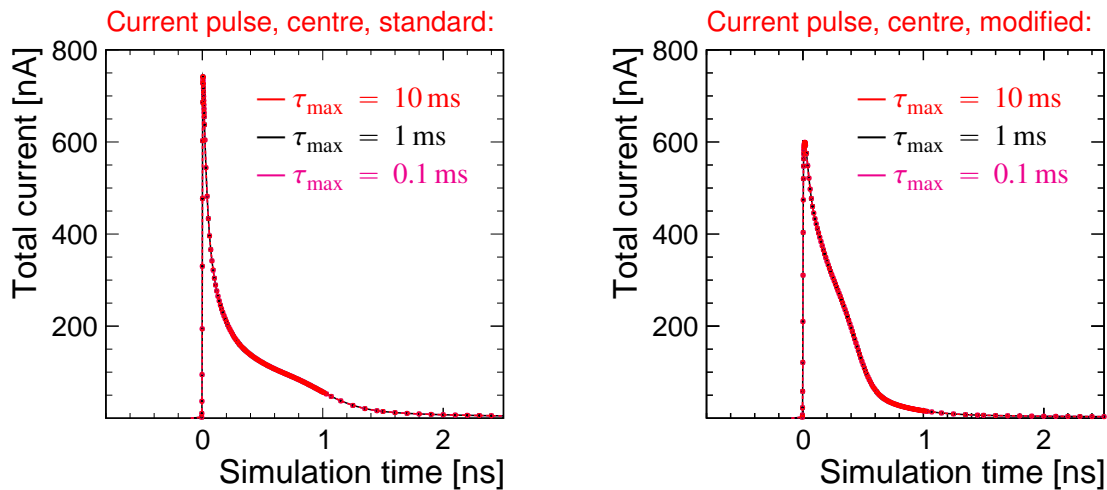


Figure 8.35: Total current versus simulation time for a particle incident at the pixel centre and different lifetime values. Results are presented for the *standard process* (left) and the *modified process* (right).

magnitude has no visible impact on the linear presentation of the current pulses, neither for the standard nor for the modified process.

However, considering the charge for different integration times, as presented in Figure 8.36, one can observe that the late diffusion component discussed previously is impacted by a change of the lifetime. Charge carriers created in the non-depleted backside substrate randomly diffuse due to the very low

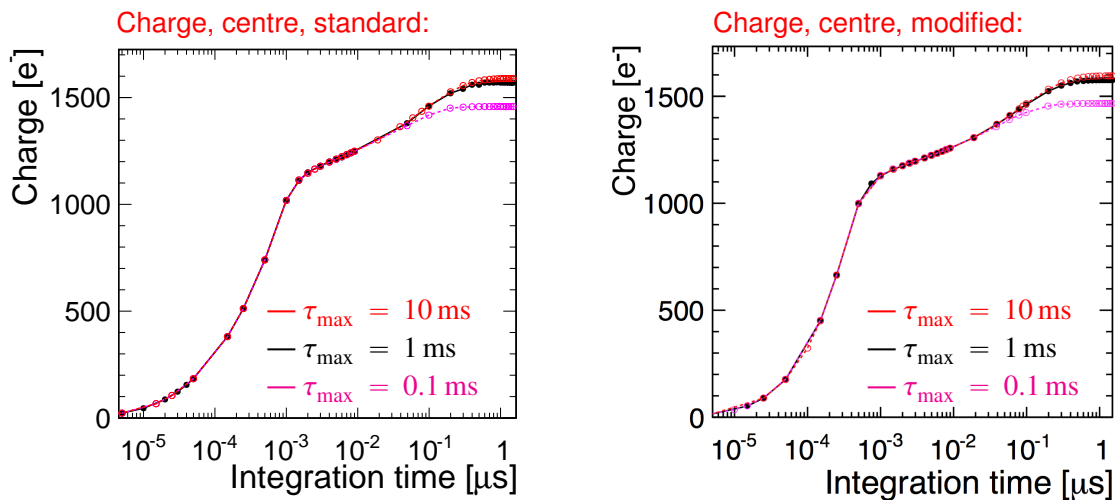


Figure 8.36: Charge versus integration time for a particle incident at the pixel centre and different lifetime values. Results are presented for the *standard process* (left) and the *modified process* (right).

electric field in the substrate. If they reach the higher electric field regions in the epi layer before recombining, they can contribute to the measured current. Consequently, shorter compared to longer lifetimes result in a higher recombination probability of the charge carriers and thus a lower probability to reach the epi layer and contribute to the overall response before recombining.

Almost no difference can be observed when increasing the lifetime by a factor of ten. Reducing the lifetime by a factor of ten results in a reduction of the late diffusion component of the total response by

approximately  $100 e^-$  (less than ten percent).

Different lifetimes of the charge carriers impact the leakage current (see Chapter 3.3.1). The leakage current has been extracted from the two dimensional TCAD simulations by calculating the current induced on the pixel implants before the particle incident and scaling that value with the area factor of the pixel size to account for the non-simulated third dimension. The leakage current is presented for different lifetimes in Figure 8.37. Generally, one can observe an increase of the leakage current for higher bias

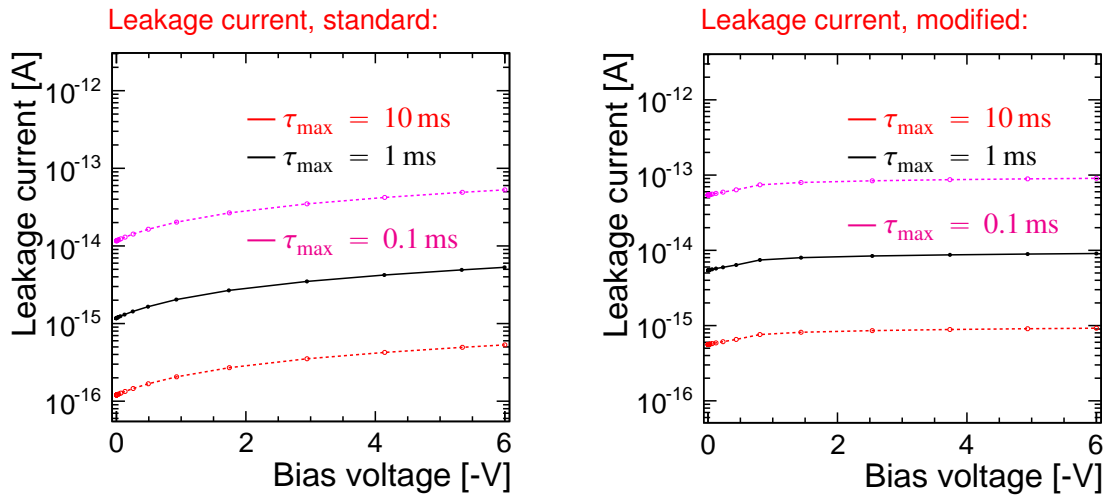


Figure 8.37: Leakage current versus bias voltage for different lifetime values for the *standard process* (left) and the *modified process* (right) for a simulated temperature of  $20^\circ\text{C}$ .

voltages and a higher leakage current for the modified compared to the standard process, both consistent with the impact of larger depleted regions on the volume current. The simulated leakage current is with values smaller than  $10^{-1}$  pA negligibly small compared to the current pulses from an particle incident (see e.g. Figure 8.35). An attempt to measure the leakage current from laboratory measurements is presented in the next chapter to compare the simulated leakage current to measurements and thus gain a more precise knowledge about the lifetime of the charge carriers.

Due to the small impact of different lifetimes affecting only the leakage current and late diffusion component and not the shape of the main current pulse (see Figure 8.35), the systematic uncertainty of the different lifetimes is not propagated on the final results (i.e. the comparison with test beam data).

### Discussion of possible further systematic effects

Further possible systematic effects are briefly mentioned.

**Implant doping** Beside the non-precise knowledge of the epi layer doping, systematic uncertainties could come from different doping values of the pixel and p well implant doping. Since the depletion and the electric field extend from the implants into the lower doped epi layer, the effect of different implant doping is neglected compared to the impact of changing the epi layer doping. Different doping values of the n layer of the modified process can impact the results. However, since the exact profile has been used for the modified process, changing the n layer doping has not been considered as a systematic uncertainty.

**Meshing** The definition of the position grid on which the finite element TCAD simulation is solved can impact the results if not being selected fine enough. The same argument holds for the time grid on which the finite element simulation has been calculated. Both meshes have been reduced until the impact on the charge has reached a level of a few electrons, such that this systematic effect can be neglected compared to the systematic uncertainty of varying the epi layer doping.

**Temperature** The uncertainty of the temperature is expected to mainly impact the simulated leakage current (see Chapter 3.3.1). However, since the temperature during data taking has not been measured on the Investigator chip, a systematic uncertainty can not be estimated.

**Dimensions** The TCAD simulations have been performed in two dimensions, representing a cut through the pixel centre of the three dimensional pixel cell, meaning that effects of the pixel edge are not taken into account. Moreover, especially the discussed impact of charge carriers on the electric field is expected to be impacted by the simulation of the third dimension. The error of the reduction of the simulation to two dimensions can be estimated by performing a three dimensional TCAD simulation and comparing the results. Thus, three dimensional TCAD simulations would be an interesting extension of the studies presented in this thesis. For the TCAD simulations the solution of the previous simulation step on all mesh points needs to be stored for each step of the finite element simulation. By the simulation of the third dimension the number of mesh points is significantly increased with respect to the two dimensional simulation. This makes three dimensional TCAD simulations challenging in view of memory consumption. The optimisation of the position mesh is a crucial point to reduce the memory consumption for three dimensional TCAD simulations.

Three dimensional electrostatic TCAD simulations of HR CMOS sensors have been shown in [4]. For the electrostatic TCAD simulation in three dimensions one can benefit from the symmetry of the pixel cell and the application of periodic boundary conditions, reducing the simulation to an eighth of the pixel cell. By this, the number of mesh points and the memory consumption can be reduced for the three dimensional electrostatic TCAD simulations.

Three dimensional transient TCAD simulations for HV CMOS sensors have been shown in [63], where the shape of the current pulse has been compared to two dimensional TCAD simulations for a particle incident at the pixel centre, simulating a full pixel cell with the application of periodical boundary conditions. For the study of charge sharing between pixels multi pixel structures need to be simulated. Thus, the optimisation of the position mesh is especially for three dimensional transient TCAD simulations a crucial point in view of memory consumption.

### 8.2.5 Summary

A comparison of the transient response after a particle incident has been performed for the standard and modified process.

Generally, it has been observed, that the lower electric field of the standard compared to the modified process results in more charge sharing but a slower readout current. This illustrates the general trade-off between the two processes of either achieving an improved spatial resolution while a worse timing performance for the standard process or an improved timing performance while a degraded spatial resolution for the modified process. However, even for a particle incident at the pixel edge of the standard process (lowest electric field region), the main rise of the charge can be observed within 10 ns.

A simulation of charge generations at different sensor depth has been performed to study the contribution of drift and diffusion to the overall response. This study shows, that a late component of the charge extending to time scales of  $\mu\text{s}$  after the charge generation can be attributed to charges created in

the backside substrate and diffusing to the depleted region. Approximately 40 % of the total charge can be attributed to this.

Moreover, the separate study of the drift and diffusion component has been used as an example to discuss the effect of the charge carriers on the electrostatic field in the sensor. The observed transient behaviour of the electric field shows that a TCAD simulation is necessary to understand the transient behaviour of the induced current in detail. It further represents an example of the relevance of a self-consistent TCAD simulation that goes beyond an electrostatic simulation and takes into account the transient impact of charge carriers on each other and the electric field.

Different epi layer doping values and charge carrier lifetimes have been discussed as the main systematic uncertainties. Varying the epi layer doping up to the value where the SRP measurement has been calibrated has a significant impact on the charge sharing and timing behaviour of the standard process, while almost not impacting the response of the modified process. Different lifetimes change the late diffusion component from the backside substrate for both the standard and modified process less than ten percent and mainly impact the leakage current.

---

## Calibration and noise characteristics

---

Measurements have been performed to characterise the studied Investigator mini matrices. To understand the results of these measurements, the signal measured in units of ADC needs to be calibrated to a physical scale of electrons and some basic characteristics, such as the noise and the leakage current need to be determined. In this chapter the calibration is presented first. Afterwards, the leakage current, the noise and its impact on the threshold settings are discussed.

Studies have been performed for different bias voltages for a mini matrix with the parameters specified in Table 9.1 for the standard and modified process. Moreover, different spacing values have been

Table 9.1: Parameters of the studied Investigator chip and pixel layout.

Parameter	Nominal value
Pitch [ $\mu\text{m}$ ]	28
Spacing [ $\mu\text{m}$ ]	3
Collection electrode size [ $\mu\text{m}$ ]	2
Thickness epitaxial layer [ $\mu\text{m}$ ]	25

investigated, while all other parameters are kept as defined in Table 9.1.

### 9.1 Calibration

Data has been recorded with a  $^{55}\text{Fe}$  source in laboratory measurements [39], irradiation the chips from the top. The known energy spectrum of the  $^{55}\text{Fe}$  source is used to calibrate the measured observables in ADC units to a physical scale of electrons.

As described in Chapter 3.4.1,  $^{55}\text{Fe}$  sources have two very close by X-ray emission lines at 5.9 keV (K-alpha lines) and one X-ray emission line at 6.5 keV (K-beta line). The K-alpha lines have a combined probability of 24.4 % and result in an energy deposit of  $1639 e^-$  in silicon. The K-beta line has a probability of 2.85 % and results in an energy deposit of  $1806 e^-$  in silicon [42].

First the calibration procedure is described, followed by a presentation of results for the standard and modified process for different bias voltages. Additionally, results for different spacings for the modified process are presented.

### 9.1.1 Procedure

A local, point like charge deposit can be assumed (see Chapter 3.4.1). Thus, the energy spectrum is expected to peak around the energy of the emission lines (in contrast to the Landau shaped energy loss spectrum of charged particles). With these assumptions, the data measured in units of ADC can be calibrated to a scale of electrons by fitting a Gaussian to the peaks of the emission lines, in the following referred to as *calibration peak*, and setting its mean value equal to the known energy of the emission lines.

The data has been reconstructed as described in Chapter 6.1.1. Some aspects need to be taken into account to not bias the calibration, that are discussed in the following. As shown in [4] charge sharing is expected for a  $^{55}\text{Fe}$  measurement of the studied mini matrices implemented in the standard and modified process. At high threshold values charge sharing effects can bias the calibration peaks to lower energy values. A single-pixel cluster is sketched in Figure 9.1, with all charge collected by one single pixel. Figure 9.2 illustrates a multi-pixel cluster, having only a fraction of the total charge collected in the seed pixel. At high threshold values the charge in the neighbouring pixels would be discarded, resulting in a

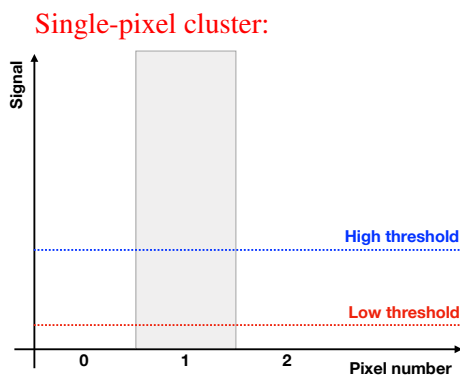


Figure 9.1: Single-pixel cluster identified as such at low and high thresholds.

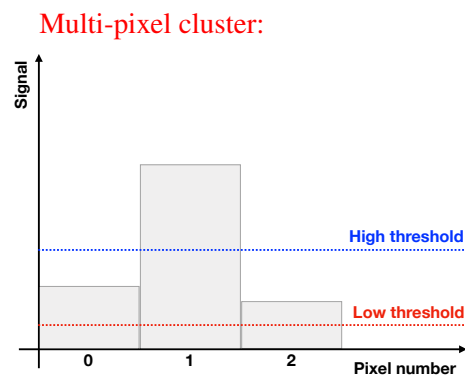


Figure 9.2: Multi-pixel cluster identified as single-pixel cluster at high thresholds.

bias of the calibration peaks to lower values. To avoid this bias of the calibration peaks by charge sharing effects, the threshold during the analysis is set to low values of three times above the noise. However, setting the threshold closer to the noise, noise contributions can add up to the measured signal and impact the calibration. To avoid this, the sum of the signal collected from pixels beside the seed pixel is required to be smaller than 5 % of the seed signal<sup>1</sup>. Moreover, pixels at the edge of the matrix are discarded, since charge created in the non-readout pixel row surrounding the Investigator mini matrix can be lost.

If all above mentioned requirements are fulfilled the sum of the signal (including the neighbouring pixels) is used to fill the calibration histogram. A Gaussian fit has been performed to the peak from the K-alpha lines and the range of the Gaussian fit has been set by eye to cover the prominent peak of the K-alpha lines. The peak from the K-beta line has not been used due to limited statistics. Thus, the calibration is performed at a single energy point, assuming a linear response of the pixel pixels for different energies.

The extracted mean values  $\mu_{\text{Gauss}}$  from the Gaussian fits can be used to calculate the *Calibration Factor* (*CF*)

$$\text{CF} = 1639 [\text{e}^-] / \mu_{\text{Gauss}} [\text{ADC}], \quad (9.1)$$

<sup>1</sup> Different cuts have been investigated for the calibration and found to perform similar. One alternative is presented in [82], where the same cut relative to the noise has been set for each pixel.

by which the measured signal amplitude, noise and threshold need to be scaled to be converted into a scale in units of electrons. The width of the Gaussian fits can originate from noise contributions.

### 9.1.2 Results for different bias voltages for the standard and modified process

Different bias voltages change the depleted region in the sensor and therefore the sensor capacitance: the smaller the depleted volume in a sensor, the larger the sensor capacitance. A different sensor capacitance results in a different gain of the measured voltage  $U = I/C$ , where  $I$  is the measured current and  $C$  is the total capacitance that also includes sensor capacitance. Accordingly, the calibration has been performed separately for each bias voltage. The  $^{55}\text{Fe}$  spectra are presented for different bias voltages in Figure 9.3.

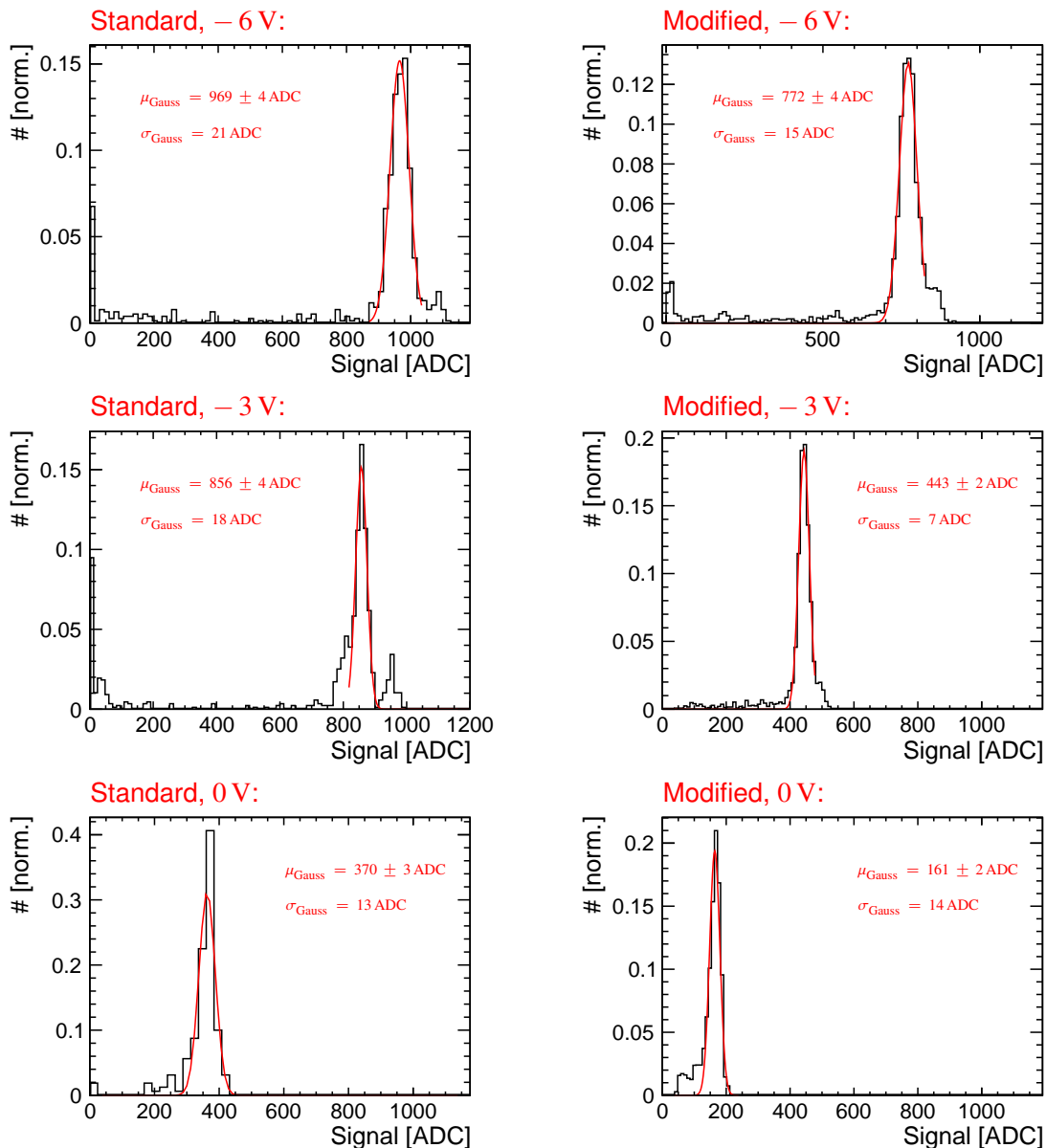


Figure 9.3: Spectrum from  $^{55}\text{Fe}$  source measurements for different bias voltages for the *standard* (left) and *modified* (right) process.

Beside peaks expected from the emission lines, the spectra show especially at low voltages a tail to lower energies, that might be attributed to more prominent charge sharing effects at lower absolute bias voltages. Also photon conversion in the non-depleted backside substrate can contribute to the measured low energy tail (see Chapter 3.4.1).

The peak at values of zero can come from noise triggers during the data taking. This can occur, since the triggering threshold during data taking is set on the distance between a readout sample and the previous sample. The signal during the analysis is defined as the difference of the mean samples before and after a particle hit. Thus, noise sparks or sample by sample fluctuations can trigger an event during data taking, but give a low signal close to zero in the analysis.

The calibration factors for the standard and modified process are presented in Figure 9.4 for different bias voltages. The uncertainties on the CF's has been propagated according to equation 9.1, using the uncertainty on the mean values of the Gaussian fits. Larger calibration factors have been measured for

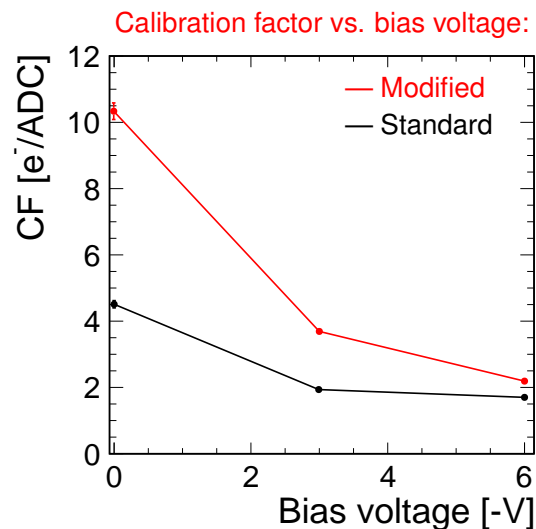


Figure 9.4: Calibration factor for different bias voltages.

lower absolute bias voltages, being consistent with the expected lower gain at lower absolute voltages, due to a larger sensor capacitance. Moreover, the calibration factors of the modified process are generally higher compared to the standard process and show a larger dependence on the bias voltage.

At a bias voltage of  $-6$  V the calibration factor for the standard and modified process is very similar, indicating a comparable sensor capacitance for both processes. At lower bias voltages the calibration factor increases much steeper for the modified process compared to the standard process, showing a significantly more prominent increase of the sensor capacitance with lower absolute bias voltage, especially at a bias voltage of  $0$  V. This can be understood by the evolution of the depleted region discussed in Chapter 8.1: since the n layer is not fully depleted at lower voltages, a non-depleted region is present directly around the pixel implants, that significantly adds up to the sensor capacitance especially for a bias voltage of  $0$  V (see Figure 8.7). In contrast to this, the depleted region for the standard process is always present around the pixel implant, due to the pn junction between the pixel implant and the epi layer (see Figure 8.1).

### 9.1.3 Results for different spacings for the modified process

The calibration has been performed for different spacings (distance between pixel implant and p wells, see Figure 5.1) for the modified process, investigating a mini matrix with other parameters as specified in Table 9.1 and a bias voltage of  $-6$  V.

The  $^{55}\text{Fe}$  spectra for a larger spacing of  $5\ \mu\text{m}$  and a smaller spacing of  $1\ \mu\text{m}$  are presented in Figure 9.5 and the resulting calibration factors versus spacing are shown in Figure 9.6.

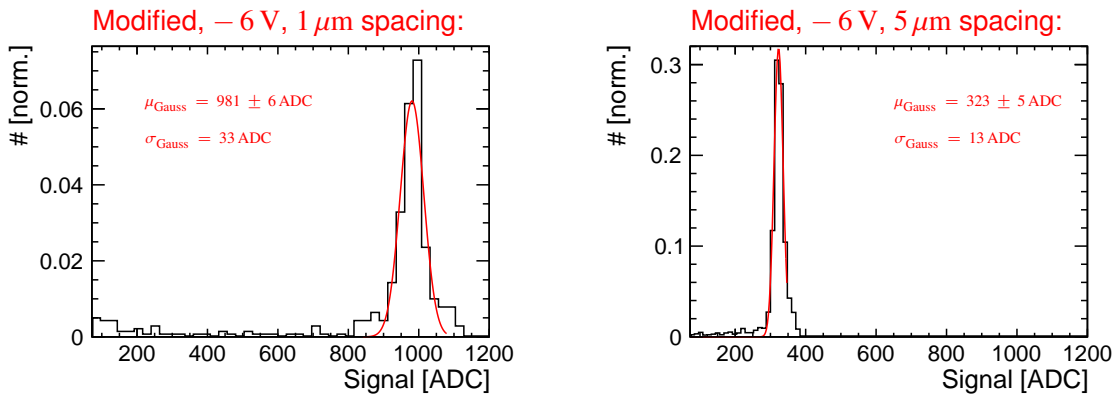


Figure 9.5: Spectrum from  $^{55}\text{Fe}$  source measurements for different spacings for the modified process for a spacing of  $1\ \mu\text{m}$  (left) and a spacing of  $5\ \mu\text{m}$  (right).

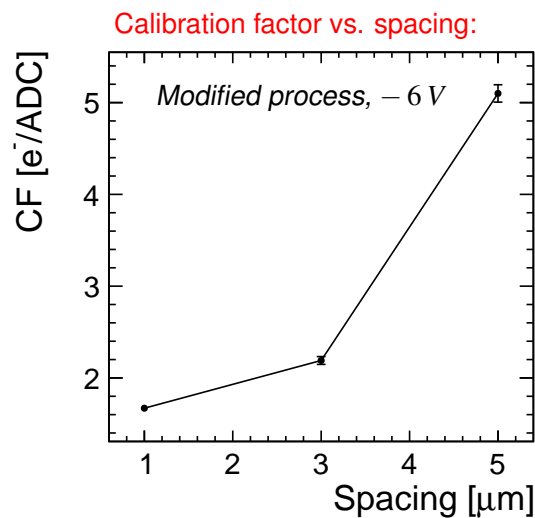


Figure 9.6: Calibration factor for different spacings for the modified process at a bias voltage of  $-6$  V.

Larger calibration factors have been measured for larger spacings, that can be explained by a change of the capacitance, discussed in the following. The capacitance over which the voltage drop is measured is composed of different components:

- The capacitance of the routing lines, bringing the signal from the pixel implant to the CMOS logic in the p wells. This contribution is expected to *increase* the capacitance for larger spacings.

- The capacitance from different sizes of non-depleted regions around the pixel implant: for larger spacings, the region around the pixel implant is less depleted (see Figure 8.13). This contribution is thus expected to *increase* the capacitance for larger spacings.
- The capacitance between the pixel implant and the p wells. This contribution is expected to *decrease* the capacitance for larger spacings.

The measured increase of the calibration factor for larger spacings thus shows that the capacitance between the pixel implants and the p wells is not significant compared to the capacitance from the change in depletion and the capacitance of the routing lines. The fact that the capacitance increases steeper than linear with the spacing indicates, that the increase of capacitance is dominated by the change of the depleted region around the pixel implant.

## 9.2 Noise and threshold

The noise and threshold have been calculated from test beam data and extracted from pixels without a particle hit (see Chapter 6.1.1). In this section the procedure to calculate the noise and threshold is introduced. Further, the results for the noise and threshold values are presented for the standard and modified process for different bias voltages and for the modified process for different spacings.

### 9.2.1 Procedure

The noise is calculated as the RMS of the amplitude fluctuations around the pedestal. A histogram is filled with a noise entry for each pixel. This is exemplary shown in Figure 9.7 for the modified process at different bias voltages<sup>2</sup>, showing that the noise during the analysis is reduced by the common mode correction with respect to the noise during data taking.

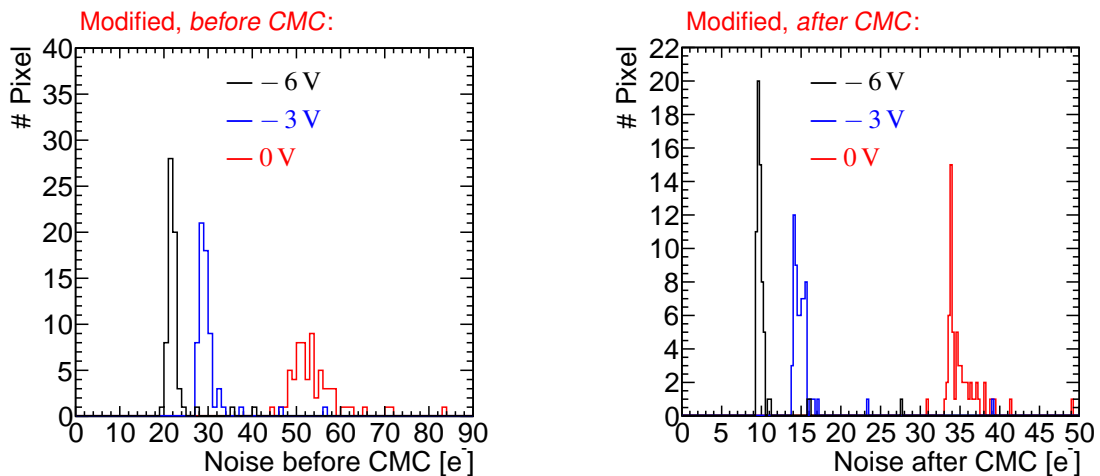


Figure 9.7: Pixel-by-pixel noise fluctuations for different bias voltages *before* (during data taking, left) and *after* (during the analysis, right) the Common Mode Correction (CMC), for the modified process.

The stated noise values per voltage point are defined as the mean value of this histogram and the spread has been calculated as its RMS<sup>3</sup>, to account for outliers in the pixel-by-pixel noise distributions.

<sup>2</sup> The pixel by pixel noise fluctuations of all studied designs can be found in the Appendix A.1.

<sup>3</sup> Being below 2.5 % the uncertainty of the calibration factor has been neglected.

To obtain the noise and its spread in units of electrons the values are scaled with the calibration factor.

All threshold values are set such, that a detected signal is required to be higher than a multiplicity  $N$  of the noise. Two different thresholds need to be distinguished. During data taking the highest pixel signal (seed signal) is required to cross a triggering threshold of

$$\text{Triggering threshold} = N_{\text{Trigger}} \times \text{Noise}_{\text{Pre common mode}} \quad (9.2)$$

During the analysis all pixels are required to cross a single pixel analysis threshold of

$$\text{Analysis threshold} = N_{\text{Single pixel}} \times \text{Noise}_{\text{Post common mode corrections}} \quad (9.3)$$

During data taking the triggering threshold has been set according to Equation 9.2 with a multiplicity of  $N_{\text{Trigger}} = 8 - 10$ . To allow for an efficient data taking, this value has been set such, that the rate of random noise triggers did not exceed a few Hz. If not stated otherwise, the single pixel threshold during the analysis has been set according to Equation 9.3 with a multiplicity of  $N_{\text{Single pixel}} = 5^4$ .

### 9.2.2 Results for different bias voltages for the standard and modified process

The noise is presented versus bias voltages in Figure 9.8. As visible by the larger error bars, larger

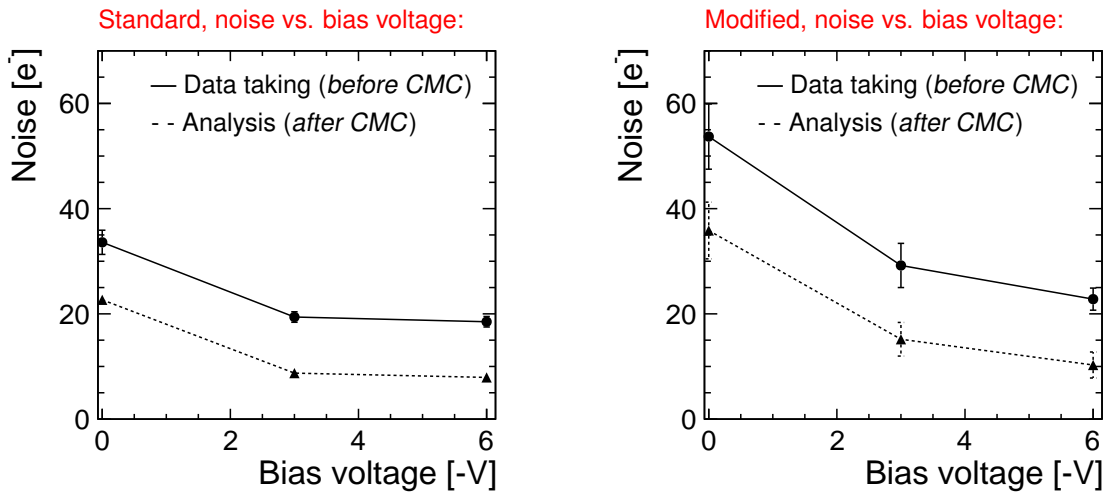


Figure 9.8: Noise versus bias voltages *before* and *after* the Common Mode Correction (CMC), for the *standard* (left) and *modified* (right) process.

pixel-by-pixel fluctuations are measured for the modified compared to the standard process. Moreover, for both processes the noise is reduced by a factor of  $\sim 1.5 - 2$  (depending on the bias voltage) by the common mode noise correction. According to the measured lower calibration factor for higher absolute bias voltages (see Figure 9.4), higher absolute bias voltages result in lower noise<sup>5</sup>. Thus, similar noise values can be noted for the standard and modified process at a bias voltage of  $-6$  V, while for lower absolute bias voltages the larger increase of sensor capacitance results in significantly larger noise values for the modified compared to the standard process.

<sup>4</sup> A scan of the analysis threshold is presented in Section 10.2.1.

<sup>5</sup> Note that this argument assumes that the noise in units of ADC does not decrease for higher voltages, as presented in Appendix A.2.

The threshold versus bias voltage is presented during data taking (before the common mode correction) and during the analysis (after the common mode correction) in Figure 9.9, resembling the trends discussed for the noise dependency on the bias voltage. The uncertainties are defined as the RMS of the single pixel threshold distribution<sup>6</sup>.

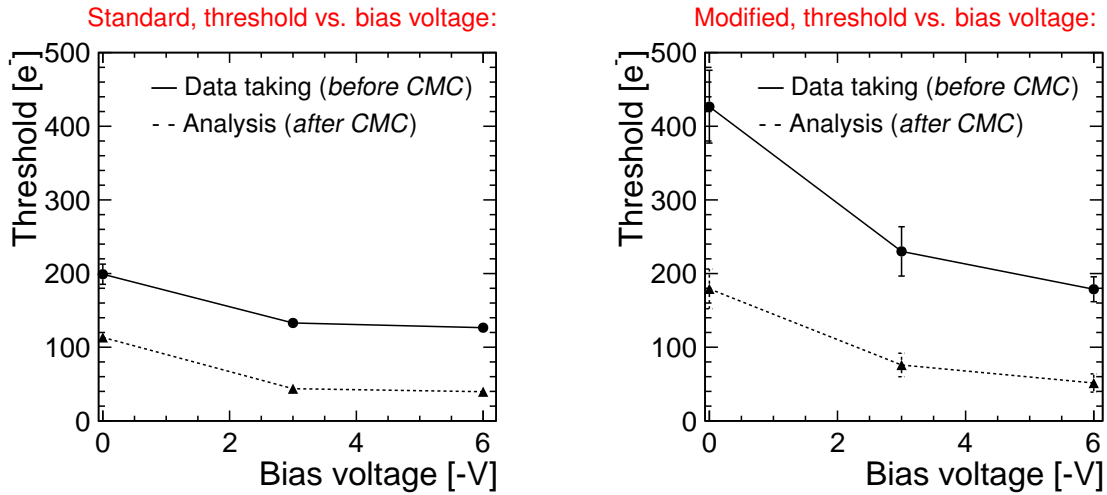


Figure 9.9: Threshold versus bias voltages *before* and *after* the Common Mode Correction (CMC), for the *standard* (left) and *modified* (right) process.

### 9.2.3 Results for different spacings for the modified process

The noise is presented for different spacings for the modified process in Figure 9.10 for a mini matrix with the other parameters as specified in Table 9.1 and a bias voltage of  $-6$  V. Larger noise values have

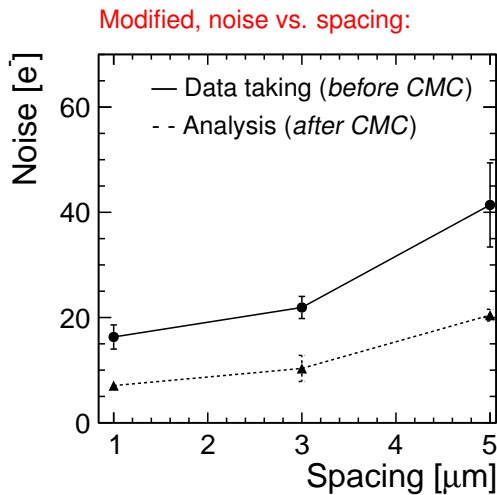


Figure 9.10: Noise versus spacing *before* and *after* the Common Mode Correction (CMC), for the modified process at a bias voltage of  $-6$  V.

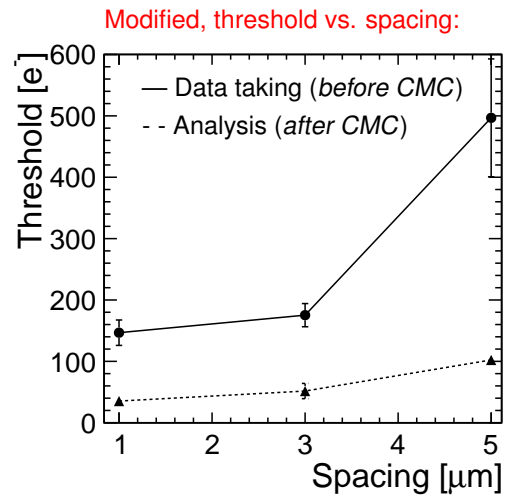


Figure 9.11: Threshold versus spacing *before* and *after* the Common Mode Correction (CMC), for the modified process at a bias voltage of  $-6$  V.

<sup>6</sup> As for the noise, the uncertainty of the calibration factor has been neglected for the threshold being a multiplicity of the noise.

been measured for a larger spacing. This can be attributed to the higher capacitance and resulting lower gain for larger spacings (see discussion in Section 9.1.3), that leads to a larger calibration factor and thus a higher calibrated noise. The larger noise results in larger threshold for larger spacings, as shown in Figure 9.11.

## 9.3 Leakage current

As for the calculation of the noise and threshold values, pixel waveforms without a particle hit have been used to extract the leakage current. The leakage current has been computed and compared to the results obtained from the TCAD simulations. First, the procedure to calculate the leakage current is introduced followed by a presentation of the results for different bias voltages for the standard and modified process and for different spacings for the modified process.

### 9.3.1 Procedure

The waveform of the common mode noise introduced in Chapter 6.1.1 is composed of two components: a drift of the waveform to lower amplitudes for later times, which is attributed to a leakage current, and an overlaying oscillation. To determine the value of the leakage current, a fit of the function  $f(t)$  has been performed to the waveforms of pixels without a particle hit:

$$f(t) = -\text{drift [ADC} \cdot 65\text{MHz]} \cdot t [1/65\text{MHz}] \\ - \text{amplitude [ADC]} \cdot \sin(2\pi \cdot \text{frequency [65MHz]} \cdot t [1/65\text{MHz}] + \text{phase}) \\ + \text{offset [ADC]}, \quad (9.4)$$

as exemplary shown for a pixel waveform of the modified process for a bias voltage of  $-6\text{ V}$  in Figure 9.12. Using the calibration factor CF one can calculate the leakage current

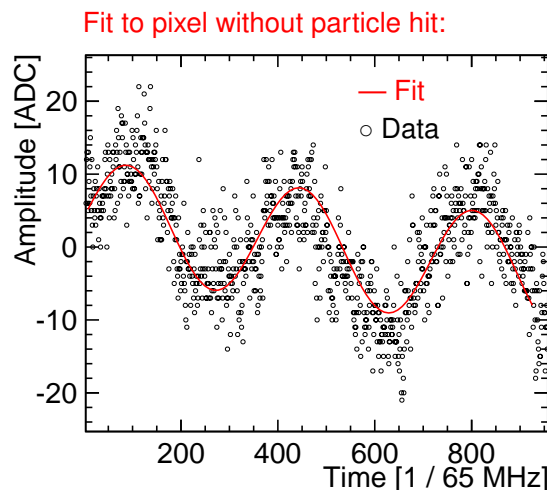


Figure 9.12: Fit of equation 9.4 to a pixel without a particle hit for the modified process at  $-6\text{ V}$ .

$$\begin{aligned}
I_{\text{Leakage}} [\text{A}] &= \text{CF} [e^-/\text{ADC}] \cdot \text{drift} [\text{ADC} \cdot 65 \text{ MHz}] \\
&= \text{CF} \cdot 1.60217646 \cdot 10^{-19} \cdot \text{drift} \cdot 65 \cdot 10^6 [\text{A}].
\end{aligned}
\tag{9.5}$$

The fit is performed for each event for each pixel without a particle hit and the leakage current per pixel is extracted from the mean value of the histogram of the fitted values, with the RMS of this histogram taken as uncertainty on the leakage current.

### 9.3.2 Results for different bias voltages for the standard and modified process

The calculated leakage current versus bias voltage is presented in Figure 9.13. The leakage current for the

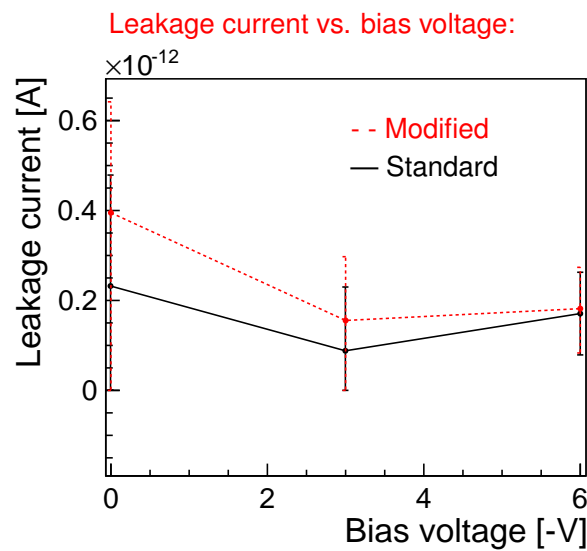


Figure 9.13: Average leakage current per pixel for different bias voltages for the standard and modified process.

studies of non-irradiated chips presented in this thesis is smaller than 1 pA per pixel and thus negligible compared to the readout current.

The large uncertainties show the limit of the described procedure to measure the leakage current <sup>7</sup>. Thus, within the uncertainties no significant dependence on the bias voltage or process can be observed, allowing for no distinction between different simulated charge carrier lifetimes (see Figure 8.37).

The temperature is expected to significantly impact the measured leakage current (see Equation 3.8). The temperature has not been measured during data taking, but is most likely decreased with respect to the simulated room temperature of 20 °C due to the power dissipation of the electronics during data taking. Moreover, contributions from currents due to surface damages can contribute to the measured leakage current, that are not taken into account by the idealised TCAD simulation. In addition, as shown in Chapter 8.2.4, the lifetime of the charge carriers assumed for the TCAD simulations can also significantly impact the leakage current. These aspects can explain why the measured leakage current lies well above the simulated leakage current.

<sup>7</sup> As for the noise and threshold the uncertainty of the calibration factor has been neglected.

## 9.4 Summary

The spectrum recorded for  $^{55}\text{Fe}$  measurements has been analysed and used to calibrate the ADC values to a scale in units of electrons. The different emission lines (K-alpha and K-beta) can be observed at bias voltages of  $-6\text{ V}$  and  $-3\text{ V}$ , while not being resolved at a bias voltage of  $0\text{ V}$ .

The calibration peak for the modified process is at approximately 20 % higher ADC values compared to the standard process, which can be explained by a slightly smaller sensor capacitance for the standard process. Due to larger sensor capacitances at lower voltages, larger calibration factors have been measured for both processes at lower voltages. However, consistent with the simulated evolution of the depleted region, the effect is more prominent for the modified process compared to the standard process, since the n layer is not fully depleted at lower absolute bias voltages. The results of the calibration factors are summarised in Table 9.2.

Table 9.2: Calibration factors for the studied Investigator mini matrices for a pixel size of  $28\ \mu\text{m}$  and an epi layer thickness of  $25\ \mu\text{m}$ .

Process	standard			modified				
	Voltage [ $-\text{V}$ ]	0	3	6	0	3	6	
Spacing [ $\mu\text{m}$ ]	3	3	3	3	3	1	3	5
CF [ $e^-/\text{ADC}$ ]	4.2	1.9	1.7	10.17	3.7	1.6	2.1	5.1

The trends measured for the calibration factor are propagated to the noise and threshold that are scaled with the calibration factor. The advantage of the small sensor capacitance of the studied HR CMOS processes is reflected in the low noise level of  $\lesssim 10\ e^-$  at a bias voltage of  $-6\text{ V}$  (after the CMN correction) and the resulting possibility to apply low threshold values. The results of the noise and threshold settings are summarised in Table 9.3.

Table 9.3: Noise and threshold settings for the studied Investigator mini matrices for a pixel size of  $28\ \mu\text{m}$  and an epi layer thickness of  $25\ \mu\text{m}$ . The analysis threshold has been set five times above the noise.

Process	standard			modified				
	Voltage [ $-\text{V}$ ]	0	3	6	0	3	6	
Spacing [ $\mu\text{m}$ ]	3	3	3	3	3	1	3	5
Noise, data taking ( <i>before</i> CMN correction) [ $e^-$ ]	34	19	18	54	29	16	23	41
Noise, analysis ( <i>after</i> CMN correction) [ $e^-$ ]	23	9	8	36	16	7	10	20
Triggering threshold ( <i>before</i> CMN correction) [ $e^-$ ]	199	130	126	425	239	145	179	495
Analysis threshold ( <i>after</i> CMN correction) [ $e^-$ ]	115	45	40	180	80	35	51	100

The leakage current has been extracted from the drift of the common mode waveform and found to be with values below pA per pixel, negligible compared to the signal for non-irradiated chips studied in this thesis.



---

## Test beam results

---

Results from various test beam campaigns are presented in this chapter for particle incidents perpendicular to the sensor surface. The results of the TCAD simulations presented in Chapter 8 are compared on a qualitative level to the test beam results<sup>1</sup>. The test beam data has been recorded with the setup described in Chapter 5.5 and reconstructed as explained in Chapter 6.

For the interplay of the triggering threshold applied during data taking and the offline analysis threshold, two different cases need to be distinguished:

**1. Analysis threshold below triggering threshold:**

The triggering threshold requires at least one pixel to be above the given value, and can be therefore considered as the threshold on the seed signal. The analysis threshold can be reduced with respect to the triggering threshold since it is set after the common mode correction and the signal definition in the analysis is more robust against sample by sample noise fluctuations. The analysis threshold is set to each single-pixel, and therefore defines the threshold on the signal of the neighbouring pixels if it is below the triggering threshold. Therefore, only the neighbouring pixels are affected when the analysis threshold is below the triggering threshold. Accordingly, the efficiency is expected not to change for different analysis thresholds below the triggering threshold while the cluster size and the spatial and timing resolution can change. On the other side, the cluster size spatial and timing resolution are not impacted by the triggering threshold as long as a fully efficient operation can be achieved.

**2. Analysis threshold at least as high as triggering threshold:**

As soon as the analysis threshold crosses the triggering threshold, the value of the analysis threshold defines a global threshold value, being the same for all pixels.

First, both processes are compared for the parameters defined in Table 10.1 using fixed operation conditions. In a next step the results for the standard and modified process are studied for the same parameters at different analysis thresholds and bias voltages. Finally, different spacings are investigated for the modified process in dependence of the analysis thresholds, keeping all other parameters as specified in Table 10.1.

---

<sup>1</sup> A quantitative comparison between results of the simulation chain to the test beam data is presented in Chapter 11, since certain cuts need to be performed on the test beam data to compare to the two dimensional simulation (see Chapter 6.5.2). To evaluate the full test beam performance in a first step, these cuts are not performed on the results presented in this chapter.

Table 10.1: Parameters of the studied Investigator chip and pixel layout.

Parameter	Nominal value
Pitch [ $\mu\text{m}$ ]	28
Spacing [ $\mu\text{m}$ ]	3
Collection electrode size [ $\mu\text{m}$ ]	2
Thickness epitaxial layer [ $\mu\text{m}$ ]	25

## 10.1 Comparison of modified and standard process at fixed parameters and operation conditions

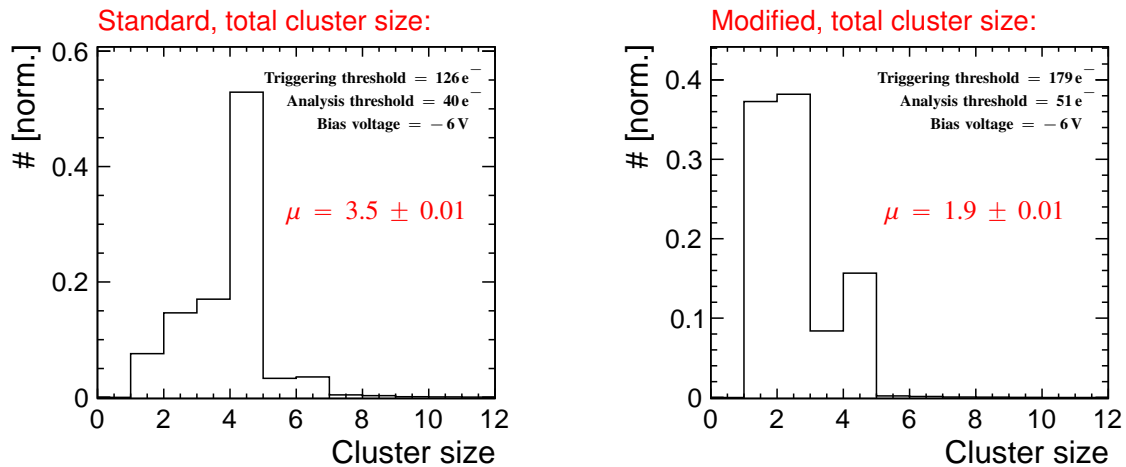
A comparison of the Investigator modified and standard process has been performed for the parameters defined in Table 10.1. The operation conditions and analysed statistics are summarised in Table 10.2.

Table 10.2: Definition of operation conditions and analysed statistics.

	Voltage [V]	Triggering threshold [ $e^-$ ]	Analysis threshold [ $e^-$ ]	# roi-tracks
Standard	-6	126	40	25660
Modified	-6	179	51	24260

### 10.1.1 Cluster size and spatial resolution

The total cluster size distribution is presented in Figure 10.1 for the modified and standard process. Despite comparable thresholds, the mean cluster size for the standard process is  $\sim 3.5$ , significantly

Figure 10.1: Total cluster size distribution for the *standard process* (left) and for the *modified process* (right).

higher than for the modified process, where a mean cluster size of  $\sim 1.9$  has been measured. For both processes a peak of the distributions at a size of four pixels is visible, which can be understood by the rectangular pixel shape, resulting in large regions in the pixel corners, where the distance to three neighbouring pixels is minimised.

To better understand the origin of different cluster sizes, the in-pixel representation of the total cluster size is shown in Figure 10.2. For both processes, the lowest cluster sizes are observed for a track intercept

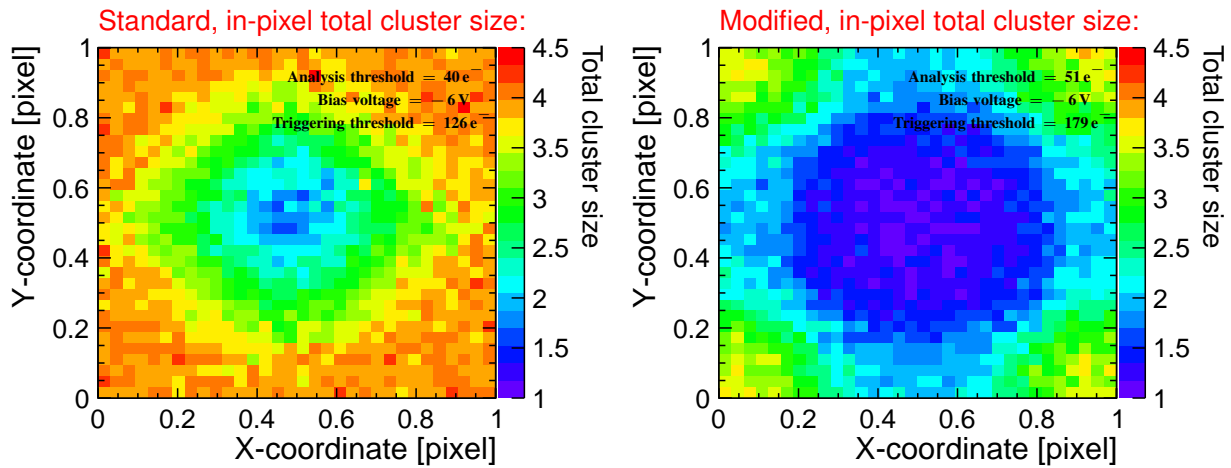


Figure 10.2: In-pixel representation of the total cluster size for the *standard process* (left) and for the *modified process* (right).

position close to the pixel centre. Close to the pixel edges an intermediate cluster size is measured and the highest cluster sizes are dominating the regions in the pixel corners.

For the standard process the cluster size is overall higher than for the modified process, even in the very pixel centre. This can be explained by the electric field along the sensor depth in the pixel centre, being lower for the standard compared to the modified process (compare Figure 8.6 and Figure 8.12).

A cluster size larger than four has been measured for the standard process for  $\sim 5\%$  of the roi-tracks. Since this large spread of the charge has been measured in the edge regions of the pixel cell of the standard process, where the epi layer is not fully depleted (see Figure 8.1), it is likely to be attributed to diffusion.

In Figure 10.3 the cluster size distribution is presented separately in the X and Y dimension of the pixel matrix. The good agreement between the cluster size in X and Y dimension shows the good mechanical orientation of the Investigator chip perpendicular to the beam axis. The charge is shared between the pixels in one matrix dimension in  $\sim 45\%$  for the modified process. For the standard process the charge is shared in one matrix dimension in  $\sim 85\%$ .

The precision with which the particle impact position can be reconstructed is expected to improve with the observed two pixel clusters in X and Y, since a charge interpolation can be performed between the pixels (see Section 6.2). The spatial residuals are shown for the X and Y dimension in Figure 10.4, showing the good performance of the alignment of the analysis by the agreement between the X and Y dimension. To obtain the spatial resolution the RMS of this distribution is calculated on a range of  $\pm 20\ \mu\text{m}$  ( $RMS_{\pm 20\ \mu\text{m}}$ ). The telescope resolution of  $\sim 2\ \mu\text{m}$  is not unfolded from the quoted values. For the standard process a spatial resolution of  $\lesssim 4\ \mu\text{m}$  and for the modified process a spatial resolution of  $\lesssim 5\ \mu\text{m}$  has been calculated. Consistent with the significant larger fraction of clusters with a size of two in X and Y direction for the standard process compared to the modified process, the spatial resolution is lower for the standard process by  $\sim 20\%$ .

The obtained values for the spatial resolution can be compared to the value of  $\text{pitch}/\sqrt{12} \sim 8\ \mu\text{m}$ , which would be the expected resolution if there were only single-pixel clusters. For both processes, a significant improvement of the spatial resolution with respect to this value has been measured. This is in line with the measured high fraction of two pixel clusters.

To understand the impact of charge sharing on the spatial resolution in more detail, the spatial residual

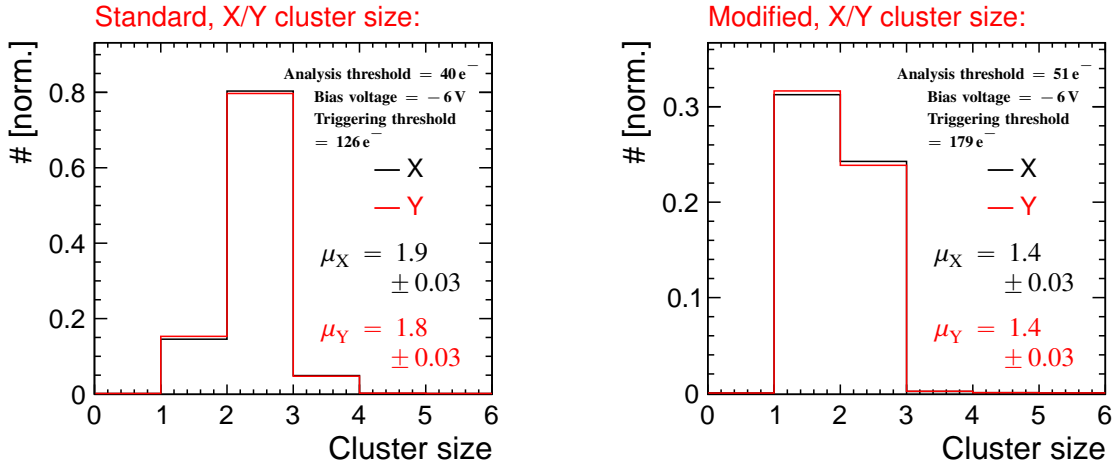


Figure 10.3: Cluster size distribution in X and Y dimension of the pixel matrix for the *standard process* (left) and for the *modified process* (right).

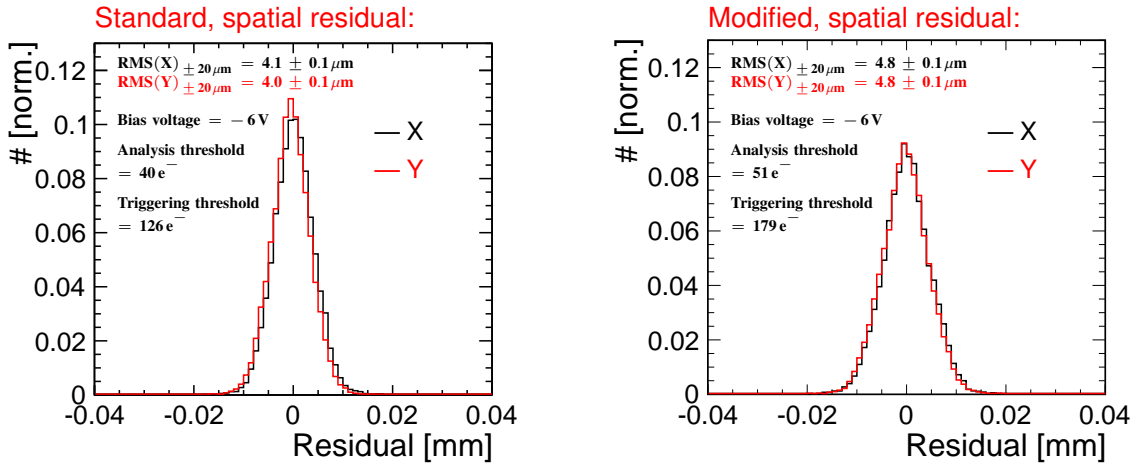


Figure 10.4: Spatial residual distributions in X and Y dimension of the pixel matrix for the *standard process* (left) and for the *modified process* (right).

distributions in X and Y direction are studied separately for single-pixel clusters and multi-pixel clusters.

**Single and multi-pixel cluster residuals for the standard process** The X and Y residual distributions are presented for the standard process separately for single and multi-pixel clusters in Figure 10.5. The single-pixel cluster resolution of  $\approx 3.3 \mu m$  is improved with respect to the value of  $\text{pitch}/\sqrt{12} \sim 8 \mu m$ . This can be understood by the enhanced charge sharing for the standard process, shrinking the area in the pixel where single-pixel clusters are generated to a small region close to the pixel centre. Accordingly, the area in which single-pixel clusters are generated is smaller than the full pixel area, so that the width in the formula  $\text{width}/\sqrt{12}$  is smaller than the pixel pitch. The effect is shown in Figure 10.6, where the in-pixel representations of the X and Y cluster size are presented.

The multi-pixel cluster resolution of  $\approx 4.5 \mu m$  is improved with respect to the value of  $\text{pitch}/\sqrt{12}$ , but also larger than the single-pixel cluster resolution. This can be explained by the contribution from

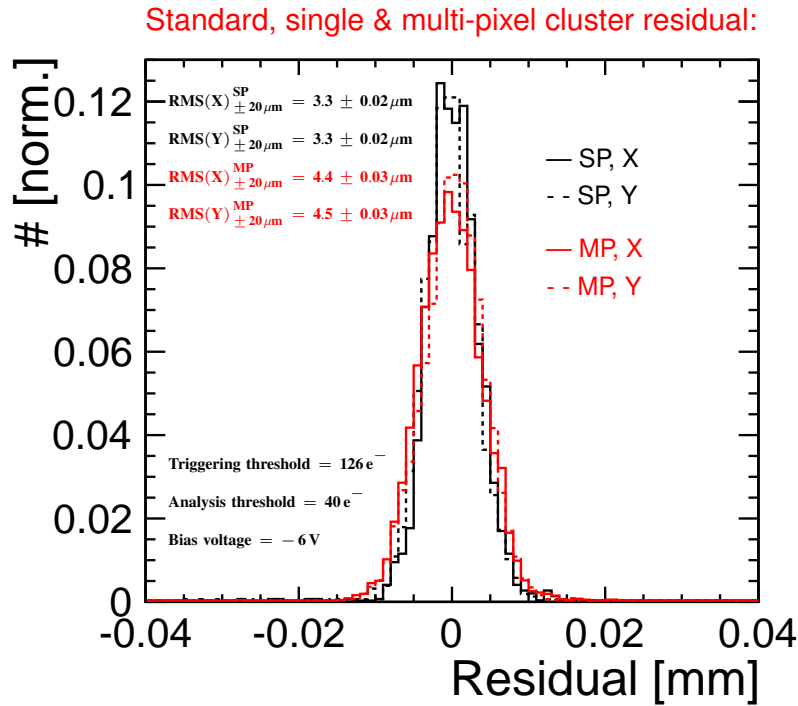


Figure 10.5: Separately normalised residual distributions for *single-pixel* (SP) and *multi-pixel* (MP) cluster for the standard process.

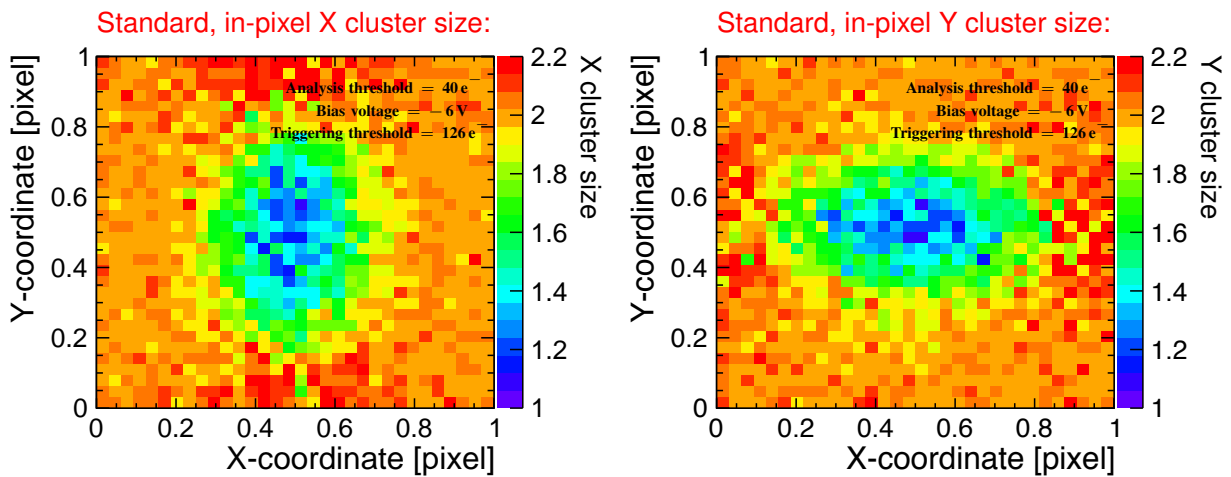


Figure 10.6: In-pixel representation of the cluster size in *X* (left) and *Y* (right) for the standard process.

diffusion in the pixel edges: from geometrical considerations the X cluster size is expected to be reduced closer to the X pixel centre. However, close to the Y edges of the pixels, the non-depleted regions of the pixels are passed by the track and the charge sharing is enhanced by diffusion, such that both neighbouring pixels in X collect a charge above threshold (the same argument holds vice versa for the Y

cluster size)<sup>2</sup>. Accordingly, the contribution of charge sharing from the non-depleted regions (diffusion) results in a dependence of the X and Y cluster size on the other dimension of the pixel cell, which is in the following referred to as *charge sharing from diffusion*.

The reconstruction of the Investigator hit position for multi-pixel clusters is performed by charge interpolation separately for the X and Y dimension. Therefore, the correlation of the charge sharing in X with the Y dimension (and vice versa) is not taken into account by the position reconstruction. In particular, the  $\eta$  correction is calculated using the assumption that the cluster size in X does not change over the Y coordinate of the pixel (and vice versa).

Following the discussion above, the precision with which the Investigator hit position can be reconstructed for multi-pixel clusters degrades due to the discussed charge sharing from diffusion. This argument explains the degradation of the multi-pixel cluster resolution with respect to the single-pixel cluster resolution.

The discussed impact of the diffusion component on the spatial resolution shows two different aspects:

- More charge sharing does not necessarily improve the spatial resolution. If the charge sharing improves or degrades the spatial resolution depends on the exact charge sharing behaviour and reconstruction algorithm.
- The multi-pixel cluster resolution is not necessarily improved with respect to the single-pixel cluster resolution. This depends on the cluster size distribution within the pixel cell (i.e. the area of the pixel where single and multi-pixel clusters are generated) and the reconstruction algorithm (i.e. if the reconstruction can use the additional information of the multi-pixel clusters to improve the reconstructed position).

The diffusion component can be suppressed by a higher analysis threshold. This is further investigated in Section 10.2.1. To gain from the charge sharing from diffusion at very low threshold values, multi-variate reconstruction techniques are interesting candidates to take into account the correlation of the reconstructed position in X and Y on the other dimension within the pixel cell. This study is however beyond the scope of this thesis. It should be noted that already the used  $\eta$  reconstruction algorithm results in a single point resolution of  $\lesssim 4 \mu\text{m}$  for the standard process, matching well the requirement of a single point resolution of  $7 \mu\text{m}$  for the CLIC tracker.

**Single and multi-pixel cluster residuals for the modified process** Figure 10.7 displays the spatial residual distributions in X and Y direction separately for single and multi-pixel clusters for the modified process. As for the standard process, the resolution for single-pixel clusters is with a value of  $\lesssim 6.5$  improved with respect to the value of  $\text{pitch}/\sqrt{12} \sim 8 \mu\text{m}$ , due to charge sharing shrinking the area in the pixel where single-pixel clusters are generated. However, the effect is less significant compared to the standard process due to less charge sharing for the modified compared to the standard process. This can be observed in the in-pixel representation of the cluster size in X and Y direction in Figure 10.8.

A larger cluster size in X and Y can be observed for track intercept positions close to the respective pixel edges. A cluster size close to one in X and Y direction is observed only in the region close to the respective pixel centre. The charge sharing in X and Y is almost not dependent on the other coordinate. This results in a good performance of the reconstruction and a gain from charge interpolation, that improves the multi-pixel cluster resolution with respect to the single-pixel cluster resolution, as well as with respect to the multi-pixel cluster resolution for the standard process, to a value of  $\lesssim 3.5$ .

<sup>2</sup> A more detailed explanation about the charge sharing from diffusion can be found in the Appendix B.

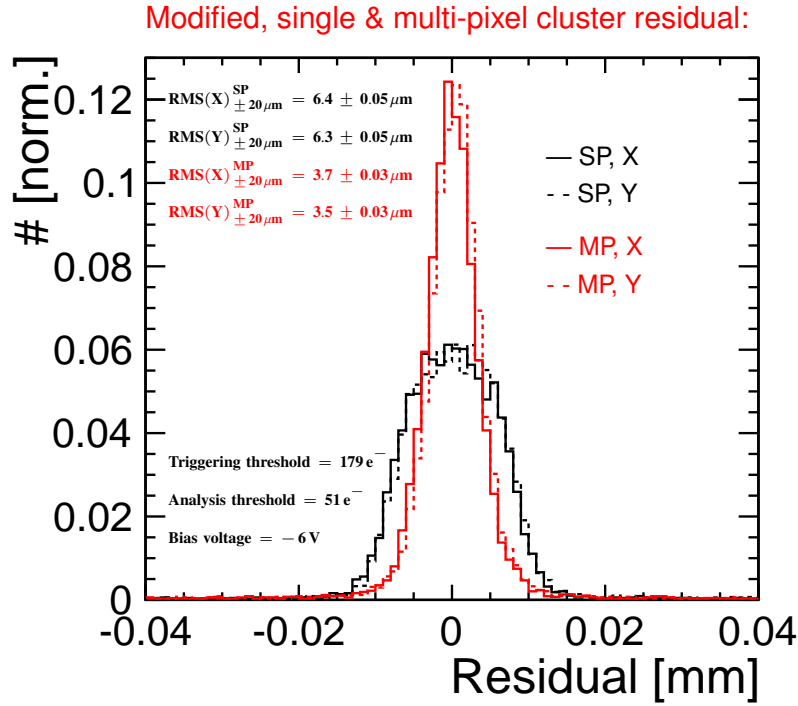


Figure 10.7: Separately normalised residual distributions for *single-pixel (SP)* and *multi-pixel (MP)* cluster for the modified process.

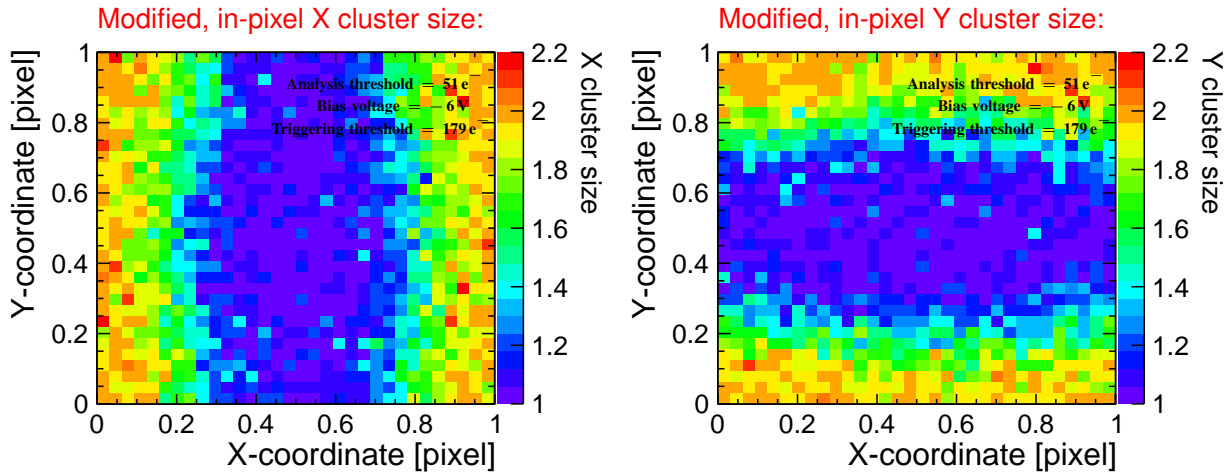


Figure 10.8: In-pixel representation of the cluster size in *X (left)* and *Y (right)* for the *modified process*.

### 10.1.2 Timing

The timing residual, as defined in Section 6.5.1, is presented in Figure 10.9. A Gaussian fit is performed to the timing residual distributions on a range of  $\pm 50 \mu\text{m}$ . The timing resolution is defined as the width of the Gaussian, giving a similar value for the standard and modified process of  $\sim 6 \text{ ns}$ . The telescope timing resolution of  $\lesssim 1 \text{ ns}$  is not unfolded from the quoted values. The fact that a similar timing

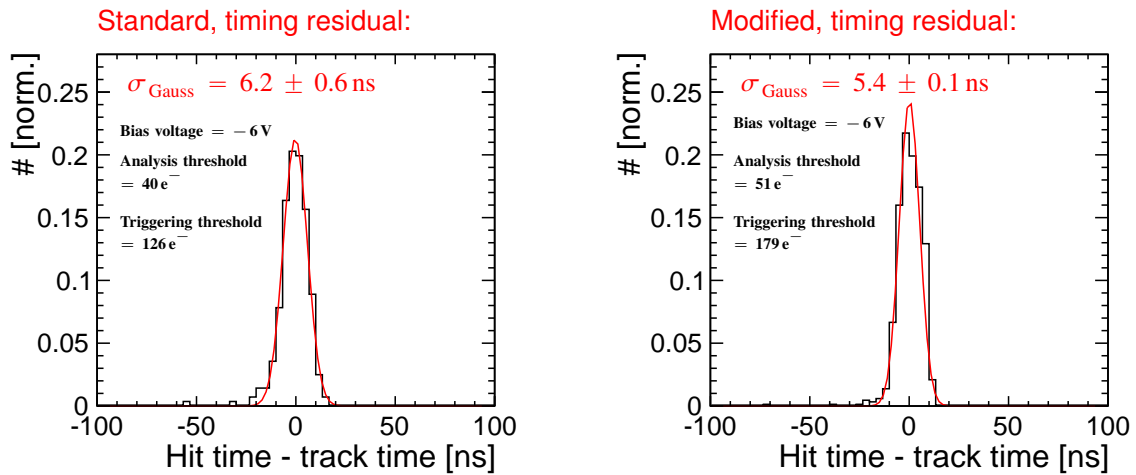


Figure 10.9: Timing residual distribution for the *standard process* (left) and the *modified process* (right). The uncertainties are defined as the uncertainty on the width of the Gaussian fit.

resolution has been measured for both processes which is larger than the value expected from the TCAD simulations in the order of  $\sim 1 \text{ ns}$  (see e.g. timing variations between centre and edge incident in Figure 8.19) can be explained by the limited precision of the readout, mainly given by the sampling frequency of 65 MHz of the external ADCs.

To understand the time dependence of the charge collection behaviour, the distribution of the time the signal needs to rise from 10 – 90 % of its amplitude ( $T_{10-90}$  time) is shown in Figure 10.10 for the modified and standard process. For the modified process the  $T_{10-90}$  time shows a peak at a value

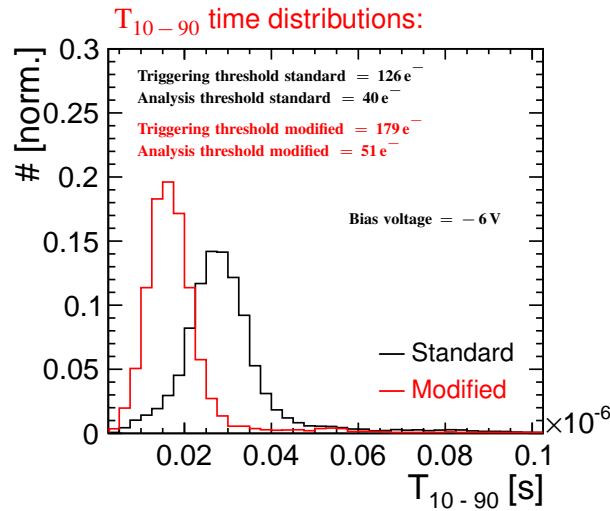


Figure 10.10:  $T_{10-90}$  time distribution for the *standard process* (black) and the *modified process* (red).

of  $\lesssim 20 \text{ ns}$ . For the standard process the  $T_{10-90}$  time peaks at later values of  $\lesssim 30 \text{ ns}$  and shows a broader distribution compared to the modified process. Both values are well above the expected  $T_{10-90}$  time contribution of  $\sim 10 \text{ ns}$  from the output buffers and thus not limited by it. Despite not limiting the measured  $T_{10-90}$  time, the output buffer can still significantly contribute to it. This makes a

quantitative comparison between the measured  $T_{10-90}$  time and the results of the TCAD simulations difficult. Nevertheless, the trends observed in the measured  $T_{10-90}$  time can be compared on a qualitative level to the trends observed in the simulated charge versus integration time presented in Figure 8.20:

- The slower measured  $T_{10-90}$  time for the standard compared to the modified process is compatible with the slower simulated rise of the charge that can be observed for the standard compared to the modified process.
- The broader distribution of the  $T_{10-90}$  time for the standard process compared to the modified process is in line with larger timing variations between the simulated response for a particle incident at the pixel centre and pixel edge, that has been observed for the standard compared to the modified process.

### 10.1.3 Signal and efficiency

The cluster signal is presented in Figure 10.11. For both processes the MPV of the cluster signal

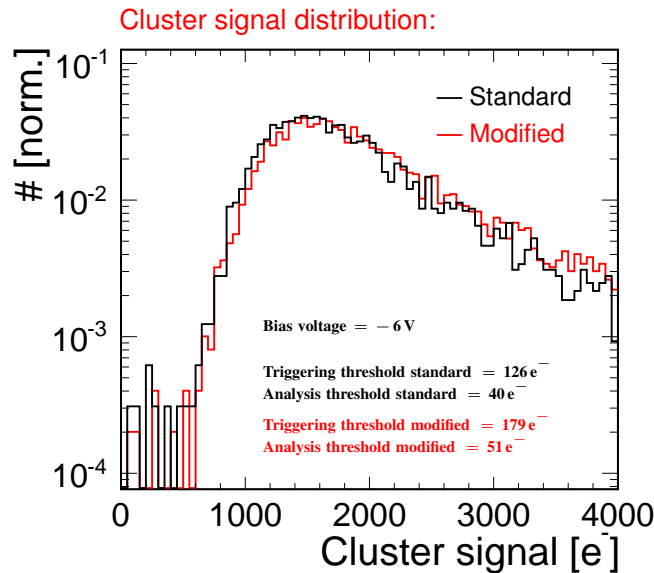


Figure 10.11: Cluster signal distribution for the *standard process* (black) and the *modified process* (red).

distribution is at  $\sim 1600 e^-$ . The cluster signal for the standard process being similar to the cluster signal from the modified process indicates that charges created in the non-depleted region between the pixels of the standard process are fully collected. This is consistent with the TCAD simulation, showing that the overall charge collected after  $1 \mu s$  in the pixel edge of the standard process is the same as the charge collected after  $1 \mu s$  at the pixel edge for the modified process (see magenta lines in Figure 8.20). Thus, because of the duration of the active readout window of  $\sim 16 \mu s$ , no charge loss is expected in the non-depleted regions of the standard process.

The distribution of the seed signal is presented in Figure 10.12. As expected from the enhanced charge sharing, a lower seed signal has been measured for the standard process. To study the effect of charge sharing on the seed signal in more detail, the mean seed signal is shown in an in-pixel representation in Figure 10.13. The more charge is shared between the pixels (see Figure 10.2), the lower the mean seed

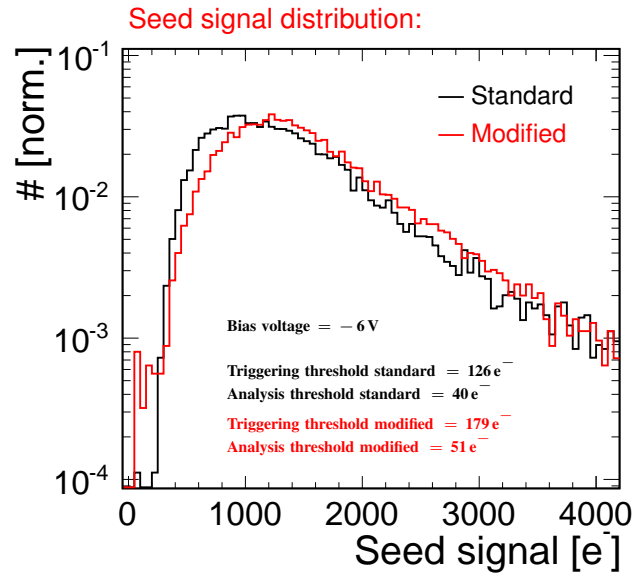


Figure 10.12: Seed signal distribution for the *standard process* (black) and the *modified process* (red).

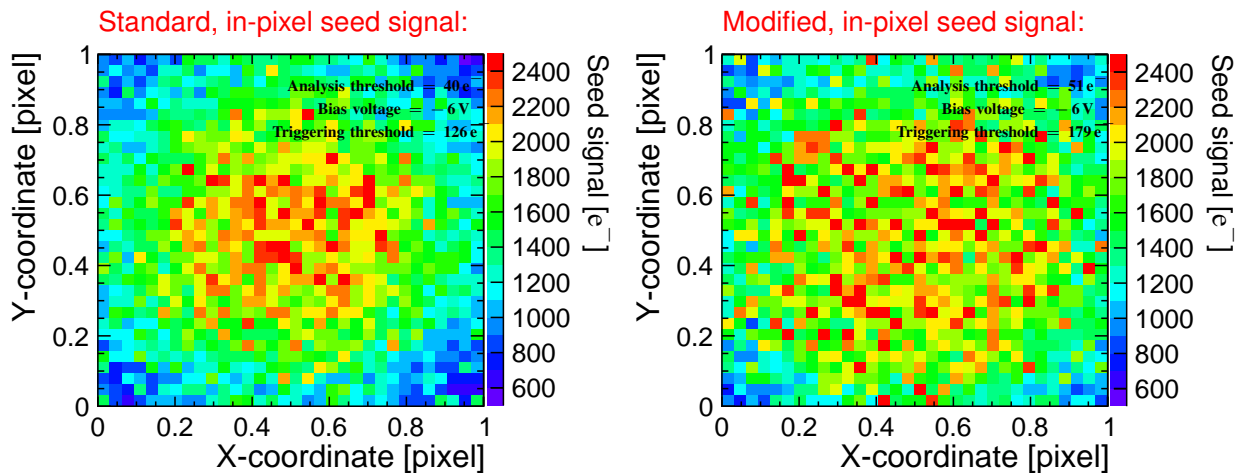


Figure 10.13: In-pixel representation of the mean seed signal for the *standard process* (left) and the *modified process* (right).

signal. Accordingly, the higher charge sharing for the standard process results in a larger drop of the seed signal towards the pixel edges and corners.

The lower seed signal in the pixel corners can result in a lower efficiency if the seed signal drops below the triggering threshold during data taking. To investigate this, the detection efficiency within the pixel cell is studied. The in-pixel representation of the detection efficiency is shown in Figure 10.14, showing some statistical fluctuations homogeneously distributed over the pixel cell. The homogenous and high efficiency within the pixel cell shows that the charge sharing does not affect the particle detection capability of the studied Investigator mini matrix.

In Figure 10.15, the efficiency across the region of interest is presented in the Investigator reference

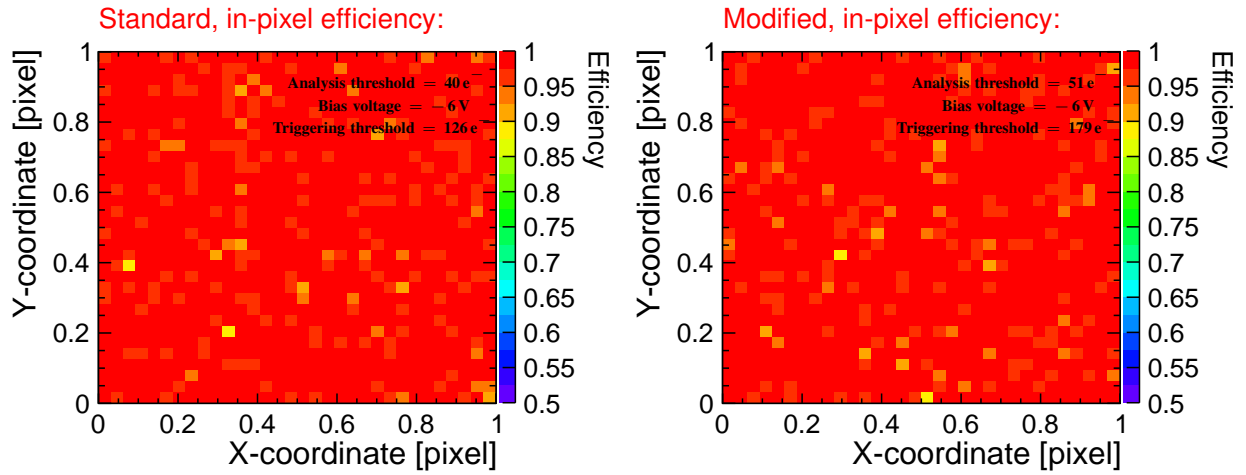


Figure 10.14: In-pixel representation of the efficiency for the *standard process* (left) and the *modified process* (right).

frame, for the modified and standard process. The size of each pixel of  $(28 \times 28) \mu\text{m}^2$  is indicated by

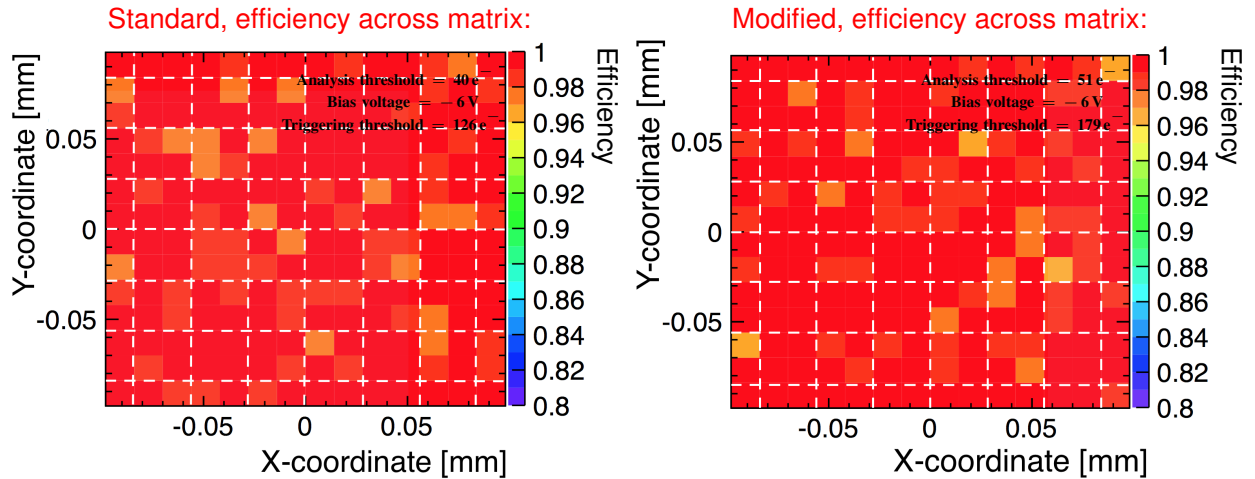


Figure 10.15: Efficiency over the region of interest for the *standard process* (left) and the *modified process* (right).

the squares surrounded by the white dashed grid. A uniform and high efficiency across the pixel matrix is visible. An efficiency of  $(99.2 \pm 0.1(\text{stat.}))\%$  has been measured for both processes. As described in Chapter 6.3, the efficiency is calculated considering only tracks with hits on at least five of the six telescope planes and a  $\chi^2/\text{ndof} < 10$ .

The statistical uncertainty has been calculated as the uncertainty on the mean value for a counting experiment with two possible outcomes: an efficiency entry of 1 if the track is matched to an Investigator hit, or an efficiency entry of 0 if the track is not matched to an Investigator hit. This results in an uncertainty of  $\sigma_{\text{stat.}} = \sqrt{p \cdot (100 - p)/N} [\%]$ , with the number of experiments  $N$  and the probability  $p$  for a positive outcome of the experiment in percent. The number of experiments corresponds to the number of region of interest tracks (# roi-tracks) listed in Table 10.2. The best guess for the probability  $p$  of a positive outcome is the measured average efficiency.

### 10.1.4 Summary

The cluster size and spatial resolution have been compared for the standard and modified process. For the standard process a spatial resolution of  $\lesssim 4 \mu\text{m}$  and for the modified process a spatial resolution of  $\lesssim 5 \mu\text{m}$  have been measured<sup>3</sup>. Significantly more charge sharing has been observed for the standard compared to the modified process, that can be explained by the non-depleted regions at the pixel edges for the standard process. In-pixel studies show that the charge sharing from diffusion results in a correlation of the X and Y cluster size on the other dimension of the pixel cell. This degrades the position reconstruction that is performed separately for the X and Y dimension, showing the effect that larger cluster sizes do not correspond to a better spatial resolution for the used  $\eta$  reconstruction algorithm.

The timing resolution of the standard and modified process have been measured, giving for both processes a result of  $\sim 6 \text{ ns}$ <sup>4</sup>. The measured timing resolution is limited by the external readout, and its 65 MHz sampling frequency. The  $T_{10-90}$  time, defined as the time in which the signal reaches from 10 – 90 %, has been presented. A larger  $T_{10-90}$  time and a broader distribution has been measured for the standard compared to the modified process, consistent with the lower electric field and the larger variations over the lateral pixel size observed in the TCAD simulations of the standard compared to the modified process.

A comparison of the calibrated cluster signal charge distribution for the standard and modified process shows no significant difference. This indicates that for the used setup with long integration times (active window of  $\sim 16 \mu\text{s}$ , see Chapter 5.4) the charge that is created in the non-depleted regions of the epi layer of the standard process is fully collected. The calibrated seed signal distribution shows a peak at lower values for the standard process, consistent with the enhanced charge sharing compared to the modified process.

The efficiency has been presented within the pixel cell as well over the pixel matrix. A high and homogenous efficiency has been measured over the full pixel cell and pixel matrix. An efficiency of  $(99.2 \pm 0.1 \text{ (stat.)})\%$  has been measured for both processes. The deviation from 100 % can not be explained by the stated statistical uncertainties. A possible origin of this can be a fluctuation of the baseline during data taking. The fact that these inefficiencies are homogeneously distributed over the pixel cell shows that it is not attributed to a cut of the threshold into the low energy tail of the seed signal distributions. This indicates for both processes a sufficiently high ratio of signal to noise to operate the chip fully efficient. Note, that this statement is made for the used active window of  $\sim 16 \mu\text{s}$ . Integration times in the order of magnitude of the  $T_{10-90}$  time presented in Figure 10.10, could result in a reduction of the seed signal and thus a loss of efficiency. However, taking into account the triggering threshold of  $\sim 200 e^-$  and comparing it to the simulations in Figure 8.20, one can see that for the slowest case of a particle incident at the pixel edge of the standard process the charge crosses a value of  $\sim 200 e^-$  after  $\sim 2 \text{ ns}$ .

## 10.2 Scan of parameters and operation conditions

In a next step different operation conditions and parameters are scanned to investigate their impact on the measured results.

---

<sup>3</sup> The spatial telescope resolution of  $\sim 2 \mu\text{m}$  has not been unfolded from these values.

<sup>4</sup> The telescope timing resolution of  $\sim 1 \text{ ns}$  has not been unfolded from these values.

### 10.2.1 Threshold scan

The dependency of the results on the analysis threshold is studied for the parameters of the Investigator pixel layout defined in Table 10.1 and the operation conditions and analysed statistics summarised in Table 10.2. In the following, the analysis threshold is varied and the values of the triggering thresholds are indicated by vertical lines in the plots of the presented results.

To study the impact of the analysis threshold on the charge sharing behaviour, the mean total cluster size is presented at different analysis thresholds for the standard and modified process in Figure 10.16.

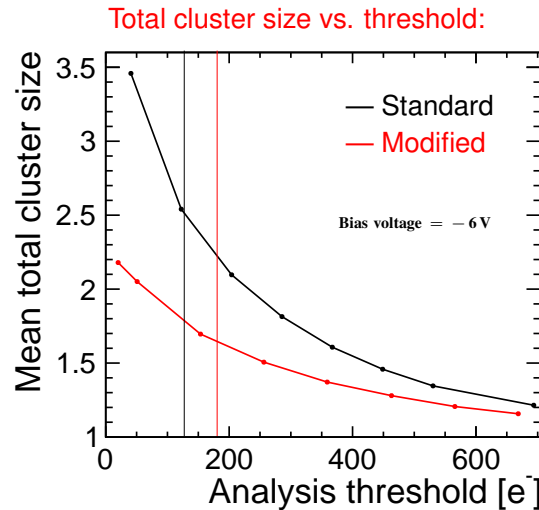


Figure 10.16: Mean total cluster size for different analysis thresholds. The error bars correspond to the uncertainty on the mean value and the thin vertical lines mark the triggering thresholds.

Generally, two different effects are observable:

- For higher analysis thresholds the cluster size is reduced, since the signal of neighbouring pixels falls below the analysis threshold and the cluster size of both processes converges to a value of one.
- At lower threshold values, where the signals in the neighbouring pixels are detected, the cluster size is significantly different for the two processes, as expected from the different electric fields in the sensor observed in the results of the TCAD simulations (compare Figure and 8.4 and 8.10).

The decrease of the cluster size with lower analysis threshold is significantly steeper for the standard process compared to the modified process: for the modified process a cluster size of two can be only achieved if the analysis threshold is pushed to low values of  $\sim 50 e^-$ . For the standard process a cluster size of two can be even reached with a four times higher analysis threshold of  $\sim 200 e^-$ .

The in-pixel representation of the total cluster size is presented at similar threshold values in Figure 10.17 for both processes. For low threshold values (left plots of Figure 10.17) the significantly higher charge sharing for the standard process compared to the modified process is visible by the higher cluster sizes in the pixel corners and the reduced area of single-pixel clusters in the pixel centre. For higher thresholds (right plots of Figure 10.17) the probability that the signals of neighbouring pixels are not detected decreases and the difference of the charge sharing in the pixel cell between the standard process and the modified process is less significant.

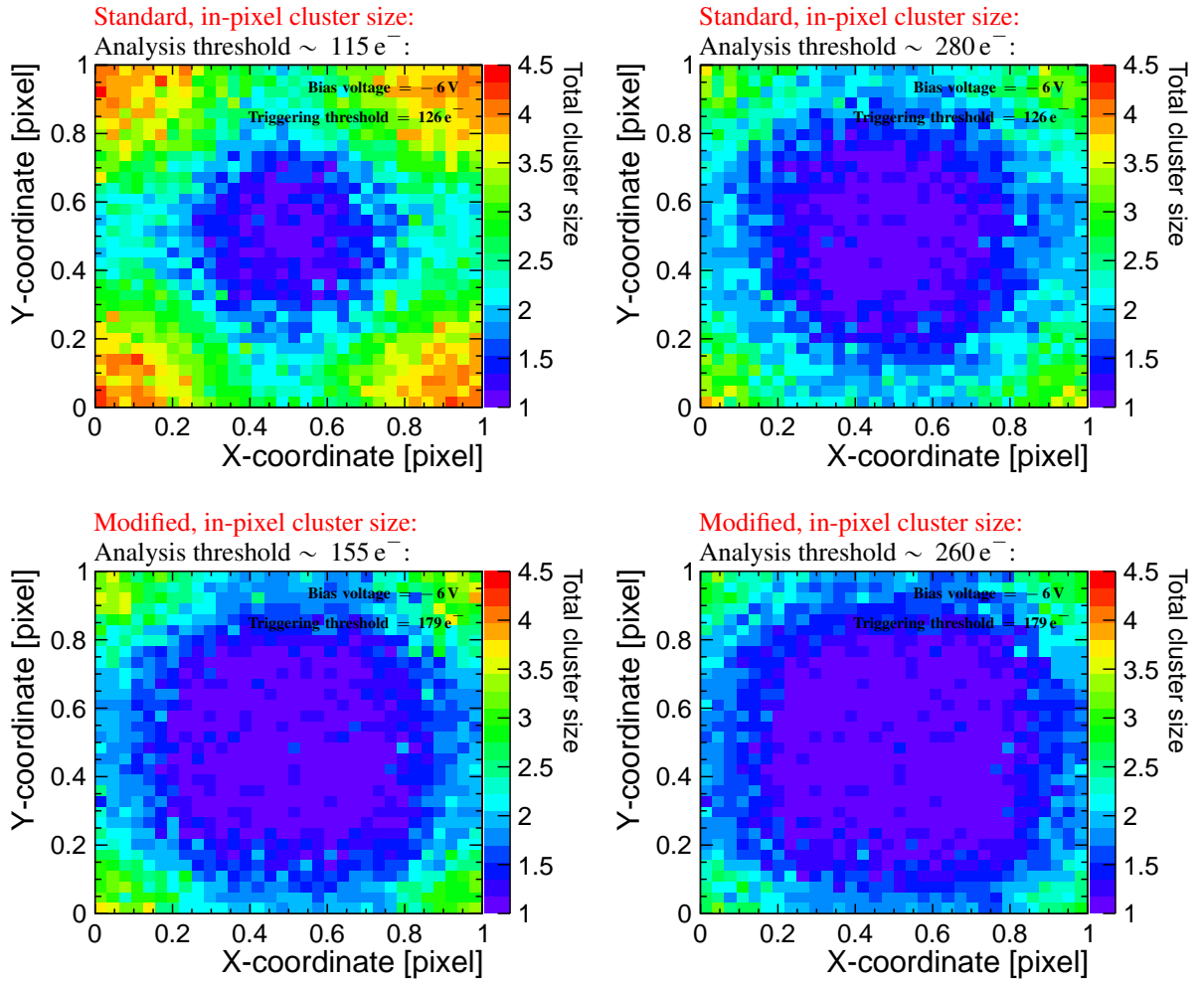


Figure 10.17: In-pixel representation of the total cluster size at different analysis thresholds for the *standard process* (up) and the *modified process* (down).

The mean cluster size in the X and Y direction is presented as a function of the analysis threshold in Figure 10.18. The same trends as for the total cluster size are visible.

The decrease of charge sharing at higher analysis thresholds as well as the significantly higher charge sharing for the standard process at low threshold values has an impact on the spatial resolution. This can be observed in Figure 10.19, where the resolution is presented separately in X and Y direction for the modified and the standard process.

For different analysis thresholds single and multi-pixel clusters are expected to give different contributions to the overall spatial resolution. To show this, the single and multi-pixel cluster residuals are compared separately in X and Y for analysis thresholds higher than the nominal one (see Figure 10.20). With higher analysis thresholds the single-pixel cluster residuals get broader, since the area within the pixel, where single-pixel clusters are generated, expands (see Figure 10.21). The in-pixel representation of the Y cluster size for standard process also shows that the contribution of charge sharing from diffusion is suppressed with higher thresholds of  $\gtrsim 115 e^-$ . As a consequence, the in-pixel cluster size in X and Y does not depend on the other dimension within the pixel cell, leading to an optimal resolution down to  $\lesssim 3.7 \mu\text{m}$  at an analysis threshold of  $\sim 115 e^-$  (see Figure 10.19).

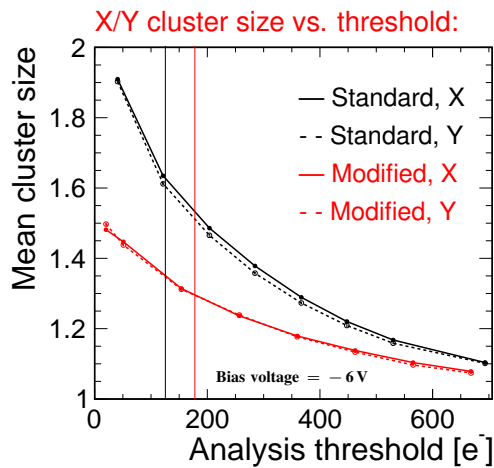


Figure 10.18: Mean X and Y cluster size for different analysis thresholds. The error bars correspond to the uncertainty on the mean value and the thin vertical lines mark the triggering thresholds.

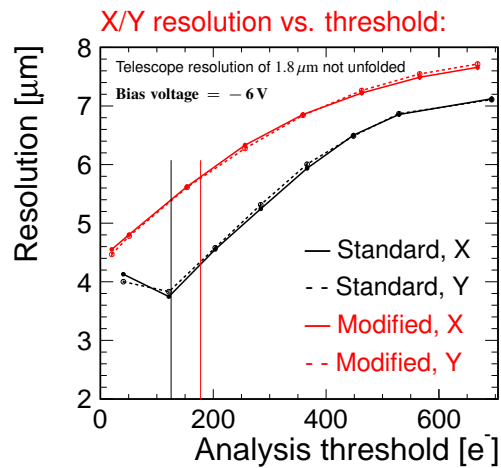


Figure 10.19: Resolution in X and Y direction for different analysis thresholds. The error bars correspond to the uncertainty on the RMS and the thin vertical lines mark the triggering thresholds.

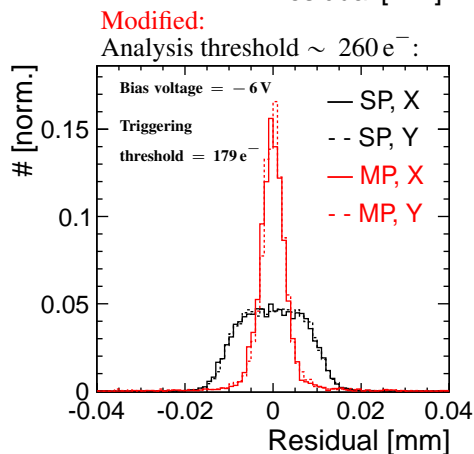
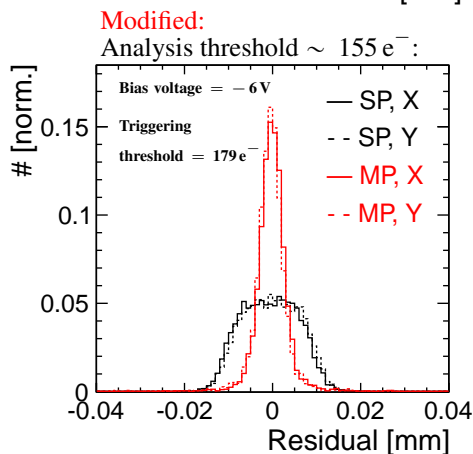
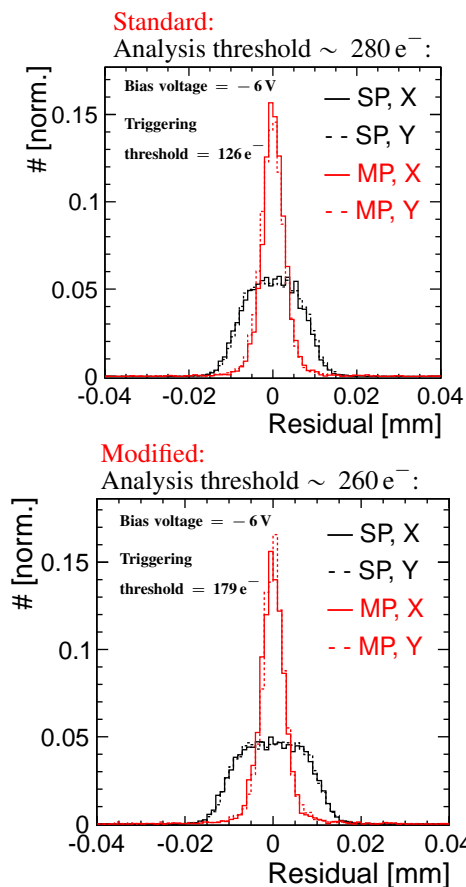
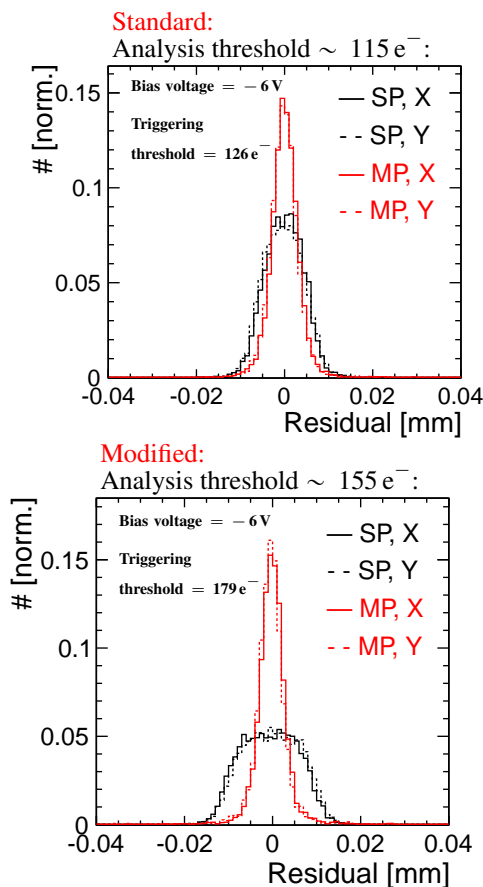


Figure 10.20: Separately normalised residual distributions for *single-pixel* (SP) and *multi-pixel* (MP) cluster for the *standard process* (up) and the *modified process* (down).

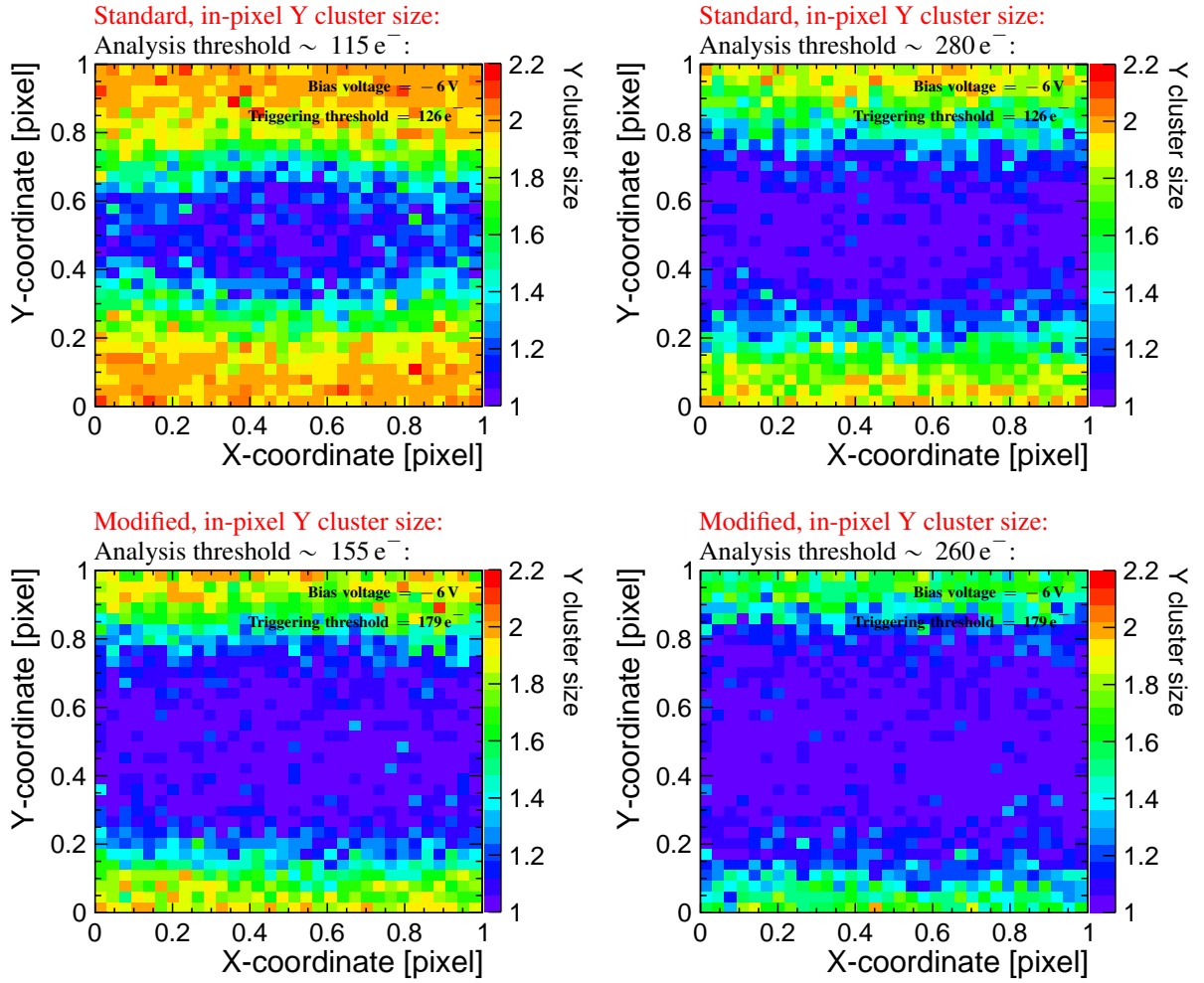


Figure 10.21: In-pixel representation of the Y cluster size at different analysis thresholds for the *standard process* (up) and the *modified process* (down).

Since the effect of charge sharing from diffusion has not been observed for the modified process, the optimal resolution for the modified process of  $\lesssim 4.5 \mu\text{m}$  has been measured at the lowest analysed threshold value of  $\sim 20 e^-$ . This low threshold can be reached for the modified process, without observing a degradation of the spatial resolution by noise contributions, since the signal, as defined in the analysis is relatively robust against sample by sample noise fluctuations (see discussion in Chapter 6.1.1).

Figure 10.19 also shows that the resolution does not converge to a value of  $\text{pitch}/\sqrt{12} \sim 8 \mu\text{m}$  (note that in Figure 10.19 the telescope resolution is not unfolded). Two different effects contribute to this: first, even for high analysis thresholds charge sharing can be observed. Especially for the standard process a significant fraction of multi-pixel clusters is visible at high analysis thresholds, explaining that the discrepancy to the value of  $\text{pitch}/\sqrt{12} \sim 8 \mu\text{m}$  is larger for the standard compared to the modified process. Moreover, the analysis threshold starts to cut into the seed signal at high analysis thresholds. Since the seed signal drops towards the pixel edges and corners due to charge sharing, tracks passing through these regions of the pixel cell are not detected, resulting in a shrinking of the area towards the pixel centre where the clusters are generated and thus an improved single-pixel resolution (see Figure 10.22).

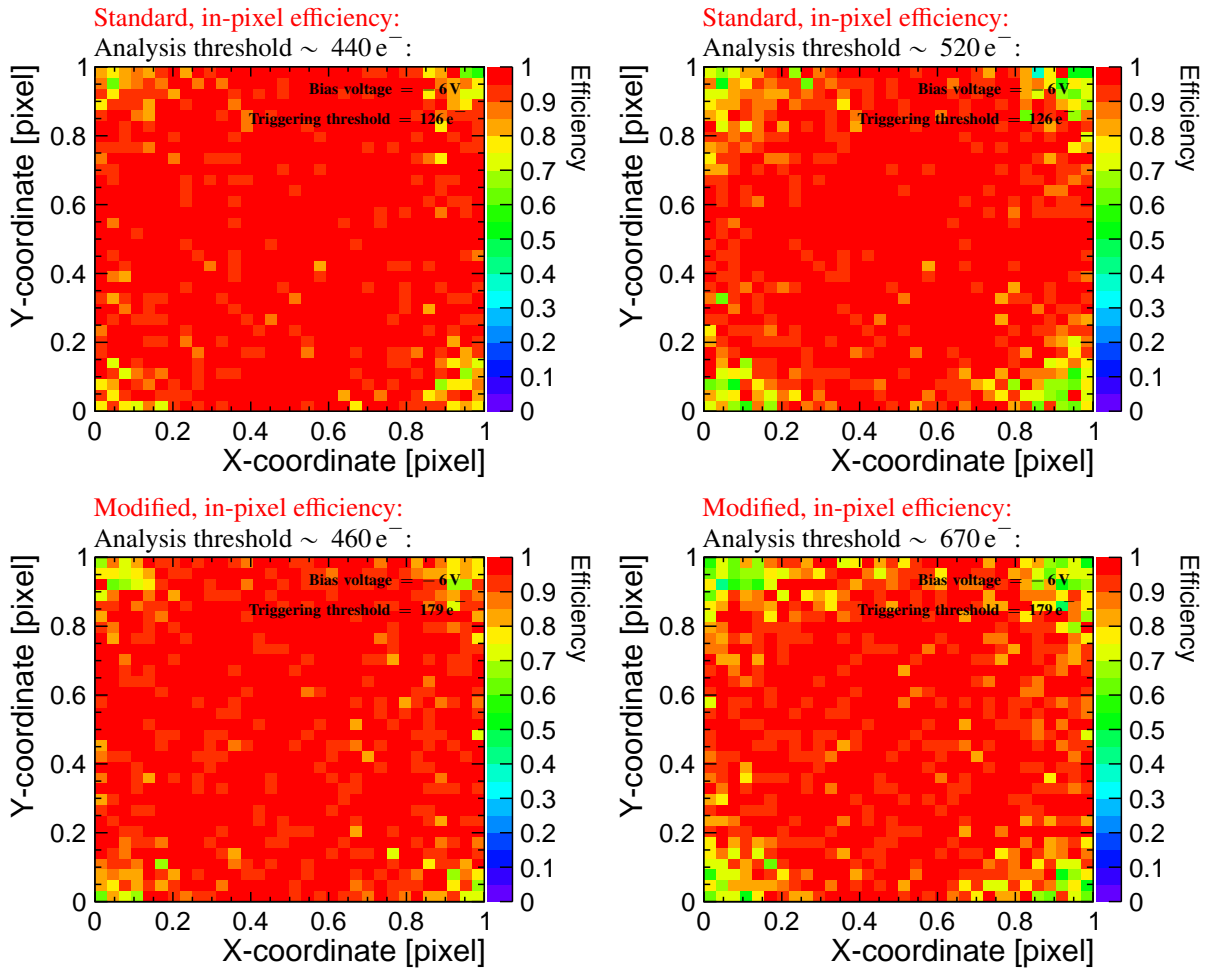


Figure 10.22: In-pixel representation of the efficiency at different high analysis thresholds for the *standard process* (up) and the *modified process* (down).

The above discussed effect of charge sharing on the efficiency at higher threshold is as well visible in the efficiency for different analysis thresholds presented in Figure 10.23: a drop of the efficiency at earlier threshold values has been measured for the standard compared to the modified process, consistent with the enhanced charge sharing and resulting lower seed signal for the standard process.

To study if the applied analysis threshold affects the precision with which the time of a hit can be resolved, the timing resolution is presented as a function of the analysis threshold in Figure 10.24. For high threshold values the timing resolution improves slightly (by  $\sim 10\%$ ) and converges for both processes to a value of  $\sim 5$  ns for very high threshold values. However, taking into account the uncertainties of the measured timing resolution the difference is not very significant. This is consistent with the fact that the measured timing resolution is limited by the sampling frequency of the external ADCs.

### 10.2.2 Comparison of different bias voltages for the standard and modified process

The dependency of the results on different bias voltages (also referred to as  $V_{bias}$ ) is studied for the standard and modified process for the parameters of the Investigator pixel layout defined in Table 10.1. The operation conditions and analysed statistics are summarised in Table 10.3.

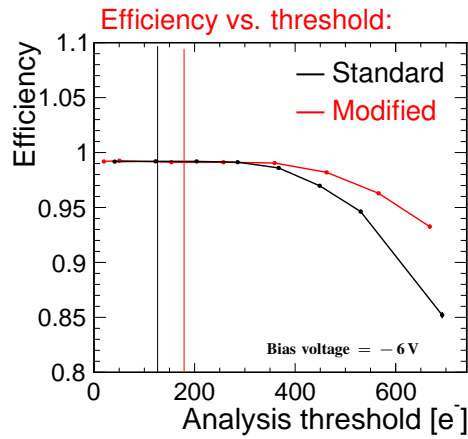


Figure 10.23: Efficiency versus analysis threshold. The error bars correspond to the statistical uncertainties. The thin lines mark the triggering thresholds.

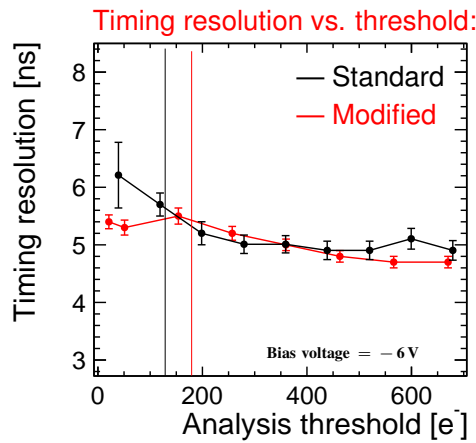


Figure 10.24: Timing resolution versus analysis threshold. The error bars correspond to the uncertainties on the width of the Gaussian fit. The thin vertical lines mark the triggering thresholds.

Table 10.3: Definition of operation conditions and analysed statistics for different bias voltages.

Process	Voltage [V]	Triggering threshold [e <sup>-</sup> ]	# roi-tracks
Standard	-6	126	25660
Standard	0	199	27495
Modified	-6	179	24260
Modified	-3	239	7986
Modified	0	425	6459

### Standard process

For the standard process bias voltages of  $-6$  V and  $0$  V have been compared.

The cluster and seed signal distributions at an analysis threshold of  $\sim 100$  e<sup>-</sup> are presented for both

voltages in Figure 10.25. The cluster signal at a bias voltage of 0 V is  $\sim 35\%$  lower compared to a bias

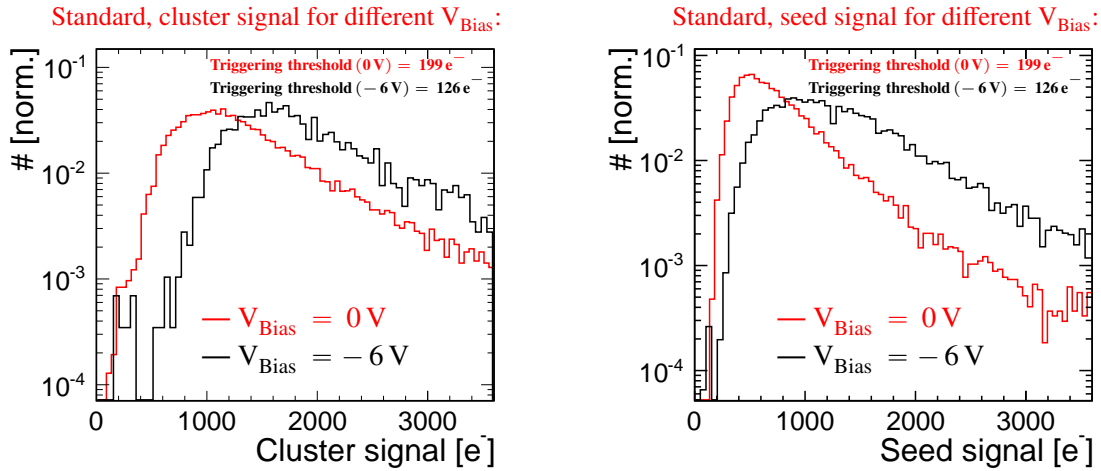


Figure 10.25: Cluster signal (left) and seed signal (right) for different bias voltages at an analysis threshold of  $\sim 100 e^-$  for the standard process.

voltage of  $-6 \text{ V}$ . In the results of the TCAD simulations in Figure 8.1 significantly larger non-depleted regions are visible for a bias voltage of 0 V compared to a bias voltage of  $-6 \text{ V}$ . The resulting enhanced diffusion component for a bias voltage of 0 V compared to a bias voltage of  $-6 \text{ V}$  is expected spread the charge over more pixels. Thus, more charge can be lost in the neighbouring pixels at the analysis threshold of  $\sim 100 e^-$  for a bias voltage of 0 V compared to a bias voltage of  $-6 \text{ V}$ . In addition, a loss of charge due to recombination in the increased non-depleted regions for a bias voltage of 0 V compared to a bias voltage of  $-6 \text{ V}$  can explain the observed charge loss for a bias voltage of 0 V.

The discussed trends are also reflected in the seed signal shown in the right plot of Figure 10.25. However, the seed signal is more than 35 % lower for a bias voltage of 0 V compared to a bias voltage of  $-6 \text{ V}$ . This can be attributed to the higher charge sharing for a bias voltage of 0 V compared to a bias voltage of  $-6 \text{ V}$  that further reduces the seed signal for a bias voltage of 0 V. In Figure 10.29 the total cluster size is shown at an analysis threshold of  $\sim 100 e^-$  for both voltages, showing significantly more charge sharing for a bias voltage 0 V compared to a bias voltage of  $-6 \text{ V}$ .

For a bias voltage of 0 V, where the charge propagation is dominated by diffusion, the charge carriers are expected to propagate for a longer time until they reach the pixel implant. This impacts the  $T_{10-90}$  time of the signal, as presented in Figure 10.27. For a bias voltage of 0 V the  $T_{10-90}$  time shows a peak at  $\sim 65 \text{ ns}$ , more than two times later compared to a bias voltage of  $-6 \text{ V}$ , where the  $T_{10-90}$  time shows a peak at  $\sim 30 \text{ ns}$ . Moreover, the  $T_{10-90}$  time distribution for a bias voltage of 0 V is much broader compared to the  $T_{10-90}$  time distribution for a bias voltage of  $-6 \text{ V}$ . This is consistent with the larger variations of the electric field over the lateral pixel size shown in the TCAD simulations of the standard process for a bias voltage of 0 V compared to a bias voltage of  $-6 \text{ V}$  (see Figure 8.4).

The different bias voltages also impact the precision with which the hit time can be determined, as presented in Figure 10.28, where the timing residual distributions are presented for different bias voltages: for a bias voltage of 0 V the timing residual distribution is significantly broader with respect to a bias voltage of  $-6 \text{ V}$ , resulting in a degradation of the timing resolution. This is compatible with the lower seed signal (see Figure 10.25) and the higher noise (see Figure 9.8) measured for a bias voltage of 0 V compared to a bias voltage of  $-6 \text{ V}$ , degrading the signal to noise ratio.

In a next step the performance in terms of cluster size, spatial resolution and efficiency is evaluated for

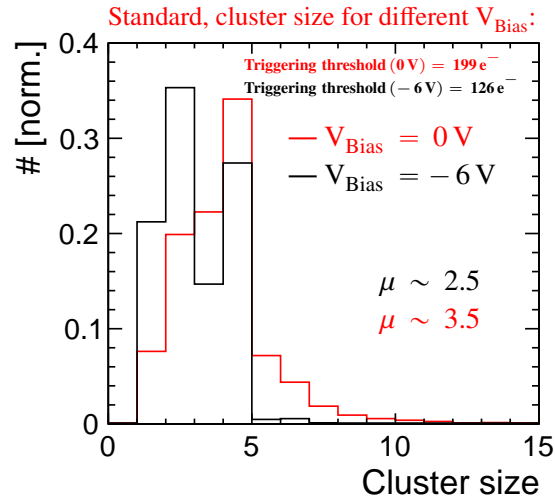


Figure 10.26: Total cluster size for different bias voltages at an analysis threshold of  $\sim 100 e^-$  for the standard process.

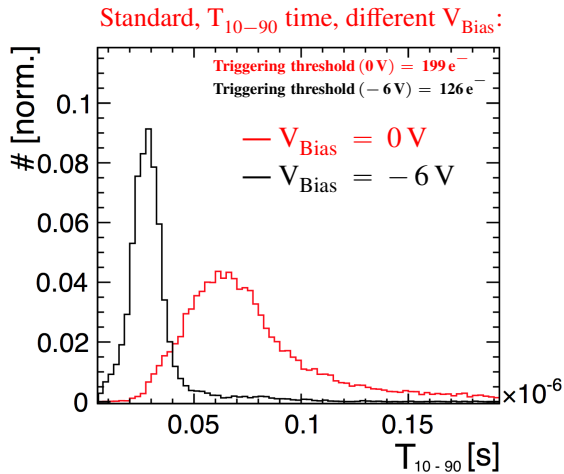


Figure 10.27:  $T_{10-90}$  time for different bias voltages at an analysis threshold of  $\sim 100 e^-$  for the standard process.

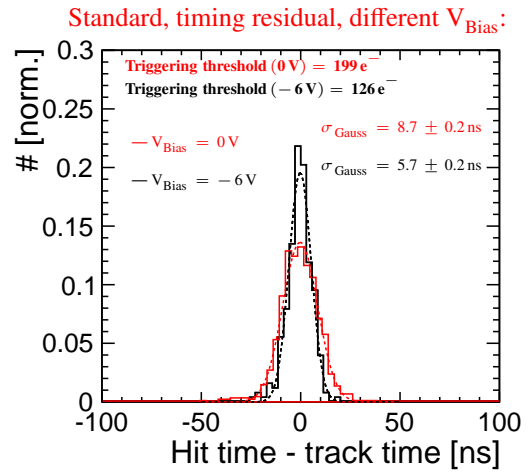


Figure 10.28: Timing residual for different bias voltages at an analysis threshold of  $\sim 100 e^-$  for the standard process.

the different bias voltages as a function of the analysis threshold. The cluster size and resolution in X and Y are shown for the different bias voltages depending on the analysis threshold in Figure 10.29 and 10.30, respectively. The efficiency versus analysis threshold is presented for the different bias voltages in Figure 10.31.

For the interplay of the cluster size, the spatial resolution and the efficiency different regions can be identified in dependence of the analysis threshold:

**Low threshold region - analysis threshold  $\lesssim 250 e^-$**  The higher cluster size measured for a bias voltage of 0 V compared to a bias voltage of  $-6 \text{ V}$  can be explained by the different depleted regions and electric fields in the sensor for the different bias voltages.

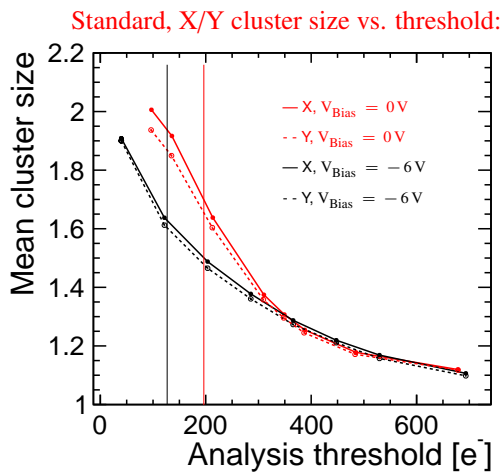


Figure 10.29: Mean cluster size in X and Y for different bias voltages versus analysis threshold for the standard process. The error bars correspond to the uncertainty on the mean value. The thin vertical lines mark the triggering thresholds.

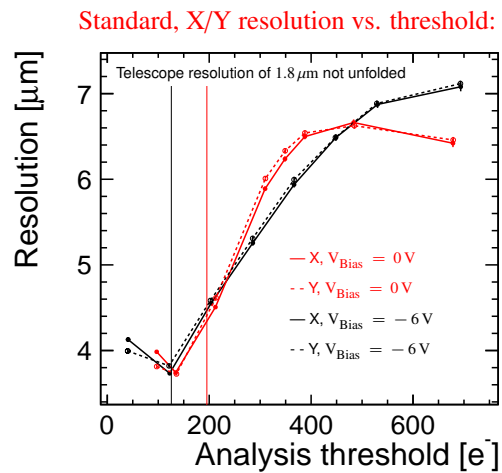


Figure 10.30: X and Y resolution for different bias voltages versus analysis threshold for the standard process. The error bars correspond to the uncertainty on the RMS of the residual distributions. The thin vertical lines mark the triggering thresholds.

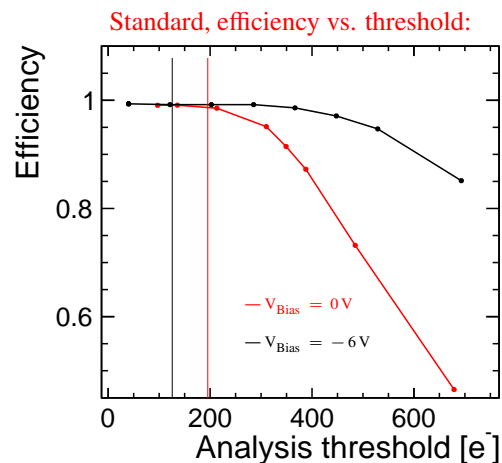


Figure 10.31: Efficiency for different bias voltages at different analysis thresholds for the standard process. The error bars correspond to the statistical uncertainties. The thin vertical lines mark the triggering thresholds.

Despite the increased cluster size, the spatial resolution for a bias voltage of 0 V is similar to the spatial resolution measured for a bias voltage of  $-6$  V. This might be explained by the fact that the charge sharing from diffusion does not improve the spatial resolution. In Figure 10.32, the in-pixel representation of the Y cluster size is presented for a bias voltage of 0 V and  $-6$  V at an analysis threshold of  $\sim 130 e^-$ . For a bias voltage of 0 V the dependence on the X coordinate as explained by diffusion (see discussion Section 10.1.1) is observable, while for a bias voltage of  $-6$  V almost no dependence on the X coordinate is visible.

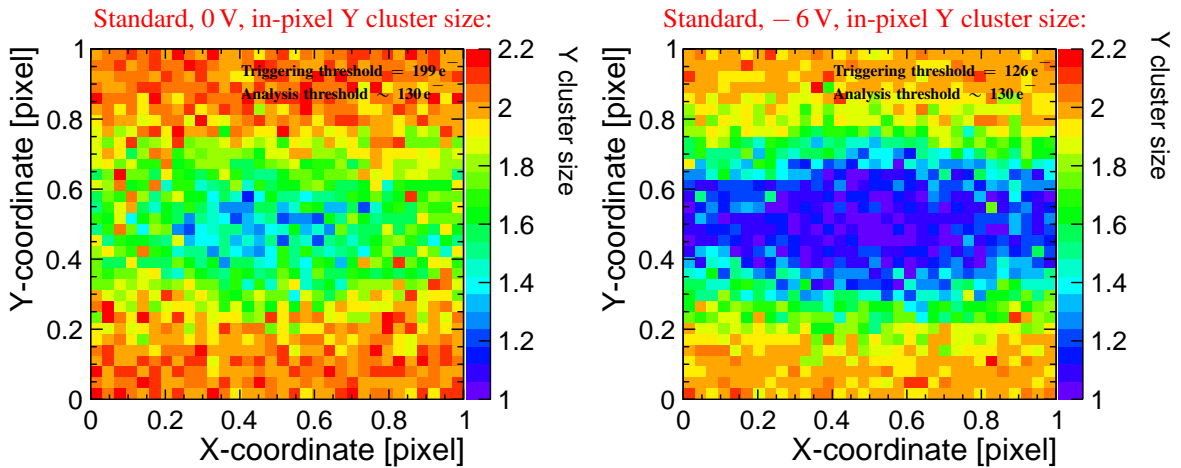


Figure 10.32: In-pixel representation of the Y cluster size at an analysis threshold of  $\sim 130 e^-$  for a bias voltage of 0 V (left) and  $-6$  V (right) for the standard process.

**Intermediate threshold region - analysis threshold between  $\sim 250 e^-$  and  $\sim 400 e^-$**  In this range of the analysis threshold the cluster size is very similar for both voltages. However, considering the X cluster size distribution e.g. for a threshold of  $\sim 370 e^-$  in the left plot of Figure 10.33, differences can be noted between both voltages. While for a voltage of  $-6$  V the larger cluster sizes can be attributed to

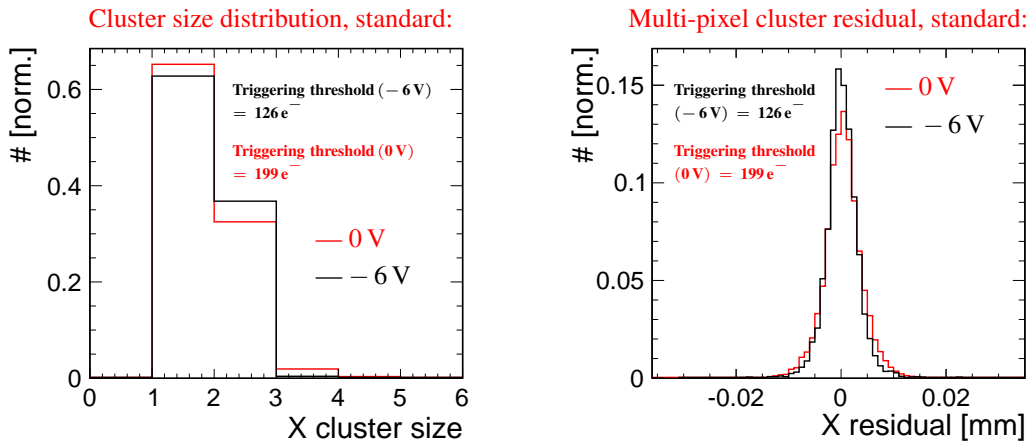


Figure 10.33: Distribution of the X cluster size (left) and the multi-pixel cluster X residual (right) at an analysis threshold of  $\sim 370 e^-$  for different bias voltages for the standard process.

a size of two only, also cluster sizes of three contribute to the cluster size distribution for a bias voltage of 0 V. The  $\eta$  correction, used for charge interpolation for multi-pixel clusters, performs best for two pixel clusters [88]. Consequently, the multi-pixel cluster residual for a bias voltage of  $-6$  V is less spread compared to a bias voltage of 0 V, as shown in the right plot of Figure 10.33, explaining the degradation of the resolution for a bias voltage of 0 V with respect to a bias voltage of  $-6$  V.

The efficiency for a bias voltage of 0 V starts to drop in the intermediate threshold range (see Figure 10.31), as expected from the lower seed signal for a bias voltage of 0 V compared to a bias voltage of  $-6$  V (see Figure 10.25).

**High threshold region - analysis threshold  $\gtrsim 400 e^-$**  At even higher threshold values the efficiency for a bias voltage of 0 V drops significantly. In Figure 10.34, the in-pixel efficiency is shown for a bias voltage of 0 V at a threshold of  $\sim 370 e^-$  (left) and a threshold of  $\sim 700 e^-$  (right). For a threshold

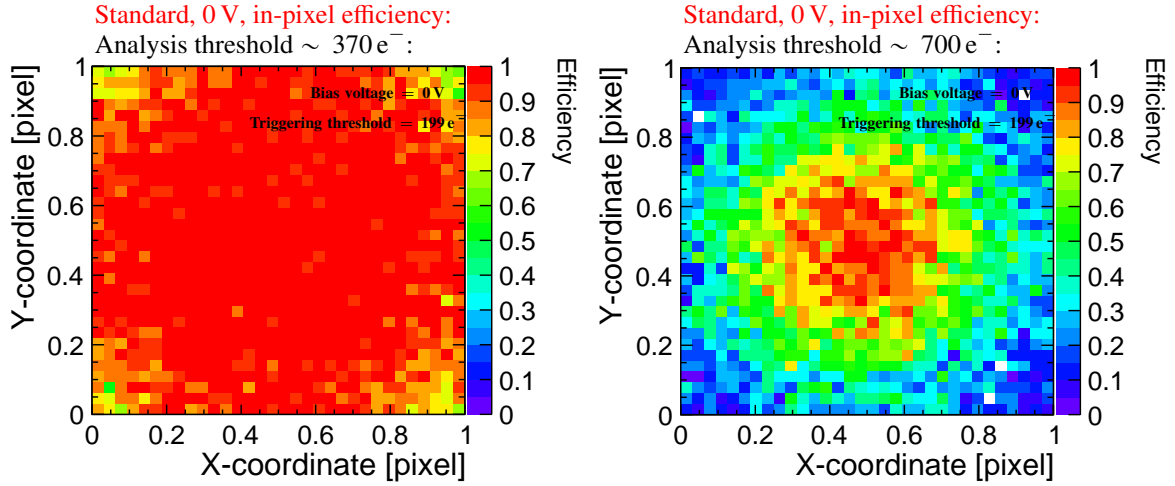


Figure 10.34: In-pixel representation of the efficiency at an analysis threshold of  $\sim 370 e^-$  (left) and an analysis threshold of  $\sim 700 e^-$  (right) for the standard process at a bias voltage of 0 V.

of  $\sim 370 e^-$  an efficiency drop is only visible in the pixel corners. For a threshold of  $\sim 700 e^-$  a significant efficiency drop is not only visible in the pixel corners, but also in the pixel edges (for the definition of the pixel corners and edges see Figure 6.15). Accordingly, the region where single-pixel clusters are generated is constrained significantly to regions close to the pixel centre and the single-pixel cluster residual is biased to smaller values (see also discussion in Section 10.2.1), explaining the improvement of the resolution for a bias voltage of 0 V at very high threshold values. For a bias voltage of  $-6$  V the efficiency drops much less significantly in the investigated threshold range, such that the explained effect on the resolution is not visible.

### Modified process

For the modified process bias voltages of 0 V,  $-3$  V and  $-6$  V have been studied.

The cluster and seed signal distributions at an analysis threshold of  $\sim 40 e^-$  are presented for the different bias voltages in Figure 10.35. The cluster signal shows a peak at similar values for the different voltages. This is consistent with the results of the TCAD simulation that show, that even at a bias voltage of 0 V a depleted region extends over the full lateral pixel dimension, originating from the deep planar junction (see Figure 8.7). Thus, even without applying a bias voltage a sizeable depleted region extends over the full pixel cell, that can explain that no significant amount of charge is lost, even at a bias voltage of 0 V.

However, small differences can be observed in the shape of the cluster signal distribution. While the cluster signal distribution is very similar for a bias voltage of  $-3$  V and  $-6$  V, tails to lower values are more prominent for a bias voltage of 0 V. This is consistent with the TCAD simulations that show some changes of the depleted region in the n layer for a bias voltage of 0 V compared to a bias voltage of  $-6$  V (see Figure 8.7).

The seed signal distribution is slightly lower for lower absolute bias voltages, as visible in the right plot of Figure 10.35. This can be explained by more charge sharing for lower absolute bias voltages, which

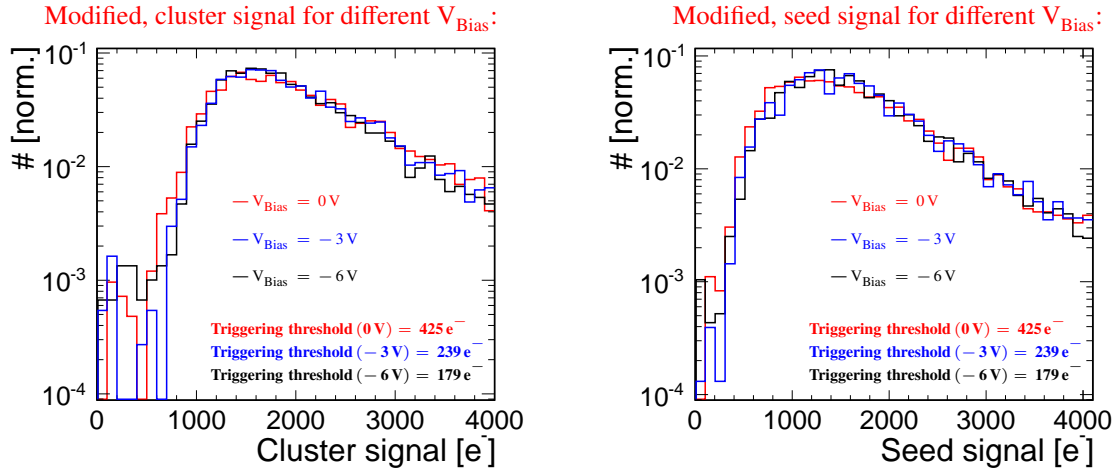


Figure 10.35: Cluster signal (left) and seed signal (right) for different bias voltages at an analysis threshold of  $\sim 40 e^-$  for the modified process.

is visible in Figure 10.36, where the cluster size in X and Y is presented versus the analysis threshold for different bias voltages. No significant difference has been measured between a bias voltage of  $-6 V$

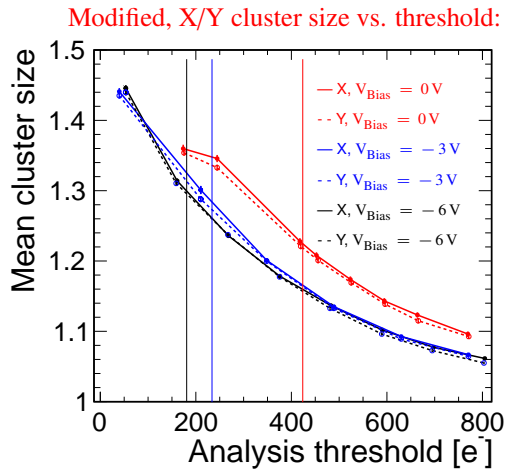


Figure 10.36: Mean X and Y cluster size for different bias voltages versus analysis threshold for the modified process. The error bars correspond to the uncertainty on the mean value. The thin vertical lines mark the triggering thresholds.

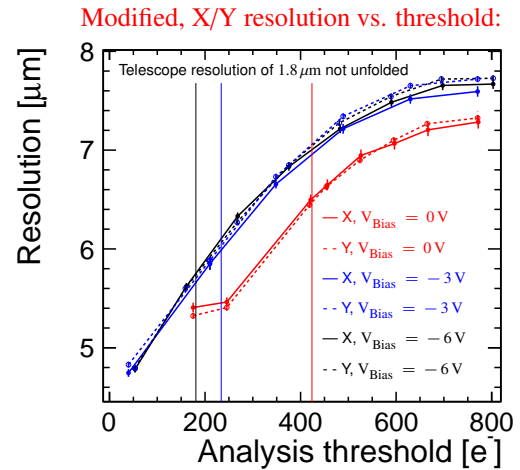


Figure 10.37: X and Y resolution for different bias voltages versus analysis threshold for the modified process. The error bars correspond to the uncertainty on the RMS. The thin vertical lines mark the triggering thresholds.

and  $-3 V$ . A significant enhancement of the cluster size can be observed for a bias voltage of  $0 V$ . This is compatible with the TCAD simulations of the modified process, where only a slight change of the electric field has been observed between a bias voltage of  $-6 V$  and  $-3 V$ , while a more significant change of the electric field has been observed for a bias voltage of  $0 V$  (see Figure 8.10).

The trends observed in the threshold dependency of the cluster size for different bias voltages are reflected in the threshold dependency of the spatial resolution, presented in Figure 10.37. A very similar threshold dependency of the spatial resolution has been measured for bias voltages of  $-6 V$  and  $-3 V$ .

For a bias voltage of 0 V the spatial resolution is improved with respect to higher absolute voltages due to the increased charge sharing.

The efficiency is presented for different bias voltages versus the analysis threshold in Figure 10.38. For the modified process, the threshold dependency of the efficiency is very similar for different bias

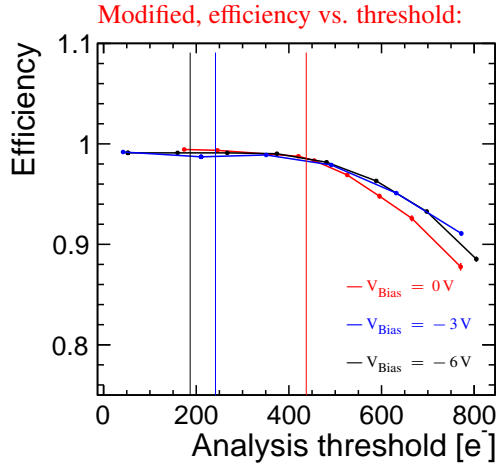


Figure 10.38: Efficiency for different bias voltages versus analysis threshold for the modified process. The error bars correspond to the the statistical uncertainty and the thin vertical lines mark the triggering thresholds.

voltages, consistent with the similar seed signal distribution for different voltages. For a bias voltage of 0 V the efficiency drops at slightly lower threshold values, as expected from the tail to lower values observed in the seed signal distribution due to the enhanced charge sharing.

To investigate how the timing performance is impacted by different bias voltages, the  $T_{10-90}$  time is presented for the different bias voltages in Figure 10.39 and the timing resolution is shown versus the bias voltage in Figure 10.40. For the modified process neither the  $T_{10-90}$  time, nor the timing resolution show a significant dependence on the bias voltage. Again, this is in agreement with the large depleted region even for a bias voltage of 0 V, extending over the full lateral pixel size (see Figure 8.10 and 8.7).

### 10.2.3 Comparison of different spacings for the modified process

Different distances between the pixel implant and the p wells have been investigated for the modified process (*spacings*, see Figure 5.1). Apart from varying the spacing, all other parameters of the pixel layout are as defined in Table 10.1. The operation conditions for which the different spacings have been studied and the analysed statistics are summarised in Table 10.4. As discussed in Chapter 9.2.3, the larger

Table 10.4: Definition of operation conditions and analysed statistics for the study of different spacings for the modified process.

Spacing	Voltage [V]	Triggering threshold [e <sup>-</sup> ]	# roi-tracks
1 μm	-6	143	510
3 μm	-6	179	24260
5 μm	-6	491	1418

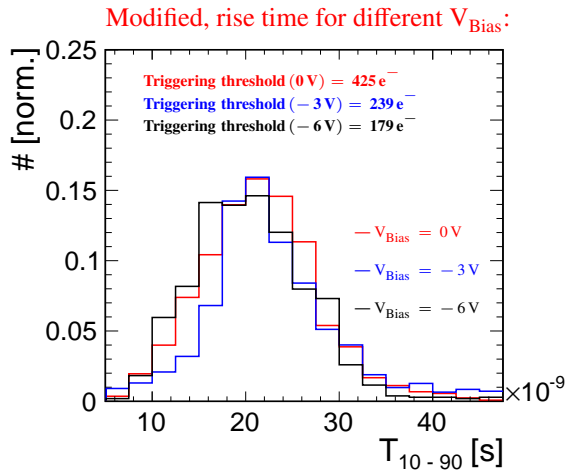


Figure 10.39:  $T_{10-90}$  time for different bias voltages at an analysis threshold of  $\sim 100 e^-$  for the modified process.

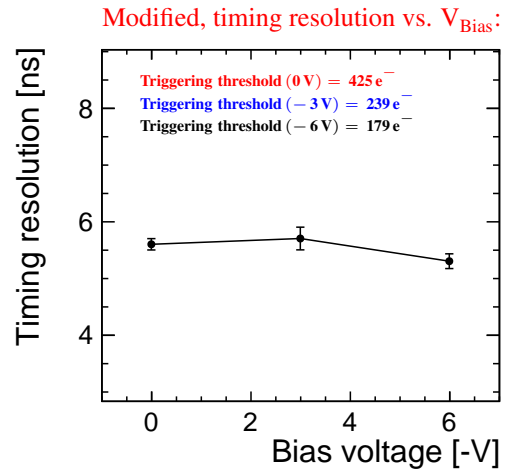


Figure 10.40: Timing resolution for different bias voltages at an analysis thresholds of  $\sim 100 e^-$  for the modified process.

triggering threshold for large spacings can be attributed to an increased sensor capacitance that originates from non-depleted regions around the collection electrode.

The cluster size and spatial resolution in X and Y are presented for different spacings as a function of the analysis threshold for the modified process, in Figure 10.41 and 10.42, respectively. Larger clusters

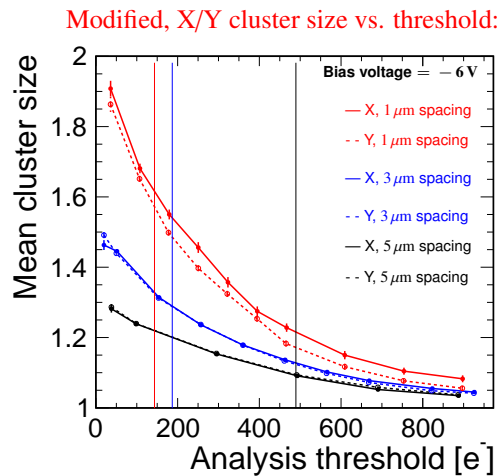


Figure 10.41: Mean X and Y cluster size for different spacings versus analysis threshold for the modified process. The error bars correspond to the uncertainty on the mean value. The thin vertical lines mark the triggering thresholds.

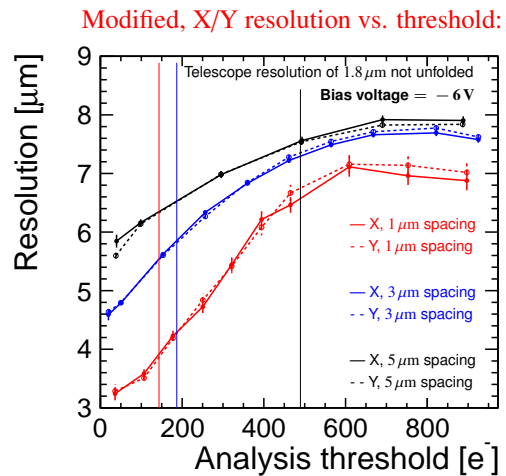


Figure 10.42: X and Y resolution for different spacings versus analysis threshold for the modified process. The error bars correspond to the uncertainty on the RMS. The thin vertical lines mark the triggering thresholds.

have been measured for smaller spacings, consistent with the lower electric field in X for smaller spacings observed in the results of the TCAD simulations (see Figure 8.13). This trend is observable especially for lower threshold values. At higher threshold values the cluster sizes converge to a value of one. The difference in the cluster size is larger between a spacing of  $1 \mu\text{m}$  and a spacing of  $3 \mu\text{m}$  compared to the

difference observed between a spacing of  $3\ \mu\text{m}$  and a spacing of  $5\ \mu\text{m}$ .

The increased cluster size for smaller spacing values improves the position reconstruction, as shown in Figure 10.42, where the spatial resolution for different spacings is presented as a function of the analysis threshold. As for the cluster size the larger difference of the spatial resolution can be observed between a spacing of  $1\ \mu\text{m}$  and  $3\ \mu\text{m}$  at low threshold values. The increased charge sharing for smaller spacing values is also visible by an earlier drop of the efficiency at lower threshold values for smaller spacings, as presented in Figure 10.43.

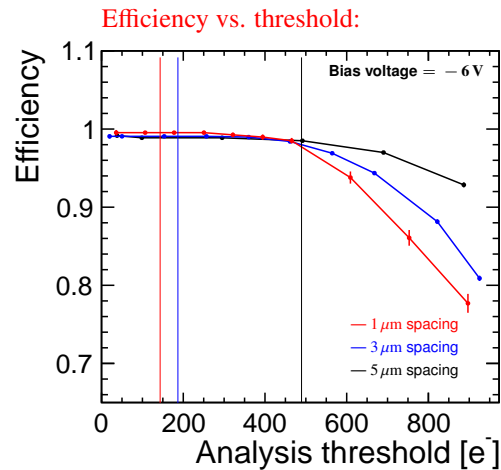


Figure 10.43: Efficiency for different spacings as a function of the analysis threshold for the modified process. The error bars correspond to the statistical uncertainties. The thin vertical lines mark the triggering thresholds.

The impact of the lower electric field for smaller spacing values is as well visible in the  $T_{10-90}$  time distribution shown in Figure 10.44 for an analysis threshold of  $\sim 50\ e^-$ . Almost no difference has been measured in the  $T_{10-90}$  time distribution for a mini matrix with a spacing of  $3\ \mu\text{m}$  and a spacing of  $5\ \mu\text{m}$ . The most significant difference of the  $T_{10-90}$  time has been observed between a spacing of  $3\ \mu\text{m}$  and  $1\ \mu\text{m}$ . For a spacing of  $1\ \mu\text{m}$  the measured  $T_{10-90}$  time is approximately a factor of two slower compared to a spacing of  $3\ \mu\text{m}$  and the distribution is significantly broader. This is consistent with the TCAD simulations, showing a lower electric field and larger inhomogeneities over the lateral pixel size for the smaller spacings (see Figure 8.13).

The lower electric field for smaller spacing values can also impact the analogue timing resolution. To investigate this, the timing resolution is presented for different spacings in Figure 10.45. As for the other observables, no significant difference has been measured within the uncertainties for mini matrices with a spacing of  $3\ \mu\text{m}$  and  $5\ \mu\text{m}$ . For a mini matrix with a spacing of  $1\ \mu\text{m}$ , the timing resolution degrades by  $\sim 20\%$ . However, taking into account the uncertainties of the measured timing resolution the difference is not very significant.

## 10.2.4 Summary

The investigation of the spatial resolution for different analysis thresholds shows, that the charge sharing contribution from diffusion degrades the position reconstruction at threshold values  $\lesssim 115\ e^-$  for the standard process. For higher thresholds this contribution is suppressed, resulting in an optimal resolution of  $\lesssim 3.5\ \mu\text{m}$  for the standard process at a threshold of  $\sim 115\ e^-$ . For the modified process, where the

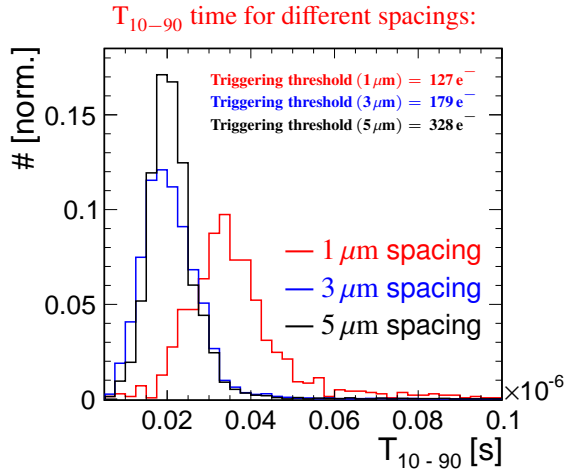


Figure 10.44:  $T_{10-90}$  time for different spacings at an analysis threshold of  $\sim 50 e^-$  for the modified process.

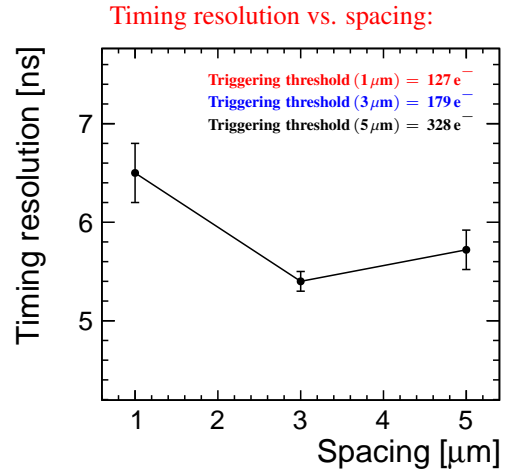


Figure 10.45: Timing resolution versus spacing at an analysis threshold of  $\sim 50 e^-$  for the modified process. The error bars correspond to the uncertainty of the width of a Gaussian fit to the timing residuals.

charge sharing from diffusion does not contribute, the optimal resolution of  $\lesssim 4.5 \mu\text{m}$  has been measured for the lowest analysed threshold value of  $\sim 20 e^-$ .

The efficiency for different analysis thresholds starts to drop at lower threshold values for the standard compared to the modified process due to the lower seed signal from more charge sharing for the standard compared to the modified process.

The timing resolution shows a slight improvement for higher analysis thresholds. The fact that the timing resolution of the standard process and modified process converge both to a value of  $\sim 5 \text{ ns}$  confirms that the readout sampling frequency limits the measured timing resolution.

Different bias voltages have been studied for the standard and modified process. For the standard process similar spatial resolution values have been measured for a bias voltage of  $0 \text{ V}$  and  $-6 \text{ V}$ , despite a significantly larger cluster size for a bias voltage of  $0 \text{ V}$ . This has been explained by the enhanced contribution of charge sharing from diffusion for a bias voltage of  $0 \text{ V}$  compared to a bias voltage of  $-6 \text{ V}$ . The increased charge sharing for a bias voltage of  $0 \text{ V}$  results in an efficiency drop at significantly lower threshold values compared to a bias voltage of  $-6 \text{ V}$ . Moreover, the  $T_{10-90}$  time degrades approximately by a factor of two and the timing resolution degrades significantly for a bias voltage of  $0 \text{ V}$  compared to a bias voltage of  $-6 \text{ V}$ .

For the modified process almost no difference has been measured for different bias voltages in view of  $T_{10-90}$  time and timing resolution. This observation is in agreement with the large depleted region evolving from the deep planar junction, that is already present without applying a bias voltage. Due to the enhanced charge sharing for lower bias voltages, an improved spatial resolution and an earlier efficiency drop have been measured for a bias voltage of  $0 \text{ V}$  compared to a bias voltage of  $-6 \text{ V}$ .

Different spacings of  $1 \mu\text{m}$ ,  $3 \mu\text{m}$  and  $5 \mu\text{m}$  have been investigated for the modified process. A smaller spacing of  $1 \mu\text{m}$  has been found to be favourable for a more precise spatial resolution down to  $\lesssim 3 \mu\text{m}$ . A larger spacing of  $5 \mu\text{m}$  has been found to lead to a later drop of the efficiency at higher threshold values and a faster rise time. Consequently, the intermediate spacing of  $3 \mu\text{m}$  is a reasonable compromise to achieve a precise spatial resolution simultaneously with a precise timing resolution and larger efficient operation window.

---

## Validation and application of the simulation

---

The charge sharing functions presented in Figure 8.16 have been integrated in the two dimensional simulation chain described in Chapter 7. As explained in Section 6.5.2 a cut has been performed on the test beam data: the track intercepts are constrained to the pixel centre in the non-simulated dimension to compare the measurement results to the results of the two dimensional simulation. This cut has been set on the Y coordinate of the pixel, such that the studied observable in X does not vary over the Y dimension of the pixel, to exclude effects originating from the non-simulated third dimension. The studied observables in X are then compared to the simulation (the same procedure is applied vice versa for the observables in Y).

The calibration discussed in Chapter 9 has been used to set the threshold in the simulation to the value of the analysis threshold. The triggering threshold applied during data taking is not considered in the simulations as it only plays a role if an efficiency loss has been measured. However, as shown in Figure 10.23, no efficiency loss has been measured in the threshold range where the analysis threshold is below the triggering threshold.

The full waveform has been recorded for the test beam data (see Chapter 5.4). Therefore, no digitisation has been applied in the simulation.

Since the measurements of the spatial resolution have shown that the used reconstruction with the signal definition as the difference of the mean values of amplitudes before and after a particle hit is robust against noise fluctuations of individual samples around the pedestal (i.e. the resolution improves for very low analysis thresholds, see Figure 10.19), the noise has been set to zero in the simulations.

Moreover, to compare the spatial resolution measured from the test beam data to the results from the full simulation, a Gaussian smearing of the true particle hit position of  $3\ \mu\text{m}$  has been applied in the simulation. This value is larger compared to the above stated telescope resolution of  $1.8\ \mu\text{m}$  [33] but has been found to give the best agreement between data and simulations for both processes at various threshold values. The stated telescope resolution of  $1.8\ \mu\text{m}$  is quoted for the width of a Gaussian fit to the telescope residual and does not include the tails of the distribution. For the simulation and test beam data the resolution is defined as the RMS on a range of  $\pm 20\ \mu\text{m}$ . Thus, it is reasonable that the Gaussian smearing assumed in the simulations needs to be larger compared to the value of  $1.8\ \mu\text{m}$  stated in [33]. However, a larger value of the Gaussian smearing in the simulation could also compensate for other effects, that can broaden the measured resolution and are not taken into account in the simulation otherwise, such as single delta rays.

The simulation results of the standard and modified process are compared to the results of the test beam data for the pixel layout and operation conditions specified in Table 11.1. As introduced in Chapter 8, two different epi layer doping values have been simulated: the epi layer doping as measured in [39]

Table 11.1: Pixel layout and operation conditions for the comparison of the simulation to the test beam results.

Parameter	Value
Pitch [ $\mu\text{m}$ ]	28
Spacing [ $\mu\text{m}$ ]	3
Collection electrode size [ $\mu\text{m}$ ]	2
Thickness epitaxial layer [ $\mu\text{m}$ ]	25
Bias voltage [– V]	6

(referred to as norm) and the same profile with doping values below  $1.3 \cdot 10^{13}/\text{cm}^3$  set to this value (referred to as limit), to take into account the limit of the calibration of the SRP measurement.

## 11.1 Comparison of data and simulation

### 11.1.1 Standard process

In Figure 11.1, the measured mean cluster size in X and Y is compared as a function of the threshold to the cluster size of the simulation with the two different values of the epi layer doping. Large variations

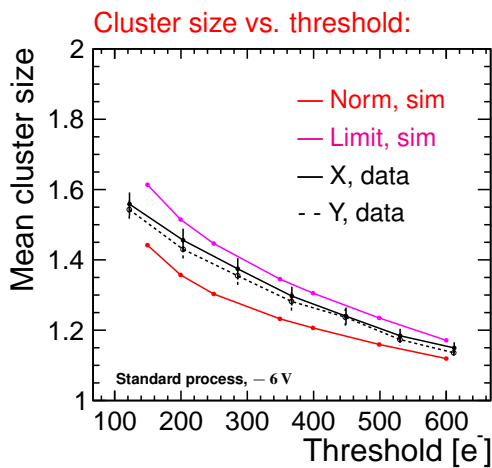


Figure 11.1: Mean cluster size versus threshold for data (black) and the simulations with different epi layer doping values (magenta and red). The error bars correspond to the uncertainty on the mean value.

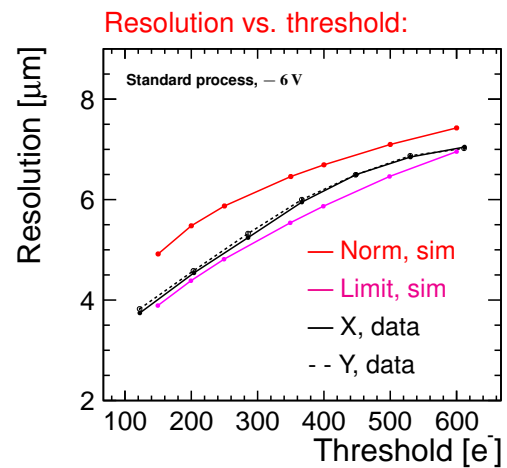


Figure 11.2: Spatial resolution versus threshold for data (black) and the simulations with different epi layer doping values (magenta and red). The error bars correspond to the uncertainty on the RMS.

can be observed between the simulated cluster size for the norm and the limit case: for the simulated limit case (higher epi layer doping) a significantly larger cluster size is visible compared to the simulated norm case (lower epi layer doping). This is compatible with the lower electric field strength and smaller depleted region for the simulated limit case compared to the simulated norm case (see Figure 8.4). While a good agreement within 10 % between the simulated limit case and the measured cluster size can be observed, the simulated norm case shows a sizeable discrepancy to the cluster size measured from test beam data. Note that the mean cluster size versus threshold does not depend on the Gaussian smearing.

The trends observed in the threshold dependency of the cluster size are reflected in the threshold dependency of the spatial resolution presented in Figure 11.2. The spatial resolution of the simulated limit

case and the measured spatial resolution are in good agreement. The spatial resolution of the simulated norm case is sizeably degraded due to the significantly lower cluster size.

To compare the measured test beam data and the simulations in more detail, the cluster size and residual distributions are presented for a threshold of  $\sim 200 e^-$  in Figure 11.3 and 11.4. While the

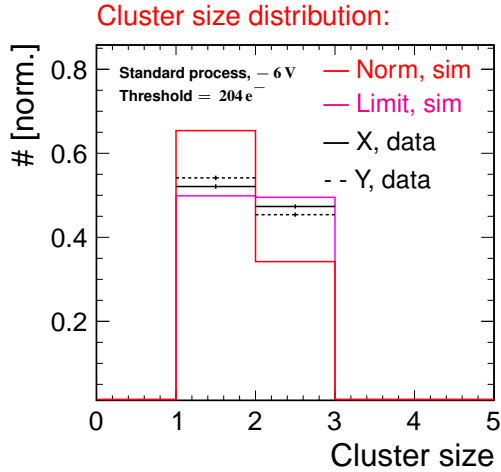


Figure 11.3: Cluster size distribution for data (black) and the simulations with different epi layer doping values (magenta and red) at a threshold of  $204 e^-$ . The error bars correspond to the statistical uncertainties.

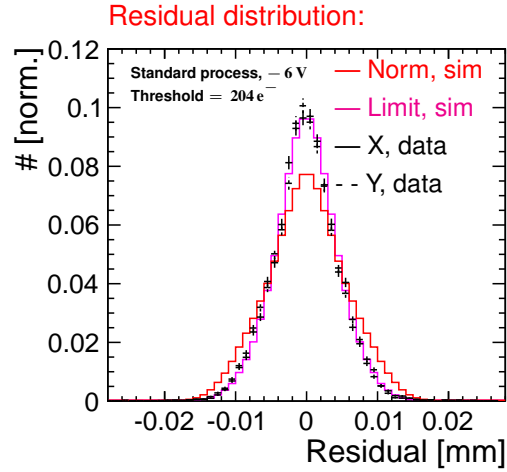


Figure 11.4: Residual distribution for data (black) and the simulations with different epi layer doping values (magenta and red) at a threshold of  $204 e^-$ . The error bars correspond to the statistical uncertainties.

discrepancy of the simulated norm case to the data is clearly visible in the shape of the distributions, an excellent agreement within a few percent is shown between the shape of the distributions of the simulated limit case and the data.

In a next step, the comparison between data and simulations is performed with in-pixel resolved precision, as shown in Figure 11.5, where the measured in-pixel cluster size is compared to the simulations. The measured cluster size within the pixel cell is well described within the statistical uncertainties by the simulated limit case.

Further, the dependency of the efficiency on the track position within the pixel cell is compared between test beam data and simulations. As presented for example in Figure 10.22, the efficiency is lost first in the pixel corners. The corners are however cut out by the cut on the pixel centre that is needed to compare the two dimensional simulation to the measured efficiency. To measure a significant efficiency loss at the pixel edges that are included in this cut, and thus create a distribution of the in-pixel efficiency that is different from a flat distribution, a very high threshold of  $\sim 690 e^-$  has been selected. The in-pixel efficiency at this threshold value is compared to the simulations in Figure 11.6. The shape of the efficiency within the pixel cell observed in data is slightly better described by the simulation limit case. However, the statistical uncertainties on the measured in-pixel efficiency are large since only tracks passing through the very pixel centre can be selected, to avoid effects of the non-simulated third dimension.

### 11.1.2 Modified process

The mean measured cluster size in X and Y are compared to the simulations with the norm and limit epi layer doping for different thresholds in Figure 11.7. As already pointed out in the discussion of the transient behaviour (see Figure 8.33 and 8.34), the difference between the two different epi layer doping

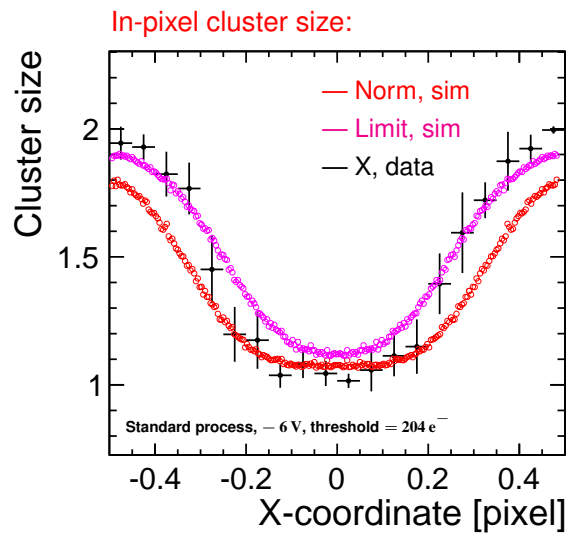


Figure 11.5: Cluster size within the pixel cell for data (black) and the simulations with different epi layer doping values (magenta and red) for the standard process at a threshold of  $204 e^-$ . The error bars are the RMS of the cluster size for one bin in the Y coordinate.

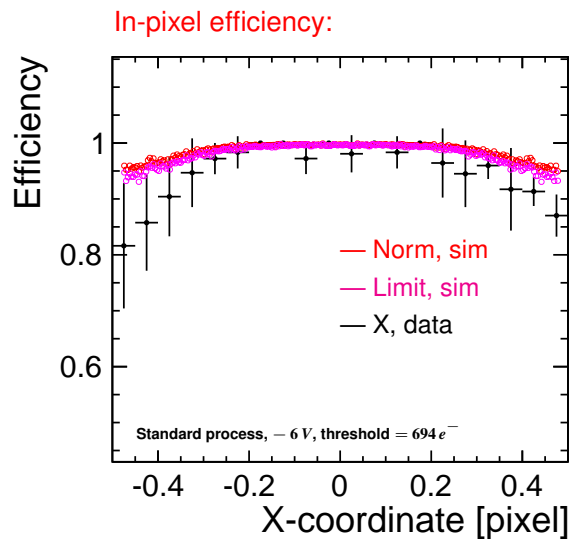


Figure 11.6: Efficiency within the pixel cell for data (black) and the simulations with different epi layer doping values (magenta and red) for the standard process at a threshold of  $694 e^-$ . The error bars correspond to the statistical uncertainties.

values is not significant for the modified process: both, the simulation of the norm and the limit case describe well the measured cluster size as a function of the threshold within 10%.

The spatial resolution in X and Y is presented versus the threshold in Figure 11.8. As for the cluster size, the measured threshold dependency of the spatial resolution is well described by the two simulations

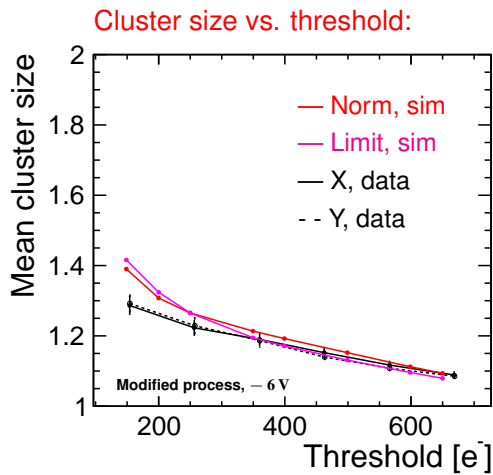


Figure 11.7: Cluster size versus threshold for data (black) and the simulations with different epi layer doping values (magenta and red) for the modified process and a bias voltage of  $-6\text{ V}$ . The error bars correspond to the uncertainty on the mean value.

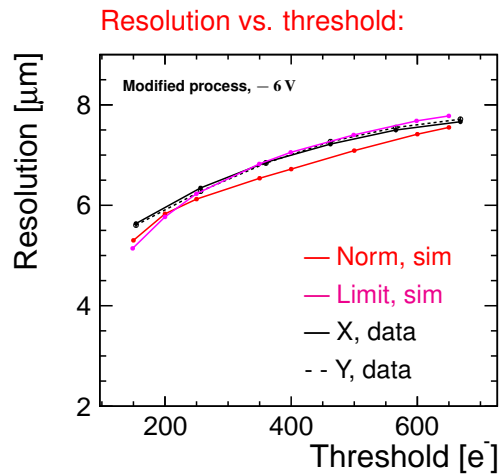


Figure 11.8: Spatial resolution versus threshold for data (black) and the simulations with different epi layer doping values (magenta and red) for the modified process and a bias voltage of  $-6\text{ V}$ . The error bars correspond to the uncertainty on the RMS.

with different epi layer doping values.

To compare the data and the simulations in more detail, the cluster size and residual distributions in X and Y are presented in Figure 11.9 and Figure 11.10 for a threshold of  $\sim 260\text{ e}^-$ . The measured shape

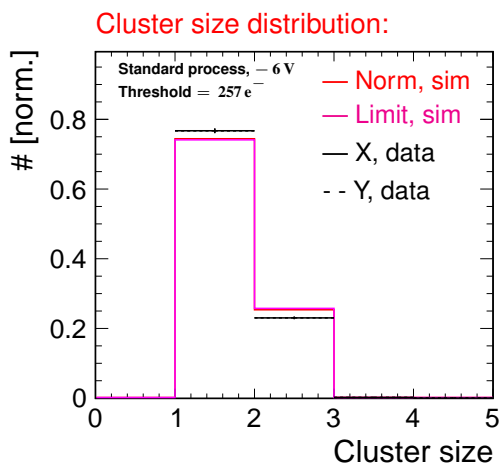


Figure 11.9: Cluster size distribution for data (black) and the simulations with different epi layer doping values (magenta and red) for the modified process at a threshold of  $257\text{ e}^-$ . The error bars correspond to the statistical uncertainties.

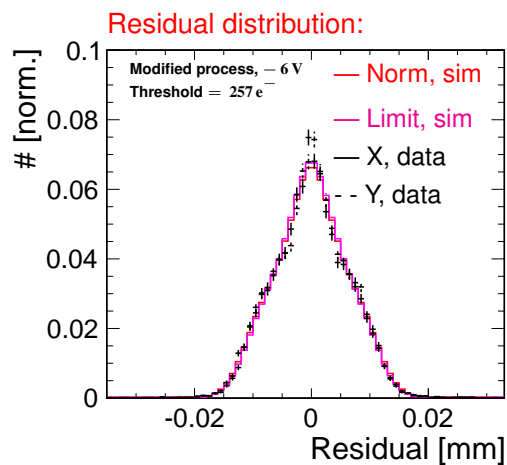


Figure 11.10: Spatial residual distribution for data (black) and the simulations with different epi layer doping values (magenta and red) for the modified process at a threshold of  $257\text{ e}^-$ . The error bars correspond to the statistical uncertainties.

of the cluster size and spatial resolution distributions are well described by both simulations.

To study the comparison between data and simulations with in-pixel resolved precision, the cluster size within the pixel cell presented in Figure 11.11. Within the statistical uncertainties of the measurements, both simulations show an agreement with the measured distribution of the cluster size within the pixel

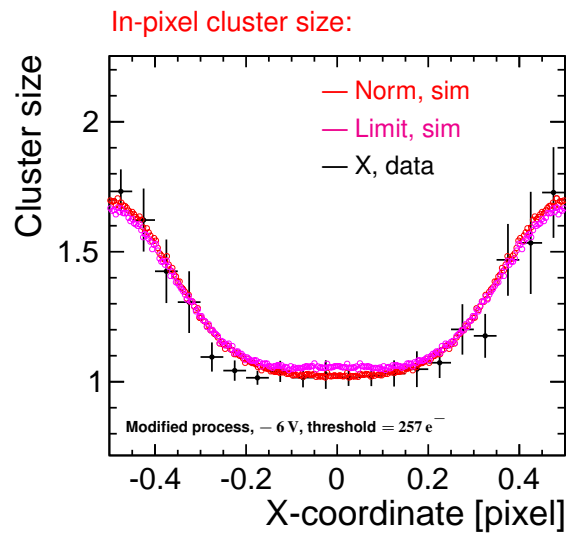


Figure 11.11: Cluster size within the pixel cell for data (black) and the simulations with different epi layer doping values (magenta and red) for the modified process at a threshold of  $257 e^-$ . The error bars correspond to the RMS of the cluster size for one bin in the Y coordinate.

cell.

The efficiency in the pixel cell is presented at a high threshold of  $\sim 780 e^-$  for data and simulations in Figure 11.12. Both simulations describe the data within the statistical uncertainties of the measurements.

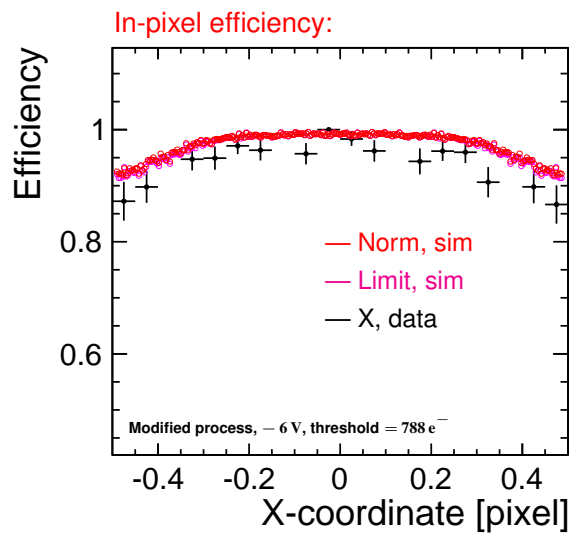


Figure 11.12: Efficiency within the pixel cell for data (black) and the simulations with different epi layer doping values (magenta and red) for the modified process at a threshold of  $788 e^-$ . The error bars correspond to the statistical uncertainty.

## 11.2 Application of the simulation

Since the simulation with the higher epi layer doping shows a good agreement to the test beam data, the simulation can be applied to predict the behaviour of various designs. As an example of such, the impact of the digitisation on the spatial resolution is discussed in the following for the modified process and the pixel layout specified in Table 11.1.

The full analogue performance of the studied HR CMOS processes has been evaluated by the presented measurements with the Investigator chip. However, for the design of a fully monolithic chip in this technology, a threshold and digitisation of the measured charge could be applied on chip level for the purpose of data reduction. The impact of this on the spatial resolution can be investigated using the digitisation implemented in the simulation chain (see Chapter 7), that has been parameterised by the threshold, the saturation and the number of bits.

In the following the true particle impact point has been used, and telescope effects have been neglected, to investigate the intrinsic resolution of the design under study.

Generally, the two dimensional simulation only reproduces the performance measured in the pixel centre. However, as for the modified process the cluster size and spatial resolution in X and Y are almost not correlated with the other pixel dimension (see Figure 10.8), the two dimensional simulation is expected to reproduce well the overall performance of the data over the full pixel cell.

The spatial resolution has been calculated for different resolutions of the applied digitisation as a function of the threshold. This is presented in Figure 11.13, for a noise of  $35 e^-$  and a saturation of  $10 ke^-$ .

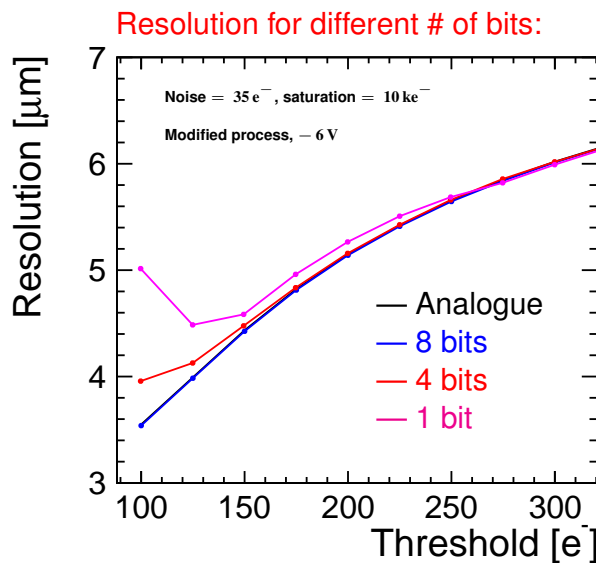


Figure 11.13: Resolution (using  $\eta$  correction) versus threshold for different number of bits. A noise of  $35 e^-$  and a saturation of  $10 ke^-$  have been simulated.

For threshold values  $\lesssim 150 e^-$  ( $SNR \lesssim 4.3$ ) significant differences can be noted in the resolution for different number of bits since the noise starts to contribute significantly to the reconstructed clusters. Generally, a stronger noise dependancy can be observed for less bits: the less bits, the stronger the degradation of the spatial resolution for higher noise values. In the extreme case of one bit, where only one state is available above the threshold, no distinction is possible between a small noise contribution or

a large signal contribution (for less bits less information is available for the position reconstruction that can be more easily "washed out" by the noise).

For a threshold of  $\gtrsim 150 e^-$  4 bits are enough to achieve a resolution very similar to the analogue resolution, whereas the binary resolution with one bit shows a slight degradation of the resolution. For threshold values  $\gtrsim 250 e^-$  even one bit is sufficient to achieve a spatial resolution similar to the analogue spatial resolution. This limited gain from a finer sampling of the signal can be understood by considering the cluster size within the pixel cell as measured for the modified process with the same pixel design as for the simulations in Figure 10.21: the multi-pixel clusters are mainly generated at the very pixel edge. For one bit, where no information about the signal height is available for the reconstruction, the reconstructed position for a cluster with two pixels is at the at the pixel edge, close to the region where the multi-pixel clusters are generated.

Note that the specific values depend on many parameters, such as for example the exact sensor design and the resulting charge sharing. Moreover, simplified assumptions have been made in the simulation, such as a noise that is Gaussian distributed or a linear ADC scale. However, general trends can be observed, for example that less bits are less robust against noise fluctuations. Overall, the gain in spatial resolution achieved by more bit states than one is in the order of a few percent small in the investigated threshold range, as explained by the in-pixel distribution of the cluster size.

### 11.3 Summary

The test beam data measured for a pixel layout with a pitch of  $28 \mu\text{m}$ , a collection electrode size of  $2 \mu\text{m}$  and a spacing of  $3 \mu\text{m}$  has been compared to the simulation described in Chapter 7 and 8 for a bias voltage of  $-6 \text{ V}$ . The comparison has been performed for the standard and modified process different epi layer doping values. The response of the standard process is well described by the higher epi layer doping, while showing sizeable discrepancies to the lower epi layer doping. In contrast to this, the response of the modified process is well described by both.

Since the simulation with the higher epi layer doping describes well the simulation of the standard and modified process, it can be used in a next step to predict the performance of different designs. As an example, the spatial resolution has been investigated for different resolutions of the digitisation in dependance of the threshold for the modified process and a pixel size of  $28 \mu\text{m}$ . Due to the charge sharing within the pixel cell, the gain in spatial resolution achieved by more bit states than one has been found to be negligible in a threshold range  $> 150 e^-$ .

---

## Conclusions and outlook

---

The small collection electrode design of High Resistivity CMOS sensors and the possibility to integrate the readout electronics in the sensor are attractive for the CLIC tracker in view of fast timing, low material budget and large area production. This makes High Resistivity CMOS technologies interesting candidates to address the challenging requirements imposed on the large area CLIC tracker: a spatial resolution of  $7\ \mu\text{m}$ , a material budget of  $1 - 2\% X_0$  per layer and a timing resolution compatible with a time slicing of 10 ns.

The Investigator chip has been studied using test beam and laboratory measurements as well as in simulations. Two different process variants have been investigated: a standard High Resistivity CMOS process and a modified process, where a full depletion can be achieved. The studies are focused on a pixel layout with a pitch of  $28\ \mu\text{m}$ , an electrode size of  $2\ \mu\text{m}$  and a spacing of  $3\ \mu\text{m}$  implemented on epitaxial layer with a thickness of  $25\ \mu\text{m}$ .

TCAD simulations show that the standard process is not fully depleted, even at the maximal bias voltage of  $-6\ \text{V}$ , resulting in a slower contribution from diffusion to the overall response. In contrast to this, the modified process shows a full depletion at  $-6\ \text{V}$  and a sizeable depletion that extends over the full lateral size even without applying a bias voltage. Moreover, the TCAD simulations of the modified process show that a spacing of  $5\ \mu\text{m}$  is too large to achieve a full depletion around the pixel implant. An impact of the charge carriers created by a charged particle incident on the electric field in the sensor has been observed in transient TCAD simulations, showing the relevance of a fully self-consistent simulation that takes into account the modifications of the electric field after the charge generation to model the time resolved current response precisely. The presented results are limited by the fact that the simulation has been performed in two dimensions. A more realistic simulation performed in three dimensions could serve as an extension and validation of the presented studies.

Data from a  $^{55}\text{Fe}$  source has been used for calibration. The spectra show a smaller capacitance for the standard compared to the modified process that is less dependant on the bias voltage, as explained by non depleted regions around the pixel implant observed for lower bias voltages in the TCAD simulations of the modified process. Moreover, the spectra show a larger capacitance for larger spacings, that can be attributed to non-depleted regions around the pixel implants.

The analogue performance of both processes has been measured and compared using test beam measurements for perpendicular particle incidents. A reconstruction method for the Investigator waveforms has been developed, including an offline common mode noise correction that reduces the noise by approximately a factor of two. Moreover, the reconstructed signal is robust against sample by sample noise fluctuations. Due to both factors, a low offline threshold down to a few tens of electrons can be achieved.

The low threshold allows for an improvement in spatial resolution with respect to the value of  $\text{pitch}/\sqrt{12}$  by benefitting from charge interpolation. This holds especially for the standard process, where significantly more charge sharing has been measured compared to the modified process. An optimal spatial resolution of  $\lesssim 3.7\ \mu\text{m}$  has been measured for the standard process at a threshold of  $\sim 100\ e^-$  and a bias voltage of  $-6\ \text{V}$ . For the modified process an optimal spatial resolution of  $\lesssim 4.5\ \mu\text{m}$  can be achieved for a bias voltage  $-6\ \text{V}$  and a threshold of  $\sim 20\ e^-$ . Both processes allow for a spatial resolution below the required  $7\ \mu\text{m}$  for the CLIC tracker up to threshold values of  $\sim 400\ e^-$ . Overall, the standard process is favourable in view of spatial resolution. However, at threshold values  $< 100\ e^-$  the charge sharing from diffusion introduces a correlation of the X/Y cluster size on the other pixel coordinate that is not taken into account in the position reconstruction and degrades the spatial resolution. Different reconstruction algorithms that take into account this correlation (using e.g. multivariate techniques) could be performed as an extension of the studies performed in this thesis, to further improve the spatial resolution, being especially interesting for the CLIC vertex detector, where a spatial resolution of  $3\ \mu\text{m}$  is required.

The timing resolution is limited by the readout system and similar values have been measured for both processes. The measured value of  $\sim 6\ \text{ns}$  is attractive for the CLIC tracking system, where a time slicing of  $10\ \text{ns}$  is required. Further measurements with a more defined assessment of the timing resolution can be performed. In a fully monolithic chip, where a threshold would be applied on chip, the timing resolution would correspond to the time where the signal crosses the threshold and be influenced by the measured distribution of the rise time. The larger fluctuations of the rise time for the standard compared to the modified process could correspond to a larger fluctuation of the threshold crossing. This could be investigated in further studies by calculating the threshold crossing and applying time walk corrections or measurements of the timing resolution for a fully monolithic chip in this technology.

A similar cluster signal has been measured for the standard and modified process and an efficiency  $> 99\ \%$  has been measured for both processes for threshold values  $\lesssim 350\ e^-$ . Due to the enhanced charge sharing for the standard compared to the modified process, the efficiency of the standard process drops at lower threshold values. Thus, the modified process is favourable in view of a larger fully efficient threshold range.

Further studies at different bias voltages show a more robust performance of the modified compared to the standard process in view of timing resolution and efficiency for lower bias voltages. Moreover, different spacings have been compared for the modified process. The results show that an intermediate spacing of  $3\ \mu\text{m}$  is a good compromise between an improved spatial resolution for smaller spacings and a faster rise time and a later efficiency drop at higher threshold values for larger spacings. Further optimisation studies could be performed e.g. for inclined particle tracks or more variants of the pixel geometry.

A simulation chain has been developed, that models the response of silicon detectors in view of cluster size, spatial resolution and efficiency. The TCAD simulations of both processes have been integrated in this simulation chain, and results have been compared to the test beam measurements for different epitaxial layer doping values. The comparison shows that the modified process is more robust against variations of the epitaxial layer doping, as already observed in the transient TCAD simulations. Overall, the simulation reproduces the test beam measurements and can be used to make performance predictions for future designs. As an example of such, the spatial resolution has been simulated for the modified process in dependence of the number of bits used for the digitisation of the measured pulse height. The results show that the benefit from more than one bit is with a few percent not significant for a noise of  $35\ e^-$  and a threshold of  $> 150\ e^-$ . However, a measurement of the signal height with a finer sampling can be beneficiary for other purposes, such as time walk corrections, measurements of the energy loss in the tracking layers ( $dE/dx$ ) or background rejection. All studies presented in this thesis have been

---

performed for a perpendicular particle incident and no magnetic field. The simulations can be used in further studies to predict the performance for inclined particle incidents and to predict the performance in presence of a magnetic field.

The results are not only relevant for the CLIC tracking system: the analogue performance evaluation and detailed simulation for different processes, bias voltages and pixel geometries are also relevant for other applications using this technology, especially for other HEP experiments with similar requirements as for the CLIC tracking system, such as the High-Luminosity upgrade of the LHC experiments. Moreover, the low noise makes this technology also attractive for low energy X-ray applications.

Overall, the evaluation of the analogue performance for the standard and modified process shows that both are interesting technologies to meet the requirements for the CLIC tracker. Based on the studies of this thesis, a fully monolithic chip is currently developed in this technology for the CLIC tracker.



## Noise characteristics

### A.1 Pixel-by-pixel noise fluctuations

The pixel-by-pixel noise fluctuations for different voltages for the standard process are presented in Figure A.1.

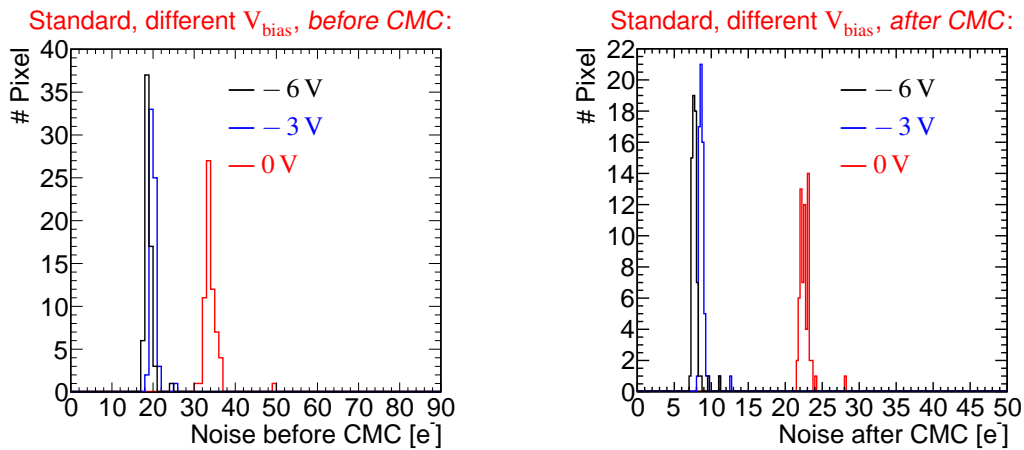


Figure A.1: Pixel-by-pixel noise fluctuations for different bias voltages  $V_{\text{bias}}$  before (during data taking, left) and after (during the analysis, right) the Common Mode Correction (CMC), for the and standard process.

For different spacings for the modified process the pixel-by-pixel noise fluctuations are shown in Figure A.2

### A.2 Noise before calibration

The noise in units of ADC before the calibration is presented for different bias voltages for the standard and modified process in Figure A.4.

The noise before the calibration is presented for different spacings in Figure A.4.

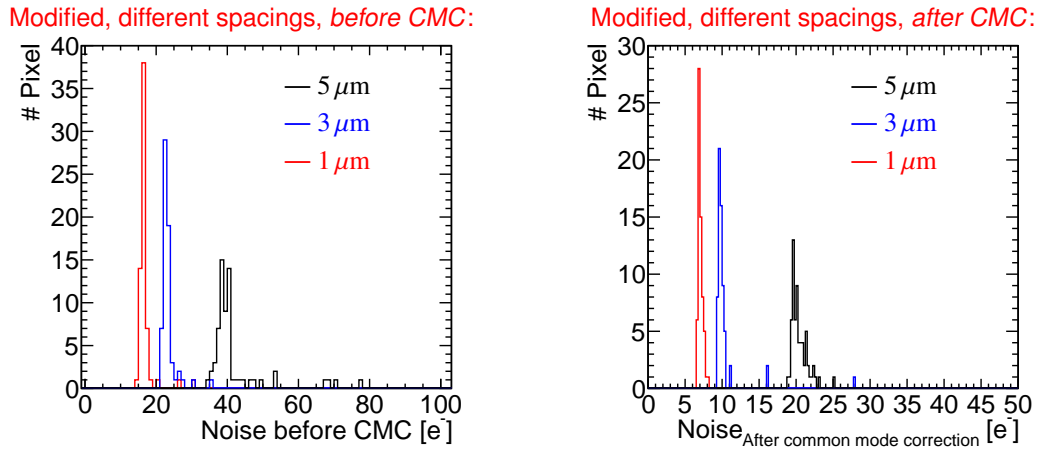


Figure A.2: Pixel-by-pixel noise fluctuations for different spacings *before* (during data taking, left) and *after* (during the analysis, right) the Common Mode Correction (CMC), for the and modified process.

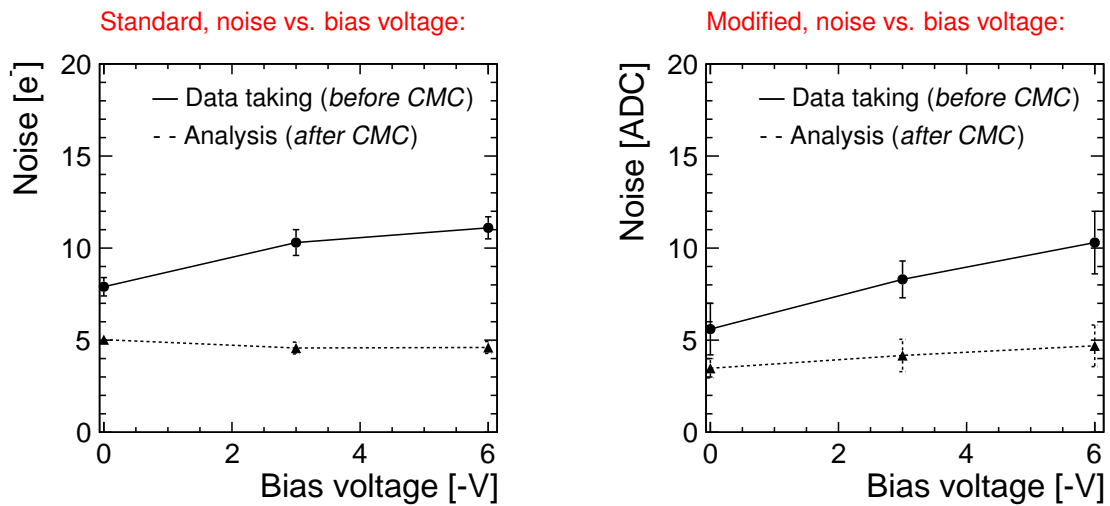


Figure A.3: Noise in units of ADC (before the calibration) versus bias voltage *before* and *after* the Common Mode Correction (CMC), for the standard (left) and modified (right) process.

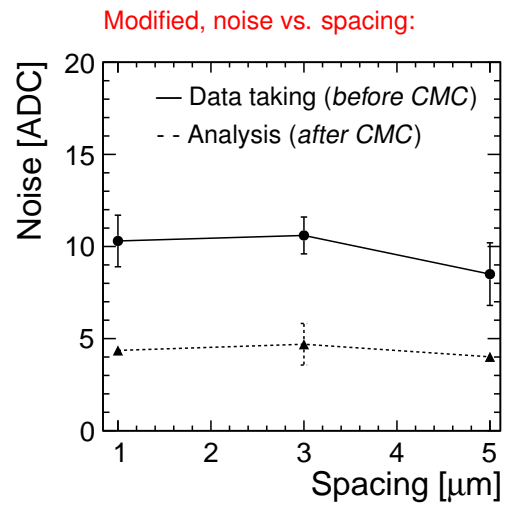


Figure A.4: Noise in units of ADC (before the calibration) versus spacing *before* and *after* the Common Mode Correction (*CMC*), for the modified process.



## Resolution for the standard process

Figure B.1 shows the Y cluster size within the pixel cell for the standard process at a bias voltage of  $-6\text{ V}$  and an analysis threshold of  $40\text{ e}^-$ .

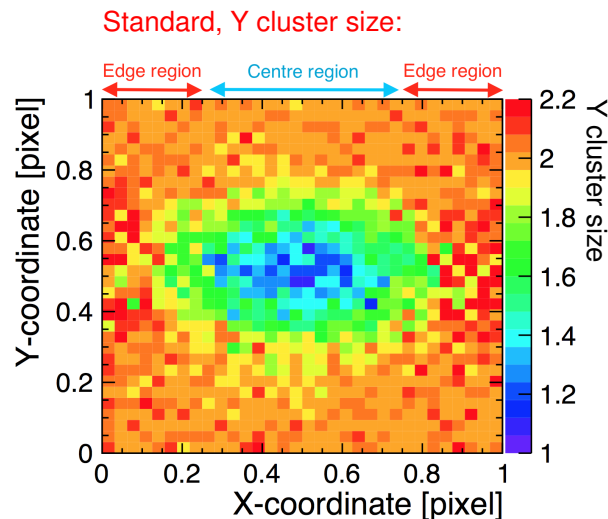


Figure B.1: In pixel representation of the cluster size in Y for the standard process at a bias voltage of  $-6\text{ V}$  and an analysis threshold of  $40\text{ e}^-$ .

Different regions can be observed in the in pixel representation of the Y cluster size:

- **Centre region:**

The *centre region* is defined at  $X \rightarrow 0$  and  $X \rightarrow 1$  (see regions marked by light blue arrow in the left plot of Figure B.1).

First, a particle passing through the Y centre at  $Y \rightarrow 0.5$  is considered (see light blue dot in Figure B.2). It traverses the depleted region and a cluster size close to one can be observed. This is illustrated by the light blue arrow in Figure B.2. The probability of charge sharing in Y is indicated by the size of the light blue arrow.

Secondly the case of a particle passing through the Y edge regions at  $Y \rightarrow 0$  and  $Y \rightarrow 1$  is considered (see light blue dots in Figure B.3). As explained for the modified process it is closer to the neighbouring pixel and the charge sharing is enhanced. However, in contrast to the modified

process the particle passes through non depleted regions at the Y edge. The charge created in the non depleted pixel region is less directed to a specific pixel, but propagates randomly. This results in an increased charge sharing in all directions of the pixel cell. From this contribution, the cluster size in Y is increased. This is illustrated by the light blue arrow in the right Plot of Figure B.3, where the increased probability of charge sharing in Y is indicated by the increased size of the light blue arrow.

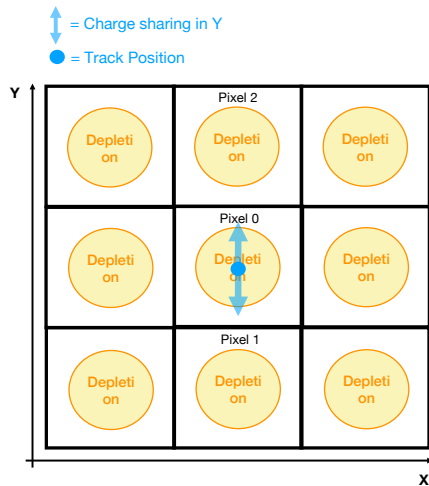


Figure B.2: Illustration of the charge sharing in Y, when the particles pass through the pixel centre.

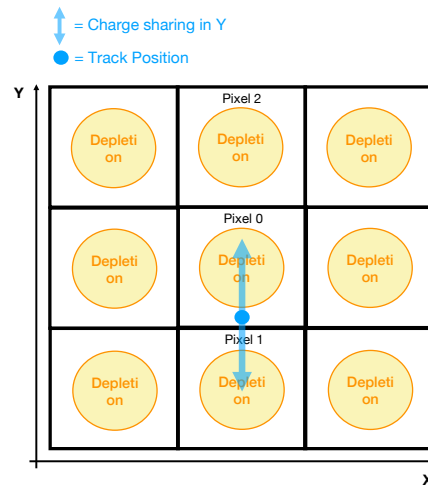


Figure B.3: Illustration of the charge sharing in Y at the edge of the pixel in Y dimension.

- **Edge region:**

The *edge regions* are defined at  $X \rightarrow 0$  and  $X \rightarrow 1$  (see regions marked by red arrows in the left plot of Figure B.1).

If a particle goes through this region it traverses the non depleted region and the created charges propagate more randomly. The increased cluster size in Y is illustrated by the increased size of the light red arrows in Figure B.4 and B.5.

The enhanced charge sharing probability in this region also results in a higher cluster size in Y if the particle passes through the Y centre of the pixel (see Figure B.4), since the distance to two neighbouring pixels in Y dimension is minimised, as illustrated by the red arrows reaching Pixel 1 and Pixel 2. For the case where the particle passes through the Y edge of the pixel (see Figure B.5) only the distance to one neighbouring pixel is minimised, as illustrated by the red arrows only Pixel 1. Consequently, the Y cluster size is higher in the Y centre compared to the Y edges of the pixel. This results in the charge sharing behaviour observed in Figure B.1.

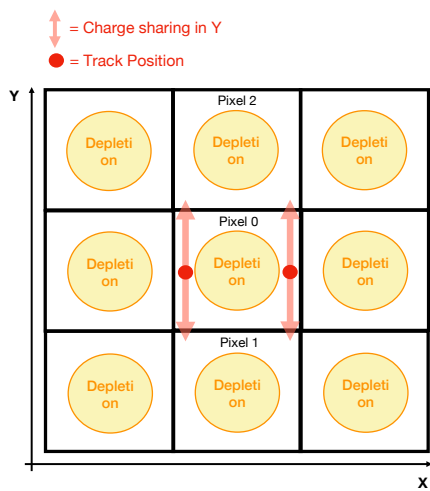


Figure B.4: Illustration of the charge sharing in Y, when the particles pass through the pixel centre.

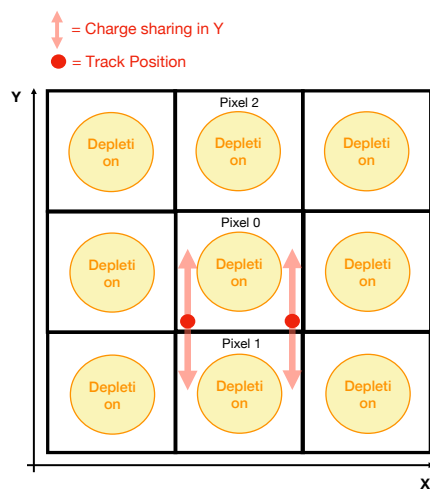


Figure B.5: Illustration of the charge sharing in Y, when the particles pass through the pixel edge.



# Bibliography

---

- [1] M. Aicheler et al., *A Multi-TeV Linear Collider Based on CLIC Technology: CLIC Conceptual Design Report*, tech. rep. CERN-2012-007, 2012 (cit. on pp. 1, 4, 6).
- [2] L. Linssen et al., *Physics and Detectors at CLIC: CLIC Conceptual Design Report*, tech. rep. CERN-2012-003, 2012 (cit. on pp. 1, 4, 7–9).
- [3] B. Abelev et al., *Technical Design Report for the Upgrade of the ALICE Inner Tracking System*, tech. rep. CERN-LHCC-2013-024, 2013, URL: <https://cds.cern.ch/record/1625842> (cit. on pp. 2, 25, 34).
- [4] W. Snoeys et al., *A process modification for CMOS monolithic active pixel sensors for enhanced depletion, timing performance and radiation tolerance*, *Nuclear Instruments and Methods in Physics Research A* **871** (2017) 90, URL: <http://www.sciencedirect.com/science/article/pii/S016890021730791X> (cit. on pp. 2, 33, 38, 63, 103, 106).
- [5] S. L. Glashow, *Partial Symmetries of Weak Interactions*, *Nucl. Phys.* **22** (1961) 579 (cit. on p. 3).
- [6] S. Weinberg, *A Model of Leptons*, *Phys. Rev. Lett.* **19** (21 1967) 1264, URL: <https://link.aps.org/doi/10.1103/PhysRevLett.19.1264> (cit. on p. 3).
- [7] A. Salam, *Weak and Electromagnetic Interactions*, *Conf. Proc.* **C680519** (1968) 367 (cit. on p. 3).
- [8] G. 't Hooft and M. J. G. Veltman, *Regularization and Renormalization of Gauge Fields*, *Nucl. Phys.* **B44** (1972) 189 (cit. on p. 3).
- [9] Wikipedia, 2017, URL: <https://commons.wikimedia.org/w/index.php?curid=4286964> (cit. on p. 3).
- [10] K. A. Olive et al., *Review of Particle Physics*, *Chin. Phys.* **C38** (2014) 090001 (cit. on pp. 4, 13, 15, 16, 19–21, 40).
- [11] P. W. Higgs, *Broken Symmetries and the Masses of Gauge Bosons*, *Phys. Rev. Lett.* **13** (16 1964) 508, URL: <https://link.aps.org/doi/10.1103/PhysRevLett.13.508> (cit. on p. 4).
- [12] P. W. Higgs, *Spontaneous Symmetry Breakdown without Massless Bosons*, *Phys. Rev.* **145** (4 1966) 1156, URL: <https://link.aps.org/doi/10.1103/PhysRev.145.1156> (cit. on p. 4).
- [13] G. Aad et al., *Observation of a new particle in the search for the Standard Model Higgs boson with the ATLAS detector at the LHC*, *Phys. Lett.* **B716** (2012) 1, arXiv: 1207.7214 [hep-ex] (cit. on p. 4).
- [14] S. Chatrchyan et al., *Observation of a new boson at a mass of 125 GeV with the CMS experiment at the LHC*, *Phys. Lett.* **B716** (2012) 30, arXiv: 1207.7235 [hep-ex] (cit. on p. 4).

- [15] L. Evans and P. Bryant, *LHC Machine*, *Journal of Instrumentation* **3** (2008) S08001 (cit. on p. 4).
- [16] G. Apollinari et al., *High-Luminosity Large Hadron Collider (HL-LHC) : Preliminary Design Report*, tech. rep. CERN-2015-005, FERMILAB-DESIGN-2015-02, 2015 (cit. on p. 4).
- [17] R. Assmann, O. Bailey R Bruning, O. Dominguez et al., *First Thoughts on a Higher-Energy LHC*, tech. rep. CERN-ATS-2010-177, 2010 (cit. on p. 4).
- [18] *Future Circular Collider Study*, (2017),  
URL: <https://fcc.web.cern.ch/Pages/default.aspx> (cit. on p. 4).
- [19] T. Behnke et al., *The International Linear Collider Technical Design Report - Volume 1: Executive Summary*, (2013), arXiv: [1306.6327](https://arxiv.org/abs/1306.6327) [[physics.acc-ph](https://arxiv.org/abs/1306.6327)] (cit. on p. 4).
- [20] C. Adolphsen et al., *The International Linear Collider Technical Design Report - Volume 3.II: Accelerator Baseline Design*, (2013), arXiv: [1306.6328](https://arxiv.org/abs/1306.6328) [[physics.acc-ph](https://arxiv.org/abs/1306.6328)] (cit. on p. 4).
- [21] C. Adolphsen et al., *The International Linear Collider Technical Design Report - Volume 3.II: Accelerator Baseline Design*, (2013), arXiv: [1306.6328](https://arxiv.org/abs/1306.6328) [[physics.acc-ph](https://arxiv.org/abs/1306.6328)] (cit. on p. 4).
- [22] H. Abramowicz et al., *The International Linear Collider Technical Design Report - Volume 4: Detectors*, (2013), ed. by T. Behnke et al., arXiv: [1306.6329](https://arxiv.org/abs/1306.6329) [[physics.ins-det](https://arxiv.org/abs/1306.6329)] (cit. on p. 4).
- [23] K. Fujii et al., *Physics Case for the International Linear Collider*, (2015),  
arXiv: [1506.05992](https://arxiv.org/abs/1506.05992) [[hep-ex](https://arxiv.org/abs/1506.05992)] (cit. on p. 4).
- [24] P. Lebrun et al., *The CLIC Programme: Towards a Staged e+e- Linear Collider Exploring the Terascale: CLIC Conceptual Design Report*, tech. rep. CERN-2012-005, 2012 (cit. on p. 4).
- [25] M. J. Boland et al., *Updated baseline for a staged Compact Linear Collider*, tech. rep. CERN-2016-004, 2016 (cit. on pp. 4, 5).
- [26] M. Munker, *Silicon pixel R&D for CLIC*, *JINST* **12** (2017) C01096 (cit. on pp. 5, 70).
- [27] A. Nurnberg, *Silicon pixel—detector R&D for CLIC*, *Journal of Instrumentation* **11** (2016) C11039,  
URL: <http://stacks.iop.org/1748-0221/11/i=11/a=C11039> (cit. on p. 5).
- [28] E. Sicking, *CLIC: Detector technology R&D for CLIC. CLIC: Detector technology R&D for CLIC*, (2018),  
URL: <https://cds.cern.ch/record/2307294> (cit. on p. 5).
- [29] H. Abramowicz et al., *Higgs physics at the CLIC electron–positron linear collider*, *Eur. Phys. J.* **C77** (2017) 475, arXiv: [1608.07538](https://arxiv.org/abs/1608.07538) [[hep-ex](https://arxiv.org/abs/1608.07538)] (cit. on p. 5).
- [30] E. Senes et al., “Results of the Beam-Loading Breakdown Rate Experiment at the CLIC Test Facility CTF3”, *Proceedings, 8th International Particle Accelerator Conference (IPAC 2017): Copenhagen, Denmark, May 14-19, 2017*, 2017 TUPAB017,  
URL: <http://inspirehep.net/record/1626346/files/tupab017.pdf> (cit. on p. 6).
- [31] D. Dannheim and A. Sailer, *Beam-Induced Backgrounds in the CLIC Detectors*, (2012),  
URL: <https://cds.cern.ch/record/1443516> (cit. on pp. 6, 9).
- [32] N. Alipour Tehrani et al., *CLICdet: The post-CDR CLIC detector model*, (2017),  
URL: <http://cds.cern.ch/record/2254048> (cit. on pp. 6, 7, 9, 10).

- [33] N. Alipour Tehrani, *Test-beam measurements and simulation studies of thin pixel sensors for the CLIC vertex detector*, PhD thesis, presented 13 Mar 2017 (cit. on pp. 7, 28, 42, 43, 49, 53, 145).
- [34] A. Nurnberg, ed., *Data taking experience with the CLICdp Timepix3 telescope*, 2017 (cit. on p. 9).
- [35] A. M. Nurnberg and D. Dannheim, *Requirements for the CLIC tracker readout*, (2017), URL: <https://cds.cern.ch/record/2261066> (cit. on pp. 10, 11).
- [36] L. Rossi et al., *Pixel detectors: From fundamentals to applications*, 2006, URL: [doi:10.1007/3-540-28333-1](https://doi.org/10.1007/3-540-28333-1) (cit. on pp. 17, 21, 23).
- [37] Wikipedia, 2018, URL: [https://upload.wikimedia.org/wikipedia/commons/6/62/Cmos\\_impurity\\_profile.PNG](https://upload.wikimedia.org/wikipedia/commons/6/62/Cmos_impurity_profile.PNG) (cit. on p. 18).
- [38] H. Kolanoski and N. Wermes, *Teilchendetektoren - Grundlagen und ihre Anwendungen*, 2016, ISBN: 978-3-662-45349-0 (cit. on pp. 18, 21, 22, 26, 29).
- [39] J. W. van Hoorne, *Study and Development of a novel Silicon Pixel Detector for the Upgrade of the ALICE Inner Tracking System*, PhD thesis, presented 24 Nov 2015, URL: <https://cds.cern.ch/record/2119197> (cit. on pp. 20, 33, 37, 39–41, 62, 71, 73, 74, 76, 80, 81, 83, 85–88, 105, 145).
- [40] H. Bichsel, *Straggling in thin silicon detectors*, Rev. Mod. Phys. **60** (1988) 663, URL: [doi:10.1103/RevModPhys.60.663](https://doi.org/10.1103/RevModPhys.60.663). (cit. on p. 20).
- [41] A. C. Thompson et al., *X-ray Data Booklet*, 2001 (cit. on p. 21).
- [42] M. Tilli et al., *Table of Radionuclides (Vol. 3 A = 3 to 244)*, 2010, ISBN: 978-0-8155-1594-4 (cit. on pp. 21, 105).
- [43] S. Ramo, *Currents Induced by Electron Motion*, Proc. IRE **27(9)** (1939) 584, URL: [doi:10.1103/RevModPhys.60.663](https://doi.org/10.1103/RevModPhys.60.663). (cit. on p. 22).
- [44] W. Snoeys, *Monolithic pixel detectors for high energy physics*, Nuclear Instruments and Methods in Physics Research Section A **731** (2013) 125, URL: [10.1016/j.nima.2013.05.073](https://doi.org/10.1016/j.nima.2013.05.073). (cit. on p. 23).
- [45] P. G. Rancoita and L. Claude, *Principles of Radiation Interaction in Matter and Detections*, 2016, ISBN: 981460318X (cit. on pp. 25, 27).
- [46] P. Valerio, R. Ballabriga and M. Campbell, *Design of the 65 nm CLICpix demonstrator chip*, (2012), URL: <https://cds.cern.ch/record/1507691> (cit. on p. 25).
- [47] N. Wermes, *From hybrid to CMOS pixels ... a possibility for LHC's pixel future?*, Journal of Instrumentation **10** (2015) C12023, URL: <http://stacks.iop.org/1748-0221/10/i=12/a=C12023> (cit. on p. 26).
- [48] S. Vähänen (Advacam), ed., *Solutions for flip chip bonding of future pixel detectors*, 2017 (cit. on p. 26).
- [49] K. Dette et al., *Commissioning of the ATLAS Insertable B-Layer and first operation experience*, Presented 24 Mar 2017, 2017, URL: <https://cds.cern.ch/record/2261168> (cit. on p. 27).
- [50] I. Peric, *A novel monolithic pixelated particle detector implemented in high-voltage CMOS technology*, Nucl. Instrum. Meth. **A582** (2007) 876 (cit. on p. 27).

- [51] N. A. Tehrani et al., *Capacitively coupled hybrid pixel assemblies for the CLIC vertex detector*, *Nuclear Instruments and Methods in Physics Research Section A* **823** (2016) 1, ISSN: 0168-9002, URL: <http://www.sciencedirect.com/science/article/pii/S016890021630095X> (cit. on pp. 27, 30).
- [52] A. Schwarz, *Silicon strip vertex detectors at LEP*, *Nuclear Instruments and Methods in Physics Research Section A* **342** (1994) 218 (cit. on p. 27).
- [53] N. Savic et al., *Investigation of thin n-in-p planar pixel modules for the ATLAS upgrade*, *JINST* **11** (2016) C12008. 9 p, URL: <http://cds.cern.ch/record/2216738> (cit. on p. 28).
- [54] G. Darbo, *Experience on 3D silicon sensors for ATLAS IBL*, *Journal of Instrumentation* **10** (2015) C05001, URL: <http://stacks.iop.org/1748-0221/10/i=05/a=C05001> (cit. on p. 28).
- [55] N. Cartiglia et al., *Tracking in 4 dimensions*, *Nuclear Instruments and Methods in Physics Research Section A* **845** (2017) 47, Proceedings of the Vienna Conference on Instrumentation 2016, ISSN: 0168-9002, URL: <http://www.sciencedirect.com/science/article/pii/S0168900216304715> (cit. on p. 29).
- [56] G. Pellegrini et al., *Recent technological developments on LGAD and iLGAD detectors for tracking and timing applications*, *Nuclear Instruments and Methods in Physics Research Section A* **831** (2016) 24, Proceedings of the 10th International Hiroshima Symposium on the Development and Application of Semiconductor Tracking Detectors, ISSN: 0168-9002, URL: <http://www.sciencedirect.com/science/article/pii/S0168900216304557> (cit. on p. 29).
- [57] A. Staiano et al., *Development of Ultra-Fast Silicon Detectors for 4D tracking*, *Journal of Instrumentation* **12** (2017) C12012, URL: <http://stacks.iop.org/1748-0221/12/i=12/a=C12012> (cit. on p. 29).
- [58] D. Lacour, *A High-Granularity Timing Detector for the Phase-II upgrade of the ATLAS calorimeter system: detector concept description and first beam test results*, *Journal of Instrumentation* **13** (2018) C02016, URL: <http://stacks.iop.org/1748-0221/13/i=02/a=C02016> (cit. on p. 29).
- [59] G. Kramberger et al., *Radiation effects in Low Gain Avalanche Detectors after hadron irradiations*, *Journal of Instrumentation* **10** (2015) P07006, URL: <http://stacks.iop.org/1748-0221/10/i=07/a=P07006> (cit. on p. 29).
- [60] A. Velyka and H. Jansen, *Enhanced lateral drift sensors: concept and development*, (2018), to appear in proceedings of the International Conference on Technology and Instrumentation in Particle physics 2017 (cit. on p. 29).
- [61] N. Wermes, *Pixel Detector Overview*, 2017, URL: <https://indico.cern.ch/event/577879/contributions/2743431/> (cit. on p. 30).
- [62] R. Turchetta et al., *A monolithic active pixel sensor for charged particle tracking and imaging using standard VLSI CMOS technology*, *Nuclear Instruments and Methods in Physics Research Section A* **458** (2001) 677, URL: <http://hal.in2p3.fr/in2p3-00012191> (cit. on p. 31).

- [63] M. D. Buckland, *TCAD simulations of High-Voltage-CMOS Pixel structures for the CLIC vertex detector*, (2016), URL: <https://cds.cern.ch/record/2159671> (cit. on pp. 32, 103).
- [64] M. D. Buckland, *Test-beam analysis and TCAD simulations of capacitively coupled HV-CMOS sensors*, 2017, URL: [https://agenda.linearcollider.org/event/7450/contributions/38593/attachments/31556/47533/MBuckland\\_LCVertexWorkshop\\_02-05-17.pdf](https://agenda.linearcollider.org/event/7450/contributions/38593/attachments/31556/47533/MBuckland_LCVertexWorkshop_02-05-17.pdf) (cit. on p. 32).
- [65] H. Augustin et al., *The MuPix high voltage monolithic active pixel sensor for the Mu3e experiment*, Journal of Instrumentation **10** (2015) C03044, URL: <http://stacks.iop.org/1748-0221/10/i=03/a=C03044> (cit. on p. 32).
- [66] B. Ristic, *Active Pixel Sensors in AMS H18/H35 HV-CMOS Technology for the ATLAS HL-LHC Upgrade*, Nucl. Instrum. Meth. **A831** (2016) 88, arXiv: 1602.02909 [physics.ins-det] (cit. on p. 32).
- [67] Y. Degerli et al., *Pixel architectures in a HV-CMOS process for the ATLAS inner detector upgrade*, Journal of Instrumentation **11** (2016) C12064, URL: <http://stacks.iop.org/1748-0221/11/i=12/a=C12064> (cit. on p. 32).
- [68] T. Obermann, *Performance evaluation of a fully depleted monolithic pixel detector chip in 150 nm CMOS technology*, PhD thesis, presented 09 June 2017, URL: <http://hss.ulb.uni-bonn.de/2017/4778/4778.htm> (cit. on p. 33).
- [69] H. Pernegger et al., *First tests of a novel radiation hard CMOS sensor process for Depleted Monolithic Active Pixel Sensors*, Journal of Instrumentation **12** (2017) P06008, URL: <http://stacks.iop.org/1748-0221/12/i=06/a=P06008> (cit. on p. 34).
- [70] Y. Arai et al., *Development of SOI pixel process technology*, Nuclear Instruments and Methods in Physics Research Section A **636** (2011) S31, 7th International Hiroshima Symposium on the Development and Application of Semiconductor Tracking Detectors, ISSN: 0168-9002, URL: <http://www.sciencedirect.com/science/article/pii/S0168900210009356> (cit. on p. 34).
- [71] M. I. Ahmed et al., *Prototype pixel detector in the SOI technology*, Journal of Instrumentation **9** (2014) C02010, URL: <http://stacks.iop.org/1748-0221/9/i=02/a=C02010> (cit. on p. 34).
- [72] H.-F. Hu et al., *An Advanced Double SOI CMOS Pixel Detector Termination With Trench Interspace*, IEEE SENSORS JOURNAL **15** (2015), URL: <http://ieeexplore.ieee.org/stamp/stamp.jsp?arnumber=7031853> (cit. on p. 34).
- [73] P. Collareta (GW-SEMI), *Epitaxial wafer trends in industry*, 2017, URL: [https://indico.cern.ch/event/635340/contributions/2763312/attachments/1552284/2439145/Silicon\\_Epitaxy.pdf](https://indico.cern.ch/event/635340/contributions/2763312/attachments/1552284/2439145/Silicon_Epitaxy.pdf) (cit. on p. 37).
- [74] W. Snoeys et al., *INVESTIGATOR TEST CHIP*, 2016, URL: [https://indico.cern.ch/event/483008/contributions/2001149/attachments/1226300/1795371/INVESTIGATOR\\_WS.pdf](https://indico.cern.ch/event/483008/contributions/2001149/attachments/1226300/1795371/INVESTIGATOR_WS.pdf) (cit. on pp. 38, 40).

- [75] C. Gao, T. Kugathasan, W. Snoeys et al., *INVESTIGATOR TEST CHIP*, (2016),  
URL: [https://indico.cern.ch/event/483008/contributions/2001149/attachments/1226300/1795371/INVESTIGATOR\\_WS.pdf](https://indico.cern.ch/event/483008/contributions/2001149/attachments/1226300/1795371/INVESTIGATOR_WS.pdf) (cit. on p. 39).
- [76] R. Sarpeshkar, D. Tobias and C. Mead, *White noise in MOS transistors and resistors*, (1993),  
URL: <https://www.ini.uzh.ch/~tobi/anaprose/noise/noise.pdf> (cit. on p. 40).
- [77] K. M. Sielewicz, *Mitigation methods increasing radiation hardness of the FPGA based Readout of the ALICE Inner Tracking System*, PhD thesis, to be presented in 2018 (cit. on p. 41).
- [78] ANALOG DEVICES, *AD9249: 16 Channel 14-Bit, 65 MSPS, Serial LVDS, 1.8 V A/D Converter*, 2013, eprint: <http://www.analog.com/media/en/technical-documentation/data-sheets/AD9249.pdf> (cit. on p. 41).
- [79] CERN SPS, eprint: <http://sba.web.cern.ch/sba/> (cit. on p. 42).
- [80] A. Nurnberg, *Timepix3 timing resolution in test beam*, 2016,  
URL: [https://indico.cern.ch/event/477007/contributions/1155207/attachments/1219119/1781274/20160128\\_vertex\\_nurnberg.pdf](https://indico.cern.ch/event/477007/contributions/1155207/attachments/1219119/1781274/20160128_vertex_nurnberg.pdf) (cit. on p. 43).
- [81] T. Poikela et al.,  
*Timepix3: a 65K channel hybrid pixel readout chip with simultaneous ToA/ToT and sparse readout*,  
*Journal of Instrumentation* **9** (2014) C05013 (cit. on p. 43).
- [82] R. M. Munker et al., *Study of the ALICE Investigator chip in view of the requirements at CLIC*, (2017), URL: <http://cds.cern.ch/record/2284145> (cit. on pp. 44, 46, 106).
- [83] I. Rubinskiy et al., *EUTelescope. Offline track reconstruction and DUT analysis software.*,  
EUNET-Memo-2010-12 (2010),  
eprint: <https://www.eudet.org/e26/e28/e86887/e107460/EUNET-Memo-2010-12.pdf>  
(cit. on p. 45).
- [84] S. J. Aplin, J. Engels and F. Gaede, *A production system for massive data processing in ILCSOFT*, (2009) (cit. on p. 45).
- [85] F. Gaede et al., *LCIO - A persistency framework for linear collider simulation studies*, (2013),  
URL: <https://cds.cern.ch/record/2119197> (cit. on p. 45).
- [86] GEAR, *GEometry Api for Reconstruction*,  
eprint: <http://ilcsoft.desy.de/gear/current/doc/html/index.html> (cit. on p. 45).
- [87] F. Gaede, *Marlin and LCCD: Software tools for the ILC*, *Nucl. Instrum. Meth.* **A559** (2006) 177  
(cit. on p. 45).
- [88] E. Belau et al., *Charge collection in silicon strip detectors*,  
*Nuclear Instruments and Methods in Physics Research* **214** (1983) 253, ISSN: 0167-5087  
(cit. on pp. 51, 138).
- [89] V. Blobel et al., *Software alignment for tracking detectors*,  
*Nuclear Instruments and Methods in Physics Research Section A* **566** (2006) 5,  
URL: <http://www.sciencedirect.com/science/article/pii/S0168900206007984>  
(cit. on p. 52).
- [90] *Geant4 a simulation toolkit*, (2003), ed. by S. Agostinelli et al.,  
*Nuclear Instruments and Methods in Physics Research: A506(2003)250-303* (physics.ins-det)  
(cit. on p. 59).

- [91] J. Apostolakis et al., *An implementation of ionisation energy loss in very thin absorbers for the GEANT4 simulation package*,  
*Nuclear Instruments and Methods in Physics Research Section A* **453** (2000) 597,  
ISSN: 0168-9002,  
URL: <http://www.sciencedirect.com/science/article/pii/S0168900200004575>  
(cit. on p. 59).
- [92] Synopsys, *Sentaurus Device User Guide*, (2013), URL: [www.synopsys.com](http://www.synopsys.com) (cit. on pp. 59, 86).
- [93] M. Be et al., *Handbook of Silicon Based MEMS Materials and Technologies*, 2006,  
ISBN: 92-822-2218-7 (cit. on p. 71).
- [94] W. Snoeys, *Private discussion*, 2017 (cit. on p. 94).



# List of Figures

---

2.1	Elementary particles of the Standard Model in 2017. From [9]. . . . .	3
2.2	Schematic layout of the CLIC accelerator complex for the highest energy stage [25]. . . . .	5
2.3	Schematic sketch of the CLIC beam structure (not to scale). . . . .	6
2.4	Luminosity spectrum for a CLIC centre of mass energy of 3 TeV. From [2]. . . . .	7
2.5	CLICdet - the CLIC detector model [32]. From [33]. . . . .	7
2.6	Layout of the CLIC vertex detector (orange) around the beam pipe (grey). From [32]. . . . .	9
2.7	Transverse momentum resolution for different single point resolutions versus momentum for muons simulated in the barrel. From [35]. . . . .	10
2.8	Layout of the CLIC tracker (green). The red structure presents the vertex detector, the orange structure the beam pipe. The black lines mark the support and the blue and magenta lines correspond to the cable routing path. From [35]. . . . .	10
3.1	Different MOS operation modes. Sketch (a) illustrates the accumulation, Sketch (b) the flat band, Sketch (c) the depletion and Sketch (d) the inversion operation mode, as discussed in the text. From [36]. . . . .	17
3.2	Schematic of a CMOS structure with an n and p type MOSFET, as described in the text. The metal is marked in white and the oxide in grey. From [37]. . . . .	18
4.1	General concept of hybrid pixel detectors. . . . .	26
4.2	Sketch of DC coupling between sensor and readout chip, using <i>bump bonds</i> . . . . .	26
4.3	Sketch of capacitive coupling between sensor and readout chip with a layer of glue: <i>without amplification in the sensor (left) and with an amplification stage integrated inside the pixel implant (right)</i> . . . . .	27
4.4	Planar p in n sensor. . . . .	27
4.5	Schematic cross section of an active edge sensor. . . . .	28
4.6	Schematic cross section of a 3d sensor. . . . .	28
4.7	Schematic cross section of an LGAD sensor. . . . .	29
4.8	Schematic cross section of an ELAD sensor. . . . .	30
4.9	General concept of monolithic pixel detector technologies. . . . .	31
4.10	Schematic cross section of HV CMOS sensors. . . . .	31
4.11	Schematic cross section of standard HR CMOS sensors ( <i>standard process</i> ). . . . .	32
4.12	Schematic cross section of HR CMOS sensors with the modification of an additional N layer ( <i>modified process</i> ). . . . .	33
4.13	Schematic cross section of a SOI CMOS sensor. . . . .	34
5.1	Schematic of view on the top of the pixel cell and definition of geometrical parameters. . . . .	38
5.2	Simplified schematic of the in-pixel circuitry of the Investigator. . . . .	38
5.3	Layout of the Investigator chip. From [75]. . . . .	39

5.4	Simplified schematic of Investigator waveform for one time cycle (not to scale), as discussed in the text. . . . .	41
5.5	Test beam setup of the CLICdp Timepix3 telescope in the H6 beam line of the CERN SPS. . . . .	42
5.6	Schematic of the veto and trigger logic. . . . .	44
5.7	Timing diagram illustrating the extension of the veto signal after a particle hit. . . . .	44
6.1	Example of a waveforms of a pixel <i>with (left)</i> and <i>without (right)</i> a particle hit. . . . .	46
6.2	Typical example of a calculated common mode noise waveform. . . . .	46
6.3	Example of a waveforms of a pixel <i>with (left)</i> and <i>without (right)</i> a particle hit after the common mode correction. . . . .	47
6.4	Illustration of procedure to estimate the particle hit time within the readout window. . . . .	47
6.5	Fit (red line) of a constant function with an exponential decay to the single pixel waveform. . . . .	47
6.6	$\chi^2/\text{ndof}$ of the waveform fits in equation 6.1. . . . .	48
6.7	Flowchart of the steps for the offline synchronisation of the Investigator and Timepix3 telescope data. The integer numbers symbolise telescope time stamps in arbitrary units. The floating point numbers symbolise Investigator pixel time stamps. . . . .	50
6.8	Example of histogram of the $\eta$ variable, as defined in the text. . . . .	51
6.9	Integral of the histogram in Figure 6.8, used to calculate the $\eta$ corrected position. . . . .	51
6.10	Biased residual on the third telescope plane with respect to the beam direction. . . . .	52
6.11	Illustration of the procedure to cut out the time windows where the Investigator or its readout are inactive, using the veto time stamp. The sketch shows the case where the Investigator active window is aligned with the veto time stamp. . . . .	53
6.12	Histogram of the difference between the track time stamp and time stamp of the telescope veto release. All tracks outside a range of $[100 \text{ ns}, 14 \mu\text{s}]$ are masked, as discussed in the text. . . . .	54
6.13	Illustration of the procedure to cut out the time windows where the Investigator or its readout are inactive, using the veto time stamp. The sketch shows the case where the veto time stamp is shifted to later times and thus not aligned with the veto time stamp. . . . .	54
6.14	Histogram of number of reset vetoes before a roi-track and after the long readout veto. . . . .	55
6.15	Description of the in-pixel representation. . . . .	57
6.16	Description of the cut performed on the test beam data to compare the observables to the two dimensional simulation. . . . .	58
7.1	Schematic and coordinate system of the Geant4 simulation (not to scale). A particle is shot into a silicon block. . . . .	60
7.2	Charge deposited by 120 GeV pions traversing a silicon block of $100 \mu\text{m}$ thickness projected into the X, Z plane. . . . .	61
7.3	Charge deposited by 120 GeV pions traversing a silicon block of $100 \mu\text{m}$ thickness projected along the depth Z ( <i>left</i> ) the transverse coordinate X ( <i>right</i> ) of the sensor (see Figure 7.1). . . . .	61
7.4	Schematic of the simulated cross section of a single pixel cell for the <i>standard process (left)</i> and the <i>modified process (right)</i> , with the pn junctions marked in yellow (not to scale). The colour intensities illustrate the doping levels: lower doping levels are indicated by a lighter colour. . . . .	62
7.5	Five-pixel structure of the Investigator standard process. . . . .	63
7.6	Position mesh of the Investigator standard process. The mesh has been adjusted to the gradient of the doping profile. . . . .	64

7.7	Sketch to illustrate the application of periodical boundary conditions to the TCAD simulation. . . . .	65
7.8	Hole density for a bias voltage of $-6$ V for the <i>standard process (left)</i> and the <i>modified process (right)</i> . The white line marks the edge of the depleted region. . . . .	65
7.9	Pixel current $I_{\text{pixel}}$ versus simulation time for a particle shot into the structure at the pixel centre for the standard process at a bias voltage of $-6$ V. The particle enters the simulated Investigator at 0 ns. . . . .	66
7.10	Charge versus integration time for a particle shot into the structure at the pixel centre for the standard process at a bias voltage of $-6$ V. . . . .	66
7.11	Total charge deposited by 120 GeV pions in a $25.5 \mu\text{m}$ thick silicon sensor. . . . .	68
7.12	Digitised charge $Q_{\text{Digi}}$ versus readout charge $Q$ for different number of bits, a saturation of $11000 e^-$ and a threshold of $1000 e^-$ . . . . .	69
8.1	Hole density for different bias voltages for the epi layer doping measured in [39] ( <i>norm, left</i> ) and for minimal doping values of $1.3 \cdot 10^{13}/\text{cm}^3$ ( <i>limit, right</i> ). The horizontal black line marks the depth up to where the doping values of the epi layer are set to a value of $1.3 \cdot 10^{13}/\text{cm}^3$ . The white line marks the edge of the depleted region. . . . .	73
8.2	Electrostatic potential for different bias voltages for the epi layer doping measured in [39] ( <i>norm, left</i> ) and for minimal doping values of $1.3 \cdot 10^{13}/\text{cm}^3$ ( <i>limit, right</i> ). The horizontal black line marks the depth up to where the doping values of the epi layer are set to a value of $1.3 \cdot 10^{13}/\text{cm}^3$ , the white line the edge of the depleted region. . . . .	74
8.3	Cuts along the sensor depth $Z$ through the electrostatic potential presented in Figure 8.2. . . . .	75
8.4	Absolute value of the electric field for different bias voltages for the epi layer doping measured in [39] ( <i>norm, left</i> ) and for minimal doping values of $1.3 \cdot 10^{13}/\text{cm}^3$ ( <i>limit, right</i> ). The horizontal black line marks the depth up to where the doping values of the epi layer are set to a value of $1.3 \cdot 10^{13}/\text{cm}^3$ , the white line the edge of the depleted region. . . . .	76
8.5	Cut along the sensor depth $Z$ through the electric field presented in Figure 8.4 for a bias voltage of $-6$ V. The plots are presented on a <i>linear scale (up)</i> and a <i>logarithmic scale (down)</i> . . . . .	77
8.6	Components in $X$ and $Z$ of the electric field presented in Figure 8.4 for a bias voltage of $-6$ V. The horizontal black line marks the depth up to where the doping values of the epi layer are set to a value of $1.3 \cdot 10^{13}/\text{cm}^3$ , the white line the edge of the depleted region. . . . .	78
8.7	Hole density for different bias voltages for the epi layer doping measured in [39] ( <i>norm, left</i> ) and for minimal doping values of $1.3 \cdot 10^{13}/\text{cm}^3$ ( <i>limit, right</i> ). The horizontal black line marks the depth up to where the doping values of the epi layer are set to a value of $1.3 \cdot 10^{13}/\text{cm}^3$ , the white line the edge of the depleted region. Without an applied bias voltage the three depleted regions evolving around the two p wells and from the deep planar junction are not overlapping and the n layer is not fully depleted. This is emphasised in the plot of the limit case at 0 V, where the depleted regions are hatched in white. . . . .	80
8.8	Electrostatic potential for different bias voltages for the epi layer doping measured in [39] ( <i>norm, left</i> ) and for minimal doping values of $1.3 \cdot 10^{13}/\text{cm}^3$ ( <i>limit, right</i> ). The horizontal black line marks the depth up to where the doping values of the epi layer are set to a value of $1.3 \cdot 10^{13}/\text{cm}^3$ . . . . .	81
8.9	Cuts along the sensor depth $Z$ through the electrostatic potential presented in Figure 8.8 for different bias voltages. . . . .	82

8.10	Absolute value of electric field for different bias voltages for the epi layer doping measured in [39] ( <i>norm, left</i> ) and for minimal doping values of $1.3 \cdot 10^{13}/\text{cm}^3$ ( <i>limit, right</i> ). The horizontal black line marks the depth up to where the doping values of the epi layer are set to a value of $1.3 \cdot 10^{13}/\text{cm}^3$ , the white line the edge of the depleted region.	83
8.11	Cut along the sensor depth Z through the electric field shown in Figure 8.10 for $-6\text{ V}$ .	84
8.12	Components in X ( <i>up</i> ) and Z ( <i>down</i> ) of the electric field presented in Figure 8.10 for a bias voltage of $-6\text{ V}$ . The horizontal black line marks the depth up to where the doping values of the epi layer are set to a value of $1.3 \cdot 10^{13}/\text{cm}^3$ , the white line the edge of the depleted region.	84
8.13	Electric field in X ( <i>up</i> ) and in Z ( <i>down</i> ) for a spacings $1\ \mu\text{m}$ ( <i>left</i> ) and $5\ \mu\text{m}$ ( <i>right</i> ), at $-6\text{ V}$ for the modified process and the epi profile presented in [39]. The white line marks the edge of the depleted region.	85
8.14	Summary of the comparison of the electrostatic simulations for the <i>standard process</i> ( <i>left</i> ) and the <i>modified process</i> ( <i>right</i> ). The hole density ( <i>up</i> ), the electrostatic potential ( <i>middle</i> ) and the electric field ( <i>down</i> ) are presented for the epi layer doping measured in [39] ( <i>norm</i> ). The white line marks the edge of the depleted region.	87
8.15	Electron density 1 ps after the charge generation for a particle incident at the <i>pixel centre</i> ( <i>left</i> ) and <i>pixel edge</i> ( <i>right</i> ) for the standard process.	88
8.16	Charge sharing functions for the <i>standard process</i> ( <i>left</i> ) and the <i>modified process</i> ( <i>right</i> ).	89
8.17	Electron density 1.5 ns after the particle incident at the <i>pixel centre</i> ( <i>left</i> ) the <i>pixel edge</i> ( <i>right</i> ) and in between, called <i>intermediate</i> ( <i>middle</i> ) for the <i>standard process</i> ( <i>up</i> ) <i>modified process</i> ( <i>down</i> ).	90
8.18	Hole density 1.5 ns after the particle incident at the <i>pixel centre</i> ( <i>left</i> ) the <i>pixel edge</i> ( <i>right</i> ) and in between, called <i>intermediate</i> ( <i>middle</i> ) for the <i>standard process</i> ( <i>up</i> ) and the <i>modified process</i> ( <i>down</i> ).	91
8.19	Total current versus simulation time for a particle incident at the pixel centre and edge for the <i>standard process</i> ( <i>left</i> ) and the <i>modified process</i> ( <i>right</i> ).	92
8.20	Charge versus integration time for a particle incident at the pixel centre and edge for the <i>standard process</i> ( <i>left</i> ) and the <i>modified process</i> ( <i>right</i> ).	92
8.21	Electron density 1 ps after the charge generation for different sensor depth for the <i>standard process</i> .	93
8.22	Electron density 1 ps after the charge generation for different sensor depth for the <i>modified process</i> .	93
8.23	Total current versus simulation time for the combined, the drift and the diffusion case for the <i>standard process</i> ( <i>left</i> ) and the <i>modified process</i> ( <i>right</i> ).	94
8.24	Readout charge for the combined, the drift and the diffusion case for the <i>standard process</i> ( <i>left</i> ) and the <i>modified process</i> ( <i>right</i> ).	94
8.25	Total current versus simulation time for the combined case and the sum of drift and diffusion. Results are presented for the <i>standard process</i> ( <i>left</i> ) and the <i>modified process</i> ( <i>right</i> ).	95
8.26	Difference of the electric field map after the particle incident with respect to the electrostatic case for the <i>standard process</i> ( <i>up</i> , $0.75\text{ ns}$ after the particle incident) and the <i>modified process</i> ( <i>down</i> , $0.3\text{ ns}$ after the particle incident).	96
8.27	Electron density 0.75 ns after the particle incident for different sensor depth for the <i>standard process</i> .	97
8.28	Hole density 0.75 ns after the particle incident for different sensor depth for the <i>standard process</i> .	97

8.29	Charge configuration after the particle incident for the combined and drift case. . . . .	98
8.30	Charge configuration after the particle incident for the diffusion case. . . . .	98
8.31	Comparison of the shape of the total current for different charge densities for the <i>standard process</i> . . . . .	98
8.32	Charge induced on the neighbouring pixel for different epi layer doping values for the <i>standard process (left)</i> and the <i>modified process (right)</i> . . . . .	99
8.33	Total current versus simulation time for a particle incident at the pixel centre and different epi layer doping values. Results are presented for the <i>standard process (left)</i> and the <i>modified process (right)</i> . . . . .	100
8.34	Total current versus simulation time for a particle incident at the pixel edge and different epi layer doping values. Results are presented for the <i>standard process (left)</i> and the <i>modified process (right)</i> . . . . .	100
8.35	Total current versus simulation time for a particle incident at the pixel centre and different lifetime values. Results are presented for the <i>standard process (left)</i> and the <i>modified process (right)</i> . . . . .	101
8.36	Charge versus integration time for a particle incident at the pixel centre and different lifetime values. Results are presented for the <i>standard process (left)</i> and the <i>modified process (right)</i> . . . . .	101
8.37	Leakage current versus bias voltage for different lifetime values for the <i>standard process (left)</i> and the <i>modified process (right)</i> for a simulated temperature of 20°C. . . . .	102
9.1	Single-pixel cluster identified as such at low and high thresholds. . . . .	106
9.2	Multi-pixel cluster identified as single-pixel cluster at high thresholds. . . . .	106
9.3	Spectrum from $^{55}\text{Fe}$ source measurements for different bias voltages for the <i>standard (left)</i> and <i>modified (right)</i> process. . . . .	107
9.4	Calibration factor for different bias voltages. . . . .	108
9.5	Spectrum from $^{55}\text{Fe}$ source measurements for different spacings for the modified process for a spacing of 1 $\mu\text{m}$ ( <i>left</i> ) and a spacing of 5 $\mu\text{m}$ ( <i>right</i> ). . . . .	109
9.6	Calibration factor for different spacings for the modified process at a bias voltage of $-6\text{ V}$ . . . . .	109
9.7	Pixel-by-pixel noise fluctuations for different bias voltages <i>before (during data taking, left)</i> and <i>after (during the analysis, right)</i> the Common Mode Correction (CMC), for the modified process. . . . .	110
9.8	Noise versus bias voltages <i>before</i> and <i>after</i> the Common Mode Correction (CMC), for the <i>standard (left)</i> and <i>modified (right)</i> process. . . . .	111
9.9	Threshold versus bias voltages <i>before</i> and <i>after</i> the Common Mode Correction (CMC), for the <i>standard (left)</i> and <i>modified (right)</i> process. . . . .	112
9.10	Noise versus spacing <i>before</i> and <i>after</i> the Common Mode Correction (CMC), for the modified process at a bias voltage of $-6\text{ V}$ . . . . .	112
9.11	Threshold versus spacing <i>before</i> and <i>after</i> the Common Mode Correction (CMC), for the modified process at a bias voltage of $-6\text{ V}$ . . . . .	112
9.12	Fit of equation 9.4 to a pixel without a particle hit for the modified process at $-6\text{ V}$ . . . . .	113
9.13	Average leakage current per pixel for different bias voltages for the standard and modified process. . . . .	114
10.1	Total cluster size distribution for the <i>standard process (left)</i> and for the <i>modified process (right)</i> . . . . .	118

10.2	In-pixel representation of the total cluster size for the <i>standard process (left)</i> and for the <i>modified process (right)</i> . . . . .	119
10.3	Cluster size distribution in X and Y dimension of the pixel matrix for the <i>standard process (left)</i> and for the <i>modified process (right)</i> . . . . .	120
10.4	Spatial residual distributions in X and Y dimension of the pixel matrix for the <i>standard process (left)</i> and for the <i>modified process (right)</i> . . . . .	120
10.5	Separately normalised residual distributions for <i>single-pixel (SP)</i> and <i>multi-pixel (MP)</i> cluster for the standard process. . . . .	121
10.6	In-pixel representation of the cluster size in X ( <i>left</i> ) and Y ( <i>right</i> ) for the standard process. . . . .	121
10.7	Separately normalised residual distributions for <i>single-pixel (SP)</i> and <i>multi-pixel (MP)</i> cluster for the modified process. . . . .	123
10.8	In-pixel representation of the cluster size in X ( <i>left</i> ) and Y ( <i>right</i> ) for the <i>modified process</i> . . . . .	123
10.9	Timing residual distribution for the <i>standard process (left)</i> and the <i>modified process (right)</i> . The uncertainties are defined as the uncertainty on the width of the Gaussian fit. . . . .	124
10.10	$T_{10-90}$ time distribution for the <i>standard process (black)</i> and the <i>modified process (red)</i> . . . . .	124
10.11	Cluster signal distribution for the <i>standard process (black)</i> and the <i>modified process (red)</i> . . . . .	125
10.12	Seed signal distribution for the <i>standard process (black)</i> and the <i>modified process (red)</i> . . . . .	126
10.13	In-pixel representation of the mean seed signal for the <i>standard process (left)</i> and the <i>modified process (right)</i> . . . . .	126
10.14	In-pixel representation of the efficiency for the <i>standard process (left)</i> and the <i>modified process (right)</i> . . . . .	127
10.15	Efficiency over the region of interest for the <i>standard process (left)</i> and the <i>modified process (right)</i> . . . . .	127
10.16	Mean total cluster size for different analysis thresholds. The error bars correspond to the uncertainty on the mean value and the thin vertical lines mark the triggering thresholds. . . . .	129
10.17	In-pixel representation of the total cluster size at different analysis thresholds for the <i>standard process (up)</i> and the <i>modified process (down)</i> . . . . .	130
10.18	Mean X and Y cluster size for different analysis thresholds. The error bars correspond to the uncertainty on the mean value and the thin vertical lines mark the triggering thresholds. . . . .	131
10.19	Resolution in X and Y direction for different analysis thresholds. The error bars correspond to the uncertainty on the RMS and the thin vertical lines mark the triggering thresholds. . . . .	131
10.20	Separately normalised residual distributions for <i>single-pixel (SP)</i> and <i>multi-pixel (MP)</i> cluster for the <i>standard process (up)</i> and the <i>modified process (down)</i> . . . . .	131
10.21	In-pixel representation of the Y cluster size at different analysis thresholds for the <i>standard process (up)</i> and the <i>modified process (down)</i> . . . . .	132
10.22	In-pixel representation of the efficiency at different high analysis thresholds for the <i>standard process (up)</i> and the <i>modified process (down)</i> . . . . .	133
10.23	Efficiency versus analysis threshold. The error bars correspond to the statistical uncertainties. The thin lines mark the triggering thresholds. . . . .	134
10.24	Timing resolution versus analysis threshold. The error bars correspond to the uncertainties on the width of the Gaussian fit. The thin vertical lines mark the triggering thresholds. . . . .	134
10.25	Cluster signal ( <i>left</i> ) and seed signal ( <i>right</i> ) for different bias voltages at an analysis threshold of $\sim 100 e^-$ for the standard process. . . . .	135
10.26	Total cluster size for different bias voltages at an analysis threshold of $\sim 100 e^-$ for the standard process. . . . .	136

10.27	$T_{10-90}$ time for different bias voltages at an analysis threshold of $\sim 100 e^-$ for the standard process. . . . .	136
10.28	Timing residual for different bias voltages at an analysis threshold of $\sim 100 e^-$ for the standard process. . . . .	136
10.29	Mean cluster size in X and Y for different bias voltages versus analysis threshold for the standard process. The error bars correspond to the uncertainty on the mean value. The thin vertical lines mark the triggering thresholds. . . . .	137
10.30	X and Y resolution for different bias voltages versus analysis threshold for the standard process. The error bars correspond to the uncertainty on the RMS of the residual distributions. The thin vertical lines mark the triggering thresholds. . . . .	137
10.31	Efficiency for different bias voltages at different analysis thresholds for the standard process. The error bars correspond to the statistical uncertainties. The thin vertical lines mark the triggering thresholds. . . . .	137
10.32	In-pixel representation of the Y cluster size at an analysis threshold of $\sim 130 e^-$ for a bias voltage of 0 V ( <i>left</i> ) and $-6$ V ( <i>right</i> ) for the standard process. . . . .	138
10.33	Distribution of the X cluster size ( <i>left</i> ) and the multi-pixel cluster X residual ( <i>right</i> ) at an analysis threshold of $\sim 370 e^-$ for different bias voltages for the standard process. . . . .	138
10.34	In-pixel representation of the efficiency at an analysis threshold of $\sim 370 e^-$ ( <i>left</i> ) and an analysis threshold of $\sim 700 e^-$ ( <i>right</i> ) for the standard process at a bias voltage of 0 V. . . . .	139
10.35	Cluster signal ( <i>left</i> ) and seed signal ( <i>right</i> ) for different bias voltages at an analysis threshold of $\sim 40 e^-$ for the modified process. . . . .	140
10.36	Mean X and Y cluster size for different bias voltages versus analysis threshold for the modified process. The error bars correspond to the uncertainty on the mean value. The thin vertical lines mark the triggering thresholds. . . . .	140
10.37	X and Y resolution for different bias voltages versus analysis threshold for the modified process. The error bars correspond to the uncertainty on the RMS. The thin vertical lines mark the triggering thresholds. . . . .	140
10.38	Efficiency for different bias voltages versus analysis threshold for the modified process. The error bars correspond to the the statistical uncertainty and the thin vertical lines mark the triggering thresholds. . . . .	141
10.39	$T_{10-90}$ time for different bias voltages at an analysis threshold of $\sim 100 e^-$ for the modified process. . . . .	142
10.40	Timing resolution for different bias voltages at an analysis thresholds of $\sim 100 e^-$ for the modified process. . . . .	142
10.41	Mean X and Y cluster size for different spacings versus analysis threshold for the modified process. The error bars correspond to the uncertainty on the mean value. The thin vertical lines mark the triggering thresholds. . . . .	142
10.42	X and Y resolution for different spacings versus analysis threshold for the modified process. The error bars correspond to the uncertainty on the RMS. The thin vertical lines mark the triggering thresholds. . . . .	142
10.43	Efficiency for different spacings as a function of the analysis threshold for the modified process. The error bars correspond to the statistical uncertainties. The thin vertical lines mark the triggering thresholds. . . . .	143
10.44	$T_{10-90}$ time for different spacings at an analysis threshold of $\sim 50 e^-$ for the modified process. . . . .	144

10.45	Timing resolution versus spacing at an analysis threshold of $\sim 50 e^-$ for the modified process. The error bars correspond to the uncertainty of the width of a Gaussian fit to the timing residuals. . . . .	144
11.1	Mean cluster size versus threshold for data (black) and the simulations with different epi layer doping values (magenta and red). The error bars correspond to the uncertainty on the mean value. . . . .	146
11.2	Spatial resolution versus threshold for data (black) and the simulations with different epi layer doping values (magenta and red). The error bars correspond to the uncertainty on the RMS. . . . .	146
11.3	Cluster size distribution for data (black) and the simulations with different epi layer doping values (magenta and red) at a threshold of $204 e^-$ . The error bars correspond to the statistical uncertainties. . . . .	147
11.4	Residual distribution for data (black) and the simulations with different epi layer doping values (magenta and red) at a threshold of $204 e^-$ . The error bars correspond to the statistical uncertainties. . . . .	147
11.5	Cluster size within the pixel cell for data (black) and the simulations with different epi layer doping values (magenta and red) for the standard process at a threshold of $204 e^-$ . The error bars are the RMS of the cluster size for one bin in the Y coordinate. . . . .	148
11.6	Efficiency within the pixel cell for data (black) and the simulations with different epi layer doping values (magenta and red) for the standard process at a threshold of $694 e^-$ . The error bars correspond to the statistical uncertainties. . . . .	148
11.7	Cluster size versus threshold for data (black) and the simulations with different epi layer doping values (magenta and red) for the modified process and a bias voltage of $-6 V$ . The error bars correspond to the uncertainty on the mean value. . . . .	149
11.8	Spatial resolution versus threshold for data (black) and the simulations with different epi layer doping values (magenta and red) for the modified process and a bias voltage of $-6 V$ . The error bars correspond to the uncertainty on the RMS. . . . .	149
11.9	Cluster size distribution for data (black) and the simulations with different epi layer doping values (magenta and red) for the modified process at a threshold of $257 e^-$ . The error bars correspond to the statistical uncertainties. . . . .	149
11.10	Spatial residual distribution for data (black) and the simulations with different epi layer doping values (magenta and red) for the modified process at a threshold of $257 e^-$ . The error bars correspond to the statistical uncertainties. . . . .	149
11.11	Cluster size within the pixel cell for data (black) and the simulations with different epi layer doping values (magenta and red) for the modified process at a threshold of $257 e^-$ . The error bars correspond to the RMS of the cluster size for one bin in the Y coordinate. . . . .	150
11.12	Efficiency within the pixel cell for data (black) and the simulations with different epi layer doping values (magenta and red) for the modified process at a threshold of $788 e^-$ . The error bars correspond to the statistical uncertainty. . . . .	150
11.13	Resolution (using $\eta$ correction) versus threshold for different number of bits. A noise of $35 e^-$ and a saturation of $10 ke^-$ have been simulated. . . . .	151
A.1	Pixel-by-pixel noise fluctuations for different bias voltages $V_{\text{bias}}$ before (during data taking, left) and after (during the analysis, right) the Common Mode Correction (CMC), for the and standard process. . . . .	157

---

A.2	Pixel-by-pixel noise fluctuations for different spacings <i>before (during data taking, left)</i> and <i>after (during the analysis, right)</i> the Common Mode Correction (CMC), for the and modified process. . . . .	158
A.3	Noise in units of ADC (before the calibration) versus bias voltage <i>before</i> and <i>after</i> the Common Mode Correction (CMC), for the standard ( <i>left</i> ) and modified ( <i>right</i> ) process. . . . .	158
A.4	Noise in units of ADC (before the calibration) versus spacing <i>before</i> and <i>after</i> the Common Mode Correction (CMC), for the modified process. . . . .	159
B.1	In pixel representation of the cluster size in Y for the standard process at a bias voltage of $-6\text{ V}$ and an analysis threshold of $40\text{ e}^-$ . . . . .	161
B.2	Illustration of the charge sharing in Y, when the particles pass through the pixel centre. . . . .	162
B.3	Illustration of the charge sharing in Y at the edge of the pixel in Y dimension. . . . .	162
B.4	Illustration of the charge sharing in Y, when the particles pass through the pixel centre. . . . .	163
B.5	Illustration of the charge sharing in Y, when the particles pass through the pixel edge. . . . .	163



# List of Tables

---

2.1	Cell sizes in the different tracker layers [35]. The <i>cell width</i> is defined in the $r - \Phi$ plane transverse to the beam direction. The <i>cell length</i> is defined in the direction of the beam for the tracker barrel layers and in the direction of the radius for the tracker disks. . . .	11
8.1	Parameters used for the TCAD simulations for the standard and modified process. . . .	71
9.1	Parameters of the studied Investigator chip and pixel layout. . . . .	105
9.2	Calibration factors for the studied Investigator mini matrices for a pixel size of $28 \mu\text{m}$ and an epi layer thickness of $25 \mu\text{m}$ . . . . .	115
9.3	Noise and threshold settings for the studied Investigator mini matrices for a pixel size of $28 \mu\text{m}$ and an epi layer thickness of $25 \mu\text{m}$ . The analysis threshold has been set five times above the noise. . . . .	115
10.1	Parameters of the studied Investigator chip and pixel layout. . . . .	118
10.2	Definition of operation conditions and analysed statistics. . . . .	118
10.3	Definition of operation conditions and analysed statistics for different bias voltages. . .	134
10.4	Definition of operation conditions and analysed statistics for the study of different spacings for the modified process. . . . .	141
11.1	Pixel layout and operation conditions for the comparison of the simulation to the test beam results. . . . .	146



# Acknowledgements

---

This work would not have been possible without the great environment I had the chance to be in the last years. I am very grateful for the opportunity to learn from excellent and very friendly experts.

First, I would like to express my deep gratitude to Professor Klaus Desch and Lucie Linssen, the group leader of the EP-LCD group at CERN, for giving me the opportunity for this PhD, their support and guidance.

I would like to thank Philipp Roloff for helping me with organising the years of my PhD and regularly dedicating time for discussions to keep up to date with my work.

I offer my heartfelt thankfulness to Andreas Nurnberg, who supported and guided my work throughout the whole PhD. Teaching me a lot and always taking time for questions and discussions, I could learn from his expert knowledge. I would like to thank him for reading my thesis and giving me very useful feedback. Thank you very much for all of it, I am very grateful and I will never forget.

My deep gratitude goes to Dominik Dannheim for many advices, guidance and generally for his interest and great support, that have contributed significantly to the work of this thesis. I am very grateful for the possibility to learn from him and his expert knowledge. I would like to thank Dominik for reading my thesis and providing me with very useful feedback.

My deep gratitude goes to Wolfgang Klempt. He has guided and supported my work from the very first day on. Coming from a background of data analysis and physics studies, he introduced me to the "hardware world", spend days with me in the lab and answered all my questions, being a great and patient teacher. I am very thankful for this.

My deep gratitude goes to Walter Snoeys. I am very thankful for his time to answer my questions on the technology. I am grateful for his guidance and support especially for the TCAD simulations and for sharing his expert knowledge with me. I would like to thank Walter for reading the TCAD chapter of my thesis and giving me very useful remarks.

I would like to thank the ALICE collaboration for providing the test chips, the readout software and readout board for several test beam campaigns. I would like to thank especially Jacobus van Hoorne, who supported the Investigator studies, shared his experience, dedicated times for discussions and provided the readout software and data of  $^{55}\text{Fe}$  measurements. I would further like to thank Krzysztof Sielewicz for the opportunity to use the INVROS in several test beam campaigns.

Beside Andreas Nurnberg, Dominik Dannheim and Wolfgang Klempt, I would like to thank Adrian Fiergolski and Daniel Hynds for making the test beam operations with the Investigator possible and sharing exciting times in the SPS test beam hall.

I would like to thank Konrad Elsener for reading the CLIC part of this thesis.

I would like to thank all people that have been part of the EP-LCD group at CERN during the last years. It was a pleasure for me to be part of this excellent and friendly group. I would like to thank especially Daniel Hynds, who was a perfect office made. As an expert on silicon technologies and as a great person he gave me support on a professional and personal level. Thank you for your friendship.

I would like to express my warm and heartfelt gratitude to my family. They believed in me and supported me in any possible way, always understanding when I am absorbed by my work. Mum and

dad, your education, support and love have brought me here.

I acknowledge the support and funding of the Wolfgang-Gentner-Programme.